Investigation on the Three-Dimensional Flow Mechanisms in Annular Axial Compressor Cascades for Aero Engines with Flow Control by Aspiration on the Hub and on the Blades

PAR

Elia COLOMBO

ÉCOLE POLYTECHNIQUE
FÉDÉRALE DE LAUSANNE

Suisse
2011

Acknowledgements

Abstract

The axial compressor is an essential component of aero-engines and gas turbines. This work investigates how flow control by aspiration applied to the hub and to the blades of axial compressor wheels can improve the static pressure rise by preventing detrimental flow features that cause aerodynamic loss and flow non-uniformity. It also investigates if the improvement obtained by this technique can compensate the increased loss that occurs if the number of blades is reduced. This would allow reducing the mass of the compressor. The three-dimensional flow related to the technique of flow control by aspiration is analyzed, yielding a better understanding of the involved flow mechanisms and supporting the further development of this technique.

To model the flow in the stator wheel of an axial compressor, different annular cascades are designed and manufactured. They are tested in the Non-Rotating Annular Test Facility of the EPFL. The flow on configurations without aspiration, with aspiration on the hub only and with aspiration both on the hub and on the blades is investigated for different aspiration rates. The last configuration is tested for two different blade numbers. This work analyzes the results obtained for same inlet flow Mach number in the high subsonic range and two different inlet flow incidence angles. Several measurement techniques are applied: aerodynamic five-hole probe measurements in the inlet and outlet planes, static pressure tap measurements on the blades and on the walls, Laser-Doppler-Anemometry measurements and skin friction line visualization. The analysis of the measurement results is supported by the analysis of numerical simulations based on the inlet flow conditions measured during the experimental investigations.

The work is contextualized by a bibliographic research on the state of the art in the domain of flow control by aspiration in axial compressors as well as on the particular flow features occurring. A simple model based on the conservation of mass and total enthalpy is derived to clarify the influence of flow aspiration on the static pressure rise. An adequate set of parameters is defined to quantify the cascade performance. To identify particular three-dimensional flow features in the outlet plane measurements, the rotational flow field is analyzed in terms of vorticity and helicity. Particular attention is given to so-called secondary flow features that are induced by the streamwise vorticity occurring in the flow. An innovative method to extract the secondary velocity field from the outlet plane measurements is derived. It is based on the Helmholtz decomposition. The approach is implemented using a finite element method and is used to post-process the outlet plane measurements. The comparison with the results of a classical approach shows that the results of the new method are significantly improved in detail and plausibility.

The investigation identifies a number of flow mechanisms occurring in the cascade that are compared for the different configurations. The tested aspiration system is shown to have a beneficial effect in several cases, especially for the lower inlet flow incidence angles, where an improved performance in terms of total pressure level, blade loading, static pressure rise and outlet flow uniformity is obtained. Also for some cases with reduced number of blades, thanks to the aspiration, a similar performance in terms of static pressure rise and total pressure loss is achieved as for the reference case with higher number of blades. Although more optimistic, especially on the influence of the aspiration on blade, the numerical results reproduce the main flow features and can thus be used to support the analysis. The detailed analysis of the flow mechanisms related to the aspiration shows and explains the occurrence of problematic recirculations in the aspiration ducts. This gives indications for the further development of the aspiration system.

Keywords: aero-engine, axial compressor, bleed, corner separation, flow control by aspiration, gas turbine, helicity, Helmholtz decomposition, secondary flow, three-dimensional separation, vorticity.

Résumé

Le compresseur axial est une composante essentielle des propulseurs aéronautiques et des turbines à gaz en général. L'augmentation du rendement et la réduction de la masse sont ainsi des enjeux majeurs de l'industrie. La technique de contrôle d'écoulement par aspiration constitue une solution qui peut s'avérer efficace. Cette étude montre comment cette technique appliquée sur le moyeu et sur les aubes de roues du compresseur permet d'améliorer la compression. Cette technique vise surtout à réduire et prévenir des mécanismes aérodynamiques défavorables provoquant des pertes et de l'hétérogénéité dans l'écoulement. Ce travail étudie aussi l'intérêt de la méthode pour compenser l'augmentation de pertes qui surviennent si le nombre d'aubes d'une roue est réduit dans le but d'alléger le compresseur. Les mécanismes aérodynamiques impliqués sont identifiés et expliqués par l'étude des écoulements tridimensionnels, ce qui permettra le perfectionnement de cette technique.

Dans cette étude, l'écoulement au sein d'une roue stator de compresseur axial est reproduit au moyen de différentes grilles d'aubes annulaires testées dans le stand d'essai annulaire non rotatif de l'EPFL. Des expériences sont effectuées sur des configurations sans aspiration, avec aspiration sur le moyeu seulement et avec aspiration simultanée sur le moyeu et sur les aubes avec différents taux d'aspiration. Des expériences ultérieures avec aspiration sur moyeu et aubes sont réalisées avec une grille dont le nombre d'aubes est réduit. Ce travail analyse les résultats obtenus pour des mesures effectuées à un même nombre de Mach en entrée en haut subsonique et à deux angles d'incidence de l'écoulement en entrée. Différentes techniques de mesure sont appliquées : mesures avec sondes aérodynamiques à cinq trous dans les plans d'entrée et de sortie, prises de pression sur les aubes et sur les parois, anémométrie laser (LDA) et visualisation des lignes de frottement. L'interprétation des résultats est supportée par l'analyse de résultats de simulations numériques obtenus à partir des conditions mesurées lors des expériences.

Une recherche bibliographique expose l'état de l'art dans le domaine du contrôle des écoulements au sein des compresseurs axiaux ainsi que des écoulements tridimensionnels associés. Un simple modèle basé sur la conservation de la masse et de l'enthalpie totale est dérivé pour clarifier l'influence de l'aspiration sur la compression. Un ensemble de paramètres appropriés pour quantifier le rendement des grilles d'aubes aspirées est défini. Pour identifier les mécanismes tridimensionnels particuliers dans le plan de sortie de la grille d'aubes, le champ aérodynamique rotationnel est analysé en termes de vorticité et hélicité. Une attention particulière est donnée à l'écoulement secondaire induit par la vorticité alignée avec l'écoulement dans la grille. Cette analyse est rendue possible par l'introduction d'une nouvelle méthode pour extraire le champ de vitesses secondaires des mesures effectuées dans le plan aval basée sur la décomposition d'Helmholtz. Cette méthode implémentée en utilisant une approche aux éléments finis pour post-traiter les résultats de mesure. La comparaison avec une approche plus classique montre que la nouvelle méthode produit des résultats significativement améliorés en termes de détail et plausibilité.

Cette étude permet d'identifier différents mécanismes aérodynamiques qui surviennent dans l'écoulement et de les comparer pour différentes configurations. Il est démontré que le système d'aspiration a des effets bénéfiques dans plusieurs cas, spécialement pour l'angle d'incidence plus faible où le rendement en termes de niveau de pression totale, charge des aubes et compression est amélioré. De même, pour certains cas avec un nombre d'aubes réduit, grâce à l'aspiration, un rendement similaire à celui des cas avec plus d'aubes est obtenu. Les résultats des simulations numériques reproduisent les principaux mécanismes aérodynamiques et soutiennent ainsi l'analyse, même si plus optimistes, en particulier sur l'influence de l'aspiration sur les aubes. L'analyse détaillée de ces résultats décrit de plus les phénomènes de recirculations intervenant dans les conduites d'aspiration, ce qui permet d'aboutir à des indications quant au perfectionnement ultérieur du système d'aspiration.

Mots clés : Aspiration, propulseur, compresseur axial, control d'écoulement, écoulement secondaire, hélicité, décomposition d'Helmholtz, séparation de coin, séparation 3D, turbine à gaz, vorticité.

Table of contents

Nomenclature

Acronyms

3D	Three dimensional
ACARE	Advisory Council for Aeronautics Research in Europe
AGARD	Advisory Group for Aerospace Research and Development
APNASA	A Navier-Stokes code for multistage compressor analysis
Aspi.	Aspiration
BL	Boundary layer
CFD	Computational Fluid Dynamics
CO2	Carbon dioxide
CNC	Computer Numerical Control
DS	Downstream
ECL	Ecole Centrale de Lyon
EPFL	Ecole Polytechnique Fédérale de Lausanne
elsA	Ensemble Logiciel de Simulation en Aérodynamique
FP6	6th European Framework Programm
GDP	Gross Domestic Product
HPC	High pressure compressor
IB	Interblade
$k - \varepsilon$	$k - \varepsilon$ turbulence model
L.E.	Leading edge (of a blade)
LDA	Laser Doppler Anemometry
LFE	Laminar Flow Element
LMFA	Laboratoire de mécanique des fluides et d'acoustique (ECL)
LTT	Laboratoire de Thermodynamique appliquée et de Turbomachines
MISES	A collection of programs developed by MIT for cascade analysis and design
MIT	Massachusetts Institute of Technology
NACA	National Advisory Commitee for Aeronautics
NACA-65	A specific airfoil prodile based on the NACA catalog
NASA	National Aeronautics and Space Administration
NEWAC	New Aero-engine Core concepts
NOx	Nitrogen oxides
P.S.	Pressure side (of a blade)
RANS	Reynolds Averaged Navier Stokes
RMS	Root mean square
S.S.	Suction side (of a blade)
T.E.	Trailing edge (of a blade)
US	Upstream
VISION 2020	Name of the ACARE recommendation for pollution reduction

Discussed aspiration configurations
A1, B1, B2, C1, C2, D1, D2   See definition in chapter 10 on page 102

Latin symbols

A	Flow surface [m^2]
c	Chord length [m]
c_x	Axial chord length [m]

c_p	Isobaric heat capacity [J/(kg K)]
C_Q	Aspiration rate $\dot{m}_{asp}\,/\,\dot{m}_1$ defined in section 2.2.3 [-]
$C_{Q,Slot}$	Aspiration rate per slot $(\dot{m}_{asp}\,/\,N_{Slots})\big/\dot{m}_1$ defined in section 2.2.3 [-]
Cx%	Position relative to the leading edge with respect to the axial chord length of the blade [-]
dA	Infinitesimal area element [m^2]
D	Deceleration parameter (see definition in section 2.3.1) [-]
DF	Lieblein Diffusion Factor (see definition in section 2.3.1) [-]
"E"	Test facility window oriented towards the East
E_θ	Probe shaft offset with respect to the cascade axis (see Figure 7-6) [m]
$\vec{e}_i$	Unit vector of vector i in carthesian coordinates [m]
$\vec{f}$	External volume force field
H	Blade height [m]
H%	Radial position with respect to the blade height $\text{H\%} = (R - R_{Hub})\,/\,\text{H} \cdot 100\%$ [%]
H	Helicity [m/s^2]
h_t	Specific stagnation enthalpy [J/kg]
K_{ij}	Curvature of streamline i with in direction of j [1/m]
L	Length of the head part of an L-shpaed probe (see Figure 7-6) [m]
$\dot{m}$	Massflow [kg/s]
Ma	Isentropic Mach number [-]
"N"	Test facility side oriented towards the North
N_{Blades}	Number of blades per cascade [-]
N_{Slots}	Number of aspiration slots per cascade [-]
P	Symbol for a stagnation point
p_s , p	Static pressure [Pa]
$p_{s,chamber}$	Static pressure in the settling chamber behind the aspiration ducts [Pa]
p_t	Total pressure [Pa]
Q	An arbitrary scalar quantity or scalar field
$\vec{Q}$	An arbitrary vector quantity or vector field
R	Specific gas constant [J/(kg K)] or radial coordinate [m]
T_s , T	Static temperature [K]
T_t	Total temperature [K]
"S"	Test facility side oriented towards the south
S	Absolute entropy [J/K]
s	Specific entropy [J/(kg K)]
s_m	Average blade pitch [m]
t	Time [s]
$\vec{U}$	Circumferential velocity vector [m/s]
$V_\perp$, V_{norm}	Velocity component normal to a specified plane [m/s]
$\vec{V}$	Velocity vector [m/s]
V_i	Component of the velocity vector in direction i [m/s]
$\vec{V}_{sec}$	Secondary velocity vector, see definition in section 3.3.2 [m/s]
$\vec{W}$	Relative velocity vector in a rotating frame defined as $\vec{V} = \vec{W} + \vec{U}$ [m/s]
x, y, z	Carthesian coordinates [m]

x_1, x_2, x_3	Arbitrary coordinates [m]
y^+	Dimensionless wall distance [-]

Greek symbols

α	Flow angle with respect to the axial direction $\arctan V_\theta / V_x$ (see Figure 6-1) [°]
α_0	Pre-rotation angle of the aerodynamic probe with respect to the cascade axis [°]
$\Delta\alpha_{12}$	Deflection $\alpha_1 - \alpha_2$
α_C, α_s	Pitch flow angle in a cylindrical or probe-attached referential (see section 7.5.3)
γ_C, γ_s	Yaw flow angle in a cylindrical or probe-attached referential (see section 7.5.3)
δ	Angle between the velocity and the vorticity vectors [°]
κ	Isentropic exponent [-]
Π_{12}	Pressure ratio p_2 / p_1
ρ	Density [kg/m^3]
ρ_0	Azimuthal displacement of the probe measurement location (see Figure 7-6) [°]
μ	Dynamic viscosity [Pa s]
ν	Kinematic viscosity $\nu = \mu / \rho$ [m^2/s]
σ	Cascade solidity $\sigma = c / s_m$ [-]
ϕ	Scalar potential field, see definition in section 3.3.2
χ	Entropy loss parameter defined in section 2.2.1 [-]
$\vec{\Psi}$	Vector potential field, see definition in section 3.3.2
$\vec{\Omega}$	Vorticity vector defined in section 3.1 [1/s]
Ω_i	Component of the vorticity vector in direction i [1/s]
ω	Total pressure loss parameter defined in section 2.2.1 [-]
$\omega_{overall}$	Total pressure loss including the aspiration path loss defined in section 2.2.4 [-]
$\vec{\omega}$	Wheel rotation

Mathematical conventions based on [Powers 2011]

$|\vec{Q}|$	Magnitude of vector $\vec{Q}$
DQ / Dt	Substantial derivative of Q, equivalent to $\partial Q / \partial t + (\vec{V}^T \cdot \nabla)Q$ [scalar]
$D\vec{Q} / Dt$	Substantial derivative of $\vec{Q}$, equivalent to $\partial \vec{Q} / \partial t + (\vec{V}^T \cdot \nabla)\vec{Q}$ [vector]
$\partial / \partial x$	Partial derivative (in this case, in x direction)
Δ	Difference or Laplace operator (depending on the context)
∇	Nabla operator equivalent to $(\partial / \partial x, \partial / \partial y, \partial / \partial z)^T$ in carthesian coordinates
$\nabla \times \vec{Q}$	Rotational of $\vec{Q}$, equivalent to $\overrightarrow{rot}\,\vec{Q}$ [vector]
∇Q	Gradient of Q, equivalent to $\overrightarrow{grad}\,Q$ [vector]
$\nabla^T \cdot \vec{Q}$	Divergence of $\vec{Q}$, equivalent to $div\,\vec{Q}$ or $\nabla \cdot \vec{Q}$ in other conventions [scalar]
$(\vec{Q}_2^T \cdot \nabla)\,Q_1$	Directional gradient of quantity Q_1 in direction $\vec{Q}_2$, equivalent to $\overrightarrow{grad}Q_1 \cdot \vec{Q}_2$ [scalar]
$(\vec{Q}_2^T \cdot \nabla)\,\vec{Q}_1$	Directional gradient of quantity $\vec{Q}_1$ in direction $\vec{Q}_2$, equivalent to $\overrightarrow{grad}\vec{Q}_1 \cdot \vec{Q}_2$ [tensor]

Coordinate systems

(x, y, z) Carthesian coordinate system. In this work x is aligned with the machine axis

(x, θ, R) Cylindrical coordinates: axial, circumferential and radial coordinates

(x, φ, R) Cylindrical coordinates fixed to the test cascase (see definition in section 7.1)

(s, n, b) Orthogonal coordinate system where the coordinate s is aligned with the local streamwise direction of the flow, n is an arbitrary direction normal to s, and b is the binormal direction that is normal to s and n

(x_s, y_s, z_s) Coordinate system aligned with the probe

(x_C, y_C, z_C) Cylindrical coordinates used in section 7.5.3

Subscripts

1   Inlet flow plane
2   Outlet flow plane
asp   Aspiration
c Compressed
irrotational   Denotes an irrotational vector field
max   Maximum of the quantity within the flow field
overall   Overall (used for observations including both main flow path and aspiration path)

Macrons

$\dot{Q}$ Quantity per time unit

$\tilde{Q}$ Area weighted average of quantity Q

$\hat{Q}$ Massflow weighted average of quantity Q

$\overline{Q}$ Average of quantity Q obtained from other averaged quantities

Averages

$p_t / \hat{p}_{t1}$ stagnation pressure normalized by mass averaged inlet stagnation pressures

$\tilde{p}_{s2} / \tilde{p}_{s1}$ static pressure rise based on area averaged static pressures

$\overline{\alpha}_1 - \overline{\alpha}_2$ average deflection based on mass averaged velocity components

$\omega = \left(\hat{p}_{t1} - \hat{p}_{t2} \right) / \left(\hat{p}_{t1} - \tilde{p}_{s1} \right)$ losses of p_t (with $\hat{p}_t$ mass averaged, $\tilde{p}_s$ area averaged)

PART I - THEORETICAL BACKGROUND

1. Introduction

1.1 Motivation

In the last decades, air travel experienced about 5% of annual growth bringing to society a significant increase in mobility and economic benefits [Quentin et al. 2008]. Air transportation contributes today to about 8% of the World GDP, handles 40% of the goods exported between regions, yields 30 Million jobs in the world and brings different cultures and nations closer [Remy 2010]. The growth however also brings new challenges: to ensure the sustainability in economic and environmental terms, steady progress is needed in the domains of fuel economy and emissions while preserving the engine security. For this purpose, the Advisory Council for Aeronautics Research in Europe (ACARE) expressed the recommendation VISION 2020: based on the assumption that the main fuel in use will still be kerosene, it is recommended to reduce amongst others the CO2 emissions by 50% and the NOx emissions by 80% until 2020. It is expected that 15 to 20% reduction can be achieved by the aero engine improvement. Considering the million miles flown each year, it is evident that each performance improvement has an important beneficial economic and environmental impact. The project NEWAC (NEW Aero engine Core concepts) that funded the present work is an integrated European FP6 research project born to work towards VISION 2020. It consists in a cooperation of usually competing industries and of several academic institutions. Its approach is to develop advanced component technology with shared efforts and shared risks.

The present work originated from a sub-project of NEWAC. It is related to axial compressors with high subsonic inlet Mach number and investigates the possible improvement by application of the technique of flow control by aspiration. Such axial compressor is an important constitutive element common to most current gas turbine aero engines. Herewith it significantly impacts the thermal efficiency, operating range and mass of the engine and hence the engine emissions, security and costs. Since gas turbines were invented, the challenge in the axial compressor development is to achieve the needed static pressure rise with least component mass and size and highest efficiency. Mass and size can be reduced if the stage loading is increased, meaning the pressure rise per component, since with higher component loading, the needed pressure rise could be achieved with fewer or more compact highly loaded stages. However, to ensure good efficiency, the aerodynamic losses that occur when the stage loading is increased must be prevented. A further requirement is an acceptable operating range, meaning a sufficient stall margin. Stall as intended here means the upper limit of loading beyond which the flow stops following the blade guidance on large regions, making massive flow separations and flow reversal occur, producing increased losses or completely compromising the operation of the machine. Aero engine compressors are often operated close to this condition since the efficiency is highest close to it. An acceptable operating range means certain insensitivity to inlet conditions as flow velocity and flow angle distributions at inlet. Good efficiency, hence aerodynamic loss prevention, also means flow distributions close to the design expectations between the stages for optimal stage matching. Different approaches to increase the stage loading without increasing the aerodynamic losses and the sensitivity to the inlet conditions are continuously investigated. Much is done in the further development of blade and duct geometries, applying endwall profiling, leakage reduction or moving towards transonic flow velocities to take profit of shocks for the static pressure rise. The technique of flow control by aspiration investigated in this work is a less common approach but it bears considerable potential as pointed out particularly by the recent investigation efforts documented in [Merchant 2003], motivating this research.

As will be shown by the literature review, only a little number of experimental demonstrators of flow control by aspiration that allowed increasing loading, efficiency and stability of axial compressor stages was built and documented in the past. This technique was however never integrated in engines except in

cases where air extraction done for other purposes casually also improved the flow quality. The demonstrators did not miss yielding encouraging performance results though. Some reasons for the retention can be identified. As will be seen, they increasingly lose validity today: air extraction through aspiration orifices on the walls and blades of a compressor requires additional ducting efforts. In the case of blade aspiration, hollow blades must be manufactured needing materials with higher strength. Great progress was achieved in these domains during the last decades due mainly to the development of hollow, internally cooled turbine blades with complex shapes manufactured e.g. by single-crystal casting of new super-alloys combined to high precision forging and milling. Also, increasingly complex ducting systems can be developed today. Another factor of retention was the limited understanding of several flow features occurring in the complex three dimensional flow of axial compressors and hence doubts on the influence that local aspiration can have on it. In addition, the measurement capabilities were less performing than today. This limited the interpretation capability of experimental results. Several loss mechanisms related to three dimensional flow - as the separation due to leakage jets or the three dimensional separations occurring in the stator hub corner - were better understood in the meanwhile. Of course also the computational power and the software tools were missing until recently, and they are needed to perform fully three-dimensional simulations of flow situations with flow extraction. Still, the approximations in the closure models for turbulence, in the wall models and in the discretization simplifications necessary to perform such computations work at their limit in cases with important separations and high turbulence as considered here. The reproduction of reality stumbles in presence of complex features as large separated regions. But as will be seen, due to the progress in this domain, the simulation instruments that could be employed here really assist the interpretation of complex experimental results. The arguments enumerated in this section illustrate why it makes sense to renew the investigations on aspiration in axial compressors today. The intention is to yield further proof and understanding of the involved mechanisms on advanced test cases taking profit of the progressed knowledge and introducing a set of partially innovative investigation methods, as is the Helmholtz-Decomposition applied to experimental results. This is done thanks to the opportunity of using the non-rotating annular cascade wind tunnel of the EPFL. Hopefully this and other ongoing efforts in this domain will make the way for further improvement of modern axial compressors.

1.2 State of the Art

1.2.1 Axial Compressors

An axial compressor uses the momentum of a rotating axe to generate a static pressure rise of the gas flowing through it. As illustrated in Figure 1-1, it consists in an axial, annular duct with blades reaching radially into it. These blades are installed on wheels arranged one behind another. Rotating wheels ("rotors") that transfer energy to the flow by accelerating it are followed by fixed wheels ("stators") that redirect the flow. A pair consisting of one rotor and one stator wheel is called a "compressor stage" and several such stages are stacked in a row to achieve the needed static pressure rise. The present work concentrates on the aerodynamic phenomena occurring in a non rotating wheel, a stator.

In an axial compressor stator, the geometry formed by a blade pair and the walls of hub and casing is designed to diffuse and deflect the flow in its outlet section. Both diffusion and deflection cause a deceleration that goes with a static pressure rise of the flow. This process is called diffusion, since the increasing cross-section formed by two blade profiles forms a geometry and hence an aerodynamic influence similar to a diffuser. The flow close to the convex and concave sides of the blades will incur respectively reduced and increased static pressures within the blade channel yielding their denomination of suction side and pressure side of the blade, as for airplane wings. In fact several notions used in designing wing profiles can be transferred to compressor blades. The highest occurring pressure difference between pressure and suction side is commonly called the blade loading and is related to the force that the blades exerts on the flow.
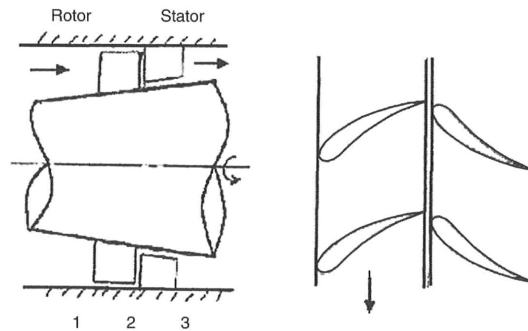
Figure 1-1. Illustration of an axial compressor stage composed by a rotor and a stator based on [Peng 2008]: : section view to the left and top view on the right.

Aero-engines must have minimal mass which means that the needed static pressure rise ought to be achieved with lowest number of stages. The pressure rise per stage must hence be maximized which is put in to practice by the development of highly loaded components. On conventional compressor geometries however, loss producing aerodynamic mechanisms as large separations and flow reversal occur if the loading is increased excessively. It will be investigated how this can be prevented by flow control by aspiration.

The blade loading can be increased by a reduced blade number (solidity), by higher diffusion obtained by increased cross-section change or increased flow angle change (deflection) between inlet and outlet of the blade pair, and by minimizing the losses. Compression shocks are a further means of effectively increasing the loading, however they go with shock losses and particular geometry sensitivities. This technique rather applies to early compressor stages. The present work will focus on the shock-less compression which is typical for high pressure compressor stages. For more detailed introduction on axial compressors the reader is referred e.g. to [Lakshminarayana 1996] and [Cumpsty 2004].

1.2.2 Past research on axial compressors with aspiration

1.2.2.1 Ancestors of flow control by aspiration in axial compressors

Flow control by aspiration was applied rather empirically but with a certain success to airplane wings since end of the 19th century to prevent flow separation at high lift conditions. This consisted in sucking air from critical locations on the wings through internal ducts towards locations of the wing with lower pressure that would drive the aspiration. As documented in different reviews as [Durand et al. 1934] and [Goldstein 1965], Prandtl first recognized that "according to the physical concept of the boundary layer, it should be possible to delay or even to prevent separation by removing the accumulation of fluid, caused by the reversal of flow, in the region where separation normally develops" in his publication [Prandtl 1904]. In [Durand et al. 1934] an interesting analytical investigation of Prandtl is cited, where he represented a laminar flat plate flow using Polhausens boundary layer approximations with continuous aspiration applied assuming a porous wall. He could herewith estimate the aspiration velocity needed to avoid boundary layer separation depending on the main flow velocity, viscosity and hence Reynolds number. The results suggest that a suitably arranged suction system can prevent the separation of a laminar boundary layer in the presence of quite large pressure gradients and with a relatively small amount of aspirated mass flow. For a turbulent boundary layer that is continuously re-energized by the mixing in of higher velocity particles from the upper flow, conditions are even more favorable.

Subsequently flow control by aspiration progressively found its application also to internal flow situations. A very illustrative experimental demonstration for flow control by aspiration related to internal flow was given in [Prandtl et al. 1929] for the case of the two-dimensional diffuser shown in Figure 1-2. Comparison of the second image to the first shows how flow separation due to an adverse pressure gradient is prevented thanks to the removal of the retarded boundary layer flow at the locations indicated by the white arrows that would otherwise separate. Figure 1-3, also derived from [Prandtl 1904], yields some explanation: a typical aspiration device as a slot normal to the wall, will induce a deflection and contraction of the streamlines going towards the slot, that consequently accelerates the flow close to the slot but even the flow upstream of it. The consequent reduction of the static pressure gradient upstream of the slot in the case with aspiration (blue curve) compared to the case without aspiration (green curve) explains how the aspiration can successfully avoid separation even if the separation onset in the case without aspiration is located further upstream than the aspiration location. On the downstream side of the aspiration slot, a stagnation point P will occur, after which the flow reattaches. As noted in the review of [Durand et al. 1934], the flow attracted towards the wall downstream of P is hitherto unaffected by friction and will hence reattach to the wall downstream forming a new, thin and strong boundary layer that will tend less to separate. As illustrated by the pressure distribution downstream of the stagnation point in Figure 1-3, locally, a positive pressure gradient occurs. The consequent beneficial pressure gradient will actually limit the boundary layer growth for a certain distance. It is evident that the considerations, presented here for introductory explanation, are related to the aspiration slot geometry and the applied aspiration rate. Further considerations to these parameters will be given in the section describing the slot design for the present investigation. A further simplification here is that a flat wall is assumed hence a disappearing pressure gradient normal to the wall, while in cases with a curved wall as on a blade profile, pressure gradients normal to the wall occur that can impact the result. Finally, three dimensional considerations occurring in real applications further influence the results and will be discussed when analyzing the results.
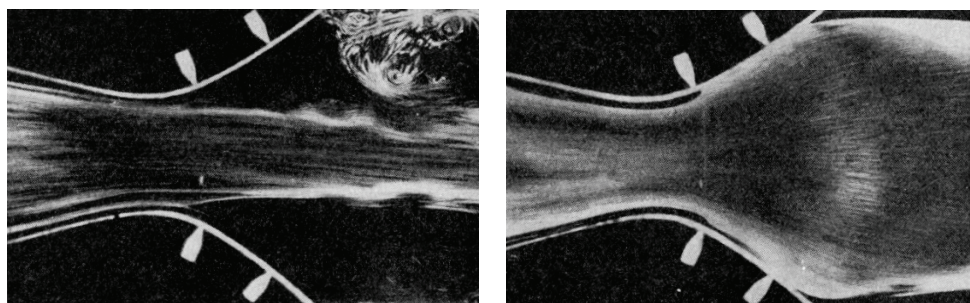
Figure 1-2. Forward flow against an adverse pressure gradient in a two-dimensional diffuser. In the second image, aspiration was applied at the locations of the white arrows (images from [Schlichting 1965], based on [Prandtl et al. 1929]).

A certain number of patents of theoretical nature are found starting in the 1940es issued by the main aero-engine manufacturers around the world, showing a considerable foresight on the possible application of flow control by aspiration in axial compressors: Not directly related but with close intentions [Ellis 1937] from Vickers Aviation Ltd in UK can be named, proposing aspiration through slots on the suction side of airscrews to avoid separation at high pitch operation. The patent [Stalker 1946] from Stalker Corp. US is noteworthy, in which, dispersed between other innovation ideas, is claimed the invention of re-energizing the boundary layer of early axial compressor blades by blowing in air through a slot on the blade suction side that was extracted from later stages. Interestingly, the extraction, which is not part of the claim, takes place through an analogous slot on the suction side of blades that are situated on a later stage, herewith representing an ancestor of boundary layer control by aspiration. In [Stalker 1952] aspiration slots on the nose of exceptionally thick axial compressor blade leading edges are mentioned "to further encourage the flow [around] the nose" intending to reduce the sensitivity to inlet flow angle variations. Far more

explicitly, the patent [Anxionnaz 1955] from Société Rateau in France claims the invention of an aspiration system through slots on axial compressor blade suction sides that aims at reducing separation occurring especially close to the hub of the blade. It is furthermore proposed to eject the flow through the tip of the blade to additionally counteract loss producing tip clearance leakage. The US patent [Erwin 1955] claims the invention of the application of aspiration through porous walls both on blades and casing to remove "the low energy gas near the aerodynamic surfaces [...] that detracts from optimum operation of the compressor.". In [Conrad 1969], Daimler-Benz claims the invention of aspirating flow from stator blade suction side through holes or slots to avoid separation and consequent loss production. It is noted that aspiration through radial slots on rotor blades with similar intention is already known and hence not part of the patent.
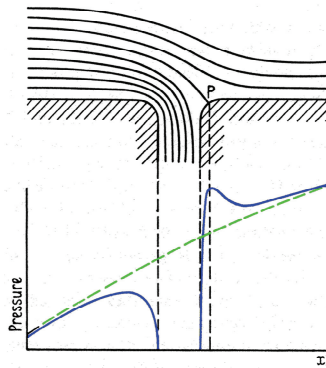
Figure 1-3. Static pressure distribution close to aspiration slot (blue) compared to case without aspiration slot (green), adapted from [Goldstein 1965], based on the review of Prandtl's Aerodynamic Theory [Durand et al. 1934].

1.2.2.2 UK investigations during the 1960es and 1970es

To date, little documented tests or real applications of the proposed techniques are found. As described in the introduction, in the beginning, several factors as e.g. the mechanical complication of using such a system in a compressor and limited investigation and computation capabilities might explain the retention of testing flow control by aspiration at real conditions. Concrete illustration of this retention is given by the research activities at Rolls Royce Derby on this subject: [Peacock 1971] cites first unpublished cascade experiments conducted in 1949 at Rolls Royce Derby by H. M. Malley on the "application of boundary layer control at the ends of airfoils in a cascade". The results indicated potential performance improvements. However, subsequent disappointing tests in real compressors with aspiration applied only through peripheral slots upstream of a blade row as well as the implicit mechanical complications led to the discontinuation of the research. According to [Stratford 1973] on this subject, only in 1964, "the further development that had occurred in gas turbine engines meant that a greater complexity in design might be acceptable".

Hence, starting 1964, Rolls Royce Derby combined its research efforts to those of Cambridge University yielding the results published in [Peacock 1971] and [Stratford 1973]. Both performed linear cascade tests on axial compressor geometries respectively on large-scale, low velocity and small-scale high velocity up to inlet Mach numbers of 0.6. The low-velocity tests yielded that for moderate loading, the hub corner separation could be successfully eliminated by aspiration through a slot located on the sidewall adjacent to the blade suction side. Less than 0.6% aspiration mass flow was necessary to eliminate the separation and this value further decreased down to 0.1% when the aspiration slot was narrowed. This yielded improved total pressure levels and more uniform velocity profiles at the cascade outlet.

A very similar aspiration slot geometry to that of Peacock was used for the complementary high velocity linear cascade tests described by Stratford. Figure 1-4 illustrates the experimental setup, as well as two representative resulting total pressure distributions – without and with aspiration. As can be seen in the reference case without aspiration, considerable regions affected by separation and reverse flow are detected in each corner. The application of 1.3% aspiration through corner slots almost completely eliminates these regions resulting in total pressure losses reduced by 25%. Stratford explains the result by the beneficial influence of the aspiration on the ensemble of loss producing mechanisms in what was commonly comprehensively labeled corner stall.

Stratford explains the reduction of the losses as follows: when a separation occurs, it causes flow reversal and thus shear and mixing losses. In addition, corner separations are fed with low energy flow by the cross-passage secondary motion. This increases shear and mixing loss. According to Stratford, the separation is induced by the fact that low energy flow can't sustain steep adverse pressure gradients and thus separates. Thus, by removing low energy flow in regions where it accumulates, i.e. in the corner between wall and suction side, avoids the separation and thus the production of total pressure loss. Estimating the loss produced in the boundary layers by bi-dimensional correlations, Stratford estimates that the remaining loss caused by the reversal must participate with about 2/3 to the overall loss.

Finally, Stratford notes that the test conditions in the linear cascade are dissimilar to the flow conditions in an annular cascade. He also notes with regards to rotating cases that the importance of the corner separation in a rotor might be different due to different total pressure and incidence distributions in the relative frame at inlet. But he concludes that the results show that under certain circumstances, considerable improvement can be achieved. In fact, the further investigations that will be described in the following sections focuses on both non-rotating and on rotating cascades. However, it will be seen that several of Peacock's and Stratford's observations are way-leading for the comprehension of the influence of aspiration and in agreement to certain extents with results from tests in annular cascades.
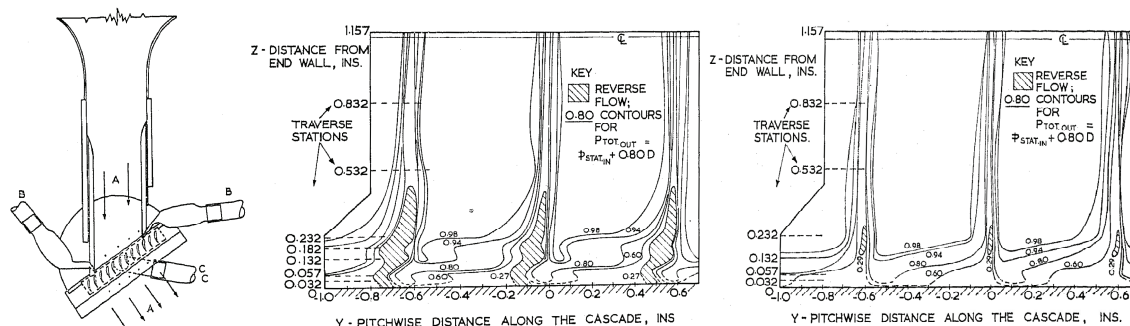
Figure 1-4. Linear cascade used for the tests of [Stratford 1973] and resulting total pressure distributions at the outlet of three blade-channel half-sections without aspiration (left) and with 1.3% aspiration rate. The inlet Mach number was 0.6.

1.2.2.3 NASA investigations

Starting in the mid 1960's, at about in the same time as Peacock's and Stratford's research in the UK, the American NASA Lewis Research Center initiated a large research program on flow control by aspiration (called "bleed") and blowing on highly loaded axial compressor blades. The work was performed in cooperation with the gas turbine manufacturer Allison owned by General Electrics. The project description and the result summary are documented amongst others in [Miller et al. 1968] and [Loughery et al. 1971]. According to [Greitzer et al. 1996] it was the last systematic research work performed in this area until the MIT started its investigations in the 1990s.
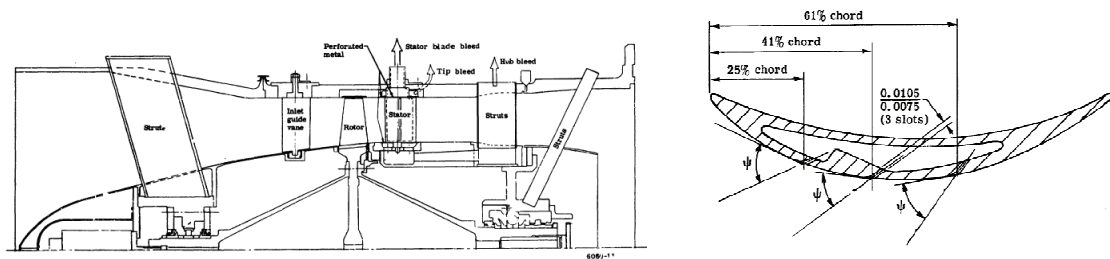
Figure 1-5. NASA compressor test rig and one of the tested stator blades, in this case equipped with three aspiration slots [Carmody et al. 1969].

For the NASA investigations, annular stator cascades with different aspiration or blowing slots on the blade's suction side were tested. They were placed behind a rotor wheel in a compressor test rig and measurements were performed for stator inlet Mach numbers around 0.75. Different stator incidence angles where tested by varying the rotor speed. Figure 1-5 illustrates the compressor test rig (to the left) and a stator blade with three aspiration slots on the suction side (to the right). The design pre-study was mainly driven by considerations of bi-dimensional boundary layer development, partially corrected for annular flow conditions. Extensive estimations were performed using common boundary layer approximations relating shape parameters and distributions of velocity and pressure. The NACA-65-based stators, representative for middle and later compressor stages, were designed for very high diffusion factors of up to 0.75 without aspiration. The aspect ratio (ratio of blade height to chord length) was 1.45 (blade height 4.36", chord length 3"). The average solidity (ratio of chord length to the blade spacing) was 1.45 (1.71 at the hub, 1.21 at the casing) confirming a blade number of 38 blades on the stator ring with outer diameter of 30" (about 762 mm).

While blowing systematically deteriorated the performance, fluid removal of 1.5-1.8% inlet mass flow from the suction side of the stator blades yielded significant benefits in stator performance. In the beginning, only one aspiration slot was planned, located slightly downstream of the predicted location of the boundary layer separation resulting in a position at 60% of the chord. Later numerical investigations using more advanced boundary layer models showed that first analysis was too conservative on the separation onset position. Hence later, a test with three slots, at 25%, 41% and 61% of the chord respectively was added, yielding even better results for similar aspiration rates. The initial location was chosen according to the results of [Prandtl 1904] that aspiration can reattach a boundary layer even if it is located further downstream than the separation location in the reference case. But the aspiration rate must be sufficiently increased. In contrast, if aspiration takes place too early, Miller notes, the boundary layer might separate regardless of the aspiration due to excessive adverse pressure gradients. The three-slot geometry was designed mainly to reduce the sensitivity to positive incidence – where the separation onset climbs further upstream – and herewith extend the stable operating range for the stator. It showed more effective than the single-slot configuration at all tested conditions. The slots were less than 1mm in width. It was chosen to suck off only a fraction of the mass flow of the estimated boundary layer mass flow. It was however estimated that this would be enough for a completely new, healthy boundary layer to start past the aspiration slot, able to negotiate the pressure rise up to the trailing edge (or up to the next slot) on at least 95% of the span. The aspiration on the blades was complemented in all cases by bleed on the tip and hub end wall at a bleed rate fixed before performing the investigations. The chosen wall bleed rate of 2% and 2.5% respectively is the level that showed to be optimal for the un-slotted reference configuration at design speed.

Unfortunately, measurement errors occurred that were considered starting in the last report, [Loughery et al. 1971]. They led to the exclusion of all the total pressure and flow angle measurements performed at the stator outlet at 10, 30, 70 and 90% span. Only results at 50% span could be trusted. Since this makes

the performance evaluation far less comprehensive, this surely has reduced the impact of the positive results of this investigation. This may explain, beyond the technical complexity, why the aspiration technique did not receive more resonance following this investigation. This is an argument that motivates the present experimental investigations at similar conditions.

Nevertheless, admitting that the results incertitude was significant outside the 50% span region, the following observations appear sufficiently pronounced to be retained: the highly loaded reference stator flow without any aspiration applied shows significant losses in the outlet plane, in the regions close to the suction side at the hub and the casing. Aspiration on the casing end wall did apparently not influence the loss source at the casing. Aspiration on the hub end wall however reduced the loss trace above the hub and improved the stage overall efficiency by about 2%. At first sight, the consequent outlet plane flow appears sane excepted close to the casing and suction side, but it must be noted that the low results accuracy hides features that contribute to the total pressure losses ω with less than 0.10.

For the aspiration on blade, only average figures of merit are given, not giving insight into the mechanisms behind. The results are positive: aspiration on blade achieves significant performance improvements reducing ω from 0.042 to 0.014 in the best case (see [Loughery et al. 1971], p. 16) with three aspiration slots and relatively low incidence, for the cases with design diffusion factor of 0.75. The comparison to the relatively high loss in the reference case without aspiration accentuates the improvement. However, it is very interesting to note that such high loading with acceptable loss levels in the aspirated cases is made possible only thanks to the aspiration. The three-slot case also shows to be less sensitive to positive incidence, indicating an increased operating range. With regards to the aspiration rate, Loughery et al. observe that if no aspiration is applied, the slots have detrimental influence on the flow, probably due to flow spilling in and out through the slots. In contrast, for all cases the losses decrease with increasing aspiration rate. Finally, the authors show that better prediction models for the boundary layer development available at the end of their investigations better predict the separation locations and will hence help in better designing the slot geometry and position.

1.2.2.4 MIT investigations

According to [Greitzer et al. 1996], after the NASA investigations, documented investigation on aspirated compressors halted for about twenty years until 1992. Then, MIT Gas Turbine Laboratories initiated a campaign of investigations on axial compressors with aspiration in cooperation with the US Airforce Office of Research (AFOSR), AlliedSignal Aircraft Engines (later Honeywell), Pratt and Whitney and NASA. They initially focused on single fan stages for aero-engines, consisting in a fan rotor followed by a stator, and later extended some of their conclusions to axial compressors in general. The function of fan stages is in principle similar to that of HPC stages investigated here. The main difference comes from the more important diameter and significant blade height of fans, since they are conceived to compress higher mass flows. As a consequence, the rotor blade tip velocities are higher than in HPC stages, reaching into the supersonic regime, often making use of shock compression. Furthermore, due to the long blades, the fan blade aspect ratio is much higher, which lowers the impact of corner disturbances as corner separations compared to HPC. However, the rotor in the investigated fans is followed by an annular stator with aspiration and with much lower aspect ratios that are closer to those investigated in the present study and can thus be compared. In any case, it is of interest to summarize the common explanations of their investigations to consider them in the present study.

As for HPC stages, for fans, maximizing the pressure rise by increasing the loading is of high interest. Particularly, since for constructive reasons fans are generally limited to a single stage only. Since increased velocity is one means to increase the loading, several of the MIT investigations focused on aspirated rotors with tip velocities close to Mach 1.5. However, motivated amongst others by the fact that

noise emission can be reduced by lower velocities, further investigations were done at lower rotor tip Mach numbers of 1.0 and 0.7 – which are closer to the flow velocities in the present study – trying to increase the pressure rise by high diffusion factors. As noted on this subject in [Kerrebrock et al. 1997], in the past, the diffusion factor was not increased much due to the concerns of the increased separation. The maximum diffusion factor was always limited by the onset of massive separation of the shear layers on wall and blades. Aspiration constitutes a solution to finally circumvent this inhibition. It is noted that the overall influence on the engine of the flow extraction by aspiration depends on how the extracted air is used. Consequently, in one analysis, an optimistic and a pessimistic compressor effectiveness are introduced for the cases where the work potential in the extracted air can be used or is lost for the engine cycle. Another investigation illustrates that the aspiration of low entropy fluid by itself can already be beneficial for the compression: it is shown that for certain, typical inlet flow velocities and compressor pressure ratios, more compression can be achieved with the same work, if high entropy fluid is removed.

The investigations at MIT started with numerous parametric studies of thermodynamic equilibrium and bi-dimensional blade flow. Further on, quasi-3D simulation was used for blade design and for the early performance estimations. They were later complemented by 3D, steady state Reynolds-Averaged Navier-Stokes computations to be able to make a more accurate design. The simulations where accompanied by single stage short-duration tests in the MIT Blowdown Test Facility, where first only some blades of the rotor and finally all the blades of both rotor and stator where equipped with aspiration slots. Finally, extensive performance measurements where performed in the 11MW compressor test facility of the NASA Glenn Laboratories on a 530mm diameter fan stage with aspiration slots on all blades illustrated in Figure 1-9. Beyond yielding the measurement results, the manufacture of the experimental setup produced constructive solutions and showed the feasibility of both rotating and fixed blades with aspiration.

Intentions and design of the aspiration systems

The main intentions enumerated in the different pubblications related to the MIT investigations for the aspiration were: remove some flow from the boundary layer on the blade suction side that is thickened and weakened due to the adverse pressure gradients and shocks; induce the formation of a new, more resistant boundary layer past the aspiration; prevent hence the separation of weakened boundary layer enabling herewith higher loading (higher diffusion, higher turning, lower solidity, higher rotor velocity) and pressure rise without increase of the losses; improve the pressure rise thanks to thinner boundary layers; remove high entropy fluid, which feeds the blade wakes, constitutes losses, produces losses when mixing with the main flow and reduces the compression efficiency of later stages; fix the shock position by eliminating the boundary layer separation and determining the highest pressure rise location past the aspiration slot, and reduce uncertainties due to viscous effects that make design difficult; by all these improvements, increase the possible stage work, delay the rotating stall cell formation and hence furthermore enhance the operation range and security.

The listed intentions lead to a blade design based on controlled diffusion airfoil approach that, thanks to aspiration, could aim at increased diffusion without increasing the losses. The blades had to be thickened to accommodate the aspiration duct. However the steeper pressure gradients due to the increased blade thickness would not lead to separation due, as well, to the aspiration. The higher profile losses would be compensated by the other benefices. Much consideration is given to the placement of the aspiration slots on the blades: by considerations of the bi-dimensional boundary layer evolution with aspiration, it is shown in [Kerrebrock et al. 1998] that highest control authority with least aspiration rate is obtained if aspiration is applied on a boundary layer close to separation just before regions of steep pressure increase. This was supported by parametric numerical studies described in [Merchant et al. 2000] for cases with different loading, solidity, and so on. Hence, the aspiration slots were placed on the blade suction sides close to the predicted shock impingement location. This is a region of rapid pressure rise and aspiration

should avoid boundary layer separation past the shock and induce the formation of a stronger new boundary layer after the aspiration slot. This should furthermore fix the shock impingement location yielding more stable and better predictable flow conditions. With regards to the shape, the slot was designed to be flush with the blade surface. It was angled to recover some dynamic head and hence reduce losses in the aspiration duct. A spanwise orientation was chosen. On this, [Reijnen 1997] arguments that such a slot has the particular merit to improve the boundary layer due to its bi-dimensional removal of fluid. Reijnen further notes that even better pressure recovery could be obtained with a forward facing scoop slot that has exactly the thickness of the boundary layer part to remove. However this would be difficult to manufacture and would not act robust to changes in the flow. He also mentions that in other investigations on shock-boundary-layer interaction control by aspiration, the slot should be segmented to reduce recirculation. He also mentions the alternative of using transpiration surfaces, which however is difficult to manufacture. But its advantage of keeping laminar boundary layers laminar is not an issue so this option was not considered. Last consideration, a field of bleed holes could be applied, which would be easier to manufacture, but its performance is not satisfactory due to its discrete and localized influence and high pressure drop. Little is documented on the sizing of the slot: one publication indicates 2% of the chord in width. This might be related to the fact that the MIT geometry is simplified in the simulations and hence investigations did not focus on the influence of the slot width. A further constructive feature is due to the finding of the first tests and the fully 3D computations that indicated severe separations close to the blade suction side at the hub originating blockage and loss production: with the purpose of controlling this, additional flow extraction slots where added, situated on the stator hub close to the blade suction sides. However the hub separation was never completely removed. Further extraction slots as e.g. circumferential bleed holes on the hub, just upstream of the stator leading edge where implemented, but they served only at off-design conditions, essentially to eject excessive air at startup.

Numerical investigations

The numerical results described in the different publications related to the MIT research predict a significant increment of the stage work and hence total pressure rise compared to the maximum achievable in conventional stages without aspiration as well illustrated by the comparison in Figure 1-6. The aspiration rates applied in the simulations are generally well below 3% for rotor and stator respectively. The experimental results confirm that the predictions could be attained to a certain extent.
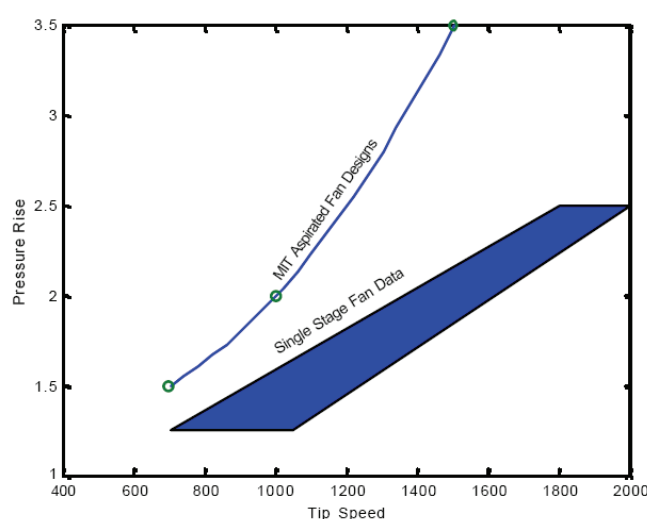
Figure 1-6.Pressure rise achieved by fan stages of the MIT fan staage with aspiration compaed to typical single stage fans according to [Lord et al. 2000].

The good performance found in the simulations is ascribed to the successful prevention of separation in regions that, due to the chosen geometry or due to the inception of the strong compression shock, incur a rapid pressure rise. Some of the weak boundary layer is removed yielding the formation of a new, more resistant profile. In [Merchant 2003] it is analyzed how in a bi-dimensional approximation, the effect of the boundary layer removal applied just upstream of regions of important pressure rise is multiplied and effectively reduces the boundary layer size up to the trailing edge. This occurs since the basis of the exponential growth of the boundary is reduced, leveraging the efect at the trailing edge, as well illustrated by Figure 1-7.
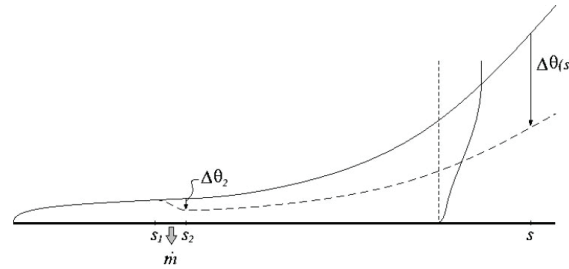
Figure 1-7. Effect of suction on the boundary layer growth (from[Merchant 2003]), with the momentum thickness θ.

According to the computation results presented in [Merchant 2002], thanks to aspiration, the turning is found to be increased and the total pressure losses and thus the entropy production are reduced. Beyond the beneficial impact on the diffusion, these factors also improve the stall behavior. As shown on the left hand side of Figure 1-8, the loss increase at off-design incidence, which is related to the inception of compressor stall is delayed, indicating an enlarged operating range. As illustrated in the numerical results to the right of Figure 1-8, the losses are concentrated close to the blade suction side and especially in the hub corner, indicating a separation on the blade and in the hub corner that persists in this case even with aspiration. As noted in [Merchant et al. 2000], addition of aspiration on hub helped in reducing this. Further noteworthy is, that in the highest loaded cases, the simulations indicate that the hub corner separation initiated already on the pressure side. This is ascribed to the high turning and camber as well as to the impingement of the shock in these cases. The resolution of the published measurement results was not sufficient to discern these predictions. However, the experiments confirmed that, beyond the wake, it is the presence of the related significant low momentum region in the hub corner that mostly deteriorates the performance. Generally, the simulations where excessively pessimistic on the performance of the aspirated stage since as described in [Merchant et al. 2004], with 30% less aspiration than assumed for the computations, the experiments presented similar performance as the simulations with nominal aspiration rate.
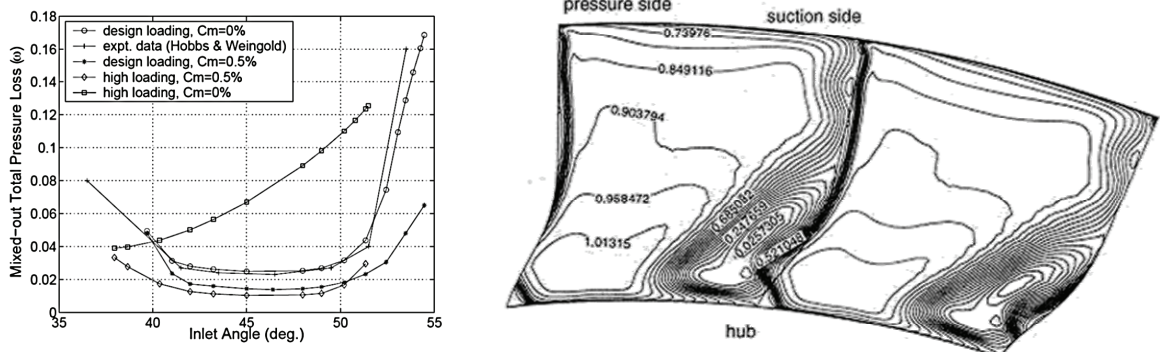
Figure 1-8. Left: Influence of the application of aspiration (aspiration rate named Cm) on the loss/incidence distribution based on numerical investigations (case Hobbs & Weigand serves for validation) from[Merchant 2002]. Right: stator wake contours of axial velocity [Merchant et al. 2000].

Experimental investigations

All the experimental investigations performed at the MIT were single stages consisting of rotor and stator with diameters at tip close to 500mm. After first encouraging tests in the MIT Blowdown Facility with aspiration only on some blades of the rotor, in the following tests, aspiration was applied on all the blades of both rotor and stator. All stages were designed to have only low diffusion in the rotor, with the static pressure rise concentrated in the compression shock. As a consequence, the inlet velocity to the stator was mostly supersonic, especially close to the hub, and an important part of the pressure rise was achieved in the stator, with particularly high diffusion factors there. To meet both requirements of sufficient stiffness and incorporation of the aspiration ducts, the compressor wheels where manufactured as bladed disks halved at mid-chord. This way, the aspiration ducts could be machined directly into the exposed blade interior on each halve before the halves were joined and bolted together at shroud and hub. The rotor bleeds ejected the removed flow towards a shroud and this further on to the casing, the flow being self-pumped due to the centrifugation and controlled by sonic blocked orifices. The flow extraction at the stator was simpler due to the non-rotation so it could directly be connected to low pressure tank or pump. The flow measurements at MIT included directional pneumatic 4-way probes, unsteady total pressure probes and total temperature probes, beyond static pressure probes on walls and blades. The NASA investigations used total pressure and total temperature rakes placed at different pitch-wise positions, as well as static pressure taps on the walls to infer the Mach number together with the total pressure measurements. The performance measurements at the related investigations performed at the NASA test facility yielded detailed performance results at part load up to stall conditions at fixed aspiration rate. While yielding highly reliable performance measurements, the measurements did not focus on producing high spatial resolution.
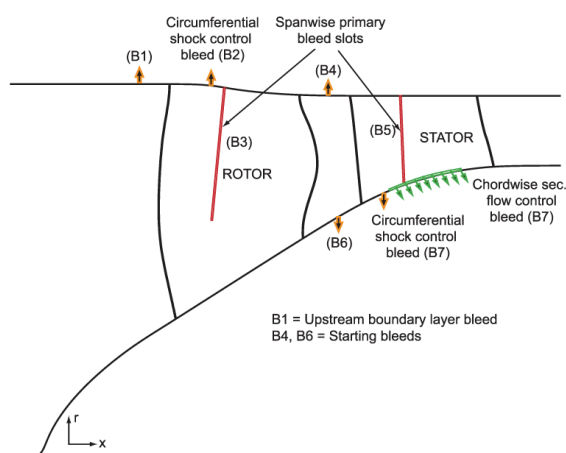
Figure 1-9. Schematic view of the compressor stage and of the aspiration scheme from [Merchant et al. 2004].

The publication [Merchant et al. 2004] mentioned earlier on the compressor stage illustrated in Figure 1-9 describes the most interesting since most comparable experiments performed at the NASA facility. Thus, it receives special attention here. It documents that a stage total pressure ratio of more than 3.0 was experimentally achieved with rotor tip speed of Mach 1.5 and with design diffusion factors of 0.76 and 0.68 respectively for the rotor and the stator. An aspiration rate of 1.5% on the rotor blade slots and of altogether 2% on the stator blade slots and chord-wise stator hub slots where applied. The relatively good measured adiabatic efficiency of 0.83 indicates that the aspiration successfully prevented the massive separation that would usually occur at the indicated diffusion levels without aspiration. The authors mention that even better efficiency levels could be obtained, if a less demanding target total pressure rise

would have been aimed. An experimental validation at such more moderate loading is presented in [Schuler et al. 2002] documenting fan stage tests performed in the MIT Blowdown facility. A stage total pressure ratio of 1.62 was achieved with rotor tip speed corresponding to Mach 0.7. For comparison with the present investigation, it is interesting to note that in this case the design diffusion factor of the stator, which according to the published plots is between 0.58 at hub and 0.36 at tip. An aspiration rate of 0.84% on the rotor blade slots and of altogether 0.85% on the stator blade slots and the chord-wise stator hub slots was applied. The achieved adiabatic efficiency of 0.89 is better than in the higher loaded test case mentioned earlier and is remarkable for a highly loaded compressor stage. The aspect ratio of the stator was 0.8 and the average solidity obtained with 31 blades is 2.5.

1.2.2.5 Summary

The linear cascade investigations described by Peacock and Stratford indicate that with aspiration on the end walls close to the suction side significant loss reduction can be achieved in highly loaded cases, if the corner separation is reduced. The experiments were performed for inlet Mach numbers up to Mach 0.6 with very low aspiration rates of 0.6%, and down to 0.1% in certain cases. It will be of interest to verify if these results obtained in linear cascade experiments are comparable to that of annular cascades at slightly higher Mach numbers as they are done in the present investigation.

The investigations at NASA described by Miller and Loughery performed on an annular stator with aspiration tested behind a rotating wheel were performed with an inlet Mach number of 0.75 that is similar to that of the present investigation. As for the present work, different inlet flow incidences were applied (in the NASA investigation this was achieved by varying the velocity of the rotating wheel) as well as different aspiration rates. Aspiration was applied on both end walls and on the blades using different slot geometries. The results indicate that aspiration of 2% on the hub wall improved the overall stage efficiency by 2% compared to the reference case without aspiration. Adding aspiration on blade up to 1.8% on a configuration with three aspiration slots on the suction side led to impressing reduction of the total pressure loss over the stator from 0.042 to 0.014 in the best case. The improvement is ascribed to the successful prevention or reduction of large separations thanks to the aspiration. The configurations with aspiration also showed to be less sensitive to positive incidence. Unfortunately, only the measurements taken at 50% blade height are confirmed. These results are an argument for the present research performed on an annular stator wheel with similar inlet Mach number of 0.8: with the advanced measurement equipement it is expected to obtain more detailed insight on the flow mechanisms related to the aspiration. However the configuration used for this work is more representative for a high pressure compressor stage: the solidity of the stator (thus the blade spacing with respect to the chord length of a blade) in the NASA experiments is higher, with about 1.45. In the present case the average solidity is 1.33 in the case with 18 blades and 1.04 in the case with 14 blades. Thus a higher loading going with higher losses can be expected in the present case. Also the aspect ratio (the blade height with respect to the chord length of a blade) in the NASA experiments is higher, with 1.45 compared to the average aspect ratio of 0.39 in the present case. It can thus be expected that disturbing features occurring close to the hub or the casing have more impact on the overall flow than in the present cases with lower aspect ratios than in the NASA investigations.

The MIT did investigations on fan blades, thus with high aspect ratio and high tip velocities. But also lower velocity tests with Mach number at the rotor tip close to 0.7 were performed that can be compared to some extent to the inlet conditions to the stator investigated in the present work. Furthermore, the aspect ratio of the stator behind the fan rotor of the MIT experiments with an average blade aspect ratio of 0.8 is closer to the 0.39 in the present investigation than that of the NASA investigations. However, the average solidity of 2.5 in the MIT experiments is significantly higher than that of 1.33 in the case with 18 blades and 1.04 in the case with 14 blades in the present investigation. Thus the blade loading can be expected to be higher in the present investigation. As a consequence also the loss level without aspiration

can be expected to be higher. The most comparable case tested by the MIT with a blade tip Mach number of 0.7 has following parameters: the design diffusion number of the stator in these tests that can be extrapolated from the graphs is of 0.58 at the hub and 0.36 at the tip without aspiration. This parameter can be compared to the present results. The results of the MIT investigations indicate that the corner separations were reduced but never completely removed. The relatively good adiabatic efficiency for the stage tests described in [Merchant 2004] indicates however that massive separations could be prevented thanks to aspiration.

It is worth noting, that also in the MIT investigations, the main source of loss is related to the onset of large separations. Thus the intentions of the aspiration technique in the MIT investigations, similar to that in the other investigations mentioned so far, were the reduction or prevention of large separated region. However also shock loss, shock induced separation and instability caused by the undefinite shock position are a matter and thus also targeted by the aspiration technique. It is expected that reducing adverse pressure gradients at selected locations will not only prevent separation but also prevent shock induced separation and will also fix the shock location. The MIT instrumentation aimed at achieving very reliable performance measurements but did not focus on achieving high spatial resolutions. This makes the present investigation complementary since it aims at identifying the flow mechanisms occurring in the cascade and the influence of the aspiration on them by detailed five-hole probe and LDA measurements.

Summarizing, none of the described investigations on compressor geometries with aspiration is completely comparable to the present investigation: the investigations documented by Peacock and Stratford were performed on linear cascades with lower inlet Mach number, the investigations at NASA with similar inlet Mach number, closer to the present cases since performed on annular stators, had higher solidity and much higher aspect ratio. The measurements performed by the MIT at the NASA test facilities had similar inlet Mach number similar aspect ratio but much higher solidity compared to the present investigation. This makes the present investigation on a configuration that represents a typical highly loaded HPC stator complementary to the former investigations. Furthermore, in most former experimental investigations, the spatial resolution of the measurements is lower than in the present measurements. Thus it is expected to obtain more detailed insight into the involved flow mechanisms. The main mechanism observed in the former investigations is the prevention of or the reduction of large separations, especially corner separations. Thus also in this work, this will receive particular but not exclusive attention. Also the flow within the aspiration duct was not investigated in detail in the preceding works. The present work contributes with some analysis of this based on the numerical investigations.

1.2.3 Contribution of this Work

The main contributions of this work are:

- Identification and explanation of the three-dimensional, steady state flow mechanisms related to flow control by aspiration on an axial compressor cascade. It is based on the analysis of results from experiments performed on annular cascades with different blade number and aspiration configurations that were developed and manufactured for this work. The cascades were tested in the Non-Rotating Annular Wind Tunnel of EPFL. The analysis is supported by the comparison to the results from 3D-RANS numerical simulations performed by the project partners and analyzed within this work.

- Demonstration of an analysis approach centered on rotational properties distributions: vorticity, helicity, secondary velocity and secondary kinetic energy. The approach is shown to significantly support the identification of three-dimensional flow mechanisms. A new procedure to extract secondary velocity and secondary kinetic energy distributions during the post-processing of experimental results based on the Helmholtz Decomposition Theorem was developed. It is demonstrated here and the results are compared to the classical approach.

- Definition of an adequate set of parameters to evaluate the performance of a compressor cascade with aspiration.

- Derivation of a model for static pressure rise estimation in cases with aspiration based on the continuity equation and the total enthalpy conservation.

- Experimental results comparing the performance of cases with the same Mach number at the cascade inlet, varied inlet flow incidence, different blade pitch and different aspiration configurations: no aspiration (reference case), aspiration only through slots on the hub or simultaneous aspiration through slots on the hub and on the blades.

- Presentation of accurate Laser Doppler Anemometry measurement results performed within this work on inlet and outlet planes of the cascades.

- Literature review on former investigations of flow control with aspiration on axial compressors

- Literature review on the relevant flow features occurring in the tested case including: three-dimensional separations, hub/blade corner separation and secondary flow.

The technique of flow control by aspiration as investigated in this work considers the continuous extraction of a certain amount of flow through slots located directly on the blades and the walls of the axial compressor to improve the flow quality and hence the axial compressor performance. In particular, it is here considered to extract this air in the late stages of the compressor where already a certain pressure rise occurred, namely in the high pressure compressor (HPC) stages. In those stages of certain modern engines, 1-2% mass flow is anyway extracted to feed the air demands of the turbine cooling and other consumers. If used for flow control, this extraction can improve the flow quality at no additional costs in terms of extracted mass flow compared to a typical HPC making this technique particularly attractive. The extraction can be driven by the pressure level in the HPC and does not need additional pumps.

This work presents a selection of results to support the indicated arguments. Further results and discussions related to this investigation are presented in the conference papers [Colombo 2009] and [Colombo 2010] as well as in the project reports [Colombo 2008], [Colombo 2009] and [Colombo et al. 2010].

1.3 Outline

This work is subdivided in three main parts:

Part I – Theoretical background: after the state of the art and the present section of chapter 1, a set of considerations to quantify the performance of a cascade with aspiration is introduced in chapter 2. To clarify the influence of aspiration on the pressure rise, a simplified model is introduced in section 2.3.2. Chapter 3 introduces the notions needed for the analysis of the rotational flow field and the secondary flow. In particular, a new method for the extraction of the secondary velocity field from measurement results is presented in section 3.3. Chapter 4 introduces some particular flow features that are common to axial compressor flow situations and relevant for this investigation.

Part II – Experiment: this part describes the most relevant characteristics of the experimental investigations. After preliminary remarks on the particularities of the test facility in chapter 5, the test cascades are introduced in chapter 6. In particular, the selected geometry is characterized as well as the aspiration systems. Section 6.4 gives some indications on the constructive solutions developed to achieve the test requirements. Chapter 7 describes the measurement technique and its peculiarities. Chapter 8 describes preliminary tests performed to assess the axisymmetry of the flow produced by the test facility as well as the repeatability of the produced test conditions. Finally, in chapter 9, the numerical models are presented that yielded the simulation results analyzed in this work.

Part III – Results and analysis: chapter 10 introduces the test cases discussed in this work. Chapter 11 presents the results for the reference case without aspiration. After discussion of the experimental results in section 11.1 and validation of the numerical results with respect to the measurements in section 11.2, a detailed analysis considering both experimental and numerical results is presented in section 11.3, identifying the main flow features that will be observed when aspiration is applied. In particular, a detailed analysis using the results of the new secondary velocity extraction method is presented towards the end of section 11.3, yielding a summary of the observed features. Chapter 12 is dedicated to the analysis of the influence of aspiration. After some introductory remarks on the comparability of the different cases in section 12.1.1 and the validation of the probe measurements with respect to the LDA measurements available for this case in section 12.1.2, the influence of aspiration is assessed based on all available experimental results in section 12.2. Section 12.2.6 has particular relevance, since it illustrates the potential of the secondary velocity analysis for this kind of investigations. Section 12.3 then introduces the available numerical results and assesses the comparability to the experimental results. In analogy to the discussion of the reference case, in section 12.4 a discussion of the influence of aspiration based on the combined consideration of experimental and numerical results is presented, uncovering the influence of aspiration on the cascade flow, but also the particular flow mechanisms occurring in the aspiration ducts and their consequences. Finally, the conclusions in chapter 13 summarize the main findings with respect to the aspiration technique and the new investigation methodologies introduced in this work.

2. Performance of a non-rotating compressor cascade with aspiration

The performance of a compressor cascade is determined by the loading achieved, by the amount of loss occurring for this loading and by the quality of its outlet flow. Aspiration within the cascade makes it necessary to reconsider the typical parameters that quantify these properties.

Loss limits the effectiveness of the compression. After a section defining the used averaging approach, the subsequent section will explain the quantification of this loss in cases without and with aspiration. Loss typically increases when the loading of the cascade blades exceeds a certain level. Hence the subsequent section summarizes typical loading parameters with special consideration for cases with aspiration. Flow quality at the outlet of the compressor is important for later loss production and for the matching with following stages. A third section will give further indications on this.

2.1 Averaging

When computing parameters to characterize the cascade flow, the inhomogeneous distributions of properties measured in the inlet and outlet planes are replaced by averages which are single value representatives. This corresponds to defining a representative uniform flow with the single value properties. However, as expressed by Pianko and Wazelt in [Pianko et al. 1982], "no uniform flow exists which simultaneously matches all the significant stream fluxes, aero-thermodynamic and geometric parameters of a non-uniform flow". Choice of the averaging approach must hence be guided by the intention of the averaging.

In the case of static conditions, [Traupel 1977] and [Cumpsty et al. 2006] point out that choosing the averaging approach implicitly corresponds to selecting the mechanism by which the non-uniform flow would mix out. For the present investigation, the following procedure is chosen: in the case of transported quantities as p_t, v, s and h, mass flow weighted averaging (marked by a hat: '^') is applied. For a quantity Q, this is defined as

$$\hat{Q} = \int \rho V_\perp Q dA \Big/ \int \rho V_\perp dA \tag{2.1}$$

with the local density ρ and the velocity component $V_\perp$ perpendicular to the surface dA.

In the case of static pressure, it is common use to apply area weighted averages (marked by a tilde: '~') to respect the resulting forces. For a quantity Q, this is defined as

$$\tilde{Q} = \int Q dA \Big/ \int dA \,. \tag{2.2}$$

As noted in [Traupel 1977], this approach might slightly overestimate the entropy (thus the loss) and underestimate the static pressure produced when an inhomogeneous static pressure distribution mixes out. This is because it would represent a mixing out via a irreversible, entropy producing process. The averages of derived parameters as Mach number and flow angle (marked by a bar: '-') are computed from the averaged properties: average p_t and p_s for the Mach number and average velocity components for the flow angle. To prevent wrong conclusions, it is avoided to compute averages in highly inhomogeneous regions as e.g. in correspondence of large separations. The entire flow field is considered instead. The computation of averages using different averaging procedures based on data of the present investigation showed that the differences are well below 1%, hence not affecting the conclusions of this work.

2.2 Loss

2.2.1 Quantification of aerodynamic loss

The deviation from ideal compression can be quantified by the production of entropy: least energy is dissipated if the compression takes place through an isentropic process, hence without production of entropy. In real compressors, entropy is produced by different mechanisms. [Denton 1993] distinguishes:

- viscous friction in boundary layers or free shear surfaces,
- heat transfer between flows or between flows and surfaces of different temperature, and
- non-equilibrium processes such as occur in very rapid expansions or in shock waves.

However, in the present investigation, only the first mechanism occurs with relevant magnitude. In the case of viscous friction, entropy is produced when kinetic energy is dissipated into heat that is generally useless for the process. Hence, as proposed in [Denton 1993], production of entropy is a good indicator to quantify the aerodynamic loss occurring in a compressor cascade.

The increase in entropy between two ends of a group of streamtubes can be directly related to the change in total pressure by the well known expression derived e.g. in [Greitzer et al. 2004]:

$$s_2 - s_1 = c_p \ln \frac{T_{t2}}{T_{t1}} - R \ln \frac{p_{t2}}{p_{t1}} \tag{2.3}$$

It can be assumed that changes in total temperature are negligible for the flow in the streamtubes between inlet and outlet of a stator cascade as investigated here. For the present configuration, this holds for cases with and without aspiration as will be discussed in section 2.2.3. Transformation of (2.3) directly relates the relative change in total pressure to the change in entropy, yielding the loss indicator

$$\chi := \frac{p_{t1} - p_{t2}}{p_{t1}} = 1 - \frac{p_{t2}}{p_{t1}} = 1 - \exp\left(-\frac{s_2 - s_1}{R}\right) \tag{2.4}$$

This shows that a decrease in total pressure directly indicates the production of entropy, meaning irreversible dissipation of kinetic energy, hence aerodynamic loss and non-ideal compression. In an isentropic compression total pressure would not change. The advantage of basing a loss indicator on the total pressures is that it can directly be measured. This will be used for the present evaluations.

A commonly used parameter that directly reflects the change in total pressure is the total pressure loss coefficient. It is composed by the total pressure difference non-dimensionalized by (p_{t1}-p_{s1}):

$$\omega = \frac{p_{t1} - p_{t2}}{p_{t1} - p_{s1}} \tag{2.5}$$

For incompressible flow, the Bernoulli equation shows that (p_{t1}-p_{s1}) is proportional to the inlet kinetic energy. For Mach numbers larger than 0.3, compressible flow effects affect this proportionality and hence the relation between ω and the occurring total pressure difference. Nevertheless, the total pressure loss coefficient established commonly as default loss indicator for comparison between different cases, also at higher Mach numbers. Note that the coefficients can be related to each other depending on the conditions at position 1 used for non-dimensionalization according to:

$$\chi = \omega \left(1 - \frac{p_{s1}}{p_{t1}} \right) = \omega \left[1 - \left(1 + \frac{\kappa - 1}{2} Ma_1^2 \right)^{-\frac{\kappa}{\kappa - 1}} \right] \qquad (2.6)$$

The introduced loss parameters can be applied to non-uniform distributions as can occur in the inlet and outlet plane of a compressor: the publication [Cumpsty 2006] indicates that the mass flow weighted average of the entropy in a plane yields a plausible indicator for the overall entropy level of that plane. It is also derived in analogous way that the mass flow weighted of the total pressure adequately reflects the overall production of loss. Thus the total pressures in equations (2.4) and (2.5) can be replaced by the mass flow weighted averages to quantify the loss between inlet and outlet of a cascade. It should be noted that this presumes that all the considered flow is connected by a group of streamtubes.

2.2.2 Loss in compressor cascade with aspiration

Figure 2-1 illustrates schematically the flow through a compressor cascade. A certain mass flow $\dot{m}_c$ is diffused to increase its static pressure level. As illustrated by increasing the schematized boundary layer thickness close to the walls, phenomena as separation and wall friction increase the level of loss in the cascade flow. The compression process is illustrated in the h-s chart on the right-hand side of Figure 2-1: the pressure level, reflected by the two isobars at p_1 and p_2, increases from state 1 to state 2A. However, due to the loss mechanisms, the entropy level also increases by Δs_A. If compression was ideal, the flow would reach the pressure level p_2 at the state 2s, without loss and hence without increase of entropy. State 2A has higher enthalpy than 2s. Assuming an almost constant level of c_p, then $h \approx c_p T$ and a higher enthalpy directly indicates the higher temperature caused by the dissipation related to the loss.
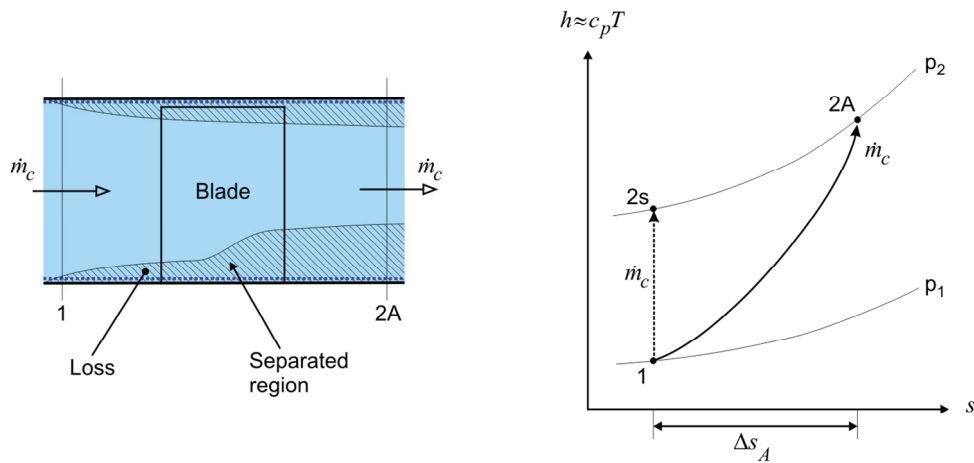

Figure 2-1. Schematic of the flow through a compressor cascade and representation in a h-s chart.
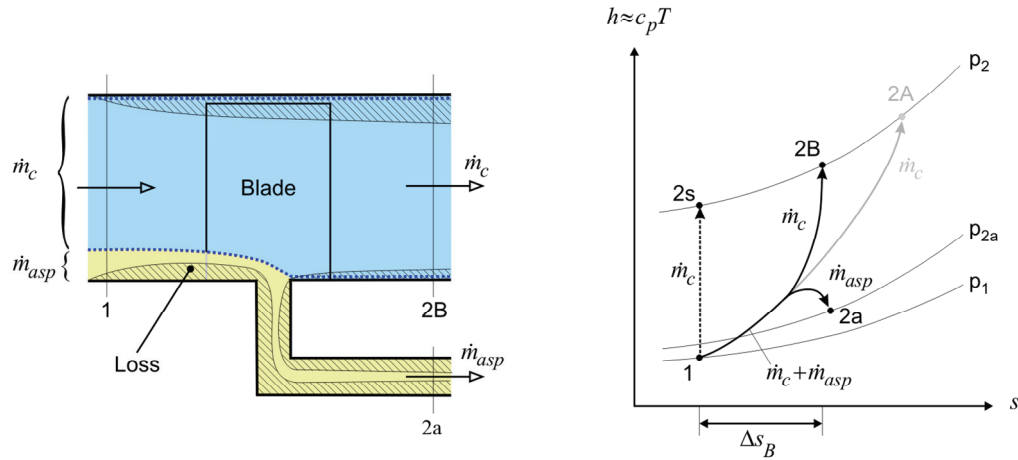
Figure 2-2. Schematic of the flow through a compressor cascade with aspiration and representation in a h-s chart.

Figure 2-2 illustrates schematically the flow through a compressor cascade with aspiration. At outlet, the same mass flow $\dot{m}_c$ and the same pressure rise p_2/p_1 as in the preceding example shall be obtained. However, the loss producing separation drawn in the preceding example is prevented and a certain amount of loss-charged flow is removed by the aspiration. To achieve this, more mass flow enters the cascade ($\dot{m}_1 = \dot{m}_c + \dot{m}_{asp}$), part of which is aspirated via slots on the hub and/or the blades ($\dot{m}_{asp}$). Hence, beyond the compressed mass flow $\dot{m}_c$, a mass flow $\dot{m}_{asp}$ is obtained at a pressure level that depends much on the extraction location and the extraction path. The h-s chart to the right of Figure 2-2 illustrates this process in analogy to Figure 2-1: the pressure level of the flow $\dot{m}_c$ is increased from p_1 to p_2. But the increase in entropy is lower than in the preceding example, mainly since the loss produced by the separation is prevented. This shows how the impact of a relatively small extraction can be significantly leveraged by its influence on loss producing mechanisms as separations. Furthermore, part of the wall friction loss collected by the inlet flow is extracted with the aspirated mass flow $\dot{m}_{asp}$.

The example illustrates the compromise implied in aspiration: at outlet of a cascade with aspiration, flow with lower loss level and less disturbed by separation can be obtained. However, the cost is a certain amount of mass flow that in the illustration is added to the cascade inlet. It only initially participates to the cascade flow, up to the extraction location. From another perspective, this cost is a gain: in the case where the extracted flow can be used because its pressure level is high enough to feed other engine subsystems. This is achieved if aspiration is applied at late stages of a multi-stage compressor, where the pressure level at the extraction location is sufficiently high for it to be used to feed other subsystems. In return, higher loaded compressor geometries that would tend to separate without aspiration can be used. As mentioned earlier, the gain of doing so is reduced component mass and number of stages and can also include improved stability and operating range.

Note that flow control by aspiration is often set equal with *boundary layer control*. Boundary layer control is evidently the main influencing mechanism related with the flow control technique. However, it is virtually impossible to extract only the boundary layer and obtain flow conditions behind the aspiration that are identical to undisturbed flow. The necessity of controlling the aspirations depending on the boundary layer size would make the system non-robust and is not feasible in real machines. Hence the extraction always implies a certain influence on the flow outside the boundary layer which as will be seen can be beneficial. So the denomination *flow control by aspiration* is chosen intentionally.

2.2.3 Loss in real investigations

In the present investigations, the conditions are more complex than in the illustrative examples described above: instead of cases with same compressed mass flow $\dot{m}_c$, cases with same inlet Mach number are investigated for different aspiration rates. Using the nomenclature of the preceding examples, this means that for constant inlet flow angles and pressure levels, $\dot{m}_1 = \dot{m}_c + \dot{m}_{asp}$ is constant instead of $\dot{m}_c$. Hence, the obtained $\dot{m}_2 = \dot{m}_c = \dot{m}_1 - \dot{m}_{asp}$ changes depending on the aspiration rate. Furthermore, the pressure rise being a result of the experiments, the achieved pressure rise p_2/p_1 can change from case to case.

This departure from the accademical simplicity of the introductory examples is based mainly on following reasons: first, inlet conditions for the investigations are specified in term of constant inlet Mach number according to real design approaches. Second, it is very demanding in terms of control efforts to set the experimental flow conditions to achieve same compressed mass flow and pressure rise while simultaneously respecting the other mentioned inlet flow condition restrictions. Doing this would explode the available time frame. Third, the results with the described varying outlet mass flow give already significant insight into the flow mechanisms involved with aspiration. This has presently more relevance than precise performance maps of an accademical model.

Nevertheless, the introduced loss parameters are valid since they are or they correspond to specific values: in the cases described in section 2.2.2, the specific entropy based on (2.3) and referred to the compressed flow $\dot{m}_c$ yields in fact the absolute rate of entropy increase $\Delta \dot{S}$ non-dimensionalized by the compressed mass flow:

$$\Delta s = \Delta \dot{S} / \dot{m}_c \tag{2.7}$$

Hence, the specific loss occurring in cases with different compressed flow $\dot{m}_c$ can be readily compared in terms of Δs. As consequence of the derivation of the total pressure loss based on the change of entropy in section 2.2.1, this is also true for the derived parameters in terms of total pressure, χ and ω.

For completeness, the indication of the loss level must be accompanied by the amount of aspirated mass flow: this can occur by additionally comparing the actually compressed mass flow $\dot{m}_c$ for same inlet mass flow. Or, to be independent of the actually incoming mass flow, the aspirated mass flow can be related to the inlet mass flow for each case by the aspiration rate defined as:

$$C_Q := \frac{\dot{m}_{asp}}{\dot{m}_1} = \frac{\dot{m}_1 - \dot{m}_2}{\dot{m}_1} = 1 - \frac{\dot{m}_2}{\dot{m}_1} = 1 - \frac{\dot{m}_c}{\dot{m}_c + \dot{m}_{asp}} \tag{2.8}$$

In the configuration investigated in the present work, the number of aspiration slots either on the hub or on the blades corresponds to the number of blades on a cascade. For evaluation of the influence of the aspiration slots, it is also important to consider the aspiration rate for a single slot compared to the inlet massflow. This is given by the aspiration rate per slot defined as:

$$C_{Q,Slot} := \frac{\dot{m}_{asp} / N_{Slots}}{\dot{m}_1} = \frac{C_Q}{N_{Slots}} = \frac{C_Q}{N_{Blades}} \tag{2.9}$$

with the number of slots N_{Slots} per cascade which in the present work is equivalent to the number of blades N_{Blades} per cascade.

2.2.4 Loss including aspiration path loss

Loss occurring in the aspiration path can be included into the loss indicators by considering the overall entropy production with the nomenclature of Figure 2-2:

$$\Delta s_{overall} = \frac{\dot{m}_c \Delta s_{1-2B} + \dot{m}_{asp} \Delta s_{1-2a}}{\dot{m}_c + \dot{m}_{asp}} \tag{2.10}$$

Considering that $\dot{m}_c = \dot{m}_2 = \dot{m}_1 - \dot{m}_{asp}$, and with (2.8):

$$\Delta s_{overall} = \frac{\dot{m}_2}{\dot{m}_1} \Delta s_{1-2B} + \frac{\dot{m}_{asp}}{\dot{m}_1} \Delta s_{1-2a} = \left(1 - C_Q\right) \Delta s_{1-2B} + C_Q \, \Delta s_{1-2a} \tag{2.11}$$

It must be considered that if the conditions in the inlet plane 1 are not homogeneous, the entropy differences must be performed over interconnected streamtubes.

In analogy to the earlier discussion, also a loss parameter based on the total pressures can be formulated:

$$\omega_{overall} = \frac{\left(1 - C_Q\right)\left[p_{t1} - p_{t2}\right] + C_Q\left[p_{t1} - p_{t2a}\right]}{p_{t1} - p_{s1}} \tag{2.12}$$

as done by [Godard et al. 2008]. In case of homogeneous inlet total pressure distribution, this can be merged to:

$$\omega_{overall} = \frac{p_{t1} - \left[\left(1 - C_Q\right)p_{t2} + C_Q \, p_{t2a}\right]}{p_{t1} - p_{s1}} \tag{2.13}$$

In the present investigation the aspiration path was not optimized. Hence the present work will focus on loss in the main flow path according to the loss parameter definition (2.5).

2.3 Loading

For the evaluation of the impact of aspiration on the cascade loading and to compare the performance with other compressor cascades, loading parameters must be defined. Loading parameters typically quantify the combination of pressure rise and deflection achieved by a cascade or single blade with respect to the level where massive separation occurs limiting the operation of the compressor. However, separation onset can occur by different mechanisms depending on several features as e.g. the geometry of the cascade, the flow conditions at inlet and outlet and the development of three-dimensional flow features within the cascade. Furthermore, often the properties announcing the separation cannot be measured and evaluation must be based on indirect measurements. Hence, no unique parameter for the loading can be defined that works universally and that can be compared between all possible geometries.

Some examples for loading parameters that are reviewed in [Cumpsty 2004] are the lift coefficient, the pressure rise coefficient, the profile circulation, the Diffusion Factor, etc. These parameters allow assessing and, if similarity is sufficient, to predict the onset of massive separation where they adequately capture the key parameters of the involved mechanisms. Even though defined for particular geometries, parameters capturing some essential physics as the Lieblein Diffusion Factor work also on different geometries. For this particular parameter, with moderate adaptations, even differences as changes in the

axial velocity density ratio or convergent hub geometries can be considered this. As a consequence, it is common use to characterize different cascades with the same typical loading parameters even though the physics are not identical. Thus, considerate comparison of several such parameters can give an evaluation of the performance of the cascades investigated here, for different aspiration configurations and in comparison to other cascades. A set of parameters will be defined hereafter that is adequate considering the properties measured in the present investigation. After this, it will be discussed how aspiration affects their interpretation due to the implicit impact of aspiration on the pressure rise.

2.3.1   Parameters

The main target of a non-rotating compressor cascade is either static pressure rise or deflection. Priority is given to either one or the other depending on the compression strategy. This yields the two principal parameters: the average static pressure rise, defined as

$$\tilde{\Pi}_{12} = \tilde{p}_2 / \tilde{p}_1 \tag{2.14}$$

and the average deflection, defined as

$$\Delta\bar{\alpha}_{12} = \bar{\alpha}_1 - \bar{\alpha}_2. \tag{2.15}$$

The static pressure rise is relevant, since it quantifies the adverse pressure gradient that the boundary layers on the blades and on the walls must overcome without separating. The deflection is also related to this since higher deflection demands a higher cross-passage pressure gradient to deflect the flow. This pressure gradient must overcome the centripetal acceleration of the flow to turn it and hence increases with higher turning, higher inlet flow velocity and higher blade distance. Thus it indirectly indicates a component of the pressure gradient that the boundary layers must overcome.

The loading of a single blade is not reflected by the average static pressure rise and the average deflection, since the load can be distributed over a varying number of blades. Hence in the present investigation, the loading of the single blades and their boundary layers is pointed out by analyzing the load distribution on the blade in form of static pressures on the blade surfaces. An increase/decrease of the spread between suction side and pressure side pressure thus indicates an increase/decrease of the blade loading. In the present investigation the static pressure on the blade surface is given normalized by the averaged inlet total pressure:

$$p / \hat{p}_{t1} \tag{2.16}$$

The pressure rise is related to the diffusion, hence the deceleration of the flow. A further parameter is consequently given by the deceleration. This can be expressed by the difference of the average Mach numbers:

$$\overline{Ma}_1 - \overline{Ma}_2. \tag{2.17}$$

As mentioned, a widely used parameter for the evaluation of a compressor cascade loading is the Lieblein Diffusion Factor. It will be used for comparison purposes in the present work. In its most common form it is formulated:

$$DF = 1 - \frac{V_2}{V_1} + \frac{V_{\theta 1} - V_{\theta 2}}{2\sigma V_1}, \tag{2.18}$$

with the inlet and outlet velocities V_1 and V_2, their circumferential components $V_{\theta 1}$ and $V_{\theta 2}$ and the solidity σ, meaning the ratio of the blade chord and the circumferential blade spacing. As described in

[Cumpsty 2004], *DF* was derived for particular geometries and flow conditions, to reflect the maximum occurring deceleration compared to the outlet velocity expressed as

$$D = \frac{V_{max} - V_2}{V_2} \; .$$

(2.19)

Since the maximum velocity typically occurs on the suction side, this deceleration is an indicator for the deceleration that the suction side boundary layer will undergo. Herewith it reflects if the suction side boundary layer, which is amongst the most sensitive flow regions in a compressor cascade, is close to separation. The formulation (2.18) also considers the deflection and the blade spacing which, as mentioned with regards to deflection, impact the loading by influencing the cross-passage pressure gradient. Typically it is said that compressor cascades tend to separate if *DF* approaches the value 0.6.

2.3.2 Influence of aspiration (1D prediction model)

Adding flow extraction by aspiration to a compressor cascade influences the loading parameters in different ways: first, adding flow aspiration to an otherwise identical geometry intrinsically increases diffusion. The reason is that past the aspiration location, the mass flow per flow surface is reduced compared to a case without aspiration. Second, by preventing loss production, aspiration makes more kinetic energy available for pressure rise. Third, aspiration can improve the flow attachment which improves the deflection. This includes preventing the aerodynamic blockage constituted by separated regions that would deteriorate deflection. The improved deflection also results in improved pressure rise. To illustrate and quantify the described influence of aspiration, the following model is defined:

Consider the flow in an adiabatic non-rotating compressor cascade. The mass flow at inlet and outlet can be related by following trivial continuity equation:

$$\dot{m}_1 \frac{\dot{m}_2}{\dot{m}_1} = \dot{m}_2$$

(2.20)

For simplicity, two-dimensional flow shall be considered, where the flow direction is completely determined by one flow angle α. Thus, the mass flow through a plane is given by

$$\dot{m} = \rho A V \cos\alpha$$

(2.21)

with the velocity magnitude V, the flow surface A, and α being the angle between the flow orientation and the flow surface normal. The density is given by the ideal gas equation: $\rho = p_s / (R\, T_s)$. The velocity magnitude shall be replaced by the isentropic Mach number given by

$$V = Ma \sqrt{\kappa R T_s} \; .$$

(2.22)

Substituting in to (2.20) and applying some transformation yields

$$\frac{p_{s2}}{p_{s1}} = \frac{Ma_1}{Ma_2} \sqrt{\frac{T_2}{T_1}} \frac{\cos\alpha_1}{\cos\alpha_2} \frac{A_1}{A_2} \frac{\dot{m}_2}{\dot{m}_1}$$

(2.23)

The model is completed by considering the conservation of total enthalpy. Note that in a non-rotating cascade considered adiabatic, the total enthalpy level is constant, since the exchange of heat and work with the environment is negligible. Under the following circumstances, it can be furthermore assumed

that even if aspiration is applied the total enthalpy level does not change between inlet and outlet of the cascade: if the total enthalpy distribution at inlet is homogeneous the total enthalpy level will be equal in all streamtubes crossing it. If the perturbations up to the extraction location are moderate, no total enthalpy will be exchanged between the streamtubes, preserving the equal level. Hence, when part of the streamtubes is extracted from the cascade by the aspiration, the total enthalpy level in the others will still correspond to that at inlet. Along the further flow path, as noted earlier, the flow has no exchange of heat and work with the environment. Hence the total enthalpy level at outlet will correspond to that at inlet. It makes no difference if perturbations past the extraction location yield a redistribution of the total enthalpy between the streamtubes. Evaluation of 3D-RANS computations on the present investigation configuration confirmed that the assumption of total enthalpy conservation also holds in the three-dimensional flow cases investigated in this work. Further considering that for the occurring small temperature differences, the isobaric specific heat c_P is almost constant yields:

$$h_{t1} \approx h_{t2} \;\Rightarrow\; c_P T_{t1} \approx c_P T_{t2} \Rightarrow\; T_{t1} \approx T_{t2} \tag{2.24}$$

Hence, if total enthalpy does not change, the total temperature too is constant. With

$$T_s = T_t \left(p_s / p_t \right)^{\frac{\kappa-1}{\kappa}} \tag{2.25}$$

this yields that in the present case,

$$\sqrt{\frac{T_2}{T_1}} = \sqrt{\frac{\cancel{T_{t2}} \left(p_{t1} / p_{s1} \right)^{\frac{\kappa-1}{\kappa}}}{\cancel{T_{t1}} \left(p_{t2} / p_{s2} \right)^{\frac{\kappa-1}{\kappa}}}} = \sqrt{\frac{\left(p_{t1} / p_{s1} \right)^{\frac{\kappa-1}{\kappa}}}{\left(p_{t2} / p_{s2} \right)^{\frac{\kappa-1}{\kappa}}}} \;. \tag{2.26}$$

Finally, considering the relation of the isentropic Mach number to the ratio of total and static pressure,

$$Ma = \sqrt{\frac{2}{\kappa-1}\left(\left(p_t / p_s \right)^{\frac{\kappa-1}{\kappa}} -1 \right)}, \tag{2.27}$$

insertion of (2.26) and (2.27) in (2.23) yields the relationship

$$\frac{p_{s2}}{p_{s1}} = \sqrt{\frac{\left(p_{t1} / p_{s1} \right)^{\frac{\kappa-1}{\kappa}} \left(\left(p_{t1} / p_{s1} \right)^{\frac{\kappa-1}{\kappa}} -1 \right)}{\left(p_{t2} / p_{s2} \right)^{\frac{\kappa-1}{\kappa}} \left(\left(p_{t2} / p_{s2} \right)^{\frac{\kappa-1}{\kappa}} -1 \right)}} \; \frac{\cos\alpha_1}{\cos\alpha_2} \frac{A_1}{A_2} \frac{\dot{m}_2}{\dot{m}_1} \tag{2.28}$$

If the change in mass flow is due to aspiration, the mass flow ratio can be replaced by the common coefficient:

$$\frac{\dot{m}_2}{\dot{m}_1} = \left(1 - C_q\right) \quad with \quad C_q = \frac{\dot{m}_{asp}}{\dot{m}_1} = \frac{\dot{m}_1 - \dot{m}_2}{\dot{m}_1} = 1 - \frac{\dot{m}_2}{\dot{m}_1} = 1 - \frac{\dot{m}_c}{\dot{m}_c + \dot{m}_{asp}} \tag{2.29}$$

Based on the described assumptions, equation (2.28) implicitly yields an estimate for the static pressure rise depending on the change in mass flow, total pressure, flow angle and flow surface. This is illustrated by the evaluation hereafter, where the equation was solved applying the Newton method. Figure 2-3 shows an application with flow conditions as encountered in the experimental investigation: the chosen reference conditions are an inlet Mach number of 0.8, an inlet flow angle of 60°, a deflection of 30°, a

total pressure loss level of 0.14 and no aspiration. Solving (2.28) with these parameters yields a static pressure ratio of 1.171 and a Mach number deceleration of 0.238 (point A in Figure 2-3).

The results in Figure 2-3 show that increasing the aspiration rate from $C_q=0.00$ to $C_q=0.01$ yields an increase in pressure ratio by almost 0.01 (point B) compared to the reference (point A). If in addition, the aspiration achieves a loss reduction from 0.14 to 0.12 (point C), the static pressure ratio increase compared to the reference improves by 0.02 units. Such total pressure level improvement can occur e.g. in the case of separation prevention by the aspiration. If furthermore a deflection improvement from 30° to 31° is achieved (point D), the total increase of the static pressure ratio reaches almost 0.03. As can be seen in the chart on the right hand side, the increase of static pressure is accompanied by an increase of deceleration.
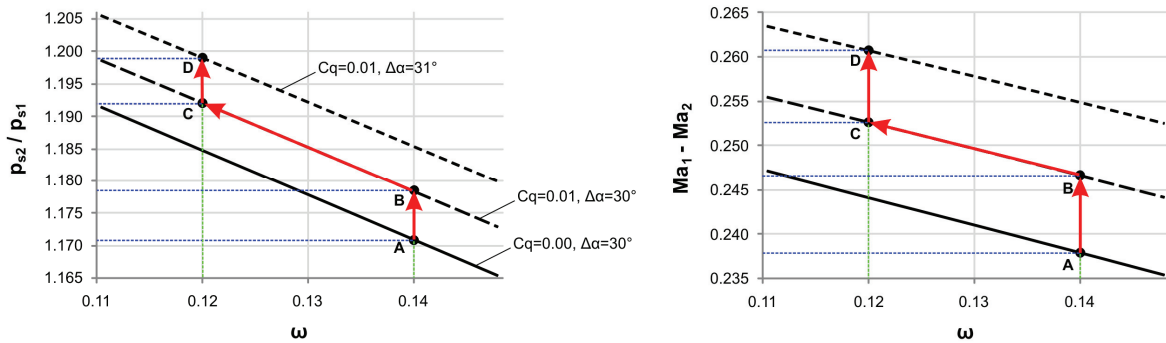

Figure 2-3. Comparison of the pressure rise and deceleration due to the change of selected parameters: A) reference, B) added aspiration with Cq=0.01, C) added reduction of total pressure loss by 0.02, and D) added improvement of deflection by 1°. The curves are solutions of equation (2.28).

Extraction of mass flow hence directly increases the pressure rise and the deceleration. This is reflected as an increased of loading by the introduced loading parameters. However, these loading parameters do not reflect the cost in terms of mass flow which is removed. Hence, the amount of extracted mass flow must always be indicated. To quantify changes of the overal engine performance, a systemic analysis must be performed on case to case basis, where a cycle analysis will consider the cost in terms of extracted mass flow and determine if the improvements in loss and deflection, compressor mass and stability as well as the gain in aspirated mass flow for secondary systems compensate the reduced compressed mass flow. In any case it is obvious that the extraction of mass flow must be limited to the minimum that is necessary to achieve significant reduction of the loss level and improvement of the loading.

2.4 Flow quality

Some flow features analysed more in detail in the following sections, induce significant non-uniformities in the outlet flow of the cascade. The non-uniform distributions of deflection, velocity, momentum and total pressure at outlet deviates the flow conditions from the design conditions, herewith perturbing the further compression in later stages. Otherwise, if the distance between blade rows is sufficient, non-uniformities mix out causing loss of total pressure. This reduced flow quality must be taken into account when evaluating the compressor performance and when comparing different configurations. They must hence be considered when comparing cases with different aspiration configurations.

2.5 Summary

A number of parameters are derived to evaluate and compare the performance of different compressor cascades or different cascade configurations. The loss is expressed by the change in entropy or by total pressure loss. Comparisons must consider the aspiration rate. Its impact on the performance must be weighted according to the utility of the extracted mass flow for other engine systems. A number of

parameters are given to evaluate the cascade loading: foremost the pressure rise and the deflection. Their respective weighting for the performance evaluation depends on the chosen compression strategy. To evaluate the blade loading, the single blade pressure rise must be compared, since the single blade loading is not reflected by the overall pressure rise. The single blade pressure rise highlights the aerodynamic impact of changing the blade number, which in turn impacts the compressor mass. The further typical loading indicators Mach number deceleration and Lieblein Diffusion Factor are introduced for comparison purpose. With a model based on continuity and enthalpy conservation it is shown, that flow extraction alone has already the effect of increasing the value of the loading indicators. This stresses the importance of also indicating the aspiration rate when evaluating the performance. The model also shows and quantifies how improvements by aspiration of total pressure loss and deflection improve the pressure rise and deceleration performance. Finally it is emphasized that a further important performance parameter is the quality of the produced flow: if the outlet flow is very non-uniform, this can yield later loss production due to mixing out. If the non-uniform flow does not coincide with the design conditions, this will furthermore compromise the performance of following stages. Hence controlling the involved features by aspiration is a further figure of merit for the performance.

3. Three-dimensional and rotational flow field analysis

One key aspect in the present work is the analysis of the three-dimensional flow that occurs in the tested annular configuration. Different flow features make the flow depart from idealized flow condition where a (θ,x)-plane representation at an average radius sufficiently reproduces the flow situation. Separations and vortices cause blockage and deflection yielding significant radial and increased circumferential variation of the flow conditions.

The involved mechanisms modify the vorticity of the flow. Beyond influencing the flow motion, the vorticity yields characteristic traces at the outlet measurement location. Part of these mechanisms can be related to so-called secondary flow defined in this chapter. Identifying these mechanisms and quantifying their intensity is important for understanding how they affect the flow quality and how they are influenced by aspiration. Hence adequate indicators to characterise these features are introduced hereafter: vorticity, helicity, secondary velocity and secondary kinetic energy. The usage of part of these indicators is relatively uncommon. However as will be seen, they significantly support the understanding of the occurring three-dimensional flow.

3.1 Vorticity

The rotational motion of fluid particles or of entire fluid regions can be described in terms of vorticity distribution. The local vorticity is formally defined at each point of velocity flow field $\vec{V}$ by

$$\vec{\Omega} = \nabla \times \vec{V} = \overrightarrow{rot}\,\vec{V} \tag{3.1}$$

Production, dissipation and transport of vorticity are subject to well defined laws based on the mathematical framework of vector fields. Only some salient features relevant for the present investigation are briefly summarized hereafter. For extensive discussion on the application of vorticity analysis to turbomachinery, the reader is referred to [Lighthill 1963], [Lakshminarayana 1996], [Greitzer et al. 2004] and [Leboeuf 2008].

Analyzing the flow field in terms of vorticity allows understanding the mechanisms inherent to apparently complex macroscopic three-dimensional motions. Within a blade channel, the influence of vorticity can be relevant, especially the re-orientation of the flow and the transport of flow properties. The underlying laws enable explaining this evolution with respect to the channel geometry, the velocity field and the pressure field. Furthermore, the intensity of the observed flow features can be quantified in terms of vorticity, which enables to measure their sensitivity to influencing parameters as e.g. the application of aspiration. Since vorticity always indicates shear, regions of high vorticity going with elevated friction and mixing are indicators for features producing losses that can impact the compressor performance.

Vorticity is always present in real internal flows, starting in the boundary layers where vorticity of either sign is continuously produced by the wall friction that decelerates the flow close to the wall. The viscous interaction between fluid particles redistributes the vorticity making it diffuse to flow regions further away from the wall. This region affected by rotational motion is in fact the boundary layer. An extensive discussion of this can be found in Lighthills Introduction to Boundary Layer Theory [Lighthill 1963]. The vorticity usually stays within the boundary layer, unless redirection makes it reach out into the inviscid flow. The redirection can be caused e.g. by solid bodies, by separations, pressure gradients. Often this makes vortical structures appear. As noted earlier, this can occur in three-dimensional separations. Wall-attached vortices or horseshoe vortices are exemplary macroscopic manifestations of concentrated vorticity that can arise from such separations. Curvature of the flow and the intrinsic pressure gradients

can re-orient, amplify or reduce the vorticity level. This is the case, e.g. for the formation of so-called secondary flow discussed in the next section.

The vorticity distribution can be represented by vortex lines, lines that are tangent to vorticity vectors in each point. Due to the general definition of a vector field, it can be derived that $\nabla^T \cdot \vec{\Omega} = 0$. As noted in [Greitzer et al. 2004], this continuity equation yields, similar as for streamline in incompressible flows, that vortex lines cannot end in a fluid and that concentrations of vortex lines occur where vorticity is high et vice versa. In analogy to stream tubes, vortex tubes can be defined. As the mass flow in a streamtube, the strength of the vortex tube, as is often called the flux of vorticity $\iint \vec{\Omega} \cdot \vec{n} \, dA$, must be the same on each surface of intersection with the vortex tube. This means that the vorticity magnitude varies inversely to the area of the vortex tube. The core of a vortex can be represented by such a vortex tube. As a consequence, as expressed by the Kelvin-Helmholtz theorem, a vortex cannot end in a fluid; it must extend to the boundaries of the fluid (either walls or the infinite) or form a closed path. Hence a vortex cannot be "cut", which is well illustrated by a horseshoe vortex that hangs on a leading edge and cannot leave. But vortices can be turned and stretched, creating changes in vorticity magnitude and direction.

It is important to note that generally, vorticity is conserved unless it is dissipated. Only at the walls, where vorticity of varying sign is continuously generated. Viscous forces redistribute existing vorticity and only a small amount is dissipated to heat. The factors that may increase or decrease the vorticity of the flow can be identified analyzing the transport equation of the vorticity of the flow according to [Leboeuf 2008]:

$$\underbrace{\frac{\partial \vec{\Omega}}{\partial t}}_{(1)} \underbrace{-2\frac{\partial \vec{\omega}}{\partial t}}_{(2)} + \underbrace{(\vec{V}^T \cdot \nabla)\,\vec{\Omega}}_{(3)} \underbrace{-(\vec{\Omega}^T \cdot \nabla)\,\vec{V}}_{(4)} = \underbrace{\frac{1}{\rho}\frac{D\rho}{Dt}}_{(5)} \underbrace{-\nabla \times \left(\frac{1}{\rho}\nabla p\right)}_{(6)} + \underbrace{\nu\,\Delta\vec{\Omega}}_{(7)} + \underbrace{\nabla \times \vec{f}}_{(8)} \tag{3.2}$$

The equation can be further simplified: contraction of terms (1) and (3) yields the substantial derivative. Term (2) considers temporal variations of the wheel rotation and can often be neglected. This yields:

$$\underbrace{\frac{D\vec{\Omega}}{Dt}}_{(1)} = \underbrace{(\vec{\Omega}^T \cdot \nabla)\,\vec{V}}_{(2)} + \underbrace{\frac{1}{\rho}\frac{D\rho}{Dt}}_{(3)} \underbrace{-\nabla \times \left(\frac{1}{\rho}\nabla p\right)}_{(4)} + \underbrace{\nu\,\Delta\vec{\Omega}}_{(5)} + \underbrace{\nabla \times \vec{f}}_{(6)} \tag{3.3}$$

With respect to the present application to a compressor stator cascade, following remarks can be made: The substantial derivative (1) indicates the change of vorticity for a particle or volume following the flow. Term (3) covers compressibility effects that are moderate in the present case and are hence no major source candidate for vorticity. Term (4) covering the interaction between density and pressure gradients is zero for isotherm cases. It should be relatively modest in the present case. Term (6) considers external forces that are also not relevant presently. This said, the remaining terms constitute relevant sources for vorticity: convected vorticity is contained in (1). The diffusion term (5) quantifies viscous effects occurring at the wall or wherever gradients of vorticity occur, as e.g. in mixing layers, the wake, etc. Term (2) is maybe the most relevant here, since it indicates that velocity gradients can amplify or reduce already existing vorticity. Hence, for the present case the transport equation for vorticity points out that vorticity is either produced at the walls or in strong mixing layers or it is advected from other sources or it is amplified or reduced by the influence of velocity gradients, which are generally consequence of pressure gradients and curvature.

3.2 Secondary Flow

As noted in [Cumpsty 2004], "many of the observed effects in turbomachinery can be put down to the transport of the vorticity already present, with only a small contribution from diffusion. The approach which concentrates on the movement of existing vorticity and neglects the diffusion is normally referred to as secondary flow theory." Secondary flow is a deviating flow motion superposed to the main flow motion resulting in a non-uniformity of the flow. In the review [Horlock et al. 1973], secondary flow is defined as the secondary motion "produced when a streamwise component of vorticity is developed from the deflection of an initially sheared flow". In other words, secondary flow occurs when vorticity oriented streamwise is originated from pre-existing vorticity oriented normal to the flow. As explained in the preceding section, such production occurs mainly by re-orientation and stretching of the pre-existing vorticity. The production is augmented by higher deflection. It is also increased by acceleration as occurs in convergent nozzles, making secondary flow even more important in turbine cascades than in compressor cascades. Once streamwise vorticity is formed, its magnitude can be increased or reduced by re-orientation and stretching. This will be shown analyzing the streamwise vorticity transport equation.

As noted, secondary flow only forms if vorticity - or sheared flow as termed by Horlock et al. - already exists. The main source of such pre-existing vorticity at the inlet of a cascade resides in the wall boundary layers. Further vorticity is formed in both wall and blade boundary layers within the blade channels. Thicker boundary layers yield increased secondary flow formation. Another source can be skewed flow at the inlet of a blade row, thus flow with a radial variation of incidence, hence pre-existing vorticity. Thus secondary flow formation can never be completely avoided but may be reduced by influencing the thickness of boundary layers and minimizing inlet flow non-uniformity.

A number of relevant flow features observed in this work can be explained by secondary flow. Based on [Lakshminarayana 1996] and [Cumpsty 2004], relevant flow features, caused by secondary flow in compressor wheels as investigated here, are:

- cross flow, resulting in three-dimensionality of the flow field,
- formation of passage vortices that may initiate and feed separations in the corner between wall and blade suction side,
- overturning in the wall regions and underturning outside the wall region, thus secondary flow affects the pressure rise,
- shear loss decreasing the efficiency,
- off-design conditions in the downstream plane affecting the stage matching with subsequent wheels, and
- inwards flow movement (towards the hub wall) in blade surface boundary layers and wakes.

Streamwise vorticity transport equation

Considering that secondary flow is defined as vorticity that is oriented streamwise, its production is given by the streamwise component of the vorticity transport equation. Based on [Leboeuf 2008], this component is found in a streamwise oriented locally orthogonal frame of reference , i.e. with streamwise, normal and bi-normal components, and can be derived from (3.3) yielding

$$\frac{D\Omega_s}{Dt} = \Omega_s \left(\frac{\partial V_s}{\partial s} + V_n K_{sn} + V_b K_{sb} \right) - \Omega_n \left(\frac{\partial V_s}{\partial n} - V_s K_{sn} \right) - \Omega_b \left(\frac{\partial V_s}{\partial b} - V_s K_{sb} \right)$$

$$(1) \qquad\qquad (2) \qquad\qquad\qquad (3) \qquad\qquad\qquad (4)$$

$$(3.4)$$

$$+ \left[\frac{1}{\rho} \frac{D\rho}{Dt} - \nabla \times \left(\frac{1}{\rho} \nabla p \right) + v \, \Delta \vec{\Omega} + \vec{\nabla} \times \vec{f} \right]_s$$

$$(5)$$

The streamwise components (5) resulting from terms (3)-(6) in equation (3.3) are not expanded since they are not relevant for this consideration. These include production or diffusion of streamwise vorticity due to compressibility, to the interaction of density and pressure gradient, to viscous dissipation and to external forces. The parameters K_{sn} and K_{sb} are the curvature (the inverse of the curvature radius) of the streamline, respectively in direction normal and bi-normal to the streamwise direction. Herewith terms (2)-(4) indicate that streamwise vorticity arises:

- if changes of the velocity components aligned with existing vorticity occur, or
- if flow with existing vorticity is deflected.

The streamwise vorticity produced according to the indicated terms is then added to existing streamwise vorticity increasing or decreasing the sum depending on the sign relations.

Since the velocity derivatives of equation (3.4) are also related to the vorticity, precise interpretation of this equation is rather complex. Horlock and Lakshminarayana describe a number of simplified derivations presented in [Lakshminarayana 1996]. For inviscid flow and the assumptions described precedently, following relationship is introduced:

$$\frac{\partial}{\partial s} \left(\frac{\Omega_s}{\rho V} \right) \approx \frac{2\Omega_n}{\rho V R} \tag{3.5}$$

It indicates that streamwise vorticity arises from existing normal vorticity along a streamline which is deflected with radius of curvature R.

Helicity

As shown by the preceding derivations, consideration of the streamwise component of vorticity is one way to quantify secondary motion in a flow. A convenient metric proposed by [Leboeuf 2008] that even better reflects the severity of the secondary motion for the considered flow is the helicity. With regards to the present concerns, helicity is a scalar formed by weighing the occurring streamwise vorticity by the local magnitude of velocity:

$$H = \Omega_s \, |\vec{V}| \, . \tag{3.6}$$

An increase of helicity indicates hence either an increase of streamwise vorticity, or an increase of velocity in a region concerned by streamwise vorticity. Both cases reflect an increase of secondary motion.

Note that streamwise vorticity is the vorticity component aligned with the flow velocity. It is hence given by the projection of the vorticity on the flow direction:

$$\Omega_s = \vec{\Omega} \cdot \vec{V}^0 = \vec{\Omega} \cdot \frac{\vec{V}}{|\vec{V}|} \tag{3.7}$$

Yielding that the helicity can be easily computed by the scalar product of vorticity and velocity vectors. In this definition, the streamwise vorticity does not appear explicitly:

$$H = \vec{\Omega} \cdot \vec{V} \qquad (3.8)$$

The definition of the scalar product yields following relationship:

$$H = |\vec{\Omega}| |\vec{V}| \cos \delta \qquad (3.9)$$

with the angle δ enclosed between the two vectors. Hence helicity will be highest, if the enclosed angle is zero, which would mean that the vorticity vector is aligned with the velocity vector and would hence be completely streamwise oriented. Such a flow describes a corkscrew motion along a trajectory. In axial turbomachinery this generally denotes a flow that significantly deviates from design conditions. The sign of the helicity reflects if the vorticity is rather parallel or anti-parallel to the velocity, indicating the rotation direction of the corkscrew motion. Helicity disappears the more the enclosed angle approaches a right angle. Hence a flow with only normal vorticity components, as occurs e.g. in a forward facing boundary layer, has zero helicity. The magnitude of helicity increases with increasing vorticity and velocity of the affected flow. It has the dimensions of energy per unit mass and unit length:

$$[H] = \frac{m}{s^2} = \frac{J}{kg \, m} \qquad (3.10)$$

It is herewith related to the energy transferred by the streamwise oriented vortical motion, i.e. by the secondary flow. As noted by [Leboeuf 2008], energy captured in such vortical motion can rarely be recuperated efficiently. Leboeuf refers to [Moore et al. 1987], indicating that vorticity past a cascade generally dissipates to heat which is rather detrimental in a compressor context.

A remarkable characteristic of helicity is that it is a transported quantity. Thus, a transport equation can be found, e.g. by considering the relationship to the transport of streamwise vorticity (3.4) in an orthogonal referential:

$$\frac{D\Omega_s}{Dt} = \frac{D}{Dt}\left(H \, \frac{1}{|\vec{V}|} \right) = \underbrace{\frac{1}{|\vec{V}|} \frac{D}{Dt} H}_{(1)} \; + \; \underbrace{H \frac{D}{Dt} \frac{1}{|\vec{V}|}}_{(2)} \qquad (3.11)$$

So in coherence with (3.6) the substantial derivative of streamwise vorticity is almost found as the substantial derivative of H divided by the local magnitude of velocity (1). However the product rule introduces a term (2) considering the convective change of $1/|\vec{V}|$ weighed with H. A more conveniently reshaped formulation of the general transport equation is presented in [Leboeuf 2008]:

$$\rho \frac{DH}{Dt} = \underbrace{-2\vec{\Omega} \cdot \nabla p}_{(2)} + \underbrace{\mu \, \vec{\Omega} \cdot \Delta \vec{V}}_{(3)} - \underbrace{\rho \, \vec{\Omega} \cdot \frac{\partial \vec{V}}{\partial t}}_{(4)} + \underbrace{\mu \, \Delta H}_{(5)} \qquad (3.12)$$

Term (2) indicates that positive or negative helicity is produced by the interaction of existing vorticity with the pressure gradient. Simplest illustration is that a pressure gradient is usually related to a streamline deflection. Depending on how this deflection changes the alignment between vorticity and velocity, the component of streamwise vorticity and hence the helicity will change. The terms (3) and (5) denote viscous diffusion of the helicity. Term (4) captures unsteady production.

Hence the transport equation supports identifying the sources of helicity. Beyond this, following considerations based on [Leboeuf 2008] support what noted earlier, on the dissipation of the energy carried by the helicity past a cascade. Past a cascade, the pressure gradient tends to settle to a radial orientation without meridional components. With regards to the production term (2), radially oriented vorticity from the blade boundary layers (wake) will produce helicity. Circumferentially oriented vorticity from the wall boundary layers or axially oriented vorticity in case of skewed flow will not. On the long

term, provided that no instationarity occurs as the passage from to a rotor to a stator or vice versa, only the diffusion terms (3) and (5) will determine the transport of helicity yielding a progressive dissipation.

While helicity is often used to describe meteorological flows, it is less common in the investigation of technical flows. However the interest in using helicity is renewed for the understanding of three-dimensional internal flows in stators and rotors (see [Leboeuf 2008]). Introduced with the name helicity into fluid dynamics by [Moffatt 1969], it is valued in topological investigations as [Moffatt et al. 1992] and occasionally recognized as means to extend investigations on classical complex flow configurations for representation of vortical structures as is done in [Levy et al. 1990]. As noted therein, normalized helicity

$$H^0 = \frac{\vec{\Omega}\vec{V}}{|\vec{\Omega}||\vec{V}|} = \frac{H}{|\vec{\Omega}||\vec{V}|} = \cos\delta \tag{3.13}$$

is maximum close to a concentrated vortex core axis, allowing its detection. Its sign changes across a separation or reattachment line. And as indicated by the relation to streamwise vorticity, mapping the helicity allows locating secondary vortices.

3.3   New secondary velocity extraction method

Often flow velocity fields can be modeled by potential (irrotational) distributions, which means that everywhere in the field, the vorticity is zero, thus:

$$\nabla \times \vec{V}_{irrotational} = 0 \tag{3.14}$$

This offers great simplifications. However, in real flow situations, as in the outlet plane of a compressor cascade, rotational features occur. In particular, secondary motion induced by streamwise vorticity cannot be represented by irrotational distributions but it significantly influences the flow field.

A method will be presented to analyze the rotational components of a measured flow field separately from the potential components. This allows focusing on certain mechanisms occurring within the cascade and it allows quantifying their intensity to indicate the deviation from optimum flow conditions. With this intention, based on [Leboeuf 2007], a method is developed to separate the measured or computed velocity field into components induced by a potential field and components induced by a rotational field.

The underlying theorem is called the Helmholtz-Decomposition. It states that an arbitrary, differentiable vector field can be decomposed into a potential and a rotational part. In particular, this method will be used here to extract the velocity components induced by the secondary flow, hence by the streamwise vorticity. Isolating this secondary velocity field, as it will be called hereafter, bears great advantages for identifying and understanding the flow mechanisms related to secondary motion. Beyond this, it allows a consistent quantification of the energy transferred by the secondary motion based on the obtained secondary velocities. It will be noticed that a fundamental advantage of this method is that it can be applied to most experimentally measured or numerically computed velocity field that have sufficient resolution. Hence it yields a post-processing approach that – if complemented with notions of the analysis of fields of vorticity and helicity – builds a powerful method for investigation of complex three-dimensional flows. Its application will be demonstrated by application on the results of the present investigation and compared to earlier research works where the computation of secondary velocities was attempted by different approaches.

3.3.1   Related former investigations

In the review by [Horlock et al. 1973] it is already mentioned that the secondary velocity flow field can be found for streams with low change of streamwise velocity by finding a solution to the equation

$$-\Omega_s = \Delta\Psi \tag{3.15}$$

with the streamwise vorticity Ω_s and an adequate secondary stream function Ψ. The normal and bi-normal components of secondary velocity would then be given by $V_n = \partial\Psi / \partial n$ and $V_b = \partial\Psi / \partial b$. As will be seen, a very similar form is found in the following derivation. However, apart some notices in [Marchal et al. 1977] only little written documentation is found of solving equation (3.15) for post-processing results from measurements or numerical simulations and for extracting the underlying secondary velocity field. The relation was rather used for analytical design studies: one would produce an analytical model of streamwise vorticity on the left hand side, representative for a certain blade flow, and use the relation to predict the secondary velocities to be expected in the outlet flow. Those would then be used to determine the deviation of the outlet flow from design condition. Such analytical approaches were documented by Squire and Winter yielding a well known correlation, and by Hawthorne dating back 1951

and 1955 respectively. The relation (3.30) introduced hereafter, de facto reproduces (3.15), but it is derived based on the Helmholtz decomposition, as will be seen. The Helmholtz decomposition was often of interest for numerical flow simulations based on the vorticity transport equations. However such simulation approaches lost relevance with the advance of computing power that made it possible to solve more laborious but less approximate formulations of the Navier Stokes equations. Some recent publications show a renewed interest in this area as [Morino 1990] and [Joseph 2010] and serve here as mathematical reference.

A number of investigations on three-dimensional flow mechanisms can be found where secondary velocities have been estimated by different approaches. Especially in the domain of turbine flow investigations, as reviewed by [Langston 2001], where the significant turning and the accelerating flow is known to increase secondary flow effects. However the approach to find the secondary flow field was mostly to compute an average velocity and then, the deviation of local velocities from the average was considered secondary velocity. Some significant publications illustrate how secondary velocity fields obtained this way support identification and understanding of particular flow features. Cited by [Lakshminarayana 1996] there are: [Hathaway et al. 1993] analyzing secondary velocities from measurements and simulations at inlet and outlet of a centrifugal compressor rotor, [Ubaldi 1993] performing similar investigations on a backward swept rotor. But also to mention are: [Sieverding 1985] making an extensive review on secondary flow and vortex topology through turbine blade passages making use of secondary velocity plots in his explanations, [Hebert et al. 1990] performing extensive analysis comparing amongst others secondary velocities, streamwise vorticity and turbulence past a turbine stator cascade, and [Schulz et al. 1990] observing the secondary velocity field relating it to a topological analysis of flow past a highly three-dimensional corner separation of an annular compressor cascade. The latter is particularly comparable to the case investigated in this work.

3.3.2   Derivation

As noted, certain flow types can be sufficiently well modeled by irrotational (potential, solenoidal) distribution. This is the case when the velocity vector $\vec{V}$ can be represented by the gradient of a scalar function ϕ, as:

$$\vec{V} = \nabla \phi \qquad (3.16)$$

The condition of irrotationality is fulfilled, since the rotational $(\nabla \times)$ of the preceding is zero:

$$\nabla \times \vec{V} = \nabla \times (\nabla \phi) = 0 \qquad (3.17)$$

according to the vector differentiation law

$$\nabla \times (\nabla a) = 0 \qquad (3.18)$$

valid for each scalar function a.

If a velocity field is not sufficiently modeled by an irrotational distribution, this means that it must partially or completely be rotational. In fact, according to the Helmholtz decomposition, an arbitrary differentiable vector field can be separated into an irrotational and a rotational distribution. Hence for any differentiable velocity field $\vec{V}$ which may result from measurements or computations, the decomposition is:

$$\vec{V} = \nabla \phi + \nabla \times \vec{\Psi} \qquad (3.19)$$

This allows defining an irrotational (potential) and a rotational velocity distribution that if superposed one to each other yield again the velocity distribution to be modeled:

$$\vec{V} = \vec{V}_{pot} + \vec{V}_{rot} \tag{3.20}$$

with

$$\begin{aligned} \vec{V}_{pot} &= \nabla \phi \\ \vec{V}_{rot} &= \nabla \times \vec{\Psi} \end{aligned} . \tag{3.21}$$

As noted in [Morino 1990], given the indicated differentiable velocity field, one can solve for a particular solution of $\vec{\Psi}$. An ingenious approach to do this is to apply the rotational operator to equation (3.19), respecting (3.18) which yields:

$$\nabla \times \vec{V} = \nabla \times \left(\nabla \times \vec{\Psi} \right) \tag{3.22}$$

a further vector differentiation law stipulates that for a vector field $\vec{b}$

$$\nabla \times \left(\nabla \times \vec{b} \right) = -\Delta \vec{b} + \nabla \left(\nabla^T \cdot \vec{b} \right) \tag{3.23}$$

which applied to (3.22) yields

$$\nabla \times \vec{V} = -\Delta \vec{\Psi} + \nabla \left(\nabla^T \cdot \vec{\Psi} \right) \tag{3.24}$$

and as further noted in [Morino 1990] citing the Helmholtz decomposition theorem, there exist one ϕ and $\vec{\Psi}$ (usually called the scalar potential and the vector potential respectively) with

$$\nabla^T \cdot \vec{\Psi} = 0 \tag{3.25}$$

that solves equation (3.24). Condition (3.25) inserted in (3.24) yields that the particular solution for $\vec{\Psi}$ must obey

$$\nabla \times \vec{V} = -\Delta \vec{\Psi} . \tag{3.26}$$

This is a Poisson problem for which numerical solution schemes exist. A particular solution to $\vec{\Psi}$ would allow computing the rotational velocity component $\vec{V}_{rot}$ according to (3.21) of the Helmholtz decomposition. The according potential component $\vec{V}_{pot}$ would then easily be found by (3.20). One would so obtain the decomposition of a given velocity field into an irrotational (potential) and a rotational part.

It must be noted that the left hand side of equation (3.26) is in fact the vorticity field related to the velocity field $\vec{V}$. In symbols:

$$\vec{\Omega} = -\Delta \vec{\Psi} \tag{3.27}$$

It can hence be inferred that $\vec{V}_{rot}$ is the velocity component induced by the vorticity of the field, such as $\vec{V}_{pot}$ is the velocity component induced by the potential part.

The next step in the consideration is to focus only on the streamwise components of the vorticity. As explained earlier on, the flow induced by the streamwise vorticity constitutes the secondary motion of the flow.

Secondary velocity can be defined by the following analogy: equation (3.27) shows that the vorticity $\vec{\Omega}$ induces a potential vector $\vec{\Psi}$ which yields the rotational component $\vec{V}_{rot}$ of the decomposition of $\vec{V}$. Thus, projection of (3.27) on the direction of $\vec{V}$ gives an equation for Ψ_s that will provide the secondary velocity V_{sec}.

As will be seen, focusing on the streamwise vorticity bears also advantages for the solution of (3.27). In an orthogonal referential with Cartesian coordinates, the Tensor Laplacian operator simplifies to:

$$\Delta(x_1, x_2, x_3)^T = \left(\Delta x_1, \Delta x_2, \Delta x_3\right)^T \tag{3.28}$$

which means that the components can be solved separately. Assuming that the flow field can be expressed by sufficiently orthogonal coordinates (this will be verified empirically on the test cases), (3.28) can be applied to equation (3.27), yielding:

$$\Delta(\Omega_s, \Omega_n, \Omega_b)^T = \left(\Delta\Psi_s, \Delta\Psi_n, \Delta\Psi_b\right)^T \tag{3.29}$$

and one obtains the equation to solve for the streamwise potential vector component:

$$\Omega_s = -\Delta\Psi_s \tag{3.30}$$

This is a scalar Poisson problem and can be solved with significantly less efforts than (3.26). The vorticity in streamwise direction is promptly given by

$$\Omega_s = \frac{\vec{V}}{|\vec{V}|}\vec{\Omega} \tag{3.31}$$

where $\vec{V}/|\vec{V}|$ is the local streamwise direction.

The components Ω_n and Ω_b could be found similarly by fixing a normal and binormal direction. Since the intention is to focus on the streamwise vorticity, these components will not further be considered. As according to (3.29) the components are sufficiently uncoupled, they can be set to zero without influencing the streamwise result: $\Omega_n = \Omega_b = 0$. Formally, this yields the trivial solutions $\Psi_n = \Psi_b = 0$ for these components. The streamwise components can be solved using a common scheme. To find a particular solution, Dirichlet boundary conditions are applied, thus $\Psi_s = 0$ along the boundary of the computation domain.

The velocity component $\vec{V}_{sec}$ is then found in the (s, n, b) referential according to equation (3.21). This yields

$$\vec{V}_{sec} = (v_{sec,s}, v_{sec,n}, v_{sec,b})^T = \nabla \times (\Psi_s, \Psi_n, \Psi_b) \tag{3.32}$$

which can be converted to Cartesian coordinates (marked hereafter with a tick) by

$$\vec{V}'_{sec} = \vec{V}_{sec} (\vec{e}_s, \vec{e}_n, \vec{e}_b) \tag{3.33}$$

The last two steps can be contracted by projecting the streamwise component of the potential vector to Cartesian coordinates before computing the rotational, yielding:

$$\vec{V}'_{sec} = \nabla \times \left(\Psi_s \frac{\vec{V}}{|\vec{V}|} \right). \tag{3.34}$$

3.3.3 Implementation

The implementation of this approach has some peculiarities in its present application that are worth being illustrated: first, the vorticity of the original field must be computed. In Cartesian coordinates, this is given by

$$\vec{\Omega} = \nabla \times \vec{V} = \begin{pmatrix} \partial V_z / \partial y - \partial V_y / \partial z \\ \partial V_x / \partial z - \partial V_z / \partial x \\ \partial V_y / \partial x - \partial V_x / \partial y \end{pmatrix} \tag{3.35}$$

As mentioned, the computation is based on measurement results. In the present case the 5-hole probe measurements from the outlet measurement plane are used. Thus, the derivatives in axial direction (x direction in the present case) are unknown. Typically, the velocity variations in streamwise direction are negligible. In direction normal to the streamwise direction they can be important and would impact the axial derivative the more, the less axial the flow is. In the present investigation, the outlet flow angle with respect to the cascade axis is usually close to 30° thus relatively shallow. Therefore, the axial derivatives are not expected to be very important and might be neglected. To verify this, a typical 3D-RANS simulation result related to this case was taken as representative case and the vorticity vectors in a plane corresponding to the outlet measurement plane were computed according to (3.35) first considering and then neglecting the axial derivatives. Since we are interested in the streamwise vorticity to solve (3.30), it was computed based on these results according to (3.31). The result is presented in Figure 3-1. The maximal difference of average values is close to 0.2% of the average vorticity magnitude. Thus neglecting the axial derivatives can be expected to have only small influence on the resulting secondary flow fields.
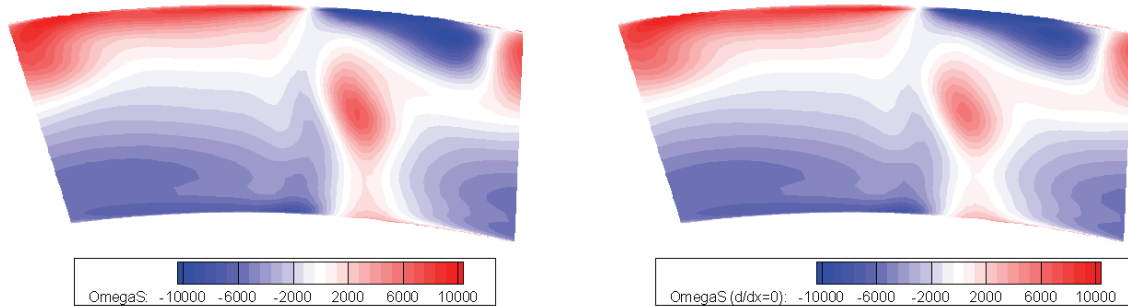

Figure 3-1. Computation of the streamwise vorticity based on a representative 3D-RANS simulation result in an axial plane corresponding to the outlet measurement plane. On the left, the exact equation was used. On the right, the axial derivatives were neglected.

In the present investigation, the mesurement results are usually obtained only for one blade step and since the accessible measurement region does not extend up to the wall, some information in that regions is missing. To avoid border effects in the solution of the Poisson problem (3.30), a computation domain is defined that is significantly larger than one blade step. It is indicated by the green box in Figure 3-2. The circumferential limitation is solved by a periodic repetition of the measured data within the computation domain, as also visible in Figure 3-2. The probe measurements are also limited in radial direction. To dampen border effects in radial direction, values that are missing are extrapolated by a linear drift algorithm as shown in the plot to the right. The drift is limited by zeroes where the flow channel walls are located. This is also illustrated Figure 3-2: to the left, the values close to the hub and to the casing are missing. In the image to the right, in these regions values are added that are obtained by linear drift computed with a common post-processing tool (Tecplot 2006). The light blue regions inside and outside the results are filled with zeroes. This operation yields a spatial distribution of streamwise vorticity values based on the measurement data that is used to solve (3.30).
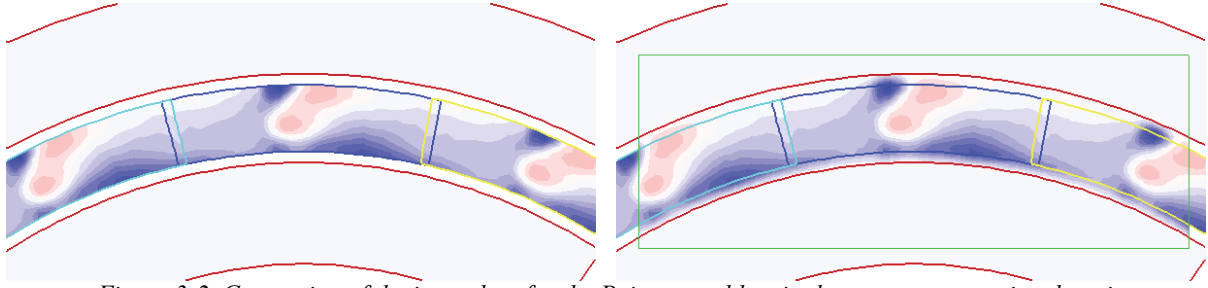
Figure 3-2. Generation of the input data for the Poisson problem in the green computation domain.

The Poisson problem is solved with a common finite element tool (Comsol Multiphysics 3.3a based on MatLab) on an unstructured mesh. Formally, certain integration constants must be chosen to solve for Ψ_s. Since they will anyway be eliminated when the rotational is computed, they are opportunely defined by chosing the Dirichlet boundary condition $\Psi_s = 0 \,|\, \partial\Omega$ along the domain borders. Numerous refinements of the meshes for the data transfer and the solving were performed to ensure that the resulting distribution of Ψ_s verifies equation (3.30). A qualitative impression of the results is given by Figure 3-3: in the computation to the right, the described measures to avoid border distortions due to limited measurement data were applied.
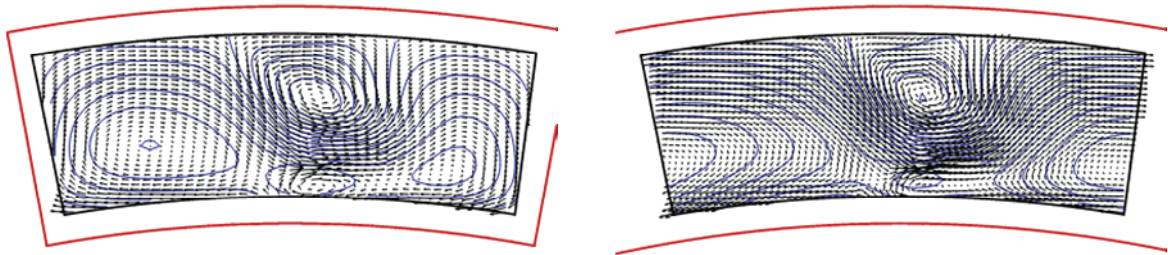
Figure 3-3.Qualitative results: the blue isolines indicate the levels of Ψ_s. The vectors are the secondary velocities. In the computation to the left, periodicity, walls and missing values were not modeled.

3.3.4   Comparison of the results to the classical approach

Finally, the results obtained by the new method are compared to results obtained by the classical approach to obtain an approximate secondary velocity distribution. This is described e.g. in [Schulz et al. 1990] yielding the results presented in Figure 4-12. It consists in first computing the mass or the mass flow weighted average velocity for the considered flow field. This average velocity is then subtracted from each local velocity of the vector field. The result thus represents the deviation of the local velocity from the average velocity and is called the secondary velocity:

$$\vec{V}_{sec,classic} = \vec{V}_{local} - \overline{\overline{V}} \tag{3.36}$$

For demonstration, the classical approach and the new approach are applied to the velocity field illustrated in Figure 3-4. It is a typical flow distribution measured by five-hole probe at the outlet plane of an annular non-rotating axial compressor cascade without aspiration investigated in the present work. A low velocity region can be noted: it is identified as the trace of an important separation that occurs between the hub and the suction side. Figure 3-5 shows the results of both approaches. As can be noted, the classical approach yields very high values of secondary velocity and representing only a rough estimate of the deviating motion. In contrast, the results obtained by the new approach really reflect the velocity induced by the streamwise vorticity of the field. A well known feature is the secondary flow towards the suction side along the hub that is identified as the hub passage vortex. The further features will be analyzed in the result part of this work.
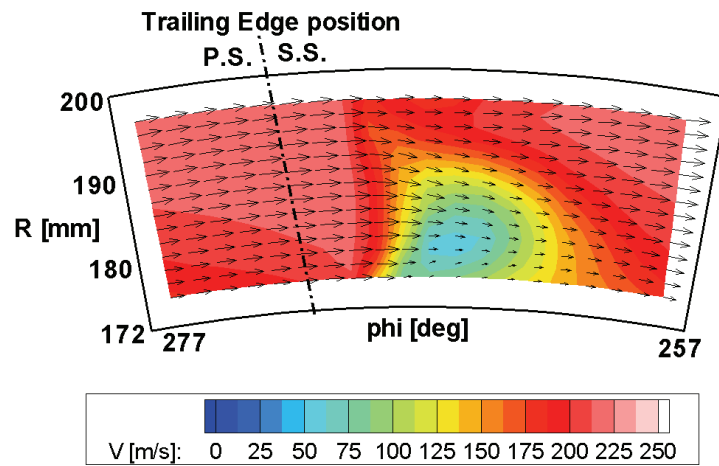
Figure 3-4. Velocity field of the demonstration case: outlet plane flow of an axial compressor cascade with inlet Mach number 0.8. The low velocity trace is related to a hub corner separation occurring in the cascade.
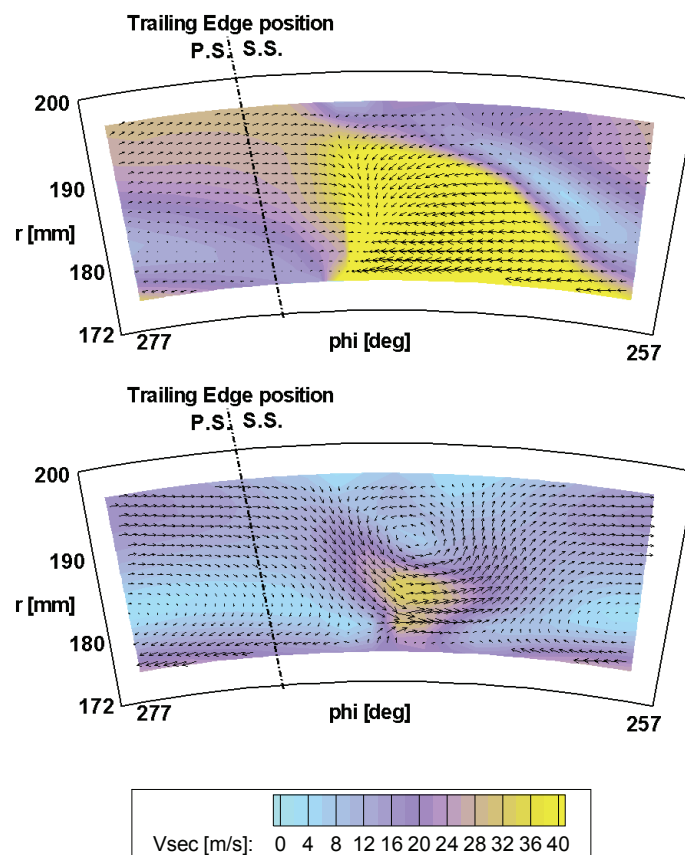

Figure 3-5. Comparison of the resulting secondary velocity field computed with the classical approach (top) and with the new approach (bottom). Note that the vector length scale is different than in Figure 3-4.

4. Relevant highly loaded compressor flow features

4.1 Separations

For long time, only bi-dimensional separations where considered. The advancement in experimental measurement of three-dimensional velocity distributions downstream of cascades, the application of vector field mathematics to flow description by topological analysis, and the fully 3D numerical simulations made more complex 3D features discernible that are relevant for the flow.

4.1.1 Two-dimensional separation

The most important feature in a bi-dimensional consideration is that due to the adverse pressure gradient, the boundary layers will grow in streamwise direction on the hub and casing wall surfaces and on the blade. The boundary layers act similar to solid walls for the main flow, hence their thickening yields an apparent flow channel restriction that limits the diffusion and hence the pressure rise. The boundary layer growth is most pronounced on the blade suction side, since there the maximum deceleration occurs, after the point of maximum velocity which is also located on the suction side. If the boundary layer grows excessively, it can separate, which can cause important aerodynamic blockage. This is captured by the deceleration parameter (2.19) introduced earlier.

In common bi-dimensional consideration as observed by [Prandtl 1904], *boundary layer separation* takes place when the adverse pressure gradient added to the wall friction decelerates the flow in the boundary layer close to the wall so much that the flow stops or even reverses as illustrated in Figure 4-1. The forward stream then leaves the surface, it is said to separate. This phenomenon can be delayed in presence of higher turbulence levels that will bring in faster particles into the boundary layer from above and support the viscous forward entrainment by the flow above. Eventually, at some distance from the separation onset, the boundary layer will reattach enclosing a so-called *separation bubble* in the region where the flow is separated. A viscous layer can form over the separation, further retracting the region available for the main flow. Small separation bubbles can occur without significantly impacting the blade performance. However, the separation can also be so important that its aerodynamic blockage completely prevents diffusion and hence pressure rise. In that case, the back pressure will eventually make the flow direction reverse. This situation is called *stall condition*.

Separation on compressor blades begins earlier if the adverse pressure gradient is increased as in the case of highly loaded compressors, e.g. by steeper blade suction side curvature and hence higher diffusion. In general the separation takes place somewhere past the position of maximum velocity (and minimum static pressure). Inversely, as noted by [Goldstein 1965], if the diffusion takes place slowly, so that the pressure rise is sufficiently gradual for the rate at which energy can be absorbed by the boundary layer from outside to balance the rate of loss in overcoming the pressure gradient and the frictional resistance, the layer adheres to the surface far longer. This strategy is implemented in the design approach of so-called controlled diffusion airfoils that are optimized specifically for subsonic and transonic applications, by minimizing boundary layer separation and by diffusing the flow from supersonic to subsonic velocities without a shock wave [Lakshminarayana 1996].
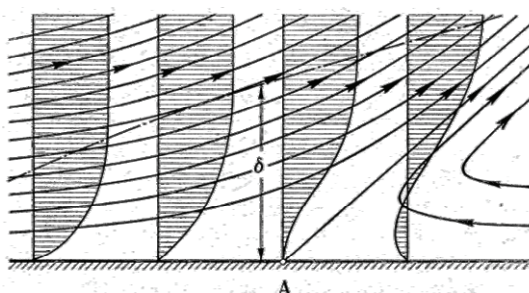
Figure 4-1. Illustration of the velocity profiles in the boundary layer of a forward flow against an adverse pressure gradient that separates after position A (from [Schlichting 1965], based on [Prandtl 1904]). The chain-dotted line denotes the limit of the boundary layer (thickness δ) and the arrow-lines represents the streamlines.

4.1.2   Three-dimensional separation

To correctly analyze three-dimensional flows occurring in a real compressor stator, it is necessary to go beyond the bi-dimensional idealization to prevent inappropriate conclusions. Bi-dimensional separations along straight lines as described right above are actually possible in three dimensions but they are special cases of three dimensional separations that occur only in exceptionally symmetrical flows. In three dimensions, the flow in such a situation can escape sidewise, thus the conditions for a three-dimensional separation to occur are more complex.

Past research on the subject of three-dimensional separations up to the most recent models considered here, which is [Surana et al. 2006], agree on following manifestations. The focus will be set on three-dimensional separation but the reader should note that the same features that will be described take place in reversed direction in the case three-dimensional reattachment. The description uses the concepts of streamlines and *skin friction line*s. Skin friction lines are trajectories on the body surface that are tangential to the flow direction just above the surface. Hence, they indicate the direction of the viscous forces on the surface; this is why they can quite well be determined experimentally by observing the traces produced by the flow on surfaces covered e.g. by oily paints. The *skin friction line pattern* on the body surface is particularly adequate to infer the flow structures occurring right above in the flow.
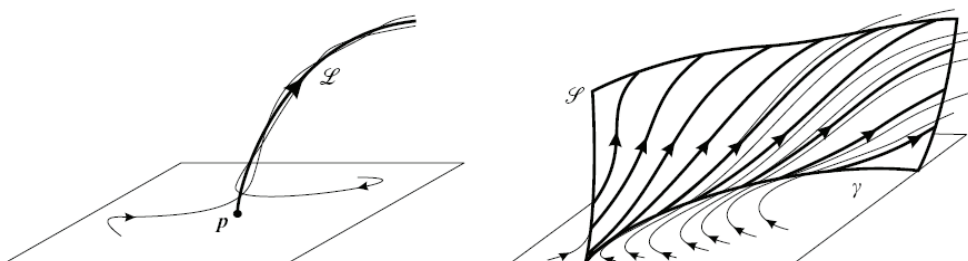

Figure 4-2. Separation profile emanating from a separation point (to the left) and separation surface emanating from a separation line from [Surana et al. 2006].

As illustrated in Figure 4-2, a separation in three dimensions can occur either above a *separation point p* or above a *separation line γ* that may be curved. In the first case, shown to the left in Figure 4-2, a pattern of skin friction lines that spiral towards the separation point can be observed on the body surface. From

the separation point, a tornado like separation originates, with the streamlines departing from the surface spiraling around a *separation profile* $\mathscr{L}$ de facto a vortex filament that rises from the separation point. In the second case, to the right in Figure 4-2, a pattern of skin friction lines occurs that converge towards the separation line γ. A *separation surface* $\mathscr{S}$ arises over the separation line that literally separates families of stream lines that depart from the body at each side of the separation surface, converging towards the separation surface. This is illustrated also in Figure 4-3 that additionally emphasizes how the separated viscous flow of the boundary layer sets forth on the separation surface, rising away from the body surface. It can be derived e.g. for the case of a separation on a compressor blade, that the separation will rise low momentum, high vorticity fluid of the boundary layer further away into the main flow. Additionally, it will yield significant deflection of the streamlines with respect to the blade profile and important aerodynamic blockage.
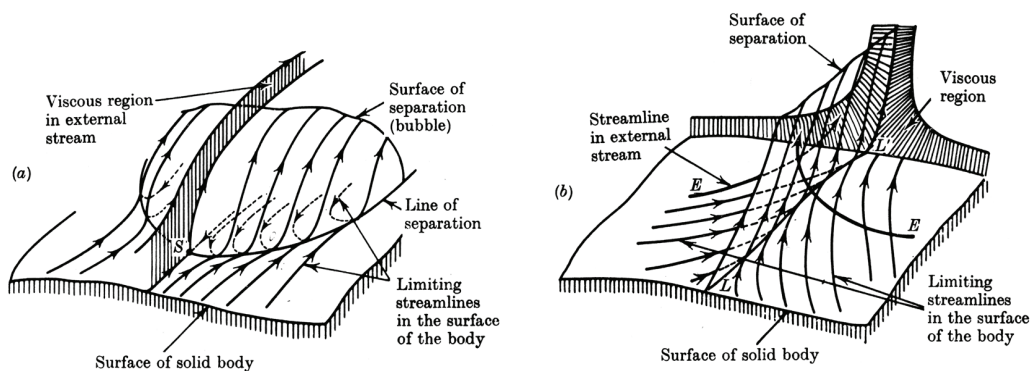
Figure 4-3. Illustration of a separation surfaces arising above a separation lines, including the skin friction line ("limiting streamlines") pattern, the streamlines converging to the separation surface and the withdrawn boundary layer (viscous region) from [Crabtree et al. 1963].

Separation surfaces arising over separation lines can take very particular forms: due to the vorticity raised within the boundary layer, the separation surfaces tend to roll up around concentrated vortex filaments. These vortices may reach into the infinite with both ends as is the case for a horseshoe vortex, illustrated to the left in Figure 4-4.The vortices may also be attached to the wall with both or only with one end as illustrated to the right in Figure 4-4. These notions can be used to infer the vortical structures formed by the separation surfaces in a compressor separation in the corner between blade and hub towards the trailing edge yielding the exemplary results shown in Figure 4-5. There, one separation line even spawns over the corner, from the blade surface to the hub surface. Separation surfaces can also roll up forming closed vortex rings shown to the left in Figure 4-6, as proposed in the case of a highly loaded compressor cascade described in [Délery et al. 2003]. The authors designate it as the three dimensional correspondent of a bi-dimensional separation bubble. Finally, [Surana et al. 2006] describe a further separation surface, where the separation line forms a closed loop – a *limit cycle* in their terminology. In all cases, the vortical structures obey the so-called Kelvin-Helmholtz theorem: A vortex cannot end in a fluid (it cannot be "cut", hence a horseshoe vortex hangs on a leading edge and cannot leave); it must extend to the boundaries of the fluid (either walls or the infinite) or form a closed path.
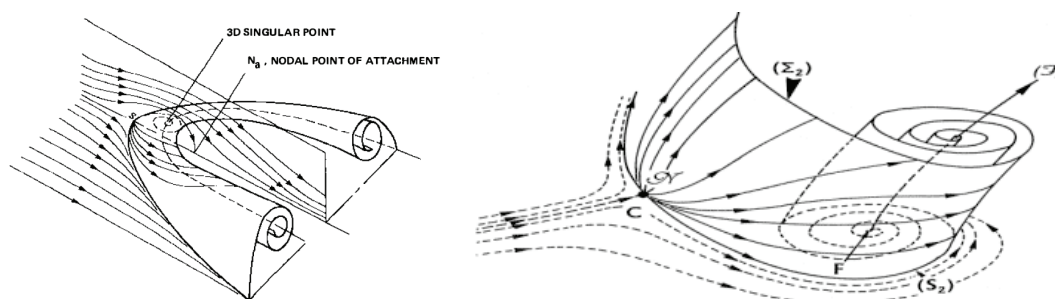
Figure 4-4. Separation surfaces rolling up on both ends (to the left) from [Tobak et al. 1982] and separation surface rolling up in an wall attached vortex (to the right) from [Délery 2001].
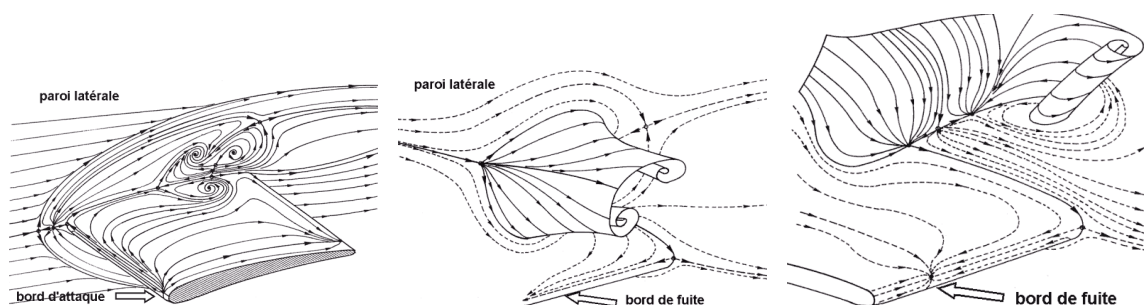

Figure 4-5. Illustration of the skin friction lines (to the left) and of the inferred separation surfaces rolling up in wall attached vortices (in the center and right hand side) in a compressor blade trailing edge separation from [Délery 2001].

The occurrence of three-dimensional separations is more difficult to identify and predict than is the case for their bi-dimensional counterparts. A fundamental distinction towards bi-dimensional models is that a bi-dimensional separation according to [Prandtl 1904] occurs, whenever the shear stress vanishes in a forward flow with adverse pressure gradient. In contrast, in three dimensions, far more flow configurations yielding separation can occur, where an adverse pressure gradient is not a necessary condition, nor is the condition of disappearing shear on the separation line. The magnitude of the described separated flow features indicates that the onset of important three-dimensional separation must be related to the main flow motion on a macroscopic scale and not only to local pressure gradient distributions close to the boundary layer as was considered for two-dimensional separation. Such macroscopic mechanisms can be secondary flows, flow bending, vorticity, etc. that make the streamlines concentrate into configurations that are disadvantageous for the flow attachment. Hence the causes of such streamline configurations can be as macroscopic, as e.g. the geometries of the blade channels, the vorticity of the inlet flow but also the presences of clearance jets or aspiration bleeds as will be observed in this investigation.

A simple fundamental observation on three-dimensional separation onset ascribed to [Lighthill 1963] can be noted. In three-dimensional flow the skin friction lines can converge and diverge, squeezing or dilating the streamtubes above and thickening or thinning the boundary layers: in all the separation configurations just described, the main flow induces skin friction lines converging towards either the separation point or the separation line. In all cases, the convergence makes the distance between the skin friction lines drop when they approach the separation point or line. Now, it can be derived that, similar as for streamlines, the skin friction lines are actually the delimitation on the surface of streamtubes above them. Hence, if the distance between the skin friction lines drops, this indicates that the streamtubes above are squeezed and – for mass conservation – they must elongate in direction opposing to the wall. One can imagine that this upwards motion can end up in a separation. This convergence of the skin friction lines was identified as a

necessary condition for separation. Hence flow conditions inducing such a pattern deserve particular consideration. However, in certain cases, skin friction lines converge without inducing a separation. To the right of Figure 4-6 is an illustration of such a skin friction line pattern yielding a separation (top figure) and yielding only an inflection (bottom figure). The described condition is hence necessary, and very illustrative, but not sufficient for identifying separation onset.
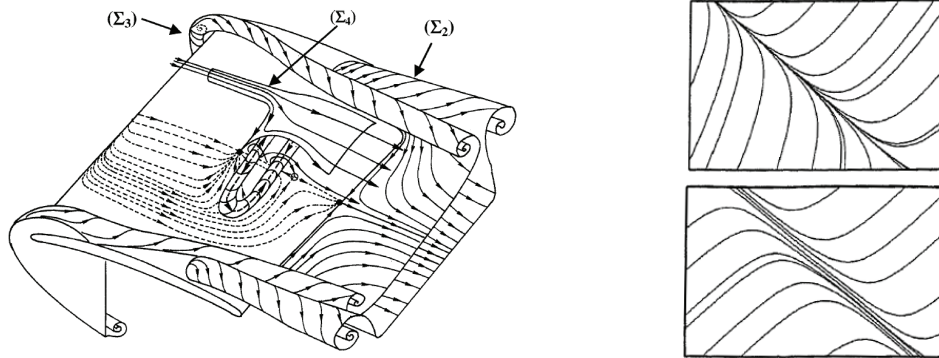

Figure 4-6. To the left, a proposal of a three-dimensional bubble type separation consisting in separation surfaces forming a closed vortex ring from [Délery et al. 2003]. To the right, of converging skin friction lines patterns yielding a separation (top) and yielding only an inflection (bottom) from [Kenwright et al. 1999].

The most common models to understand three-dimensional separations are closely related to the topological analysis of the patterns formed by skin friction lines and *vortex lines* on the surface of a body. Similar to the skin friction lines that are tangent to the direction of the flow right above, vortex lines are trajectories on the body surface tangential to the vorticity vector orientation just above. By definition, the vortex lines of boundary layers are orthogonal to the skin friction lines in each point. According to the review [Délery 2001], it was Robert Legendre who first postulated in his publication of 1956 that in a three-dimensional flow, the trajectories of skin friction lines and vortex lines on the wall must form the trajectories of continuous vector fields. As a consequence, the understanding of the topological organization could and can be backed by the mathematical laws for such a field. These laws were first identified by Henri Poincaré's Critical Point Theory at the end of the 19th Century.

A central notion of Legendre's approach is that *singular points* occur on such a field where the shear stress disappears – these points are also called *zeroes* – and they largely determine the pattern of the skin friction lines on the wall, in a similar way as asymptotes determine the shape of an hyperbola. The points can be classified in distinct categories distinguished both by the character of the eigenvalues of the Jacobian matrix for the differential system formed by the shear stress derivatives at that points as well as by the topological manifestations close to the points on the flow pattern. These categories are: *nodal points* (nodes and isotropic nodes, foci and centers) and *saddle points*. They are illustrated in Figure 4-7. Nodal points and saddle points can coincide, e.g. nodes and saddle points often occur very close to each other at a separation onset. Extensive descriptions of such singular point properties and manifestations in the flow can be found in [Tobak et al. 1982] and [Délery 2001].
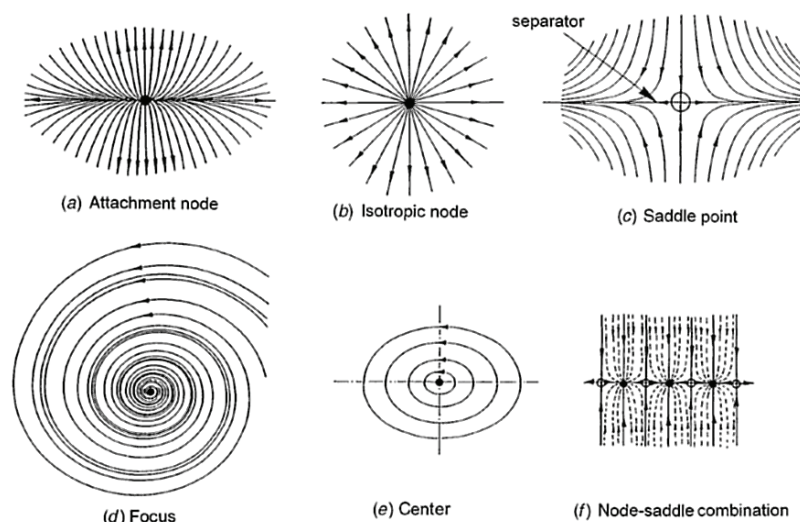
Figure 4-7. Different singular points (from [Délery 2001]).

Legendre's approach yields certain rules for the occurrence of the singular points, e.g.: on a simple body, there must always be exactly two more nodal points than saddle points; if a separation line crosses several singular points, saddle points and nodal points must always alternate; nodal points are sources or sinks of skin friction lines; in a saddle point, two particular lines cross each other and skin friction lines never cross them but deviate towards directions adjacent to the particular lines; a focus always appears in conjunction to a saddle point as to the right in Figure 4-4, and so on. The reader is referred to [Délery 2001] for further details. Legendre did way leading work demonstrating the validity of this approach for various practical flow configurations. His results were supported by the experimental results that were performed by other researchers at the same time. Legendre and few others further developed the technique – the reader is referred especially to [Lighthill 1963], [Tobak et al. 1982] and [Délery 2001] for further references – and numerous applications with regards to compressor flow are known, as most recently [Gbadebo et al. 2005], [Zhang et al. 2007] and [Sachdeva 2010] that we will refer to later on.

Some important points can be summarized to conclude this introduction to three dimensional-separations. The onset of three-dimensional separations is not simply related to the presence of local adverse pressure gradients as is the case for two-dimensional idealizations. Often, it rather depends on much more macroscopic flow features that induce unfortunate streamline configurations yielding separation onset. As such macroscopic flow features, the examples of secondary flows, flow bending, and vorticity were cited that may be ascribed to similarly macroscopic causes as e.g. the blade channel geometry, the inlet vorticity but also the presence of clearance jets or aspiration bleeds. As noted by [Délery 2001], in most cases the flow organization yielding three-dimensional separation is such a catastrophic and overwhelming phenomenon that it is nearly independent of the Reynolds number and the Mach number. The separations may have considerable influence on the main flow: they yield deflection of the flow from the bounding walls and can bring low-momentum flow from the walls into the main flow, generating losses when mixing out. They may constitute significant aerodynamic blockage and they are often related to the arising of vortex filaments as horseshoe vortices or wall-attached vortices extending into the main flow, causing further blockage, deflection and mixing. Skin friction line patterns on the body surface help inferring the presence of separations. Several types of separation can be recognized by identification of specific singular point patterns or analyzing the pressure and shear fields on the surface based on the theories of e.g. Lighthill and Surana. However, further separation types can be observed, that are not captured by existing theories. Some of them, which are observed in compressor cascades, are denominated open separations or unbounded separations depending on the author and often involve

separation lines that extend to far upstream or downstream from the body and don't necessarily cross singular points on the body surface. Present theories work for simple bodies without holes or handles, which might exclude their application to cascades with aspiration slots connected to outlets separated from the main flow.

4.2 Flow features related to secondary flow

4.2.1 Hub passage vortex and casing passage vortex

A relevant example of secondary flow formation is the formation of hub or casing passage vortices as illustrated in Figure 4-8 based on the description by [Lakshminarayana 1996]. To follow the curved path AAA with radius of curvature R_A, a flow particle A right outside the boundary layer must be submitted to a centripetal force $\rho u_A^2 / R_A$ towards the center of the curve. This is provided by a pressure gradient obeying at each point to:

$$\left.\frac{\partial p}{\partial n}\right|_A = \frac{\rho u_A^{\,2}}{R_A} \tag{4.1}$$

with n normal to the velocity component u_A and to the sidewall. This relation neglects viscous effects, velocity variations in direction of n and assumes the flow to be incompressible (with constant density) and steady. Based on the boundary layer approximation however, the pressure gradient normal to the sidewall should be the same also on a streamline BBB within the boundary layer:

$$\left.\frac{\partial p}{\partial n}\right|_B = \left.\frac{\partial p}{\partial n}\right|_A \tag{4.2}$$

However, since the velocity of a particle B within the boundary layer is lower than that of a particle A right outside of it, particle B will be forced by this pressure gradient to follow a path BB'B" with stronger curvature than A: equating the centripetal accelerations according to (4.2),

$$\frac{\rho u_A^2}{R_A} = \frac{\rho u_B^2}{R_B} \tag{4.3}$$

yields that $R_B < R_A$, since $u_B < u_A$. The resulting cross flow component $v_{B"}$ which is a deviation from the primary flow is called the secondary flow. From continuity considerations, there should be spanwise velocities w towards the sidewall close to the pressure side and away from the sidewall on the opposing side. A spiralling motion results, which illustrates how turning a shear layer originates secondary vorticity, i.e. three-dimensional flow in a duct or a cascade.
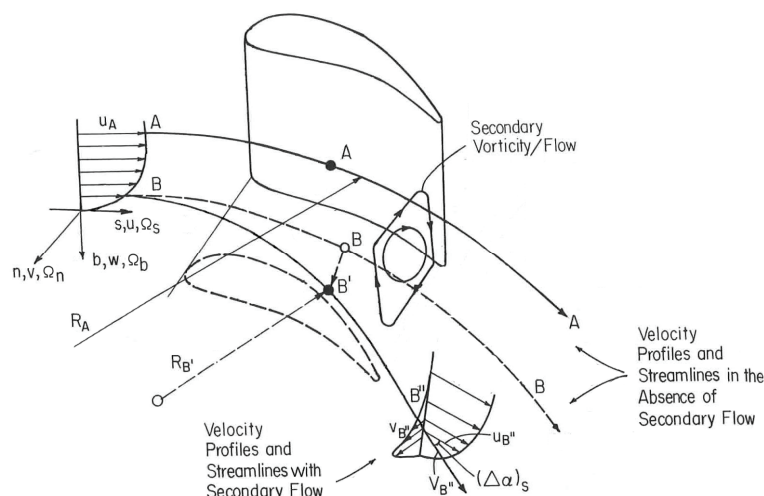
Figure 4-8. Illustration of the formation of secondary flow on the example of passage vortex formation based on [Lakshminarayana 1996].

Passage vortex formation always occurs in the blade channel of an axial compressor in presence of thick boundary layers close to the hub and casing wall, as is often the case. A secondary motion forms that goes from the pressure side towards the suction side along the walls. The resulting vortices at hub and wall are called *passage vortices*. They rotate in inversed direction to each other as illustrated in Figure 4-9. As shown in [Leboeuf 2008], this can also be derived as vorticity in the boundary layers at inlet being redistributed as consequence of the deflection making a component in streamwise direction arise. The resulting vorticity is stronger for higher curvature (deflection, bending) and less strong in the case of a diffusing channel. The latter explains why even though important in compressor cascades, the passage vortices are even more pronounced in the converging ducts of turbine cascades. However the secondary flow becomes more important in highly loaded compressors, where the deflection is more important and the increased pressure gradients make the boundary layers grow fast. Especially if the aspect ratio is small, the passage vortex can affect significant portions of the blade span.
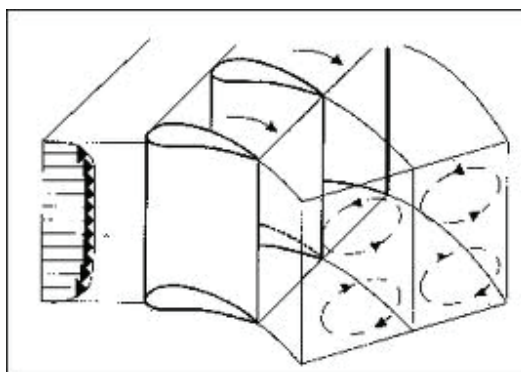
Figure 4-9. Passage vortices generated by secondary flow due to the inlet boundary layers submitted to deflection (from [Japikse et al. 1994]).

Passage vortices significantly influence the flow angle distribution at outlet (hence the turning), yielding overturned flow angles close to the hub and the casing wall. This is beneficial with regards to the achieved deflection. However, this cross passage motion along the wall transports low-energy fluid from the wall boundary layers towards the blade suction side, yielding an accumulation of low-energy fluid in the corner region. In case of hub corner separation, this fluid can feed the separated region, further increasing its size and the concentration of detrimental low energy fluid. At midspan, the passage vortices

can yield underturning, although this effect might degenerate due to the main flow and hence be less pronounced than close to the walls.

Squire and Winter developed a well known expression mentioned in [Horlock et al. 1966] that approximates the production of streamwise vorticity Ω_s as function of the normal vorticity Ω_n at inlet of the blade channel- hence the wall boundary layer thickness at inlet – and the deflection $\Delta\alpha$:

$$\Omega_s = -2\,\Delta\alpha\,\Omega_n \tag{4.4}$$

This reflects that the intensity of passage vortices increases with increasing thickness of the wall boundary layer thickness at inlet and deflection. Of course, if the wall boundary layer is thickened within the passage due to the adverse pressure gradient, this leads to even higher intensity of the passage vortices.

4.2.2   Hub corner separation and hub corner stall
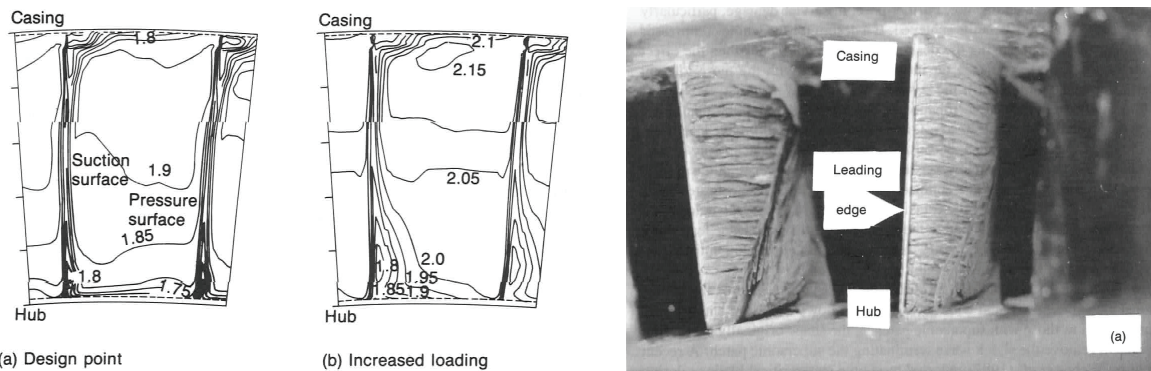
Figure 4-10. Growth of the hub separation disturbance in dimensionless total pressure plot downstream of a third stage stator (left) and visualization of hub a corner separation on a stator cascade without clearance on the right hand side (from [Cumpsty 2004] p. 313 and p. 192, based on works published by Wisler in 1988 and MacDougall in 1992).

Based on [Lakshminarayana 1996] and further authors that will be cited along the discussion, following observations can be summarized. In most compressor cascades, a separation occurs in the corner between hub and blade suction side, as noted e.g. in [Gbadebo et al. 2005]. In most cases the extents are not significant. However, the size of this feature can grow significantly, e.g. when loading is increased, as illustrated by growing perturbation in the corner between hub and suction side visible in the plots on the left of Figure 4-10. The separation can become so important that it causes severe impact on performance and stability. Such extreme separation is named corner stall and a representative case can be seen on the flow visualization on the right hand side of Figure 4-10. There, most of the span downstream of the evident separation line is separated.

The corner separation is caused by the coincidence of different factors. One is the accumulation of low energy fluid in the corner region: the boundary layer on the end wall is carried towards the corner by the secondary motion (hub passage vortex) going from the pressure side towards the suction side along the end wall described earlier. In the case of a stator and - under certain circumstances - also in the case of a rotor, the boundary layer of the blade has a tendency to move inwards towards the hub corner due to an unbalance between the radial pressure gradient and the centrifugal forces. In all cases, the merging of boundary layers from the blade and from the hub creates a highly three dimensional cross flow condition in the corner that can originate three dimensional separation. The adverse pressure gradient in that region further promotes the separation.

In the recent publication [Lei et al. 2006], Lei et al. define a diffusion parameter D to predict corner stall based on design parameters. Thereby they identify several factors promoting the stall formation: the diffusion parameter considers the overall pressure rise as a function of turning, the magnitude of crossflow which depends approximately on the inlet flow skew (inlet vorticity) for a fixed turning, and the blade loading which is function of the solidity for a fixed pressure rise. They also define an indicator for the occurrence of corner stall based on the blade pressure distribution: considering that a corner stall is characterized by extreme excursion of the skin friction lines and a large magnitude of flow reversal on both the blade suction side and the end wall, they indicate that corner stall must have a significant impact on the fluid force on the blade. Hence, they define that corner stall is reached if the fluid force on the blade, at 10% height above the hub, has a lower level than the fluid forces at midspan by a certain threshold. The difference of blade force between mid span and hub, defines the Stall Indicator S. It is used as ordinate in the plot shown on the right hand side of Figure 4-12. The sketches in the Figure also indicate qualitatively, how the skin friction pattern of a case defined "stalled" would compare to a less separated case: in a "stalled" case a larger region of the hub is affected by separation and reversal. As shown in the plot, the diffusion parameter correlates well with the stall indicator, supporting the assumptions for the considered cases with regards to the prediction of corner stall onset. Only for a certain number of cases within 0.4±0.05 false positives and false negatives occur. Interestingly, even though the parameter was developed on linear cascade configurations without explicitly considering the influence of rotation, end wall scraping and clearance - features that are known to counter balance corner stall - the parameter worked as well on several real engine configurations as discussed in [Lei et al. 2006].

Different flow topologies can occur in a corner separation, often involving vortex formation related to the reorientation of boundary layer and inlet flow vorticity. Some examples are presented here to support the interpretation of the corner stall observed in the present investigation: [Schulz et al. 1990] inferred the corner stall separation structure presented on the left of Figure 4-11 from flow measurements and visualizations in an annular compressor cascade. That cascade is illustrated by the flow visualization pictures shown on the right hand side of Figure 4-11. In the proposed topology, separation is delimited by a separation surface arising from separation lines on the hub and on the blade. Vortices are inferred rising from the focal points a and b identified on the hub and on the blade, from which fluid is transported away from the walls in spiralling motion. Schulz et al. estimate that these vortices could form a single vortex attached to both walls, winding up the separation surface. A further vortex is assumed to form in point c where the main flow hits the obstruction by the separation and another is assumed in point d, where the backflow occurs within the separation. Evidence for reversed flow coming from downstream and from the trailing edge pressure side is found. The plot on the left hand side of Figure 4-12 shows the secondary velocities obtained by subtracting the average flow velocity from the local velocities. It will be interesting to compare this representation to the secondary velocity plots obtained by the new measurement post-processing approach introduced in the present investigation. An evident clockwise motion close to the hub can be seen, resulting from the flow merging past the separation. The inwards motion in the wake is discernible as well as a concentrated, clockwise rotating trace of the clearance vortex. The general clockwise secondary motion of the main flow can be ascribed to the passage vortices and it can be seen how this secondary motion feeds the corner separation with low energy fluid.

A slightly different topology was observed by Legendre and Delery in the case of a highly loaded transonic axial compressor shown earlier in Figure 4-5. There too, vortices arise from two foci, one on the hub, one on the wall and reach out downstream, however without forming a conjoint vortex sheet as in the case observed by Schulz and Gallus. In the case observed by Delery also a third focus occurs within the separated region from which a third vortex arises reaching downstream.
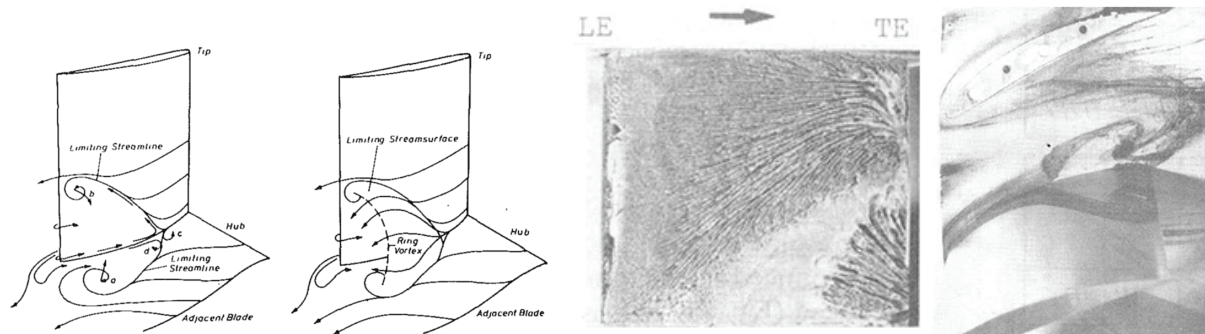
Figure 4-11. Inferred flow topology of a corner stall configuration based on experimental study on an annular compressor cascade (from [Schulz et al. 1990]). Illustrations of the corresponding flow visualization can be seen on the right hand side.
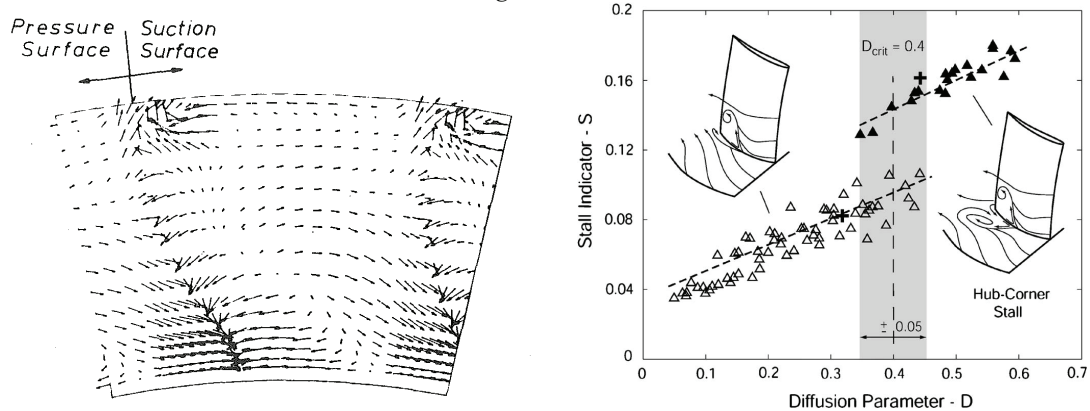

Figure 4-12. Left: secondary flow vectors of the downstream flow (from [Schulz et al. 1990]) and [Lei et al. 2008]).

As noted by [Lakshminarayana 1996] in his review on end-wall losses in axial flow compressors, rotation influences the hub corner stall formation: the blade boundary layers at the hub root tend to be thin due to centrifugation and hence radial transport outwards. The hub-wall boundary layer too is swept towards the suction side and transported outwards or mixed further downstream. Hence measurements indicate reduced separation and losses due to hub corner stall in rotating cases. Rotation has herewith a beneficial effect by reducing the accumulation of low energy fluid in the hub corner.

Often stators without shroud are used, where the blades are fixed on the outer wall pointing inwards and a clearance exists between the blade tip and the hub. This clearance causes a leakage flow to occur from the pressure side through the clearance towards the suction side. The leakage flow is opposing to the secondary flow, herewith preventing to some extent the low energy flow from accumulating in the corner. An illustration was given, e.g. by the linear cascade tests described in [Horlock et al. 1966]. Hence the leakage flow can be beneficial in reducing the effects of corner stall. However leakage flow can induce other loss types as the separation wall boundary layer at further distance from the suction side. This will be considered in the next section.

It can be retained that hub corner stall will appear more severe in cascade experiments and stators without hub clearance than in stators with hub clearance or in rotors. Nevertheless, hub corner stall losses are significant in real machinery. For instance, [Joslyn et al. 1985] observed a significant region of high loss fluid at the suction side-hub corner of a highly loaded axial compressor rotor, which extended up to 75% span. The consequent increased incidence led to an increased loading of the subsequent stator, causing further losses. Inversely, [Schulz et al. 1988] cites other investigations of cases, where no notable hub corner stall was seen past the rotor, but still, small hub corner stall traces where detected past the stator

that could be further reduced by the introducing a clearance between stator blade and hub. Hence reduction of corner stall by flow control by aspiration can be significant even if the phenomenon is generally less important in real applications than in the cascade case.

Summarizing, corner stall constitutes a region of significant losses since it is fed by secondary flow and accumulates low energy fluid. It produces further losses due to the friction of the reversed flow inside the separation and at the interface to the main flow. Further downstream, the separated flow reattaches and mixes with the mainstream in the hub region, giving rise to losses, flow redistribution and spanwise mixing. Hence corner separation can be identified by a region of reduced total pressures as in the plot on the left hand side of Figure 4-10. Beyond this, the corner stall separation acts as a solid wall constituting a blockage that can be significant. For low-aspect-ratio blades, endwall losses due to corner separation may represent a major portion of the total losses. By reducing the area available for diffusion it prevents the pressure rise impacting the compressor performance. The flow is deviated by the separation yielding off-design flow conditions causing matching issues and hence further performance impacts. Since the energy captured in the vortical motion will most probably not serve further pressure rise, further losses will arise due to their dissipation. Since the size of the separation increases with increased loading, corner stall is one major factor that hinders compressor blade loading to be increased indefinitely. In the worst case, corner stall can constitute such massive flow reversal that it can drive the compressor into stall.

4.3 Clearance vortex

The clearance vortex is induced by the clearance flow crossing the clearance gap between blade and casing from the pressure side towards the suction side. The flow crossing the clearance gap consists of flow aspirated from the pressure side. Different configurations of clearance vortex can occur: the clearance flow can separate past the pressure side edge and form a separation bubble, a similar mechanism can occur past the suction side edge. Different separations can occur at different locations of the blade tip. As noted in [Leboeuf 2008], the clearance flow can form one vortex or several vortices following different mechanisms. In the most common situation, a large vortex sheet will form as illustrated in Figure 4-13 transporting low momentum flow frome the shear in the clearance and the entrained boundary layer flow. The clearance jets typically also entrain some of the boundary layer flow on the suction side away from it. The jet vorticity deflection by the main flow motion is involved in the formation of the clearance vortex that is continuously fed by the clearance flow further downstream. Generally, the intensity of the clearance vortex increases with increased loading: the increased pressure difference between pressure side and suction side promotes the flow through the clearance gap. The clearance vortex disturbs the compressor flow due to its aerodynamic blockage and the reduced deflection. Furthermore it concentrates low momentum flow and causes mixing losses that deteriorate the main flow. Further reading on this subject can be found in [Kang et al. 1996] and [Leboeuf 2008]
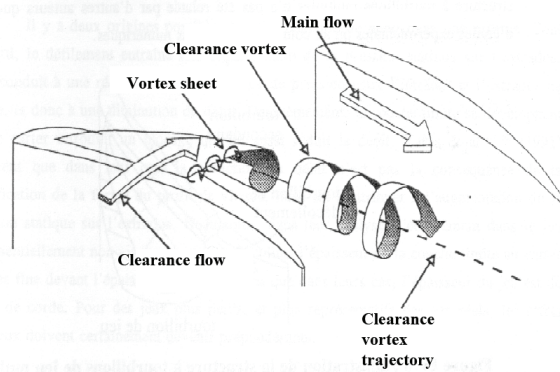

Figure 4-13. Simplified illustration of the clearance vortex formation based on [Leboeuf 2008].

PART II - EXPERIMENT

5. Non-Rotating Annular Cascade Test Facility

5.1 Description of the test facility

The EPFL Non-Rotating Annular Test Facility in its configuration for the present investigation is schematically drawn in Figure 5-1. This facility allows investigating the flow on annular cascades that represent real rotor or stator wheels. The particularity of the EPFL Facility is that the investigated annular rotor or stator geometry does not rotate. Instead, the inlet flow is swirling to reproduce the velocity triangles that would occur at the wheel inlet. The non-rotation of the cascade simplifies the access of optical and pneumatic measurement equipment. Compared to a linear cascade, the annular cascade has the fundamental advantage of the self-adjustment of the flow periodicity and hence the absence of boundary-disturbances. Furthermore, the geometrical similarity of the annular cascade geometry better approximates the geometries occurring in real turbomachinery than linear cascades or single blade tests. Compared to real rotors, the flow conditions produced on the non-rotating cascade are similar to the relative flow conditions that would be observed on a rotor, meaning the conditions that would be observed in a referential rotating with the rotor. However, the conditions are not identical since the non-rotating cascade does not reproduce the fictitious forces that must be introduced in a rotating referential. Those are the Coriolis forces and the part of the centrifugal force due to the system rotation. Similarities and differences to real stators and rotors will be discussed more in detail in the following section.
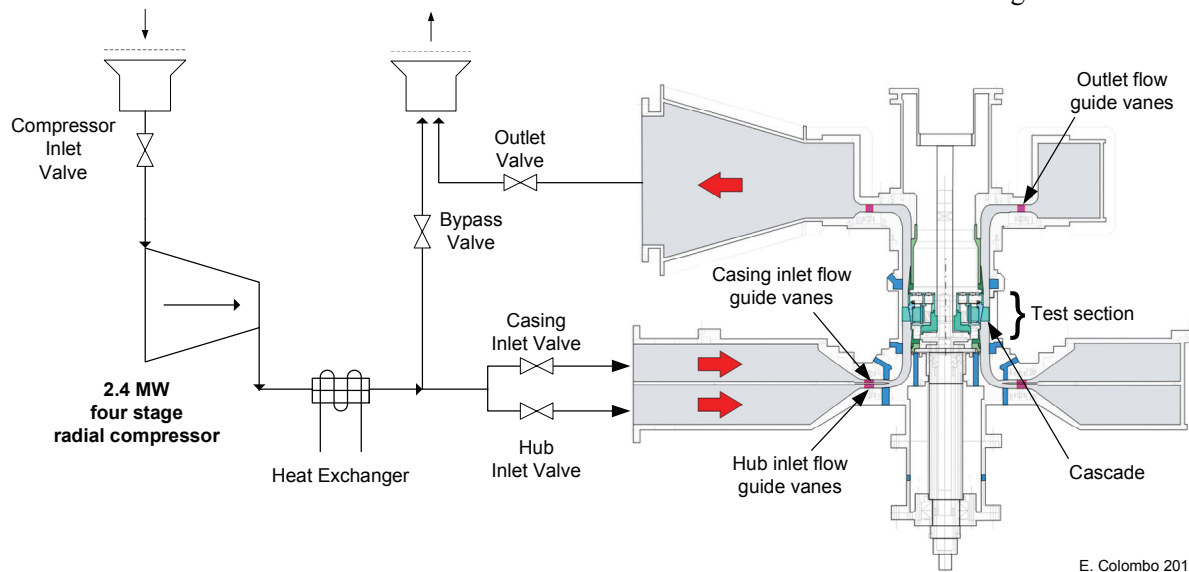
Figure 5-1. Schematic of the EPFL Non-Rotating Annular Cascade test facility including a diagram of the main air circuit and the main control elements. Note that the cascade axis is vertical and the flow comes from the bottom.

The design and early operating experiences of the Non-Rotating Annular Test Facility are described in [Bölcs 1983]. Beyond this, the following characteristics and adaptations are noteworthy. The outer diameter of the annular test section is 400 mm and the maximum blade span is 40 mm. The main flow is provided by an after-cooled 2.4MW four stage radial compressor. The conditions at the inlet of the test section as Mach number and flow angle can be varied over a large range: as illustrated in Figure 5-1, the radially inwards oriented flow coming from two separate settling chambers is pre-swirled by circumferentially arranged rows of inlet guide vanes. The pre-swirled flow from the two chambers is then united where the separation disk ends. After this, the flow is reoriented in a radial-axial nozzle. The end of the nozzle constitutes the axial annular test section. The radial distributions of total pressure and flow angle resulting at the test section inlet are influenced mainly by two means: first, by regulation of the

pressure in each settling chamber; second, by separately adjusting the orientation of the guide vane rows located at the outlet of each settling chamber. The static pressure and Mach number at the test section inlet then adjusts itself depending on the characteristic of the cascade and the settings of components located further downstream, as the row of outlet flow guide vanes and the outlet valve. As illustrated in Figure 5-2, an additional three stage geared radial compressor is used to suck off the wall boundary layers at different locations of the facility. This aspiration introduces further degrees of freedom in the control of the flow to the test section. In the present investigations this second compressor is also used to extract the flow from the slots on the hub of cascades with aspiration (red line in Figure 5-2). A further rotary vane vacuum pump was installed to suck off the flow aspirated from the blades of cascades with aspiration (green line in Figure 5-2).
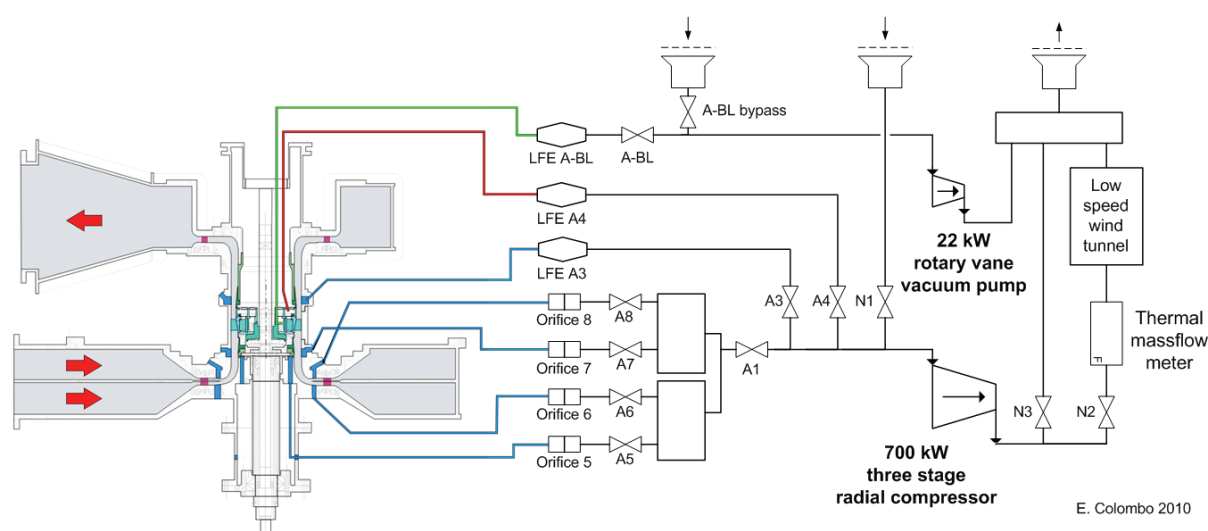
Figure 5-2. Schematic of the peripheral aspiration circuit of the EPFL Non-Rotating Annular Cascade test facility including the main control and mass flow measurement devices (Laminar Flow Element: LFE; hub slot aspiration line: red, blade slot aspiration line: green, control valves: A1-A8, N1-N3, A-BL and A-BL bypass)

The measurement equipment was upgraded to improve the ability of controlling the inlet flow conditions faster and with increased accuracy. This was done to ensure good repeatability for the numerous tests that had to be performed in a limited time frame. It was essential to obtain comparable inlet flow conditions for reference cases and aspirated cases. As part of the upgrade, the orifice flow meters indicated in Figure 5-2 were connected to remotely monitored sensor arrays and were recalibrated with respect to the thermal mass flow meter of the Low Speed Wind Tunnel installed downstream of the aspiration compressor. Furthermore, for the most sensitive mass flow measurements, new laminar flow elements (LFE A3, LFE A4 and LFE A-BL in Figure 5-2) were installed that had afore been externally calibrated for the expected low pressure flow. Further description can be found in the Master thesis [Mirzaei et al. 2008] related to this work.

It is worth mentioning that the number of configurations and cases that could be tested arises mainly from the use of the Non-Rotating Annular facility: several configurations could be built in relatively short time and at more moderate cost than what the manufacture of rotating models would demand. Especially the implementation of different instrumented flow extraction paths that were needed for the studied aspiration caused fewer issues than what would occur on a rotating case. Another advantage was that the inlet flow conditions could be varied with vey moderate efforts thanks to the control offered by the facility. An important factor therefore was that changing flow conditions is simplified by the self assessment of flow periodicity in the facility since it does not depend on laborious tailboard setting or sidewall aspiration as is the case in single blade, linear cascade or annular segment models. The non rotation also simplifies the

installation of different measurement systems, which allowed a detailed characterization of the investigated cases.

5.2 Comparison of annular cascade models to real stators and rotors

In the present investigation, it was chosen to model the flow through an axial compressor or stator using annular cascades. Such a cascade with aspiration slots on the hub is illustrated in Figure 5-3. The cascades were tested in the Non-Rotating Facility to investigate the impact of aspiration on certain relevant flow mechanisms.
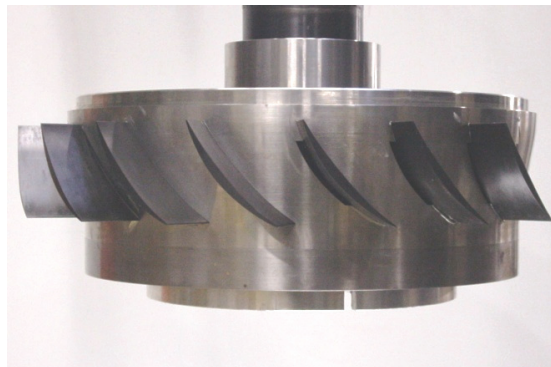
Figure 5-3. Picture of the cascade with aspiration on the hub only before chemical blackening of its surface.

An inevitable constraint of the annular cascades tested in this facility is that the blades are fixed on the hub. For constructive reasons the cascades forms a clearance between the blade tips and the casing. Nevertheless the annular cascades yield significantly improved geometrical similarity to axial compressor rotors and stators compared to linear cascade or single blade models: worth mentioning are the curved end walls, the radial growth of circumferential distance between the blade surfaces, the geometry occurring at the blade base that well compares to that occurring in a rotor or in a shrouded stator and the geometry of the annular casing clearance which is the same as for common rotors without casing treatment.

The flow through a non-rotating cascade reproduces several properties of the flow through an axial compressor stator or rotor. Hence, several of the features occurring in the cascade flow are very similar to the analogous features occurring in real conditions. The analysis of these features on the experimental model supports the comprehension of the involved mechanisms which in turn can yield the trends to be expected in real stators and rotors. However, to correctly transfer the results, the main differences between cascade tests and real axial compressor stators or rotors flow must be noted:

Compared to a typical stator, it is unusual to have a clearance gap at the casing as is the case for the cascade models investigated here. A stator has generally a clearance close to the hub, except for the case of a shrouded stator. Features arising from the clearance at the casing on the model will hence modify the results compared to a typical stator, whereas typical features due to the clearance flow at the hub of real stators will be missing. Another difference is the missing of the rotation of the hub with respect to the stator blades. Consequently, there is no scraping influence of the rotating hub which results in lower circumferential velocities in that region in the cascade tests.

Compared to a typical rotor, two main differences are relevant: first, the relative motion of the casing wall with respect to the blade channel is not reproduced. Consequently, the scraping influence of the casing wall is missing, similarly to what noted for the non rotating hub wall when comparing to a real stator. Second, and less evident: the flow conditions are not identical to those measured in the rotating frame of

real rotors due to missing Coriolis and centrifugal force terms that influence different aspects of the flow. This deserves the following more detailed discussion.

When modeling a rotor flow in the non rotating annular cascade, the flow properties occurring in the non-rotating cascade frame of reference can be approximately compared to the relative flow properties expressed in the rotating frame of reference of a corresponding rotating rotor. That is, the velocity $\vec{V}c$ of a particle measured in the cascade would represent the relative velocity $\vec{W}$ of a particle in a corresponding rotor, with $\vec{W}$ conventionally defined as

$$\vec{V}_C = \vec{W} + \vec{U} \tag{5.1}$$

with the circumferential rotor velocity $\vec{U}$. But, identity of $\vec{V}c$ and $\vec{W}$ for identical flow conditions can only be found if the particles in a fixed and in a rotating frame of reference would be submitted to the same physics, i.e. obey to the same equations of motion. Though this is not the case, since as can be found e.g. in [Lakshminarayana 1996], if observed in a rotating frame of reference (non-inertial), the particles incur apparent additional acceleration. This acceleration is simply the manifestation of the particle inertia. The impact is best seen when considering the equation of motion for flow particles in the relative frame. In the equation, which is otherwise identical to that for a fixed frame, two additional fictious body force terms occur on the right hand side

$$\frac{D\vec{W}}{Dt} = -\frac{\nabla p}{\rho} + [...] - (2\vec{\Omega} \times \vec{W} + \vec{\Omega} \times \vec{\Omega} \times \vec{R})$$
$$\qquad\qquad (0) \qquad (1) \qquad\qquad (2) \tag{5.2}$$

changing the acceleration that the flow incurs along streamlines in a rotating case compared to a non-rotating case (see p. 274 in [Lakshminarayana 1996] for more detailed derivation). The term (1) is the Coriolis force and the term (2) is the centrifugal force due to the system rotation (force per mass unit). The vector $\vec{R}$ is the radial vector; the body force and viscous and compressibility-related terms (0) were replaced by [...] for clarity.

As noted in [Lakshminarayana 1996], for typical axial turbomachinery flow, both Coriolis force (1) and centrifugal force (2) caused by the rotating frame are approximately oriented in the radial direction pointing outwards. Hereby they influence mainly the radial pressure gradient and hence especially the radial transport in blade boundary layers. This results in flows inside rotating blade boundary layers going radially outwards. The consequent thickening of the boundary layer towards the casing in rotating cases increases the losses and casing stall tendency due to the interaction of the blade boundary layer and the casing boundary layer. In contrast, on stator blades, and on non rotating cascades, the centrifugal forces inside the boundary layer are always smaller than the radial pressure gradient, giving rise to radial inward flow. As a consequence, in non-rotating cases, flow separation near the hub is augmented.

Thus, as for linear cascade investigations, the described differences must be considered with the needed circumspection during the transfer of the results to real cases.

6. Test cascades

6.1 Cascade geometries

The investigated cascade geometry was designed during the numerical investigation that accompanied this work. It was performed by the industrial partner Snecma (Safran Group) and is described in [Sachdeva 2010]. The main parameters for the blades and the cascades are summarized in Table 6-1 and Table 6-2.

Blade parameter	Symbol	Leading edge	Trailing edge
Chord length	c	85 mm	
Axial chord length	c_x	64 mm	
Height	H	39.5 mm	27.5 mm
Aspect ratio	H/c	0.46	0.32
Clearance at tip	-	0.5 mm ($1.5\%\,\bar{H}$)	
Maximum Thickness	t_{max}	6 mm ($7\%c$)	
Angles	-	60°	30° PS 18.5° SS

Table 6-1. Principal blade parameters.

Cascade parameter	Symbol	Leading edge	Trailing edge
Radius at blade tip	R_{tip}	199.5 mm	
Radius at hub	R_{hub}	160 mm	172 mm
Radius ratio	R_{hub} / R_{tip}	0.80	0.86
Average hub ramp angle	-	10.6°	
Area ratio	A_2 / A_1	0.723	
Solidity (medium loaded, 18 blades)	$(\sigma = c/s_m)_{18}$	1.35	1.31
Solidity (highly loaded, 14 blades)	$(\sigma = c/s_m)_{14}$	1.05	1.02

Table 6-2. Principal cascade parameters.

The geometry of blades and hub are illustrated in Figure 6-1. The blade is prismatic. Its profile is that of a typical controlled diffusion airfoil. It can serve, as a stator mid-span section in high pressure compressor stages. The blade thickness is higher than usual: the maximum thickness is 6 mm, hence 7% of the blade chord. This thickness is necessary to be able to accommodate the aspiration duct within the blade. The leading edge bisectrix angle is 60°. The trailing edge metal angles is 30° on the pressure side and 18.5° on the suction side aiming to an outlet flow angle close to 30°. All angles are measured against the cascade axis. The leading edge is elliptical; the trailing edge is circular with a radius of 0.5 mm.
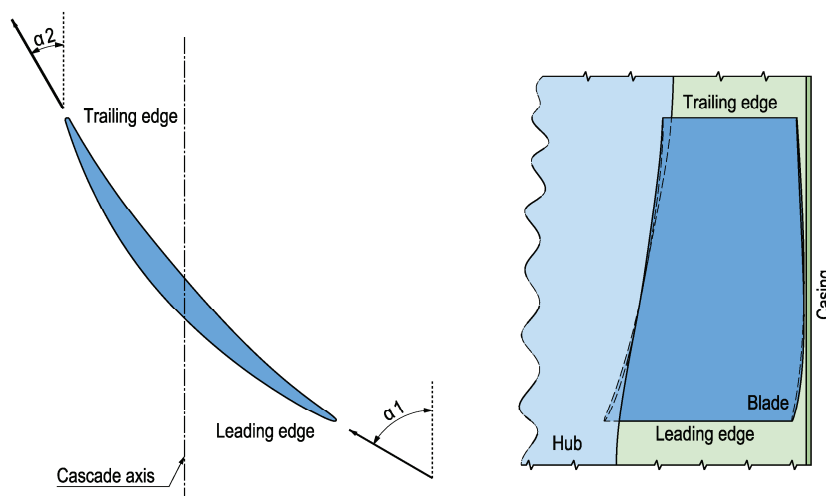
Figure 6-1. Geometry of the blades and the hub. Note also the definition of the flow angles α₁ and α₂.

As can be noted on the right hand side of Figure 6-1, the blades are installed on a convergent hub: the hub diameter smoothly increases from the inlet to the outlet with an average ramp angle of 10.6°. The intention is to accelerate the flow close to the hub and herewith to reduce the secondary flow formation in that region by limiting the hub boundary layer growth. The resulting blade aspect ratio is 0.46 at the inlet and 0.32 at the outlet. As noted in section 1.2.2.5, both the aspect ratio and the solidity of the present configuration are significantly lower than for the former investigations on annular aspirated cascades. Thus higher loading and higher loss levels can be expected in the reference case. The unshrouded blade tips form a clearance with the casing measuring 1.5% of the average blade height. The blade number is 18 for the medium loaded cases and is reduced to 14 to investigate highly loaded cases.

Figure 6-2 shows early numerical estimate results performed a-priori with theoretical inlet flow conditions on a case without aspiration. It can be noted that minimum total pressure loss is predicted for inlet flow angles between 57° and 59° and that the loss rapidly increases with positive and negative incidence. This behavior is typical for compressor cascades, however it is notable that the loss level here is always relatively high, the inlet flow angle range with minimum loss is comparatively small and the increase of loss at off-design conditions is significant. The total pressure distribution at outlet on the right of Figure 6-2 for a case with 60° inlet flow angle indicates significant loss close to the hub indicating a hub separation. There are also significant losses close to the casing which are presumably clearance leakage losses.

Summarizing, it can be noted that the present geometry presents a certain loss level, a notable inlet flow angle sensitivity and different loss mechanisms. It will be investigated how aspiration on the hub and on the blades influence these characteristics.
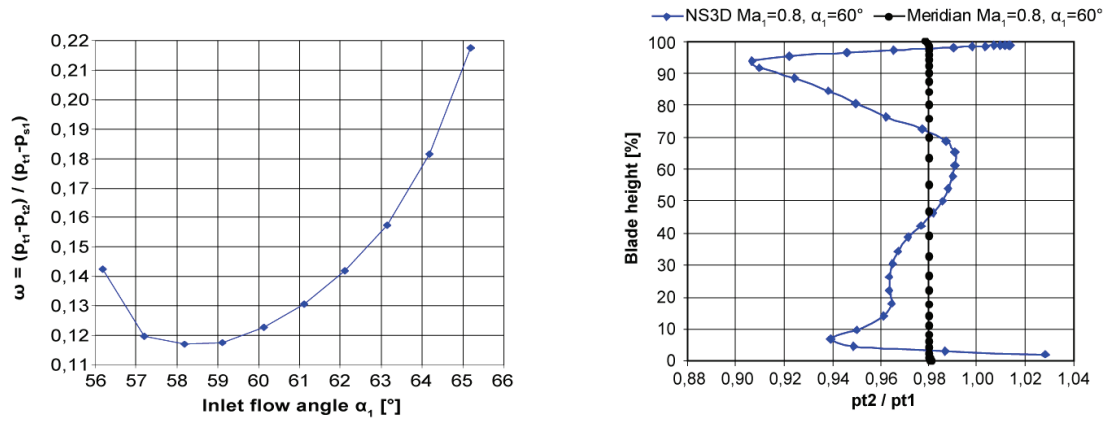
Figure 6-2. Early numerical estimates for a medium loaded case (18 blades) of total pressure loss over the inlet flow angles (left) and outlet total pressure for a 60° inlet flow angle case (right) based on [Sachdeva 2007].

6.2 Aspiration slots

The definition of the aspiration slot geometry and position was performed in cooperation with the project partners. The notions retrieved in past investigations led to the definition of some dozen of geometry candidates. The selection of the design that was finally applied to the experimentally tested models was mainly driven by the results of three-dimensional viscous calculations. These numerical investigations and their analysis were performed in cooperation with the project partners at ONERA and Snecma (Safran Group). Only some relevant arguments are mentioned here on the aspiration slot definition. However, the reader is referred to [Sachdeva 2010] for further information.

Figure 6-3 and Figure 6-4 illustrate certain candidate geometries similar to that finally retained to illustrate the investigated variations as shape, size and position. The geometries selected for the experimental investigations were the candidates that at fixed inlet Mach number and different incidences yielded the best reduction of total pressure loss and improvement of the overall flow quality, needing the lowest aspiration rates and having the least sensitivity to changes in the aspiration rate. A number of assumptions had to be made to perform a-priori numerical investigations. They were not all confirmed by the experimental measurements, as e.g. the thickness of the hub boundary layer or the turbulence level at inlet. This explains certain divergences between results and expectations, beyond the challenge of performing valid numerical simulations on the present, rather complex case with difficulties as e.g. the large hub corner separation and the high shear regions in the clearance.
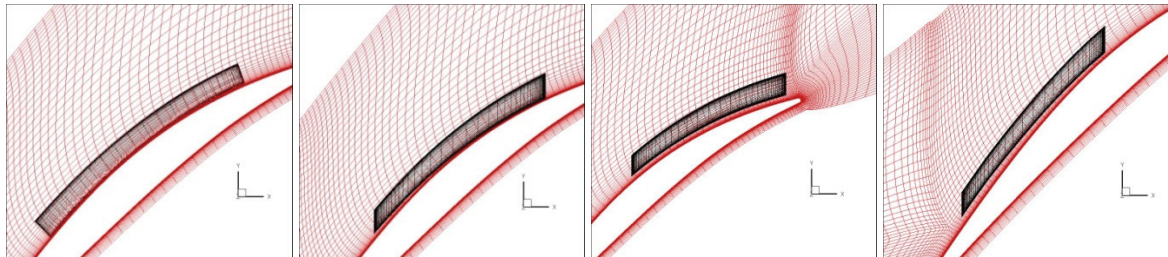
Figure 6-3. Illustration of different investigated geometries for the aspiration slot (black) on the hub (red) located close to the blade suction sides. The blade leading edge is at the bottom left ([Castillon et al. 2006]).

The decision to apply aspiration both on the hub and on the blades was taken since former investigations as [Merchant et al. 2000] indicated that separation on hub can seldom be completely avoided. It was estimated that a considerable mass flow would have to be aspirated through blade aspiration slots to

control the separation on the hub as well as separations on the blades by aspiration on blade alone. This would require excessively thick blade profiles to duct all the mass flow out of the cascade. Furthermore, separation on hub is much more relevant on stator cascades than on rotor cascades that should also be represented. Thus the intention of adding aspiration on hub was mainly to reduce the separation on hub to be able to refine the aspiration on blade to control separations occurring on the blade. The first test series focused on cases with aspiration on the hub only. In the further test series, aspiration was added on the blades, keeping a constant aspiration level on the hub.
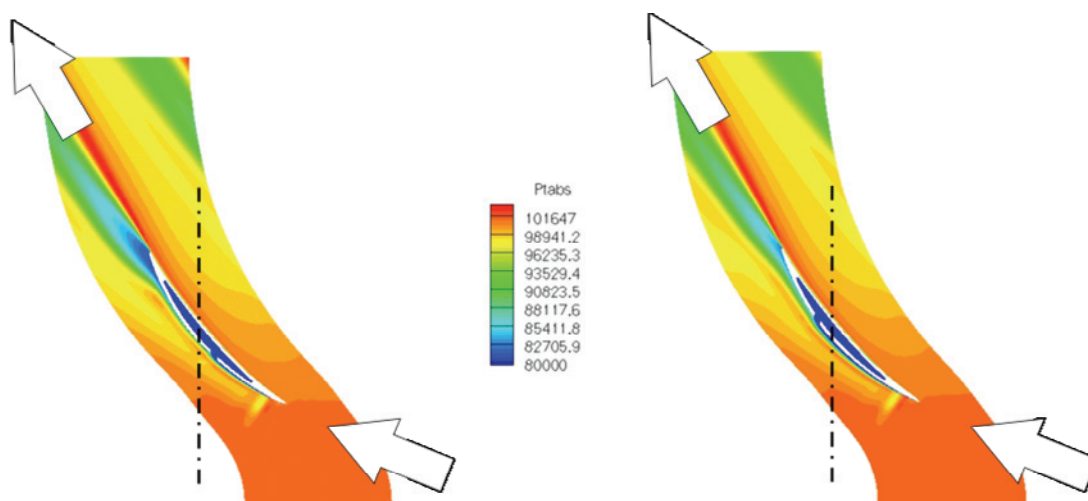
Figure 6-4. Qualitative illustration of different investigated geometries for the blade aspiration slot location on the blade suction side. Left: blade slot at 40% of the chord. Right: blade slot at 60% of the chord ([Cartieri 2008]).

6.2.1 Selected design of the aspiration slots on the hub

As illustrated in Figure 6-5, the hub slots are contiguous to the suction side and extend from about 20% to 80% of the axial chord. Their width is not varied when passing from the medium loaded cascade with 18 blades to the highly loaded cascade with 14 blades. Hence the width with respect to the blade pitch was of 8.5% and 6.5% respectively.
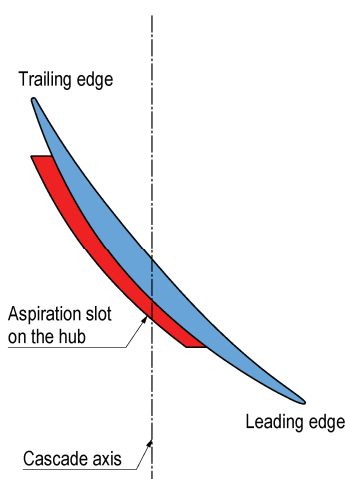
Figure 6-5. Illustration of the aspiration slot on the hub.

The decision to install the hub aspiration slot in the corner between hub and blade suction side is in agreement with the observation of [Stratford 1973]: he notes that this location is particularly

advantageous since the low static pressure and the secondary flow naturally make low energy flow accumulate there. It can thus be conveniently be extracted.

6.2.2   Selected design of the aspiration slots on the blades

The blade aspiration slots are located on the blade suction side at about 60% of the blade chord and the flow is ducted over a generous inlet radius over to a rectangular aspiration slot of 0.03 chords width to a duct inside the blade towards a settling chamber inside the hub before being removed. The slot extends over about 95% of the blade span.
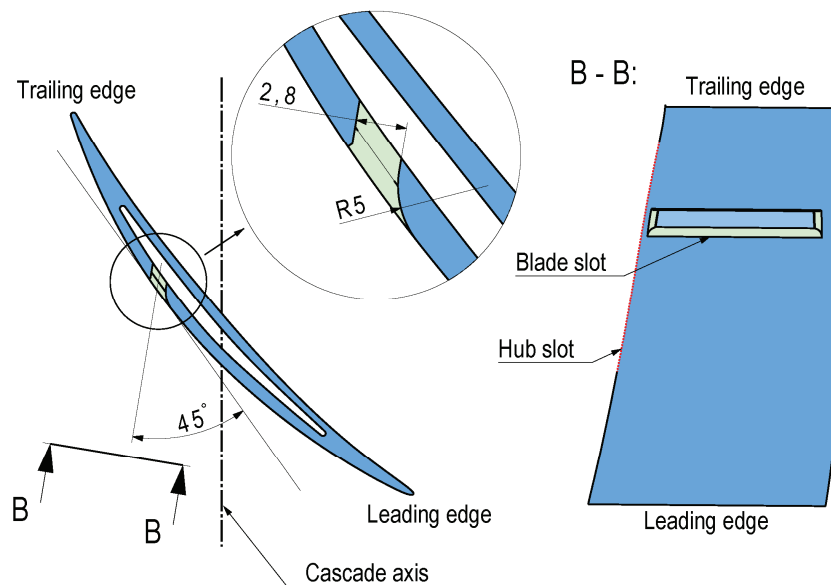
Figure 6-6. General characteristics of the aspiration slot on the blade.

According to [Schlichting 1965] citing an investigation of Popleton, in a two-dimensional boundary layer model, the most effective boundary layer control in terms of needed aspiration rate would be achieved by a continuous aspiration with everywhere the same aspiration rate. The geometry that would most approximate this would be a porous material surface as is considered for transpiration cooling in turbines. However, this is difficult to realize as well in a model as in real products. Thus a discrete aspiration slot was used instead. In [Reijnen 1997], a series of investigations are cited indicating that the most efficient solution would be a scoop that has exactly the thickness of the boundary layer and would literally peel away only the viscous flow region. This approach fails, since the thickness of the boundary layer can hardly be predicted with sufficient precision and the scoop would have to be excessively thin to limit its disturbance to the flow. Thus in the present case, an inclined slot geometry with a generous inlet radius was chosen. The slot lip opposed to the inlet can be considered as a very robust scoop. The inlet radius is motivated by results mentioned in [Godard et al. 2008] indicating that a surface with such a fillet is less prone to induce separation and loss and thus reduces the efforts needed to remove the flow. The inclination of the slot was chosen to recuperate some momentum of the flow and use it to drive the extraction. The relatively late position of the aspiration slot at 60% of the chord is motivated by different arguments: as mentioned, already [Prandtl 1904] noted that the aspiration location can be downstream of the location of the separation onset location without aspiration since the aspiration will accelerate the flow upstream of it if the aspiration rate is sufficiently increased and support its attachment to the blade. [Miller et al. 1968] noted that the aspiration should never occur to early, since this would increase the pressure gradients and the flow would separate regardless of the separation. Accordingly, the numerical

the blade aspiration slot location at 60% of the chord was confirmed as the most robust candidate by the numerical investigation.

6.3 Tested cascade configurations

Due to the requirements of the underlying projects, not all possible configurations could be tested. A rapid overview of the tested configurations is given by Table 6-3.

	No aspiration slots	Aspiration slots on the hub only	Aspiration slots on hub and blades
Medium loaded (18 blades)	X	X	X
Highly loaded (14 blades)			X

Table 6-3. Investigated cascade configurations.

6.4 Constructive solutions

6.4.1 Material

The main hub and blade components are manufactured in a tempered stainless steel alloy that ensures high strength, good surface quality and resistance to wear. The strength is relevant especially for the hollow blades with minimum wall thickness of 1 mm. All the exposed components are chemical blackened to reduce backscattering noise during the LDA measurements.

6.4.2 Hub with internal settling chambers

As illustrated by the schematics in Figure 6-7, it was chosen to build the cascade hub of three concentric rings. The outermost constitutes the convergent hub wall. The blades are inserted through equally shaped openings in the two outermost rings. The ring thickness and the manufacturing tolerances are chosen such that the fit between blades and rings is sufficiently air-tight. Together with an upper and a lower cap, the three rings constitute two separate internal annular chambers.
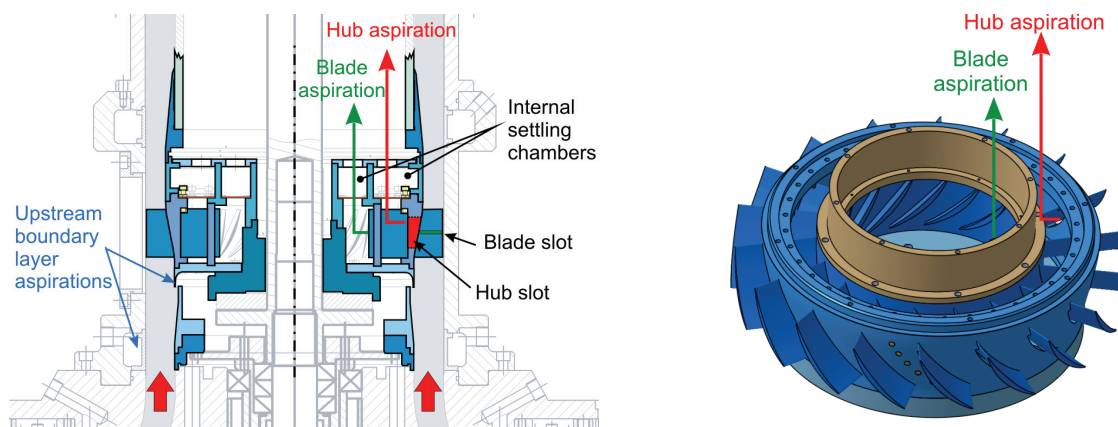
Figure 6-7. Schematics of the developed cascade design.

The outer chamber serves as collector and settling chamber for the aspiration slots on the hub: the slots can hence be manufactured rather simply as enlargement of the blade openings in the outer ring. As a result, the inwards opening of two neighboring hub aspiration slots are always separated by one blade. This prevents the slot flow from influencing each other herewith helping the adjustment of steady, periodic conditions. The flow is sucked away from the chamber by a discrete number of tubes on the upper cap.

The inner chamber serves as collector and settling chamber for the flow aspirated from the blade surface. This flow is ducted through the hollow blades. It then reaches this innermost chamber and is extracted by further tubes fixed to the upper cap. The probability of flow aspirated from different blades influencing each other in the chamber causing stability issues is estimated to be small due to the damping effect of the relatively long ducts within the blades and to the size of the settling chamber.

Horizontal grids divide both settling chambers into a lower half where the flow is collected, and an upper half where the flow is extracted through the extraction tubes. By producing a certain velocity dependent pressure loss, the grate dampens out velocity differences. This makes the velocity of the flow traversing it more uniform. Herewith it prevents that the flow through slots or ducts that are situated closer to an extraction tube is accelerated with respect to the flow through other slots or ducts.

The chosen design yields further advantages, especially compared to former designs with short blades, where each slot and blade duct would be connected to a dedicated tube located just behind the hub wall:

The two separated chambers make it possible to control the aspiration through the slots on the hub independently of the aspiration through the slots on the blades. An uniform aspiration through all slots and ducts is ensured by the uniform pressure level within the internal settling chambers. Since With this design, no dedicated interconnectors between extraction tubes and aspiration slots must be built. Hence the geometry of blades and aspiration slots can be fixed quite late in the manufacturing process. This allowed to pre-machine the rings while the further design studies went on. Another advantage is that the blades can be replaced with relatively moderate efforts. This permits to compare blades without aspiration slots to blades with aspiration or to displace instrumented blades. The radial position of the blades is mantained by secured brass screws and can hence be adjusted with moderate effort to yield the required clearance size.

6.4.3 Upstream boundary layer aspirations

As indicated in Figure 6-7, two boundary layer aspirations are located relatively close upstream of the leading edge. One is located at the casing at about two axial chords distance from the leading edge. It is formed by an array of narrowly spaced inclined aspiration slots. The second aspiration is located on the hub. It is formed by a conically converging hub wall followed by a sharp lip intended to peel away part of the hub flow including the boundary layer. The flow is aspirated to the ducts within the hub. Both devices are controlled separatedly and connected to the auxilliary aspiration circuit indicated in Figure 5-2.

6.4.4 Pressure taps on the hub

The pressure taps must have a small diameter. For the given flow conditions, based on [Arts et al. 2002], a hole diameter of 0.3 mm was chosen. It is not possible to drill a hole with this diameter through the whole thickness of the outer hub ring. Hence, brass inserts pre-drilled close to the expected hub thickness are manufactured. They are press-fitted into the ring wall as illustrated by the schematic on the left of Figure 6-8. The different drilling depths and insert sizes arise from the fact that the hub wall is convergent. They are illustrated in the schematic on the center of Figure 6-8. The hub is then CNC turned to produce the required hub wall convergence, forming a seamless surface with the inserts. The 0.3 mm

holes are finally drilled from outside into the inserts, at an angle perpendicular to the local wall inclination. The pressure occurring at the pressure taps is then ducted to the measurement sensor by tubes at the inner side of the hub wall. The image on the right hand side shows a cascade at an intermediate assembly step. The brass inserts can be clearly recognized.
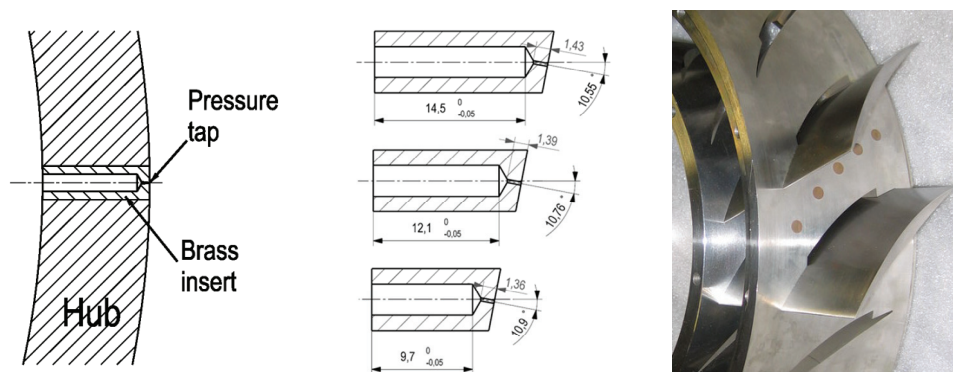

Figure 6-8. Pressure taps on the hub realized by pre-drilled inserts installed before turning of the profiled surface.

6.4.5 Hub aspiration slots

The hub aspiration slots visible in Figure 5-3 and to the right of Figure 6-8. Pressure taps on the hub realized by pre-drilled inserts installed before turning of the profiled surface.. As mentioned, the aspiration slots are manufactured as enlargement of the blade openings. The slots are adjacent to the blade suction sides that form one side of the aspiration slot duct. The edges are almost unblunted to enable a seamless sealing. Due to the thickness of the outer ring, the aspiration slots form a duct of 10 to 15 mm before they reach the settling chamber. This is illustrated by the red marked cross-section of the hub aspiration slots in Figure 6-5.

6.4.6 Hub aspiration slot sealing plugs

To reversibly seal the aspiration slots on the hub, a certain effort was put into manufacturing the accurately shapped plugs illustrated in Figure 6-9. The CNC-milled surface of the plugs reproduces with tolerance within ±0.02 mm the double curvature resulting on the hub surface. The fit with the hub wall ensures sufficient air-thightness. This yields is a seamless sealing of the hub aspiration slots. A headless screw on the inner side allows to reversibely fix the plugs.
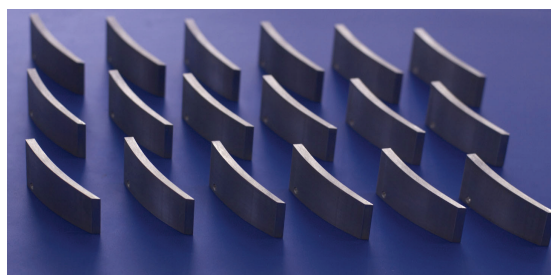
Figure 6-9. Hub aspiration slot plugs realized by CNC machining to seal the slots on the profiled hub surface.

6.4.7 Blades

The blades were manufactured according to the geometry described earlier on. The particularity is that the blades have a significant span length even though only a part of them is in the flow channel. This is done to duct the flow aspirated on the blade surface towards the innermost settling chamber. The prismatic

geometry of the blades makes it possible to manufacture them by electric discharge machining (wire erosion). Manufacturing the uncomonly long blades is a minor issue since increased length blades does not go with a drammatic increase of manufacturing cost and time as would be the case for e.g. CNC milling. The internal ducting in the case of hollow blades is manufactured with the same technique. As illustrated in Figure 6-10, similar to the approach adopted by [Hubrich 2005], the tip side opening is then closed with a plug fixed by strong adhesive before cutting the cylindrical shape. This ensures a seamless sealing of the duct on the tip side. The blades are hand-polished to decrease the surface roughness.
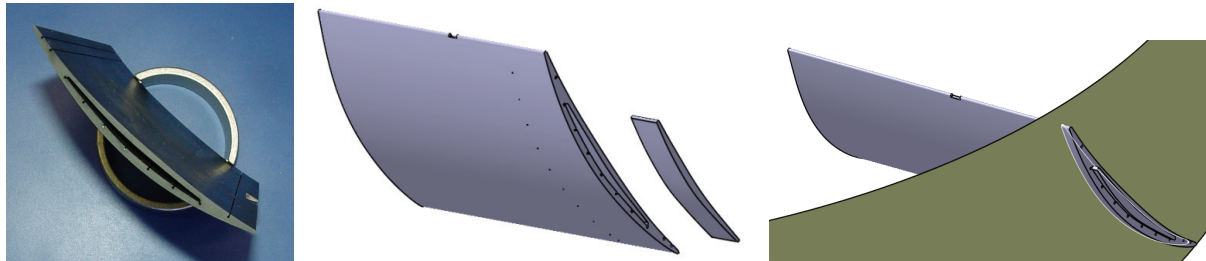
Figure 6-10. Blades with internal aspiration cavity realized by different manufacturing steps.

6.4.8 Pressure taps on the blades

The pressure taps were built applying a technique commonly used at this laboratory. Long spanwise oriented holes were wire-cut into the side opposing to the side where the pressure taps will be located. As illustrated to the left and in the center of Figure 6-11, a capillary tube (red) was then installed into this hole and fixed with adhesive. By hand-polishing, excessive adhesive is removed. The tube is sealed on one side. After this preparation, the pressure tap consisting, as the hub pressure taps, of a 0.3 mm diameter hole is drilled from the measurement side, perpendicular to it. This approach reduces the depth of the drilling of the 0.3 mm diameter holes. This is necessary, since depths are difficult to be drilled into the tempered steel. In the same time, the small surface modifications due to the adhesive are located on the side opposite to the pressure taps. This way, it does not influence the flow between the blade pair to be measured as illustrated by the scheme on the right hand side of Figure 6-11. The capillary tube is connected to a pressure sensor further away and measures the pressure established in the tube that corresponds to the static pressure at the pressure tap location.
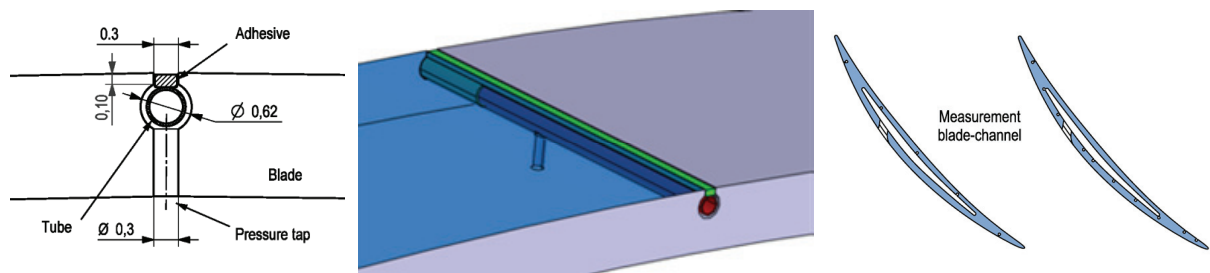
Figure 6-11. Blade pressure taps and instrumented blades.

6.4.9 Aspiration slots on the blade suction sides

The aspiration slots on the blades are manufactured by die sinking, a particular form of electric discharge machining. First, electrodes with the shape of the volume to remove are manufactured by CNC milling. One example is shown to the left of Figure 6-12. They are made of copper, which has the important characteristic of being a highly conductive material. Then, electrodes and blade are inserted into a dielectric liquid bath, subjected to pulsed electric voltage and progressively approached to each other. Electrical discharges then occur between electrode and blade. Whenever such a spark occurs, blade material is melted and removed by the back-flowing liquid. The image to the middle of Figure 6-12 shows

the alignment of electrode and blade during the die sinking. The image to the right of the same figure shows to completed blades with aspiration slots and internal ducts. One of the blades is already chemically blackened to reduce reflections during the LDA measurements.
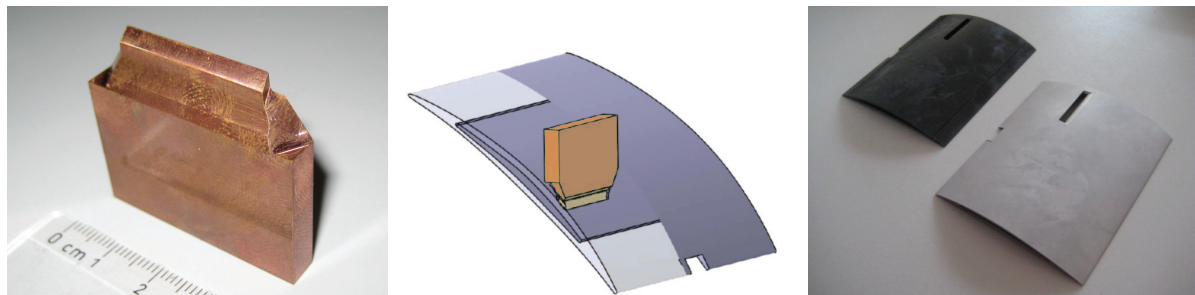

Figure 6-12. Left: one electrode used for the aspiration slot manufacture. Middle: die sinking alignment. Right: two finished blades with aspiration slot, one is chemically blackened.

This machining method submits the hollow blades to almost no stress, avoiding deformation of the otherwise completed blade. Also the thermal stress is very local. As a consequence, the removal is relatively rapid. CNC milling would demand a multiple of the time needed, since the stress rapidly increases with the advancement velocity. Furthermore, the die sinking allows to machine complex shapes, which is the case for the blade aspiration slot due to the radius and the inclined flanks.

Even though the spark concentrates close to the less conductive material of the blade, the electrode deteriorates too, especially when much material is removed at high voltages. To guarantee a high precision, several identical electrodes are manufactured. Electrodes that are weared out are used only for the rough machining at high voltage. Undeteriorated electrodes are used for the finishing, at lower voltages. The resulting aspiration slots adequately satisfy the required similarity between different blades.

6.4.10 Manufacturing tolerances

The hub rings are manufactured by CNC turning achieving tolerances better than ±0.02 mm on the diameter and negligible form tolerance. The blade openings are manufacutred by CNC electric discharge machining (wire erosion) with tolerance better than ±0.01 mm. Due to the manufacturing approach, the circumferential positioning tolerance for the openings relative to each other was estimated to be better than ±0.02°. The resulting worst case cumulated error for the last channel size is of less than 2% of one blade pitch which is largely acceptable. The outher surface is submitted to chemical blackening to reduce backscattering noise during the LDA measurements.

The blades including the internal duct are manufactured by eletronic discharge machining with tolerance better than ±0.01 mm. Only on the pressure sides a resumption line related to the batch processing causes two small groove of about 0.02 mm depth that are smoothed by hand-polishing. The leading edge and the trailing edge shapes were verified by shadow-microscopy. A control sample was three-dimensional scanned with measurement error below ±0.05mm. This confirmed the blade profile shape. Cross verification is given by the fit of all blades in all blade openings with similar clearance. Additional hand-polishing of all blades furhter improved the surface quality.The surface roughness measured on control samples is close to Ra=0.3.

With respect to the measurement precision, the manufacturing tolerance of the aspiration slot geometry resulting from die sinking is better than ±0.05mm. After fine-tuning the procedure, perfectly tangent transition from the blade surface to the radius of the aspiration slot is obtained. The quality of the slot surface is of the same order of that of the blade surfaces.

7. Measurement techniques

7.1 Coordinate system

Measurement locations and instrumentation positions are given in a cascade-fixed, cylindrical coordinate system with x, φ, R denoting respectively the axial, circumferential and radial component. Following deliberate conventions were adopted for all tested cascades: the axial position x = 0 is tangent to the blade leading edges. The circumferential position φ = 0 is aligned with the generatrix of blade numbered 14. The circumferential coordinate is also used to indicate the cascade rotation with respect to the wind tunnel: this is done by indicating the circumferential coordinate of a fixed reference point with respect to the cascade, as e.g. the LDA measurement locations.

7.2 Pressure measurements

All steady state pressure measurements are performed using 6 Dynamic Sensor Array modules from Scanivalve Corporation of type DSA3016/16Px. Each module has 16 channels yielding a total number of 96 available measurement channels. Each channel has a separate, temperature compensated, piezoresistive pressure sensor. In the used configuration, each channel measures the relative pressure with respect to the atmospheric pressure outside the wind tunnel. Each channel has a nominal pressure range of 210kPa. The measurement error according to the calibration in 2002 and the verification in 2009 is smaller than 0.04 % full scale, i.e. ±80 Pa.

7.3 Static pressure taps

Figure 7-1 illustrates the position of the static pressure taps for the example of the cascade with 18 blades. In the case of the cascade with 14 blades, only the position of the instrumented blades changes, as can be seen to the right in Figure 7-2.
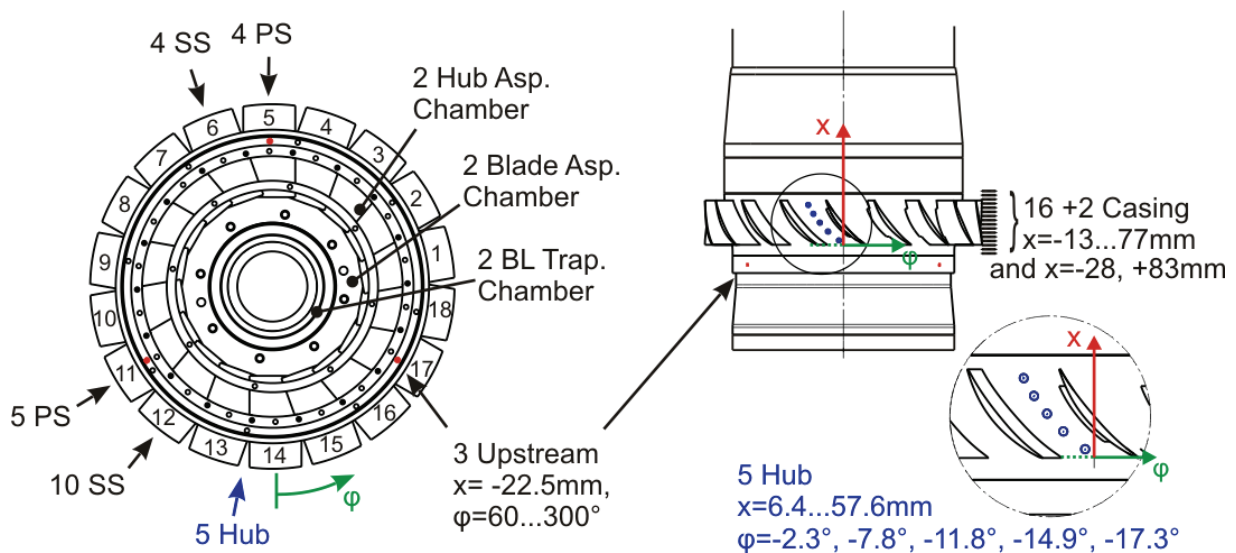
Figure 7-1. Position of the pressure taps on the cascade with 18 blades (pressure side=PS, suction side=SS).

In the illustrated case, blade pressures at mid-span (50% of the local blade height) are measured on the blade pairs (5, 6) and (11, 12). PS or SS indicates if the pressure side or the suction side of the blade is instrumented. The number afore, indicates the number of pressure taps on the blade, e.g. 4 PS means that 4 pressure taps are installed on the pressure side. The blade pressure taps are located at mid-span and are generally equally distributed.

Hub pressures are measured by 5 pressure taps on the hub (indicated as 5 Hub) that are located at average circumferential distance between two blade surfaces. Three further pressure taps (indicated as 3 Upstream and marked by red dots) are located on the hub at x = -22.5 mm, i.e. upstream of the leading edge, at equal circumferential distance from each other.

On the casing, an array of 18 pressure taps (indicated as 16+2 Casing) measures the static pressures on the outer wall. The 16 pressure taps between x = -13 mm and x = 77 mm are equally spaced. The two further pressure taps at x = -28 mm and x = 83 mm were added later to complement the measurements in the inlet and outlet measurement plane.

As further indicated in Figure 7-1, six further pressure taps were distributed at different locations in the settling chambers behind the hub aspiration, the blade aspiration and the hub boundary layer aspiration (the latter is indicated as BL trap chamber). These taps are intended mainly to evaluate the suction efforts and to verify that the pressure level is uniform in the aspiration chambers.

7.4 Aerodynamic probes and LDA measurement locations

The aerodynamic probe measurements are performed in planes at fixed axial positions: upstream (US) measurements at 0.4 axial chords upstream of the leading edge; downstream (DS) measurements at 0.3 axial chords downstream of the trailing edge. The LDA measurements are taken at the same axial positions. Additional LDA measurements are done in an inter-blade (IB) plane 0.57 axial chords downstream of the leading edge, hence 0.1mm downstream of the blade aspiration slot. The resulting measurement plane locations with respect to the cascade are illustrated by the schematic on the left in Figure 7-2.

The aerodynamic probe and the LDA are installed at fixed positions with respect to the wind tunnel as illustrated by the schematic to the right of Figure 7-2. The upstream and downstream aerodynamic probes are mounted respectively in the access windows "N" and "S", whereas the LDA is installed on the window "E". This approach takes profit of the circumferential periodicity of the flow, meaning that measurements taken at one blade channel are valid for all the others. The widespread disposition is chosen mainly to avoid that the obstruction caused by one aerodynamic probe influences the flow measured by the second probe. Furthermore, only by this disposition both probes and the LDA could be installed on the wind tunnel at the same time: otherwise, the encumbrances of the probe supports and of the LDA optics make it impossible to install all elements on one window at the same time.
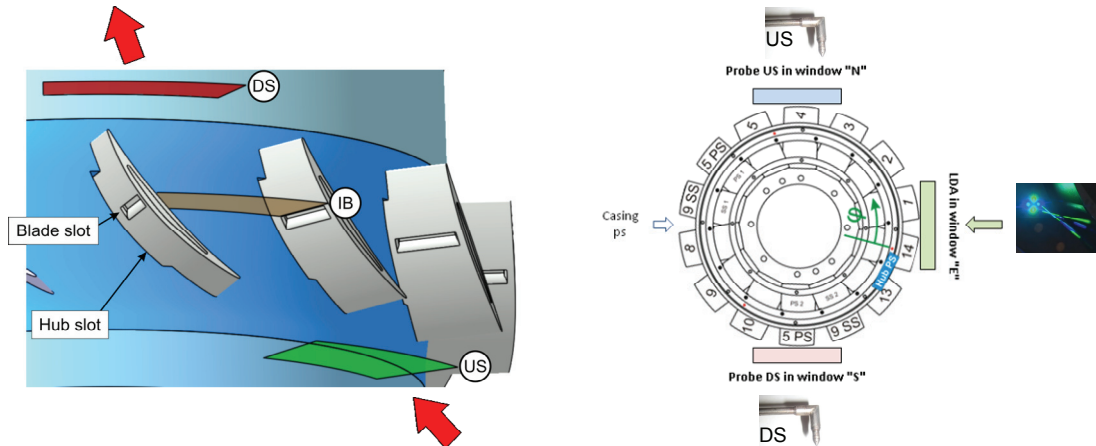
Figure 7-2. Left: upstream (green), interblade (white) and downstream (red) measurement plane locations. Right: locations of the aerodynamic probes (US, DS) and the LDA with respect to the wind tunnel windows (N, E, S).

The aerodynamic probes and the focal point of the LDA can be displaced in radial direction to measure radial distributions. To obtain radial distributions at different locations with respect to the blades, the cascade is rotated into the required position before each measurement.

The measurement grid for one blade passage consists generally of 240 and 364 points per plane for aerodynamic probe measurements on cascades with 18 and 14 blades respectively. For the LDA measurements it consists generally of 420 and 540 measurement points for each plane.

7.5 Aerodynamic probes

The aerodynamic probes used for the experiment yield the steady state Mach number, the flow direction (pitch and yaw angle) and the total and static pressure at the measurement location. They are five-hole probes, a commonly used instrument, hence a broad bibliography exists on the subject. Refer e.g. to [Arts et al. 2002]. The probes used in the present case consist in a conical head with a diameter of 2.5 mm with classical hole arrangement as illustrated on the schematic view in Figure 7-3. The conical head is mounted on an L-tube of 2.5mm diameter through which the pressures of the five holes are connected towards external pressure sensors. The probes were manufactured in-house at EPFL.
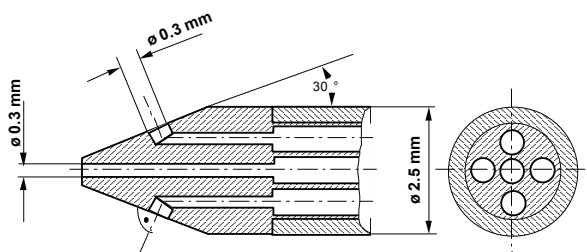
Figure 7-3. Aerodynamic five-hole probes: Probe head schematic view (left) and photo of the completed probe (right).

7.5.1   Probe calibration

The probes are calibrated in the Laval Nozzle test facility of the laboratory shown schematically in Figure 7-4. The calibration was performed for Mach numbers from 0.2 to 0.95 and flow angles between -20° and +20° in pitch (α) direction and -16° and +16° in yaw (γ) direction. The automated probe holder used for the calibration is shown in Figure 7-4.
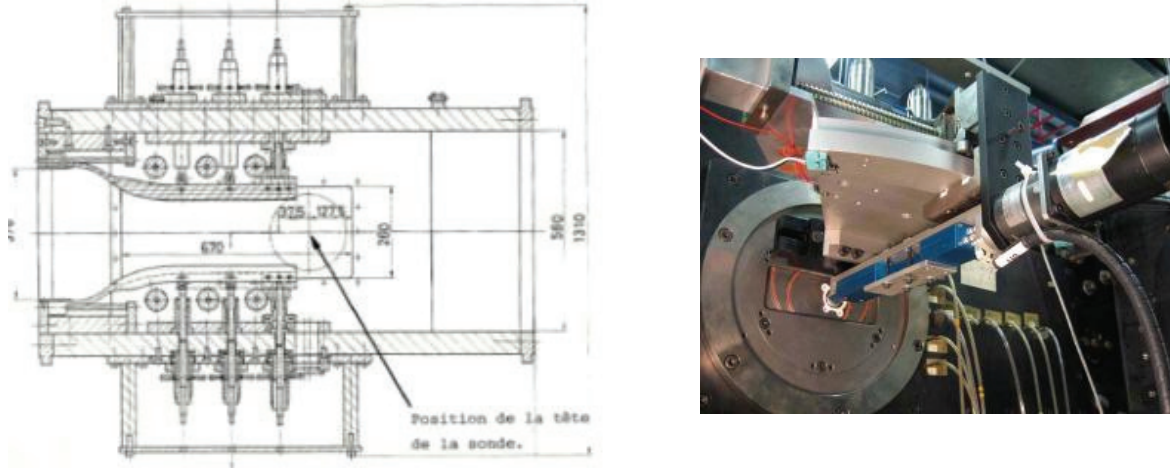
Figure 7-4. Schematic view of the Laval nozzle test rig for probe calibration (left), and of the probe holder during the calibration tests (right).

Calibration and post-processing of the probe measurements are performed according to the procedure described by [Vogel 1998]. The calibration consists in setting the flow in the Laval Nozzle test facility to known isentropic Mach numbers. These are based on the total conditions measured in the upstream settling chamber and the static pressure measured at the wall close to the probe head location. The angle of the probe relative to the flow is then varied, and the probe pressures measured at each position yield the calibration parameters in terms of non dimensionalized coefficients. The set of calibration coefficients used in the present case is:

$$X_{23}(Ma,\alpha,\gamma) = \frac{2p_1}{p_2 + p_3} \qquad K_4(Ma,\alpha,\gamma) = \frac{p_2 - p_3}{p_1 - 0.5(p_2 - p_3)}$$

(7.1)

$$K_5(Ma,\alpha,\gamma) = \frac{p_4 - p_5}{p_1 - 0.5(p_4 + p_5)} \qquad K_t(Ma,\alpha,\gamma) = \frac{p_t}{p_1} \qquad K_s(Ma,\alpha,\gamma) = \frac{p_s}{p_1}$$

with the probe hole pressures p_1 to p_5, the total pressure p_t and the static pressure p_s. Those calibration coefficients measured for each combination of Mach number and probe angles are saved in lookup tables used for the post-processing. The post-processing consists in finding the set of Ma, p_t, p_s, α and γ that best solves (7.1) for the measured p_1 to p_5.

The precision of the reference Mach number measurement in the Laval nozzle based on the isentropic relationship of total pressure and static pressure was verified by LDA measurements at different flow speeds. It was shown, that considering the measurement error of the LDA, the measurement error of the reference Mach number measurement based on total and static pressure is below 1% for all the tested flow rates. Further details can be found in [Wojciak et al. 2007] related to this work.

To verify the calibration quality, a series of arbitrary flow conditions at Mach numbers of 0.5 and 0.9 and different angles were set in the Laval Nozzle test facility and measured with the aerodynamic probes. The average angle measurement error was within +/-0.2° for the probe angle (pitch and yaw) with maximum values of +/-0.5°. The average Mach number measurement error was within an average error of +/-0.005 with maximum values of +/-0.010.

7.5.2   Probe positioning

For the measurements in the non rotating annular cascade test rig, the aerodynamic probes are fixed on probe holders with automated displacement in radial direction, as shown in Figure 7-5. Mounting the probes introduces an additional incertitude of about +/-0.5°. However, since once the probe is fixed, it is usually not disassembled for the entire campaign duration, this incertitude acts as a constant offset on the angle measurements and does not discredit the reciprocal comparison of the results. Anticipating on the results part presented later on, it can be noted that ab initio the agreement of aerodynamic probe and LDA measurements in homogeneous flow areas was better than +/-1°. The incertitude on the radial position is negligible since it is within ±0.1 mm.

7.5.3   Coordinate transformation

Due to constructive reasons, in the present configuration, the probe head cannot be aligned with the circumferential and axial direction of the cylindrical referential frame of the cascade. This is illustrated by the top view of a facility window to the left of Figure 7-6, where x_C, y_C and z_C are aligned with the axial, circumferential and radial axis of the cascade. Instead, the probe referential (x_S, y_S, z_S) is oriented as illustrated on the front view of a facility window on the right of Figure 7-6. It can also be noted that the probe positioned with a certain angle α_0 to center the measurement range on the expected flow direction.
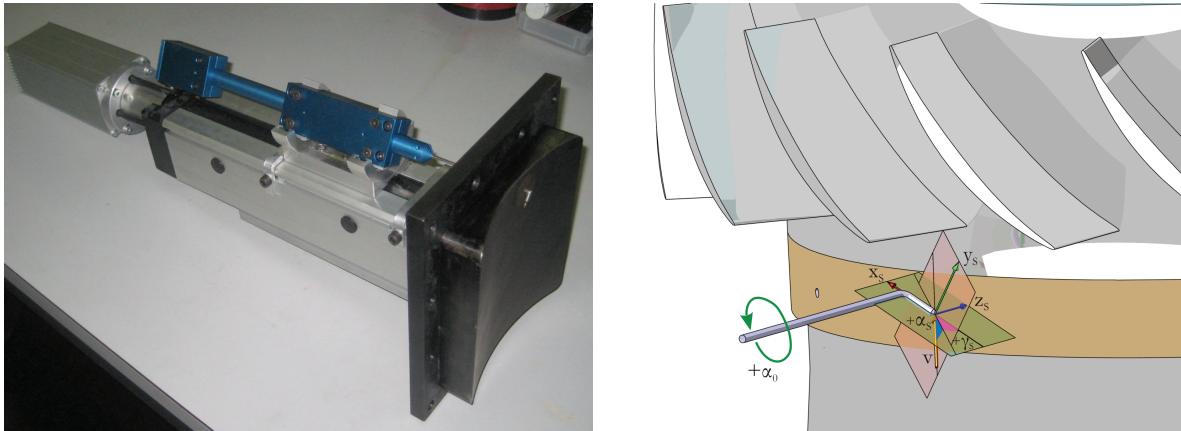
Figure 7-5. Left: aerodynamic probe mounted on the automated probe holder for non rotating annular cascade measurements. Right: upstream probe in front of the cascade and definition of the pitch (α_S) and yaw (γ_S) angles with respect to the probe referential (x_S, y_S, z_S).
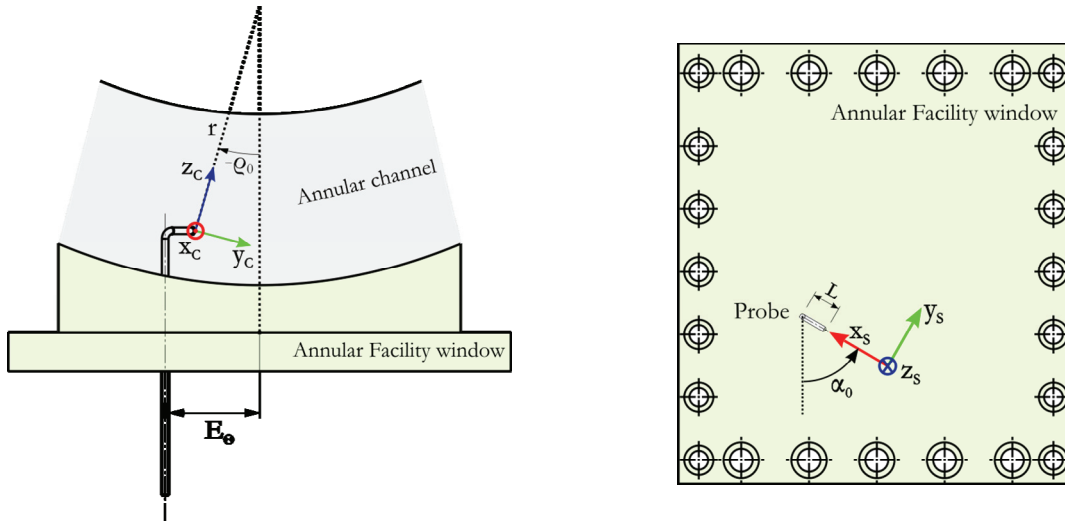
Figure 7-6. Left: top view of the facility window with the cylindrical coordinate system at the probe head. Right: front view of the facility window with the probe coordinate system.

In the report [Colombo 2009] related to this work, the following transformation is derived that is used to find the flow angles (α_C, γ_C) in the cylindrical cascade referential based on the flow angles (α_S, γ_S) measured by the probe in its own referential:

$$\sin\alpha_C = -\cos\rho_0 \sin\alpha_0 \cos\alpha_S \cos\gamma_S + \cos\rho_0 \cos\alpha_0 \sin\alpha_S + \sin\rho_0 \cos\alpha_S \sin\gamma_S \qquad (7.2)$$

$$\sin\gamma_C = \frac{1}{\cos\alpha_C}\left(\sin\rho_0 \sin\alpha_0 \cos\alpha_S \cos\gamma_S + \sin\rho_0 \cos\alpha_0 \sin\alpha_S + \cos\rho_0 \cos\alpha_S \sin\gamma_S\right) \qquad (7.3)$$

This transformation induces a further coupling between pitch and flow angle measurements. Errors in the measurement of the pitch component can propagate inducing errors in the measurement of the yaw component et vice versa. A sensitivity analysis of this transformation is summarized in Table 7-1. It was performed for the configuration of the upstream probe with typical nominal parameters. It indicates that the pitch angle is much less sensitive to biases of the measured yaw angle than the yaw angle measurement to biases of the measured pitch angle. Hence the error in pitch angle measurements is only moderately increased by the transformation in presence of yaw measurement errors. However, the pitch angle error is of course almost directly related to errors in the pre-alignment angle α_0. Another notable result is that the sensitivity of the yaw angle to biases in the measured yaw angle is augmented by the transformation. In conclusion it can be noted that the transformation will not significantly affect the sensitivity of pitch angle results. However it increases the sensitivity of yaw angle measurements to both pitch and yaw measurement errors.

Parameter	Symbol	Nominal value	Bias	Sensitivities
Probe length	L	13 mm	-	-
Probe shaft offset	E_θ	35.7 mm	-	-
Prealignement angle	α_0	60°	0, ±1°	$\delta\alpha_C / \delta\alpha_0$ = -0.991 … -0.953

				$\delta\gamma_C / \delta\alpha_0 = -0.758 \ldots +0.256$
Pitch measurement	α_S	-7°, 0, +7°	0, ±1°	$\delta\alpha_C / \delta\alpha_S = +0.941 \ldots +1.000$ $\delta\gamma_C / \delta\alpha_S = -0.107 \ldots +0.838$
Yaw measurement	γ_S	0, 5°, 10°	0, ±1°	$\delta\alpha_C / \delta\gamma_S = -0.344 \ldots +0.059$ $\delta\gamma_C / \delta\gamma_S = +1.574 \ldots +2.571$

Table 7-1. Results for the sensitivity analysis caused by the coordinate transformation.

7.5.4   Measurement difficulties

When the distance to the walls approaches the order of magnitude of the head sizes, the influence of the probe head on the flow is not longer negligible for the measurement: a throat with complex shape is formed by the probe head and the wall which tends to accelerate or diffuse the flow in between. This distorts the pressure measured by the probe holes closest to the wall. Due to the complex flow channel shape formed by the probe and the wall and due to the non-linearity of the probe calibration, the impact on the measurement cannot easily be predicted. Hence probe measurements taken close to the walls must be considered with care and verified by other techniques as for instance the LDA measurements. This comparison is limited by the fact that LDA does not measure the flow pressure but only the velocity and orientation.

A further difficulty is that in presence of strong spatial gradients of the flow properties, a pair of holes located at opposite sides of the probe head can be subjected to different flow conditions. This is not considered by the calibration since, as mentioned, the probes are calibrated in homogeneous parallel flow. As a consequence, measurements in presence of strong gradients may be biased and must be analyzed with care.

The flow path curvature of the annular facility itself constitutes certain gradients that might distort the probe measurements. However, past comparisons of probe measurements with other techniques applied in the annular facility as mentioned in [Fransson] confirm that the influence of this on the measurement results is negligible.

To prevent probe measurements to be distorted by excessive vicinity to the walls, limitations to the measurement region are introduced. The resulting measurement region for the upstream probe covers 8 to 90% blade height and for the downstream region from 13 to 88% blade height.

7.6   LDA

The LDA measurements were performed with the expertise of the collaborators from Laboratoire de Mécanique des Fluides et d'Acoustique from Ecole Centrale de Lyon. This section briefly describes the LDA setup they developed for the present investigation.

7.6.1   LDA working principle

Laser Doppler Anemometry measures the velocity of small seeding particles suspended in the flow that are assumed to have velocities that are very similar to that of the flow that carries them. The working principle can be summarized as follows: two coherent laser beams intersect forming the measurement volume in the region of intersection. As indicated in Figure 7-7, the intersection causes a particular interference pattern to occur in the measurement volume. The pattern has several fringes (maxima and minima of intensity) perpendicular to the velocity component to be measured. The fringes are spaced with

known distance d_f from each other. The distance depends on the intersection angle θ and the light source wavelength λ. Particles crossing the fringes will scatter back the minima and maxima of the light to the detector while passing the fringes. The time spacing t between these peaks is directly related to the velocity magnitude v by $t \sim |1/v|$. Without making further efforts, the LDA system would have the disadvantage that the direction of particles moving at same velocity but in opposite direction would not be distinguishable: they would produce identical time spacing. To prevent this, a Bragg cell is used to shift the frequency of one of the beams. As a result, the fringe pattern will continuously move with a constant velocity $v_{fringes}$ in direction of the velocity component to be measured. The relation between velocity magnitude and time spacing between backscattered peaks becomes $t \sim |1/(v+v_{fringes})|$, so all velocities $-v_{fringes} < v < \infty$ will be distinguishable. For two-dimensional detection, two pairs of beams are used that are arranged perpendicular to each other for best accuracy. They intersect at the same location forming the measurement volume. To separate the signals from each component, different wavelengths are used for each pair. Separation is then obtained using adequate wavelength-filters. It can occur that noise or absorption hinders the detection of the signal from one of the components. To avoid misleading conclusions due to a missing component, particular filtering ensures that only those signals are considered that are detected for both components at same time.
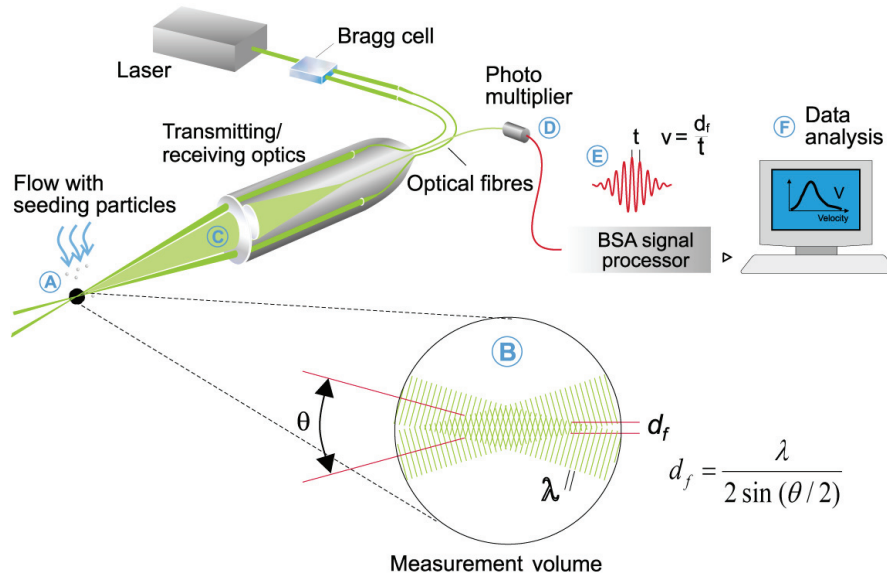
Figure 7-7. Schematic of the LDA working principle (based on Dantec Dynamics Fiber Flow documentation).

7.6.2 LDA system used for the present investigations

For the present investigation, a two-dimensional Laser Doppler Anemometry system is used. It detects two components of the particle velocity. The components lay in a plane parallel to the optical head, yielding the circumferential and the axial component in the present case. The radial component is not measured. The system is of type Dantec Dynamics Fiber Flow with BSA F80 processor. It uses the backscattering method of which an illustration for a one-dimensional LDA is given in Figure 7-7: for the backscattering method, transmitter and receiver are located in a single optical head and only the light scattered back by the seeding particles is used for the measurements. The installation advantages of using a single optical head outweigh the low intensity of the backscattering light. The optical head is connected to both the beam sources and the receiving sensors via fiber optics. This further simplifies the installation of the head and decouples the sensitive components for the emission and detection of the beams from the vibrations of the facility.

In the present configuration, automated processing of the backscattered light samples yields the distribution of velocity components of the detected particles. The system was parameterized to stop the detection after that 100'000 samples are successfully acquired.

The spacing between the beams at the optical head is 60 mm. With the used optics, the beams intersect at a focal distance of 250 mm from the head.

An Argon-Ion laser is used as light source. The lines with 488 nm (green) and the 514.5 nm (blue) wavelength are used, one color corresponding to one measured velocity component. The laser power used for the present investigations goes up to 1 W.

7.6.3   Optical access

As described in section 7.4, the LDA measurements are performed through window "E" of the Non-Rotating Annular test facility. The adapted window can be seen in Figure 7-8. It was manufactured on purpose for the present investigation to allow for optical access of the LDA to the cascade flow. In its latest design, sketched on the right hand side of Figure 7-8, it allows for optical access through one opening at a time of a total number of three openings. The three openings give access to the measurement planes upstream (US), interblade (IB) and downstream (DS). The axial position of the upstream and downstream measurement planes with respect to the cascade correspond to the position of the aerodynamic probe measurement planes.

Figure 7-8. Left: LDA head (black) in front of the optical access window. Right: schematic view of the optical access window (source: [Bario et al. 2008]).

As illustrated on the schematic in Figure 7-8, the optical access consists of glass windows fitted into brass fittings that can be mounted alternatively on each opening. The glass is flat to avoid distortion of the beams. The flat glass segment measures only few millimeters in diameter. This minimizes the influence of the flat segment on the flow. For measurements close to the casing wall, the glass is recessed and replaced by a pinhole tangent to the casing wall. This avoids reflection noise during measurements close to the casing.

7.6.4   Displacement systems

The optical head is installed on a three axis displacement system. After the initial adjustments, it is used mainly for the adjustment of the radial measurement location. Since the focal length is fixed, a radial displacement of the head changes the radial position of the measurement volume. The sidewise degree of freedom is used only for small displacements as are needed in boundary layer measurements. The accuracy of both radial and sidewise displacement is 0.001 mm.

The circumferential position of the LDA measurement location is adjusted by turning the annular cascade with respect to the fixed LDA measurement volume illustrated in Figure 7-9. The Non-Rotating Annular test facility allows for cascade rotation with minimum steps of 0.25° and accuracy better than ±0.1°.
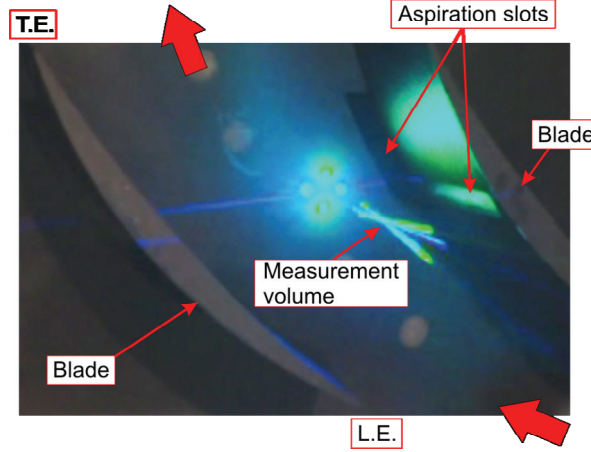
Figure 7-9. Measurement volume formed by the intersection of the LDA beams adjusted for measurements in the interblade plane of a cascade with aspiration on the hub and on the blades.

7.6.5   Seeding particles

Earlier investigations performed by the ECL-LMFA led to the selection of olive oil droplets as seeding. Olive oil is vaporized using industrial air and then injected into the test facility. For constructive reasons, the seeding is injected at several meters distance from the measurement location. The injection was performed with L-shaped probes and the injection position was adjusted before each measurement to ensure that the measurement location is correctly seeded.

7.6.6   Fluctuations and turbulence measurement

The LDA measurements allow computing the root-mean-square (RMS) of the fluctuation of the velocity components. The fluctuations are denoted as *u'* and *v'* respectively for the components aligned with and normal to the average local velocity vector. Their RMS value is denoted by a bar above the symbol.

With the measured fluctuations, the following indicator for the turbulence intensity is defined:

$$I = \frac{\sqrt{\overline{u'}^2 + \overline{v'}^2}}{\sqrt{u^2 + v^2}} \tag{7.4}$$

as can be noted, this definition does not consider the third spatial component. This is necessary since it is not detected by the 2D-LDA system. The validity of this intensity definition assumes a certain isotropy of the turbulence. It is not uncommon to use this assumption to obtain an indicative value of the turbulence intensity.

A further fluctuation indicator is obtained by computing the RMS of the product of the fluctuations for each measurement denoted as $\overline{u'v'}$. This is one component of the Reynolds Stress terms. It is related to turbulence production in the turbulence transport equations. It will hence be used here to identify regions of increased turbulence production in shear regions.

7.6.7　Measurement uncertainty

The measurement uncertainty of measurements on reference bodies with velocities above 2.5 m/s is estimated by the manufacturer of the LDA system in less than 0.1%. During the investigations, the main source for uncertainty is how the seeding particles follow the flow. At locations with strong velocity gradients and velocity fluctuations the seeding particles movement can deviate from the flow movement. Experience tells that for the chosen measurement configuration with the used seeding approach, the overall measurement uncertainty for the velocity component magnitude is below ±1.5%.

The uncertainty for the flow direction measurement is dominated by the adjustment of the optical head angle with respect to the test facility. The flow angle uncertainty is hence estimated in ±0.5°.

7.7　Measurement position uncertainties

The measurement location precision is estimated to be within ±0.5 mm for all measurements. It is even better for particularly accurate measurements: for instance, the LDA measurements of the boundary layers performed at 0.1 mm downstream of the blade aspiration slot location.

7.8　Mass flow meters on the aspiration lines

The most relevant mass flow measurements in the present investigation are those of the flow aspirated from the aspiration slots on the hub and on the blades. As illustrated in Figure 5-2, these measurements are performed with two dedicated laminar flow elements (LFE). They are calibrated by an external sub-contractor for the low pressure conditions on the aspiration lines. The precision is estimated in ±5g/s and the accuracy in better than ±1 g/s.

7.9　Total temperature

The total temperature of the flow entering the test facility is measured by thermistor sensors embedded in cylindrical probes reaching into the adduction pipes at some distance upstream of the wind tunnel. Due to the important diameter of the adduction pipes, the velocity of the flow within is relatively slow. Thus, even though the flow is not completely at rest on the probe, the measured temperature is very close to the total temperature and in this case the total temperature of the flow. The error due to this is estimated to less than 0.5K.

It can be assumed that the total temperature does not vary significantly between its measurement location and test section: before an experiment is started, the temperature of the pipes settles to that of the flow, which is close to atmospheric. Thus the heat transfer from the pipes compared to the passing mass flow is negligible for the measurement accuracy required in the present investigations.

The total temperature in the present case is used mainly with two intentions: first, it is an indicator that compared measurements had similar total temperature. Second, it is used to compute the Mach number based on the velocities measured by LDA measurements for comparison to the five-hole-probe measurements.

8. Verification measurements

8.1 Axis-symmetry verification

As described earlier, upstream (US) and downstream (DS), casing static pressure and LDA measurements are performed at different locations of the test rig. The typical configuration is shown to the right in Figure 7-2. This approach assumes an axis-symmetric inlet flow. To verify the axis-symmetry, the static pressures occurring at mid-span of the instrumented blades and on the center of a blade-passage on the hub of a cascade were measured during a full rotation of the cascade in the test facility. This was done for flow conditions close to the test conditions presented in this work. The results of this measurement are presented in Figure 8-1. It can be noted that the variations of the hub pressures with the rotation angle of the cascade are low. A similar observation can be done for the blade pressures, excepted for the results from the first two static pressure taps on the suction side. The larger variations were explained by the fact that the blade was located close downstream of the upstream probe location during the concerned measurements. Thus, the blockage constituted by the upstream probe slightly influences the blade channels located in proximity. Thus care was taken, never to perform blade flow measurements close to the location of the upstream probe. This is one reason for installing the downstream probe on the opposite side of the cascade. Considering the presented results, it was concluded that the axis-symmetry of the cascade flow is acceptable.
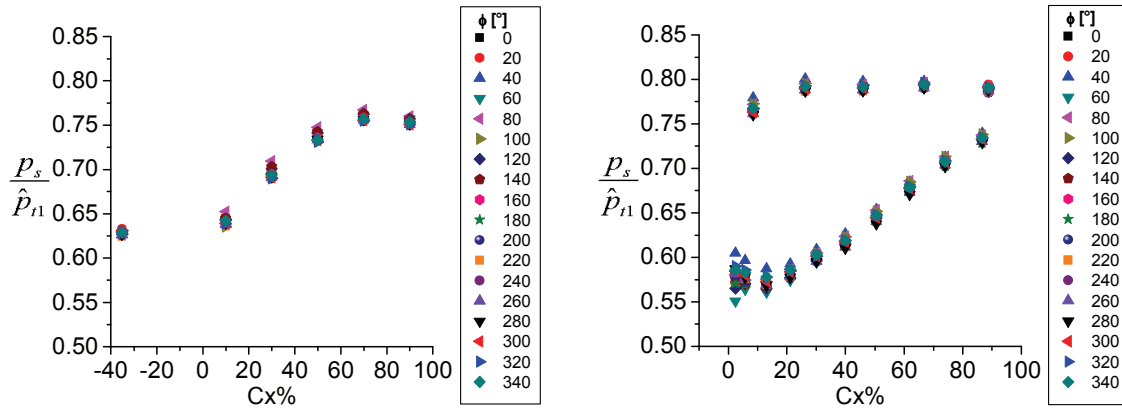
Figure 8-1. Non-dimensionalized static pressures measured on the cascade hub (left) and on one blade-pair (right) during a full rotation of the cascade in the test facility to verify the axis-symmetry of the inlet flow.

During the comparison of probe and LDA measurements, more remarkable differences were observed. Beyond differences related to the different techniques, as will be discussed in more detail in section 12.1.2, this suggests the presence of axis-symmetry deviations that were not captured by the pressure taps measurements described in the preceding paragraph. In fact, the first test did not exclude the eventuality that the cascade facing homogeneous downstream conditions might mitigate differences in the inlet conditions at the location of the pressure taps used to verify the symmetry. Thus verification measurements with a second upstream probe installed at the LDA measurement location were performed. They had to be performed using a different cascade than those investigated in this work and were performed for different test cases than those discussed in this work. The investigation results, presented in [Colombo et al. 2010], allowed to identify some stationary, repeatable differences concerning the flow angles at inlet. As a consequence, also the static pressures and the Mach number measurements are concerned. However the total pressures proved to be almost perfectly constant at each circumferential position of the inlet plane.

The described variations do not affect the comparability of outlet plane measurements with each other, for measurements that were performed with same inlet flow conditions. To regulate the test facility, always the same upstream probe is used which is installed always at the same location. This ensures that for comparable cases, the inlet conditions are indeed unchanged. Furthermore, the repeatability and correspondence of inlet conditions regulated with this probe was extensively proven by the LDA measurements performed at a different location during different campaigns.

The inlet total pressure measurements performed with two upstreams probes showed that the total pressure distribution is insensitive to the detected circumferential variations of flow angle and static pressure. Thus the total pressure measurements performed at the upstream probe location are also valid for the blade channel located on the opposite side of the wind tunnel, for which the downstream conditions are measured and evaluated. Hence comparisons of inlet and outlet total pressures can be performed without concern. For this reason, within this report, particular importance is given to loss indicators based on the total pressures. Furthermore, eminent importance is given to the analysis and interpretation of the flow mechanisms as separations, vortices, turbulence and the distribution of the flow properties detected within the interblade and outlet planes. This way, the qualitative influence of the aspiration and the blade loading is identified. The quantitative influences are partly derived by the comparison of outlet plane measurements for the different configurations. Since the outlet plane measurements are taken at the same location of the test rig, no difference due to circumferential inlet flow variations is due.

Care must be taken when comparing other flow parameters that compare the inlet and outlet plane probe results, since they were measured at different locations of the test rig: The tendencies of the average static pressure rise $\tilde{p}_{s,2} / \tilde{p}_{s,1}$ ($\tilde{p}$ indicates an area weighted average, see section 2.1) are verified with the tendencies obtained by static pressure taps measurements at the casing $p_{s,2} / p_{s,1}$. For the latter, the circumferential location of upstream and downstream measurements is identical. Some differences in the absolute values are found which are partially due to the fact that e.g. the radial pressure gradient modifies the pressure value over the channel heigt. However, the trends indicated by the probes are confirmed. This indicates that the variations in circumferential direction do not have a drammatic influence on the cascade flow. However, for the absolute values of $\tilde{p}_{s,2} / \tilde{p}_{s,1}$, as well as for the absolute values of the deceleration $\overline{Ma_1} / \overline{Ma_2}$ and the deflection $\hat{\alpha}_1 - \hat{\alpha}_2$, a certain incertitude must be stated. Since for the LDA measurements, the upstream and downstream measurements are performed at the same circumferential position, they serve as reference to quantify the uncertainties. The results are shown for different measurement series (s0040, s0175, s0173) in Table 8-1. The observations in the following chapters were performed respecting the noted uncertainties in the conclusions.

The mentioned static pressure measurements performed on the casing wall are presented in 13.Appendix B (p. 179). They are not further discussed in this work, since not fundamental in the explanation of the of the relevant flow mechanisms and of the influence of the aspiration technique.

		s0040	s0175	s0173	$\overline{\Delta}$
$DF = 1 - \dfrac{\hat{V}_2}{\hat{V}_1} + \dfrac{\Delta\hat{V}_\theta}{2\sigma\hat{V}_1}$	Probes	0.46	0.57	0.59	0.02
	LDA	0.48	0.59	0.60	
$\overline{\alpha}_1 - \overline{\alpha}_2$	Probes	28.6°	30.7°	31.2°	0.53°
	LDA	28.5°	31.5°	31.9°	
$\hat{Ma}_1 / \hat{Ma}_2$	Probes	1.43	1.62	1.66	0.03
	LDA	1.46	1.66	1.69	

Table 8-1. Estimation of the uncertainties for the average diffusion factor, the average deflection and the average deceleration by comparison of the probe results with the LDA measurements for different cases (s0040, etc.).

8.2 Repeatability

The test facility conditions were regulated with respect to the measurements of the upstream aerodynamic probe. Figure 8-2 illustrates the comparability of the test conditions for measurements of the same case performed at different days.
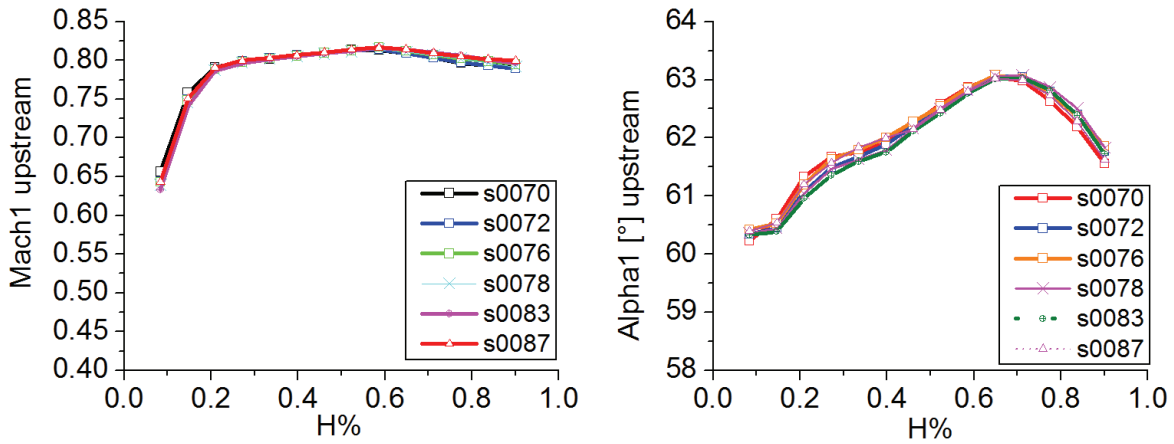
Figure 8-2. Inlet flow conditions obtained at different measurement days for the same measurement case measured with the upstream aerodynamic probe.

The illustrated variations are relatively moderate. The presented results are related to the earliest measurements, thus the reference case measurements. During the following measurement campaigns, the measurement technique was further refined allowing an even better fine-tuning of the inlet flow conditions. Thus the repeatability is widely ensured.

9. Numerical Simulations

Selected results obtained by numerical simulations of the cascade flows are analyzed in this work to support the analysis of the experimental results. The simulation conditions are derived from the results of the present experimental investigation. The computation results are reprocessed in this work to get indications on the mechanisms occurring beyond the scope of the measurement instrumentation, herewith supporting the explanation of the flow mechanisms related to the aspiration technique. The computations were performed by the project partners within the project NEWAC. For the models introduced in section 9.3.1 and 9.3.2 complementary analyses can be found in [Sachdeva 2010] and [Sachdeva 2008] performed by the author of these computations. The results based on the model introduced in section 9.3.3 are first discussed in this work, aside of the related publication [Colombo et al. 2011] and internal project reports.

9.1 Solver

The steady state simulations are carried out with the code elsA v3.3.03 developed by ONERA, described in [Cambier et al. 2008]. The solution is steady state. The $k - \varepsilon$ turbulence modeling is applied.

9.2 Boundary conditions

The inlet conditions for the CFD computations are based on the aerodynamic probe measurements in the inlet plane for all the computed cases. The turbulence intensity at inlet is based on the LDA measurements. As further parameters, the measured aspiration mass flow for the hub and the blade aspiration slots as well as the measured total temperature at inlet are applied.

Following approach is used to derive the boundary conditions for the computations from the measurement results: the measured distributions of total pressure, flow angles, turbulence intensity and total temperature level are applied on the inlet plane of the computational domain. At the outlet section, a radial equilibrium condition is imposed for the static pressure distribution. The inlet Mach number measured during the experiments is applied indirectly via the level of static pressure at the outlet: in an iterative process the static pressure level at outlet is varied until the correct Mach number level at inlet is obtained. The correct aspiration rate is obtained by prescribing the mass flow rate at the outlet of the aspiration ducts. For the wall modeling, a typical adiabatic non-slip condition is used.

9.3 Computational meshes

Due to the condition of azimuthal axis-symmetry, in all meshes only one blade passage is meshed.

9.3.1 Cases without aspiration

The mesh used to compute the reference case without aspiration is illustrated to the left of Figure 9-1. It consists of 7 blocks with a total of 1.3 million nodes. A typical meshing strategy is applied yielding the illustrated topology. The mesh is refined to produce a first cell height with an y^+ close to 1.0. A structured meshing approach is used. All the nodes at the block interfaces are coincident. Further information by the author of this model can be found in [Sachdeva 2010].

9.3.2 Cases with aspiration on the hub

The mesh used to compute the cases with aspiration only on the hub is illustrated to the right of Figure 9-1. It consists of 8 blocks and a total of 1.6 million nodes. The mesh corresponds to that described in section 9.3.1 but an additional block was added to model the aspiration on the hub. This flow region is modeled by the so-called "Chimera" technique: the additional block overlaps into the adjacent block of

the main flow, thus the nodes of its mesh are not coincident with those of the adjacent block. During the solution, the two flow regions are solved separately and an interpolation scheme transfers the results of the overlaping nodes at each iteration step. This approach simplifies the meshing but makes the solving more complex. Further discussion on this technique can be found in [Cambier et al. 2008]. Also for this mesh, the obtained y^+ is close to 1.0. Further information by the author of this model can be found in [Sachdeva 2010].
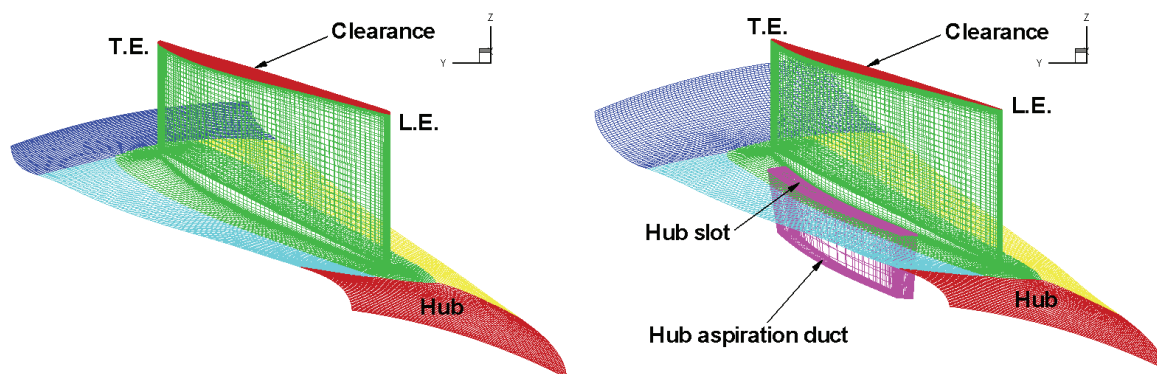
Figure 9-1. Limiting surfaces of the meshes used for the computations without aspiration (left) and with aspiration on the hub only (right).

9.3.3   Cases with aspiration on the hub and on the blades and different blade pitch

For the numerical simulations of the cases with aspiration on the hub and on the blades, a more elaborate structured computational mesh is used. It consists of 23 blocks with 85 radial subdivisions. Almost all the blocks are coincident, especially the blocks modeling the blade aspiration slot and the aspiration duct within the blade. Only the hub aspiration slot is modeled non-coincidently using the Chimera technique. The tip clearance is also modeled. Renouncing to the use of the Chimera technique for the blade aspiration slot yields significant advantages for the solution process. The achieved y+ values are close to 1.0. The resulting mesh consists of 4.4 million nodes. To modify the blade pitch to model the cases with a reduced number of blades, the blocks in the center of the blade channel are stretched. Particular care was taken to ensure sufficient mesh quality in both cases. Figure 9-2 illustrates the mesh representing the cascade configuration with 18 blades to the left, and the cascade with 14 blades to the right. Further information by the authors of this model can be found in [Castillon et al. 2009].
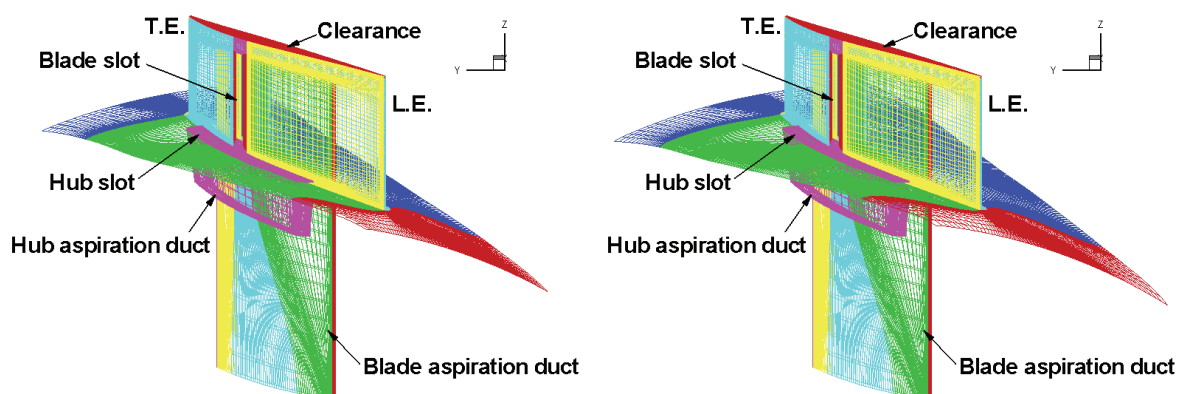
Figure 9-2. Limiting surfaces of the meshes used for the computations with aspiration both the hub and on the blades. To the left: cascade configuration with 18 blades, to the right: cascade configuration with 14 blades.

PART III – Results and analysis

10. Overview of the discussed cases

The present work discusses results of measurements performed with the same average inlet Mach number of 0.8. Results for two different incidence levels are compared: i=3° and i=5° with respect to the design inlet flow angle α_1=60°. For each incidence level, the configurations listed in Table 10-1 are compared. For clarity, they are labelled A1...D2. A1 is the reference case without any aspiration applied, thus without aspiration slots. In the cases B1 and B2, aspiration on the hub with different aspiration rates is applied. In cases C1, C2, D1 and D2, the aspiration on the hub is fixed to 2% of the inlet mass flow while aspiration on the blades is added at the same levels respectively in case C1 and D1 as well as C2 and D2. The blade pitch is 20° in the cases A1...C2 representing the medium loaded cases. The blade pitch is increased to 26° in the cases D1 and D2 by reducing the number of blades from 18 to 14. These are the highly loaded cases. The same aspiration rates per cascade are applied for the 20° and 26° blade pitch cases, to compare cases with the same "cost" in terms of aspirated mass flow. This allows evaluating if comparable performance can be achieved on a cascade with reduced blade number but same with "cost" of aspirated mass flow. For configuration B1, LDA measurements were performed that will be compared to the probe measurements.

Label	Hub aspiration C_Q	Blade aspiration C_Q	Blade pitch
A1	no	no	20°
B1	2 %	no	20°
B2	4 %	no	20°
C1	2 %	0.8 %	20°
C2	2 %	1.5 %	20°
D1	2 %	0.8 %	26°
D2	2 %	1.5 %	26°

Table 10-1. Definition of the configurations discussed in this work. They are tested for same inlet Mach number of 0.8 and two inlet flow incidences: i = +3° and i = +5°. The shaded case is the reference case. The aspiration rate is expressed as aspiration rate per cascade (see definition of C_Q in section 2.2.3).

It should be noted that since the number of slots on either blades or hub corresponds to the number of blades, when changing from 18 to 14 blades, the mass flow is aspirated through a reduced number of slots. The resulting aspiration rate per slot compared to the inlet mass flow are listed in Table 10-2.

Label	Hub aspiration $C_{Q,Slot}$	Blade aspiration $C_{Q,Slot}$	Blade pitch
A1	no	no	20°
B1	0.11 %	no	20°
B2	0.22 %	no	20°
C1	0.11 %	0.04 %	20°
C2	0.11 %	0.08 %	20°
D1	0.14 %	0.05 %	26°
D2	0.14 %	0.11 %	26°

Table 10-2. Definition of the configurations discussed in this work with the aspiration rates expressed as aspiration rate per slot (see definition of $C_{Q,Slot}$ in section 2.2.3).

Further parameter and averages not discussed here are given in Appendix C on page 182 for reference.

11. Reference case

As mentioned, the reference case has an average inlet Mach number of 0.8 with configuration A1, thus no aspiration slots and a blade pitch of 20°. The case with an incidence level of 3° is analyzed in detail such that the other cases can be compared to it.

11.1 Experimental results

11.1.1 Inlet flow

Radial distributions

The control parameters of the test facility were adjusted to yield a constant Mach number over most of the channel height at the inlet of the test section, at a level close to 0.8. The result is shown in the radial distribution in Figure 11-1. The average inlet flow angle is 62.6° which is close to a positive incidence of +3° and will hence be named as such in the following. As can be noted in the radial distribution, the inlet flow angle slightly increases towards the casing.
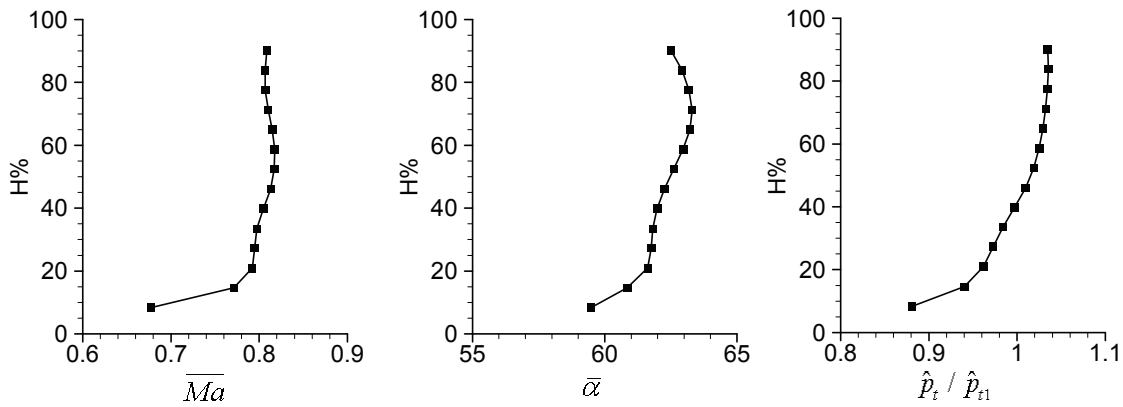
Figure 11-1. Radial distributions of the inlet conditions of the reference case: non-dimensionalized total pressure, Mach number and flow angle.

As can be noted both in the radial distributions in Figure 11-1 and the contours in Figure 11-2, the test facility tends to yield a positive radial total pressure gradient at the test section inlet. An increase in total pressure of about 18% is measured between 15 and 90% of the channel height. This is related to the fact that the facility was originally conceived to simulate rotor sections that typically have positive radial total pressure gradient. Forcing a lower or even inversed pressure gradient would affect the uniformity of the inlet flow velocity and inlet flow angle distribution. The total pressure gradient is accepted in favour of a rather uniform velocity and inlet flow angle distribution.

Below 15% channel height, the total pressure decreases rapidly. This indicates a relatively thick hub boundary layer that is not completely controlled by the auxiliary boundary layer aspiration of the facility located further upstream on the hub wall. The hub boundary layer can also be identified as region of lower Mach number in Figure 11-1 and on the contours in Figure 11-2.

Potential effect of the blade leading edge

As can be noted in the static pressure plot in Figure 11-2, regions of higher static pressure extending in radial direction disturb the axisimmetry. They are detected at exactly one blade pitch circumferential distance from each other. They indicate that the probe measurement location is already within the region of influence of the blade leading edge that is located 0.4 axial chords further downstream. In agreement with typical potential effect manifestation, the flow is decelerated in front of the leading edge in streamwise direction. This yields the measured reduced Mach number and hence increased static pressure. In contrast, the flow between the two leading edges has higher Mach number and thus lower static pressure. The streamlines are deflected around the leading edge, which yields the region with higher and lower flow angles visible especially in the region towards the casing in the flow angle distribution in Figure 11-3.

Note that the region influenced by the leading edge does not coincide with the location of the leading edge indicated in the plot since the measurement is taken at 0.4 axial chords upstream of the leading edge. The circumferential velocity produces a certain circumferential displacement before the flow reaches the leading edge.

Skewed inlet flow, inlet vorticity

The flow angles presented in Figure 11-3 are generally found to be slightly higher towards the casing. This shows that the flow has flow angle distribution with values that increase from the hub towards the casing. In other words, the inlet flow is slightly skewed, beginning with a more axial orientation close to the hub that becomes more circumferential towards the casing. This reflects in a notable level of axial vorticity with negative sign, as can be noted in Figure 11-4 and Figure 11-5, especially close to the hub and at mid-height. Vorticity cannot form from nothing, so an explanation was searched for this occurrence. Understanding the originating mechanism should answer the question if this condition is repeatable. The numerical investigation [Deslot et al. 2010] on the facility inlet flow performed to analyze these effects indicates that the vorticity is formed as a direct but not trivial consequence of the flow generation configuration: as illustrated in Figure 11-6, the axial vorticity observed at the test section inlet arises essentially from the wake of the upper side of the disk that separates the two inlet settling chambers upstream of the test section. Also, a certain component originated by the hub wall boundary layer adds in. It was found that both curvature and pressure gradients occurring in the upstream radial-axial nozzle of the facility are advantageous for the conservation of these particular vorticity sheets, while inversed sign vorticity originated at the other walls is dissipated. Furthermore it was found that this mechanism is triggered by the orientation (both absolute and with respect to each other) of the inlet guide vanes for the upper and lower inlet settling chamber: configurations yielding particular wake sizes or particular shear (as e.g. very different orientation of upper and lower guide vane arrays) can increase this effect. Since part of this vorticity is oriented streamwise, it also reflects in significant levels of helicity, which is also plotted in Figure 11-4 and Figure 11-5. The most important conclusion of the investigation [Deslot et al. 2010]is that the observed flow angle and vorticity distribution is perfectly repeatable for a given test condition.

The vorticity and helicity levels found upstream of the cascade are of interest for the investigation since pre-existing vorticity is transported and amplified or reduced through streamline curvature and velocity gradients. Since such mechanisms are expected to occur within the cascade flow, pre-existing helicity can explain the arising of certain levels of vorticity through the cascade. As will be noted, a certain amount of vorticity is actually conserved throughout the blade channel yielding an offset of the values found at outlet.

The repeatable presence of the inlet vorticity is a particularity of this study compared to former cascade tests where, as noted on p. 318 of [Cumpsty 2004] conventionally no inlet skew is present. Since inlet skew actually occurs in real compressors, the noted levels enhance the meaningfulness of this study to real cases concerned by inlet flow skew.
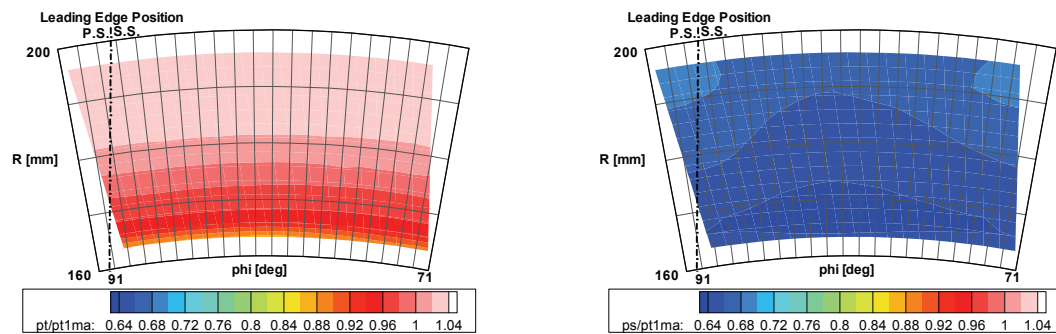
Figure 11-2. Inlet total pressure and static pressure measurement results (5-hole probe).
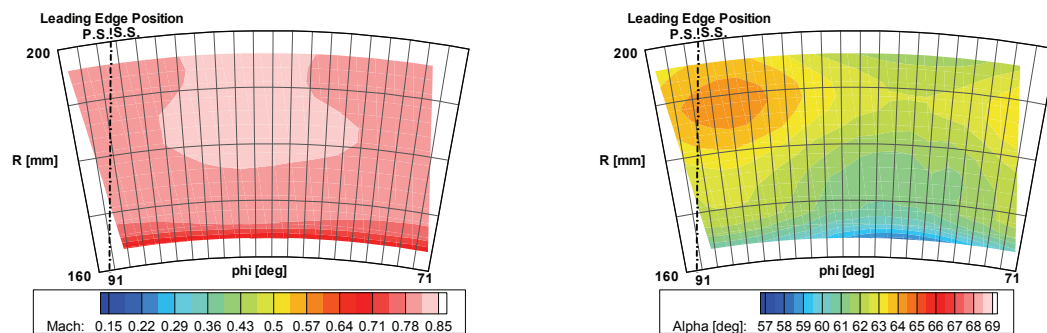
Figure 11-3. Inlet Mach number and flow angle measurement results (5-hole probe).
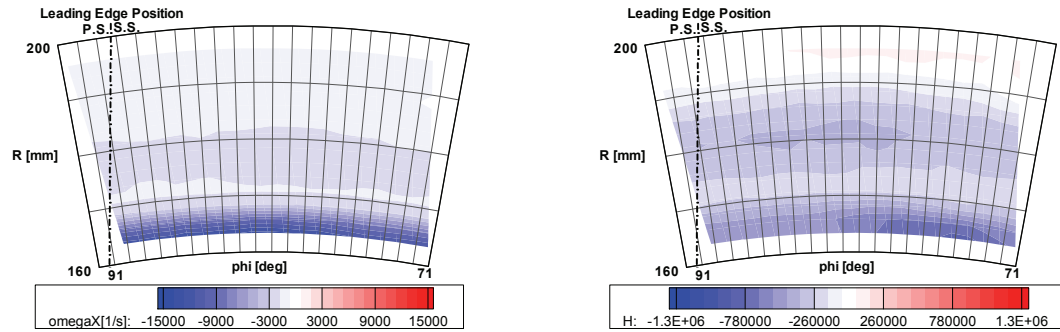
Figure 11-4. Inlet axial vorticity and helicity based on measurement results (5-hole probe).
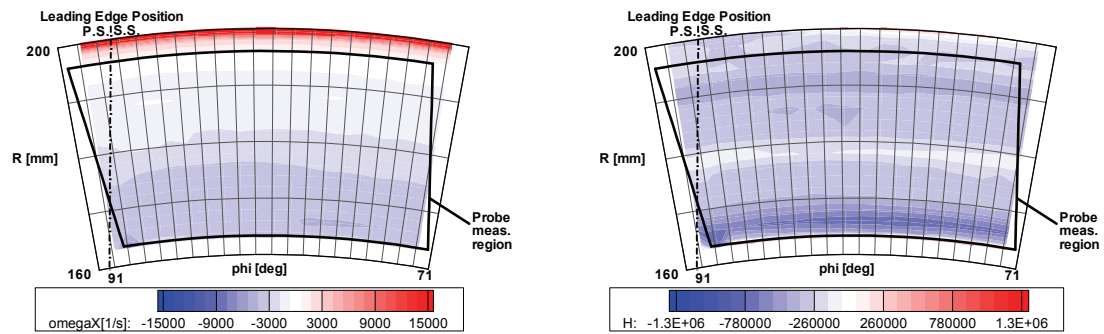
Figure 11-5. Inlet axial vorticity and helicity based on measurement results (LDA).
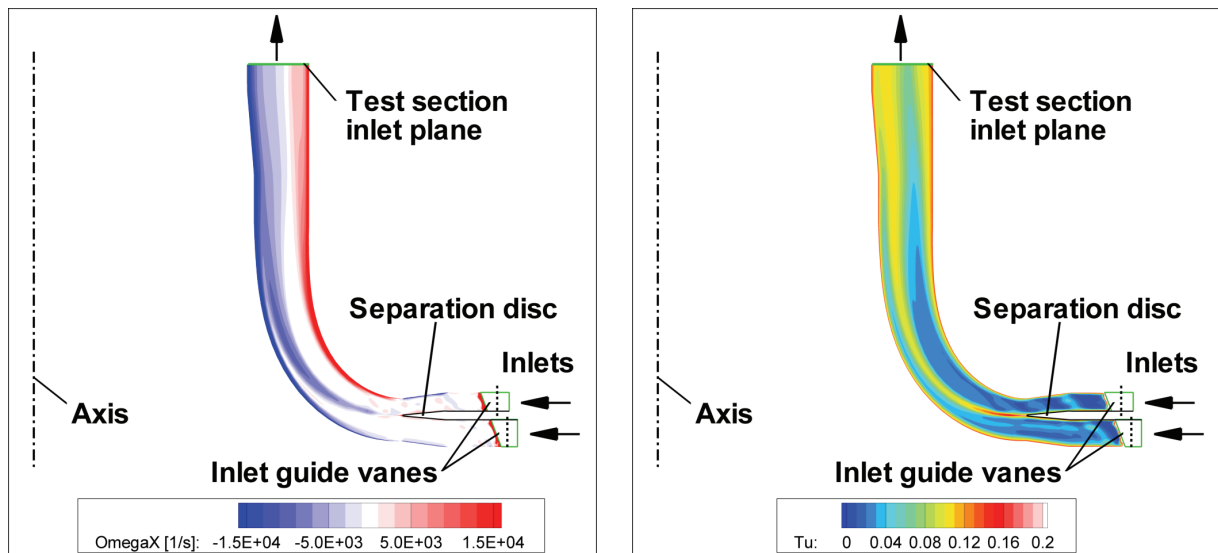
Figure 11-6. Helicity and turbulence distributions in the test facility inlet nozzle based on numerical investigation [Deslot et al. 2010].

Turbulence and fluctuations

As noted earlier, the RMS of the velocity fluctuations u' and v' that are respectively aligned with and normal to the average local velocity vector, measured with 2D-LDA, allow estimating a two-dimensional turbulence intensity defined by (7.4) in section 7.6.6.

The results are plotted in
Figure 11-7. The detected turbulence intensity measured upstream of the cascade is close to 7.5% in a band located at mid-height measuring about 1/3 of the height. The turbulence intensity increases to 10% towards hub and casing, reaching higher values in the boundary layers. The high level of inlet vorticity suggested that the detected fluctuations might indicate inlet flow unsteadiness rather than fully developed turbulence. However, as illustrated by the right hand side plot in Figure 11-6, and by the comparison with measurement results on the left of
Figure 11-7, similar turbulence distributions were found in the numerical analysis presented in [Deslot et al. 2010]. The simulations were steady state and based on a two-equation turbulence model. This indicates that such levels of turbulence can actually be produced by the occurring steady state flow mechanisms. The investigation shows that the turbulence is generated by different mechanisms: the wake of the disk separating the inlet settling chambers, the wall boundary layers and the mixing region between the flow from the upper and the lower inlet settling chambers. The inlet nozzle geometry yielding deflection and acceleration and the stabilizing/destabilizing influence of the concave/convex walls of the nozzle yields amplification/attenuation of the fluctuations producing the turbulence distribution measured at the test section inlet.

The measured RMS of the fluctuations, also presented in
Figure 11-7 show that fluctuations aligned with the velocity vectors are prevalent in the channel half towards the hub and normal fluctuations are prevalent in the half towards the casing (except at the casing). The Reynolds stress term on the right of
Figure 11-7 indicates three discernible bands with significant non-zero values, indicator of shear regions producing turbulence. The two non-zero bands of opposed sign close to the hub compare well to the bands of increased vorticity coming from the disk wake and from the hub wake observed in Figure 11-4, Figure 11-5 and Figure 11-6 described earlier indicating a correlation with the mechanisms originating the vorticity.
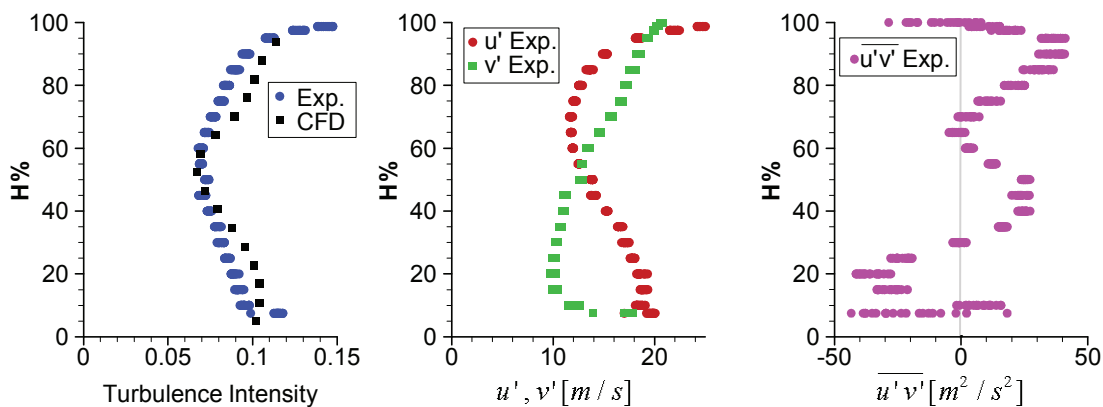
Figure 11-7. Inlet duct turbulence intensity, fluctuations u' and v' (RMS of u and v) and time average of u'v' based on LDA measurements compared to CFD results from [Deslot et al. 2011]. The LDA results at all circumferential positions are represented in the scatter plots.

As for the inlet vorticity distribution described earlier, an important conclusion is that the observed turbulence distribution is repeatable for a given test condition. The described turbulence levels are relatively high but not completely uncommon for multistage axial compressors. On p. 179, [Cumpsty 2004] cites turbulence level measurements from a highly loaded but very efficient multistage axial compressor performed by Wisler et al. (1987): away from the endwalls and outside the wakes from preceding stages, turbulence levels of 5% at design conditions and of 10% at reduced mass flow were found. Near the endwalls or in the wakes the levels were much higher, around 20%. Hence the levels found in the present investigations are in the middle of this range. Grieb comments in [Grieb 2009] that common wind tunnels achieve only 0.5% turbulence intensity. It is thus advantageous for the representativeness of the results to be able to repeatably produce the described turbulence levels in the present case. With respect to the expected influence of this turbulence, Cumpsty furtheron cites results where cases with increased turbulence reduces the production of loss by preventing separation in cases with moderate-high Reynolds numbers of e.g. $1.3 \cdot 10^5$. Herewith they perform similar to how cases with less inlet turbulence would perform at higher Reynolds numbers. However, the inlet flow Reynolds numbers referred to the blade chord in the present investigations of around $1.3 \cdot 10^6$ are so high that such influence of the inlet turbulence is not expected to be significant. The high turbulence might however increase dissipation loss. Hence it is important to note that experiments presented hereafter that have the same inlet conditions also have the same inlet turbulence distribution. Occurring loss differences can hence be ascribed to the applied modifications of the aspiration configuration since the inlet flow turbulence is identical from case to case.

11.1.2 Outlet flow

General observations

The flow properties averaged over the measured region are summarized in Table 11-1. As expected for a compressor cascade, they indicate that the flow is decelerated, turned and the static pressure is increased. However for a compressor cascade working with the diffusion factor based on measurement results far below 0.7, the total pressure losses are relatively important. Such loss levels and the moderate diffusion factor must be related to the occurrence of separation which means that at the incidence level chosen for the reference case, separation is already important.

Average parameter	Symbols	Units	Upstream	Downstream
Dimensionless total pressure	$\hat{p}_t / \hat{p}_{t1}$	[-]	1.000	0.969
Dimensionless static pressure	$\tilde{p}_s / \hat{p}_{t1}$	[-]	0.657	0.785
Flow angle	$\overline{\alpha}$	[°]	62.2	33.4
Mach number	$\overline{Ma}$	[-]	0.797	0.587
Reynolds number (ref. to chord)	Re_c	[-]	$1.3 \cdot 10^6$	$7.4 \cdot 10^5$
Turbulence Intensity (estim. av.)	$\hat{Tu}$	[-]	0.085	
Deceleration	$\overline{Ma}_1 / \overline{Ma}_2$	[-]	1.358	
Pressure ratio	$\tilde{p}_{s2} / \tilde{p}_{s1}$	[-]	1.159	
Pressure rise coefficient	$C_p = \dfrac{\tilde{p}_{s2} - \tilde{p}_{s1}}{\hat{p}_{t1} - \tilde{p}_{s1}}$	[-]	0.304	
Diffusion factor	$DF = 1 - \dfrac{\overline{V}_2}{\overline{V}_1} + \dfrac{\Delta \overline{V}_\theta}{2\sigma \overline{V}_1}$	[-]	0.417	
Deflection	$\overline{\alpha}_1 - \overline{\alpha}_2$	[°]	28.8	
Total pressure losses	$\omega = \dfrac{\hat{p}_{t1} - \hat{p}_{t2}}{\hat{p}_{t1} - \tilde{p}_{s1}}$	[-]	0.089	
Dimensionless total pressure difference	$\chi = \dfrac{\hat{p}_{t1} - \hat{p}_{t2}}{\hat{p}_{t1}}$	[-]	0.031	

Table 11-1. Averaged measurement results. All results are based on 5-hole probe measurements excepted for the turbulence intensity which is based on LDA measurements.

110

Flow features

Several flow features can be identified by their trace in the outlet plane measurement results presented in Figure 11-9 to Figure 11-12. The schematic in Figure 11-8 summarizes the main features. They will be analyzed in the following sections. The schematic also shows that the aerodynamic probe measurement region does not extend up to the walls of the flow channel since it is limited by the size of the aerodynamic probe head and the occurrence of wall effects if measuring too close to the annulus walls. The circumferential distance between the marked trailing edge position and the location where the wake is visible is due to the axial distance between the trailing edge plane and the measurement plane located at 0.3 axial chords distance.
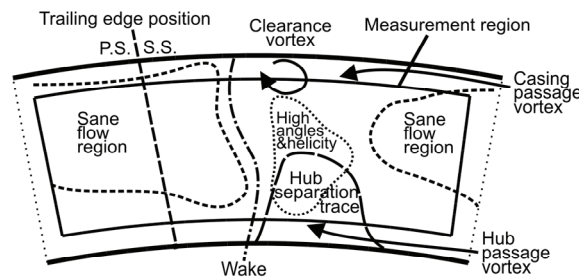
Figure 11-8. Schematic of the flow features in the outlet plane.

Secondary flow features

Secondary flow, hence streamwise vorticity, has a significant influence on the flow pattern detected in the present case. This is pointed out by the contour plot of helicity in Figure 11-12. As mentioned in section 3.2, helicity results as the scalar product of vorticity and velocity vectors. It hence indicates the magnitude of occurring streamwise aligned vorticity weighted by the local velocity magnitude. The weighting emphasizes the relevance of the considered vorticity on the considered flow. The sign indicates if the streamwise vorticity vector is aligned with or reversed to the flow direction. In addition to the helicity plot, the secondary velocity field is presented in Figure 11-12. It is computed based on the probe measurements according to the method introduced in chapter 3.3. The secondary velocity field indicates the direction of the secondary motion caused by the streamwise vorticity as well as the magnitude of secondary velocity. The helicity contours and the secondary flow features will be analyzed more in detail in section 11.3.
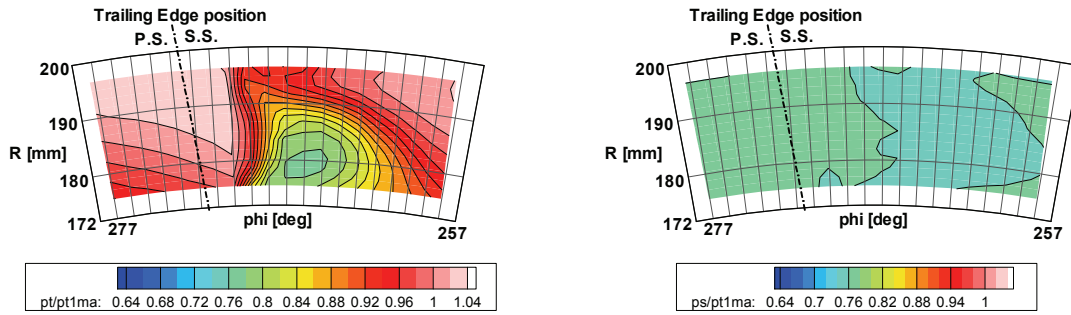
Figure 11-9. Outlet total pressure and static pressure measurement results (5-hole probe).
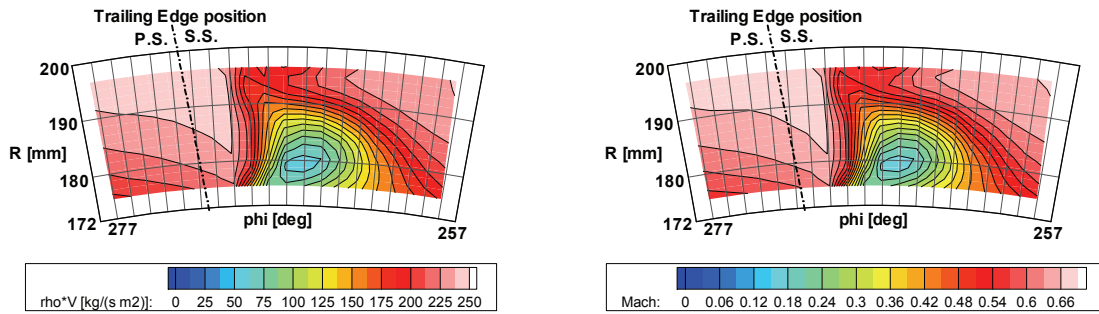
Figure 11-10. Outlet momentum and Mach number measurement results (5-hole probe).
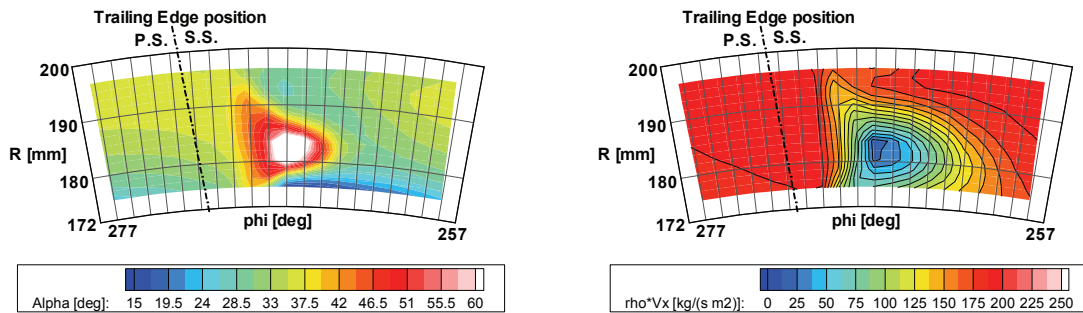
Figure 11-11. Outlet flow angle and axial momentum measurement results (5-hole probe).
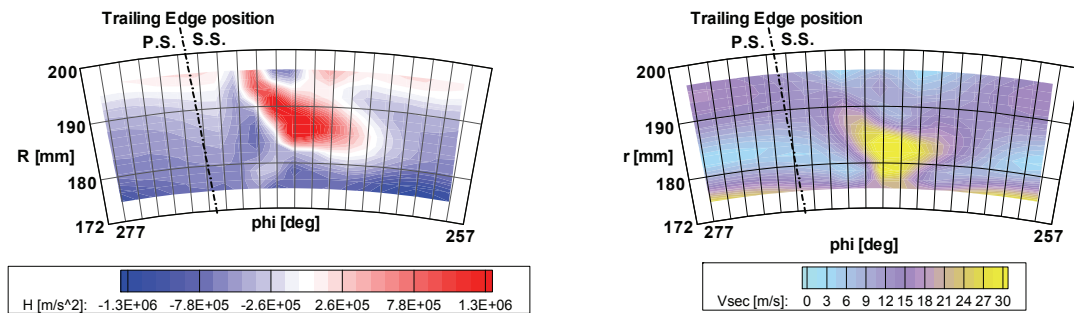
Figure 11-12. Outlet flow helicity and secondary velocity distributions based on measurement results (5-hole probe).

Low variations of static pressure and similarity of Mach number and momentum

For the present case, comparison of the outlet measurements of Mach number, total pressure and momentum plots with adequate scales shows remarkable similarity of the distributions, as can be seen comparing Figure 11-9 and Figure 11-10. This apparent similarity is ascribed to the fact that the outlet flow adjusts itself to a relatively homogeneous static pressure level with relatively small variations, as shown by the static pressure plot in Figure 11-9. This is due to a reduced radial pressure gradient that goes with the reduced average outlet flow angle of the deflected flow and the mixing out of further static pressure heterogeneities because of the distance to the trailing edge. The standard deviation of $p_s / \hat{p}_{t1}$ between the measurements at all locations is 0.6% referred to the average; hence 99.6% of the values are within ±2% from the average value. Almost constant static pressure means that the Mach number almost only depends on the total pressure according to the isentropic relationship

$$Ma^2 = \frac{2}{\kappa-1}\left[\left(\frac{p_t}{p_s}\right)^{\frac{\kappa-1}{\kappa}}-1\right]$$
(11.1)

yielding the Mach number plot in Figure 11-10. The relationship between total pressure and Mach number is of course not linear, but strong enough to yield a Mach number behaviour which is very similar to the total pressure plot. The Mach number in the outlet plane is still relatively high. Its variation with almost constant p_s and constant total temperature T_t yields compressibility effects reflected by the variation of the density:

$$\rho = p_s \frac{1}{RT_t}\left(1+\frac{\kappa-1}{2}Ma^2\right)$$
(11.2)

To give an idea of the density variation, note that the standard deviation of the downstream plane values is of 2.6% referred to the average of all measurements. Nevertheless, the variations in density are small enough not to cause significant differences between the Mach number and the momentum distribution that can be obtained by

$$\rho V = Ma\sqrt{\kappa p_s \rho}$$
(11.3)

Hence for the present evaluation it can be noted that low total pressure regions coincide with low Mach number and low momentum regions.

Mass flux (axial momentum) distribution

The mass flux distribution is given by the axial component of the local momentum. It is hence strongly related to the momentum magnitude introduced in the preceding section:

$$\rho V_x = \rho V \cos\alpha \cos\gamma$$
(11.4)

However, the local mass flux is directly influenced by the flow orientation, which is very heterogeneous in this case. This is illustrated by the flow angle distribution presented in Figure 11-11. As a consequence the variation of mass flux distributions can be different than the variation of momentum distribution. In the middle of the trace, reduced momentum coincides with high flow angles yielding even more reduced mass flux. This is important since the mass flux distribution directly expresses the weight of the occurring features with respect to the overall mass flow. As an example, due to this, large parts of the low total pressure regions in Figure 11-9 have a small impact in the mass flow weighted averages introduced earlier on. Similar considerations can be done on the average flow orientation.

11.2 Validation of the numerical simulations

Figure 11-13 to Figure 11-15 illustrate the comparison of the simulation results for the reference case introduced in chapter 9 with the results of the measurements. The traces of relevant macroscopic features can be recognized, although differences can be seen in intensity and shape. A similar wake position can be seen. The low total pressure region related to the corner separation can be noted close to the hub, although it seems less intense in the simulations with respect to the size of the affected region. The hub and casing passage vortices marked by helicity with negative sign close to the hub and helicity with positive sign close to the casing are reflected by the simulations although the casing passage vortex extends further away from the casing in the numerical results. The trace of the clearance vortex visible in the total pressure and as region with high helicity of negative sign in the helicity plot is more pronounced in the simulations extending more distant from the suction side, pushing the casing passage vortex away. This might explain a higher concentration of the casing passage vortex. The notable region with high levels of helicity with positive sign at mid span is clearly predicted by the simulations and is similar in intensity, shape and orientation. Finally, the region with high flow angles is visible in the simulation results, although it is significantly less pronounced than in the measurement results.
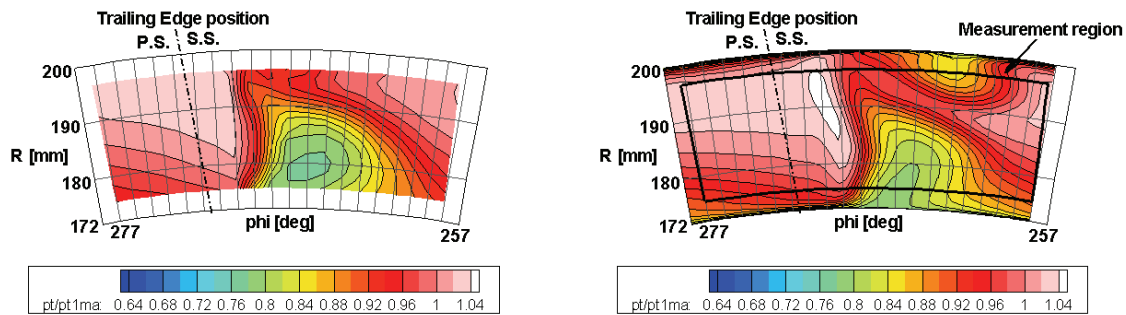
Figure 11-13. Comparison of outlet Mach number distributions (5-hole probe measurements and CFD).
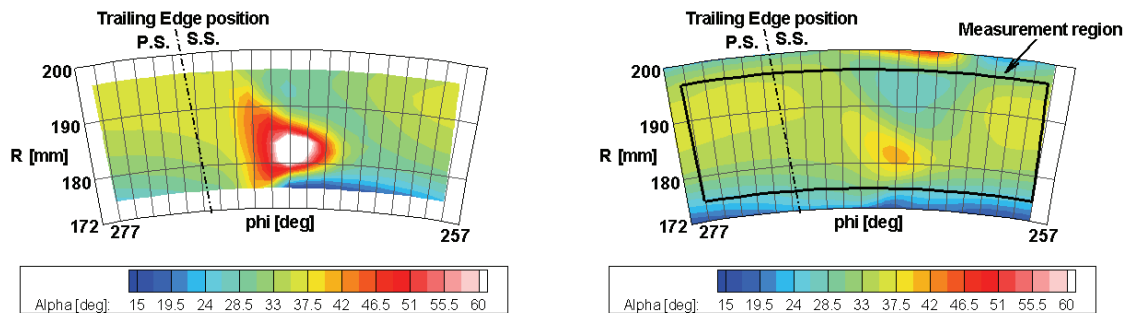
Figure 11-14. Comparison of outlet flow angle distributions (5-hole probe measurements and CFD).
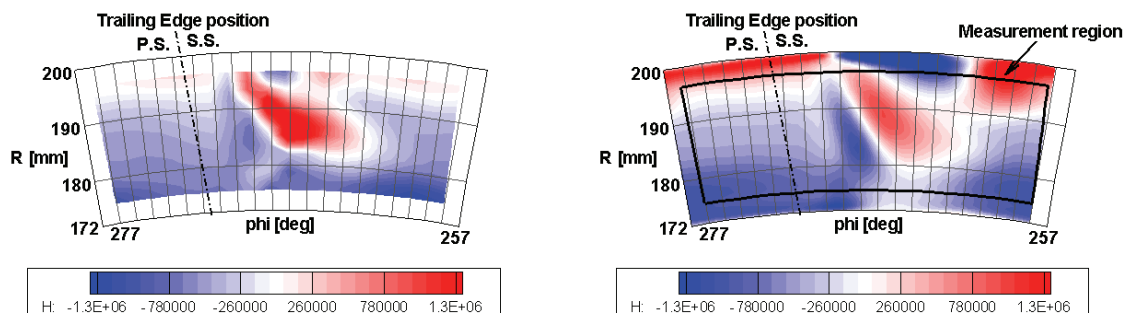
Figure 11-15. Comparison of outlet helicity distributions 5-hole probe measurements and CFD).

The similarity of the described features indicates that the macroscopic mechanisms leading to their occurrence are well predicted by the simulations compared to the experimental results, although with different intensity. Hence the simulation results can be used to support the explanation of the macroscopic mechanisms common to simulation and experiments as will be done in the following section.

As mentionned, the measured absolute values are not exactly matched by the simulation results. This is related to the difference observed in the main features. The spread is quantified by comparing the average values in Table 11-2. The averages of the numerical results are computed over a region corresponding to the measurement region. The differences are ascribed mainly to the difficulties modeling the flow phenomena in the separated region by the turbulence model and to a high sensitivity of the model to the small incertitudes of the measured inlet flow conditions discussed in section 8.1.

Averaged parameter	Symbols	Units	Measurements	CFD
Dimensionless outlet total pressure	$\hat{p}_{t2} / \hat{p}_{t1}$	[-]	0.969	0.967
Dimensionless outlet static pressure	$\tilde{p}_{s2} / \hat{p}_{t1}$	[-]	0.785	0.771
Outlet flow angle	$\bar{\alpha}_2$	[°]	33.4	33.5
Outlet Mach number	$\overline{Ma}_2$	[-]	0.587	0.578
Deceleration	$\overline{Ma}_1 / \overline{Ma}_2$	[-]	1.358	1.384
Pressure ratio	$\tilde{p}_{s2} / \tilde{p}_{s1}$	[-]	1.159	1.176
Pressure rise coefficient	$C_p = \dfrac{\tilde{p}_{s2} - \tilde{p}_{s1}}{\hat{p}_{t1} - \tilde{p}_{s1}}$	[-]	0.304	0.335
Diffusion factor	$DF = 1 - \dfrac{\overline{V}_2}{\overline{V}_1} + \dfrac{\Delta \overline{V}_\theta}{2\sigma \overline{V}_1}$	[-]	0.417	0.482
Deflection	$\bar{\alpha}_1 - \bar{\alpha}_2$	[°]	28.8	29.6
Total pressure losses	$\bar{\omega} = \dfrac{\hat{p}_{t1} - \hat{p}_{t2}}{\hat{p}_{t1} - \tilde{p}_{s1}}$	[-]	0.089	0.095
Dimensionless total pressure difference	$\chi_s = \dfrac{\hat{p}_{t1} - \hat{p}_{t2}}{\hat{p}_{t1}}$	[-]	0.031	0.033

Table 11-2. Comparison of the results averaged over corresponding regions based on the measurement results and on the numerical (CFD) results.

11.3 Analysis of the relevant flow features

Wake

Identifying the trace of the wake gives first indications on how the flow evolved past the trailing edge up to the measurement plane. The wake is composed by both suction side and pressure side boundary layers which have significant radial vorticity of opposed sign. In other words, the axial velocity within the boundary layers decreases approaching the blade surface yielding a positive $\partial V_x / \partial \theta$ on the suction side and negative on the pressure side. Consider the radial vorticity in cylindrical coordinates given by

$$\Omega_R = \frac{1}{R}\frac{\partial}{\partial \theta}V_x - \frac{1}{R}\frac{\partial}{\partial x}(RV_\theta)$$

$$\text{(1)} \qquad\qquad \text{(2)}$$

(11.5)

and note that for the present consideration term (2) representing the variation of circumferential velocity in axial direction can be neglected. Close after the trailing edge, in absence of other disturbances as trailing edge separations, the wake position is denoted by the region with zero radial vorticity.
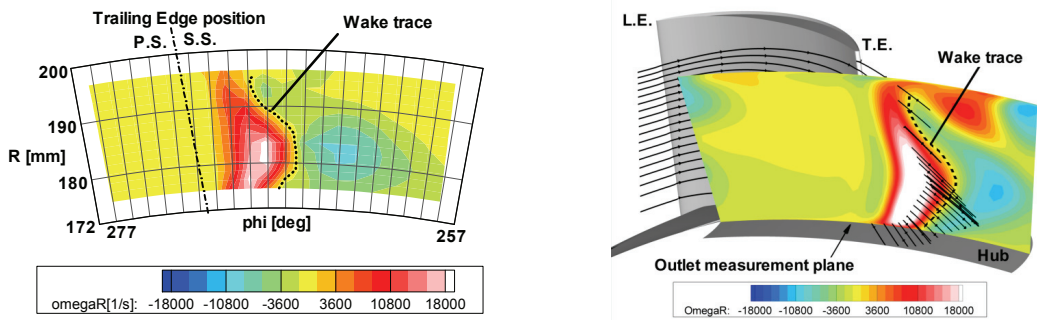
Figure 11-16. Outlet radial vorticity distribution based on five-hole-probe measurement results (left) and CFD results (right). The plotted streamlines come from either pressure or suction side boundary layers.

According to the vorticity transport equation (3.3) introduced earlier, if all production terms are zero, hence $D\vec{\Omega}/Dt = 0$, even in the measurement plane located 0.3 axial chords downstream of the trailing edge, the region with zero radial vorticity will denote stream regions close to the wake. Obviously however, the production terms need not to be zero. Especially due to the diffusion term $\nu\,\Delta\vec{\Omega}$, the radial vorticity of the wake diffuses to the neighbouring regions on the way from the trailing edge to the actual measurement location. This can distort the apparent localisation of the wake in case of strong disequilibrium between the intensity of the vorticity on the pressure side and on the suction side: the vorticity diffusing from the stronger side to the weaker would make the zero radial vorticity location drift towards flow regions on the weaker side. This is reflected by the numerical results on the right hand side of Figure 11-16: the streamlines denote the path followed by particles coming from either pressure side or suction side boundary layers. As can be noted, the streamlines cross the contour plot more to the left than the zero vorticity region marked by a dashed line. This reflects that the zero vorticity line drifted to the right. Hence the intensity of the vorticity of the pressure side boundary layer was more important that of the suction side boundary layer. A thin suction side boundary can be caused by a separation that repelled part of the suction side boundary layer earlier on. Another perturbation according to the vorticity transport equation can be given by strong radial velocity gradients. Thus, the result can also be distorted close to the wall boundary layers and in shear regions above or below a separation.

Even though the zero vorticity line does not exactly indicate the location crossed by streamlines coming from the blade boundary layers, it gives a good approximation. Thus in the present case it can be observed that the wake trace is rather deformed. The part coming from lower mid span seems to have migrated further away from the suction side. This can be explained by a separation on the suction side: since a separation goes with lower static pressure rise, it can be imagined that it made pressure side streamtubes passing the trailing edge bend towards the lower pressure. This is confirmed analyzing the pressure field in the simulation results occurring right behind the trailing edge. This bending also manifests as an underturned flow region which is reflected by the high flow angles in Figure 11-11.

Hub corner separation

An outstanding feature that can be noted in Figure 11-9 to Figure 11-11 is a relatively large region with low total pressure, low Mach number and low momentum. It is located mostly on the right hand side of the wake trace extending significantly in circumferential direction. It indicates that a hub corner separation as described in section 4.2.2 occurred in the corner between hub and suction side of the blade. The sources of low momentum fluid in such a case are multiple: hub boundary layer is advected by the hub passage vortex stagnating within and past the separation; blade and hub boundary layer is raised above the separated region concentrated close to the hub by the radial pressure distribution; flow reversal within the separation causes shearing with the main flow reducing its momentum. These mechanisms are illustrated with the support of the numerical results:
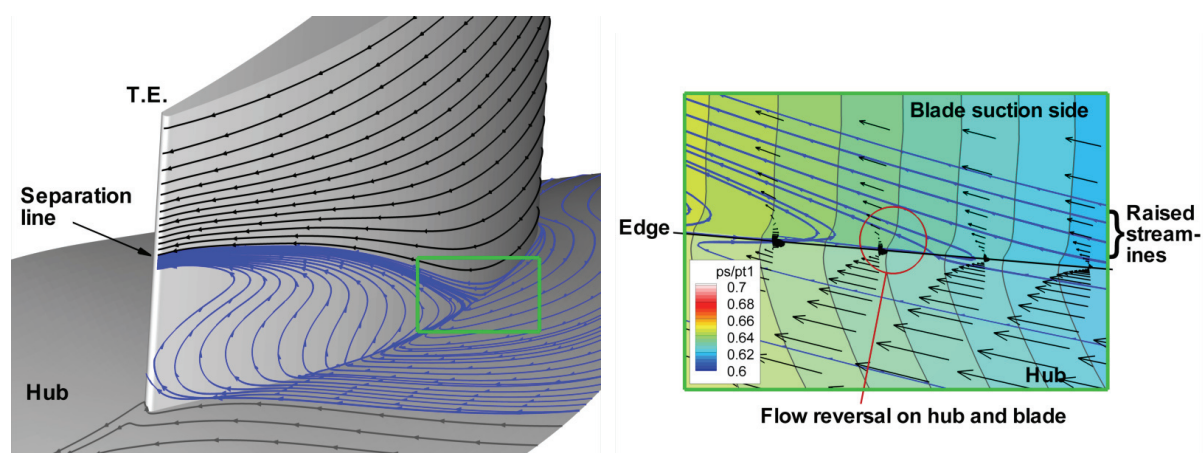
Figure 11-17. On the left: skin friction lines at the corner separation. On the right: detail view at the separation onset showing skin friction lines (blue), velocity vectors close to the surface (black) and static pressure contours on the wall. Both plots are based on the CFD results.

The plot of skin friction lines presented in Figure 11-17 illustrates the outline of the separation based on the simulation results. It appears plausible compared to the observations of corner separations mentioned in section 4.2.2: close behind the leading edge, hub boundary layer flow is carried by the secondary motion along the hub towards the corner between hub and suction side. As shown in the enlargement in Figure 11-17, the fluid reaching the corner has a forward momentum that is so low - due to the wall friction and the deceleration by the adverse pressure gradient - that it eventually stops. The adverse pressure gradient then starts a reversed motion. The reversed flow region grows forming a separation bubble. On the left hand side in Figure 11-17, it can be noted that skin friction lines converge forming a separation line where the flow separates away from the suction side.

The separated region is continuously fed with the hub boundary layer advected by the cross flow. This flow has very low momentum and almost stagnates within the separation. As indicated by the skin friction lines in Figure 11-17 and by the streamline plot in Figure 11-19, the incoming flow is eventually raised up within the separated region. Friction with the main flow entrains some particles out of the separated region and then out of the blade channel.
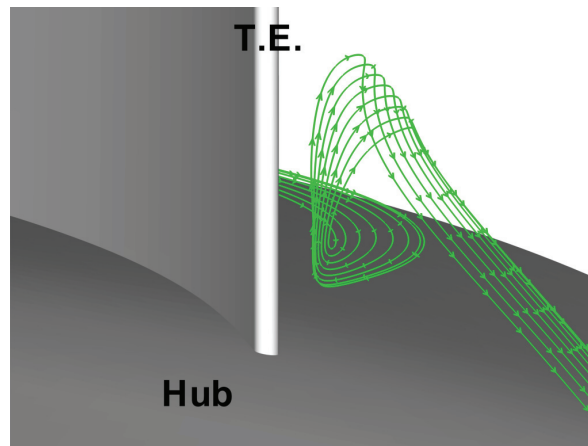
Figure 11-18. View from downstream based on CFD results: streamlines reaching the separated region along the hub, being raised and redirected downstream within the separation.

As can furthermore be noted within the separated region plotted on the left of Figure 11-17, even close to the trailing edge the skin friction line direction is reversed compared to the main flow direction. This indicates that some fluid is attracted from downstream into the separated region by the lower static pressure level in the separation. The static pressure level in the separation is only slightly higher than the pressure level at the separation onset. It does not grow towards the trailing edge, thus it tends to be lower than the pressure level occurring after the trailing edge. This makes flow with moderate momentum from the pressure side boundary layer turn around the trailing edge and then flow in reversed direction within the suction side separation. Eventually it turns forward again, absorbing further momentum from the flow around it and quits the separation at some distance from the suction side.

The stagnating flow of the separated region constitutes an aerodynamic blockage for the main flow. As already shown by the black skin friction lines in Figure 11-17, the suction side streamlines above the separation line are compressed together to pass the separation. This counteracts the diffusion and pressure rise in the blade channel. The plot to the left in Figure 11-19 shows how streamlines that flow close to the suction side at inlet are raised above the separation. The plot to the right in Figure 11-19 shows how streamlines that are located close to the hub at inlet but at some more distance from the suction side, bend away from the suction side to get around the separated region. The latter indicates how the separation counteracts the deflection of the flow. Both contour plots in Figure 11-19 indicate that the stagnating flow accumulated within the separation is characterized by a very low total pressure level.
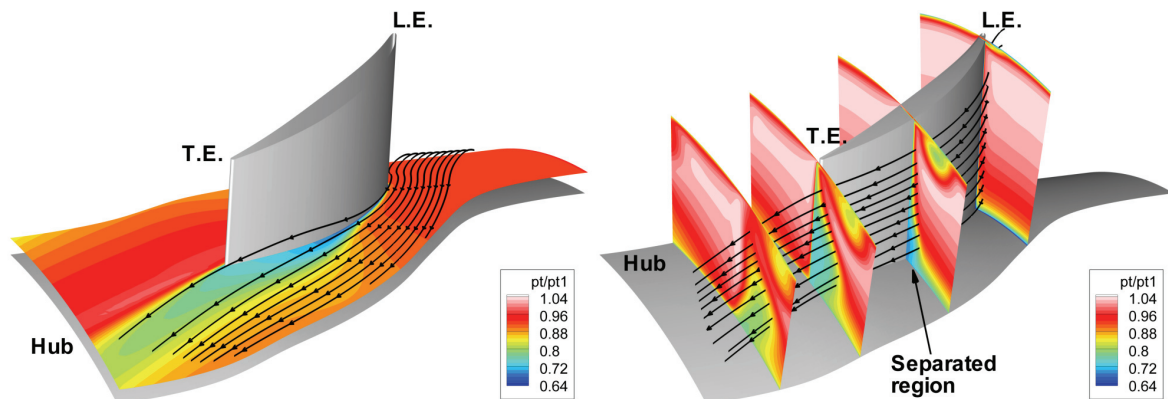
Figure 11-19. CFD results illustrating the deflection of streamlines passing close to the separated region and showing the distribution of the total pressures in the concerned regions.

Figure 11-20 illustrates that significant amounts of boundary layer coming especially from the suction side is raised above the separation. The boundary layer is there distinguished as region of high vorticity. The red vorticity lines indicate the general orientation of the vorticity that is normal to the flow direction in the boundary layers. Close to the separation, the vorticity lines are bent around the separation, also testifying how the boundary layer is raised above the separation. The shear with the stagnating and reversed flow in the separation yields an entrainment of particles from within the separation as indicated by the streamline plot in Figure 11-18,
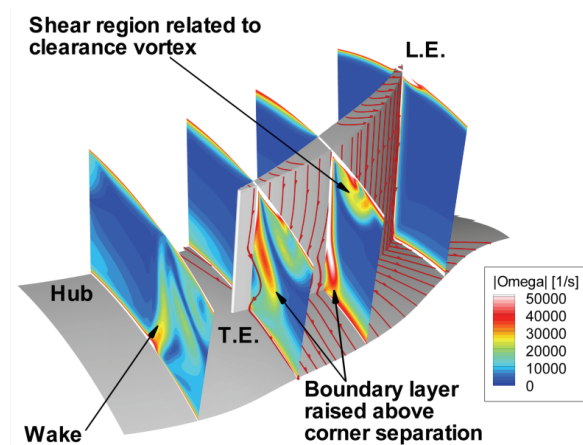
Figure 11-20. Distributions of vorticity magnitude based on the CFD results indicating how suction side boundary layer is raised above the separated region. This is also reflected by the vorticity lines (red).

After the trailing edge, the streamlines from both pressure side and suction side converge, increasingly enclosing and hence terminating the separated region. The flow that passed directly above the separation consists mainly of raised boundary layer and of some entrained flow from within the separation. It has low momentum and hence reduced total pressure. This flow with relatively low momentum is pressed towards the hub by the pressure gradients that occur past the trailing edge. On both sides it is bordered by the main flow. This concentration constitutes the low momentum and low total pressure region detected in the outlet plane measurements. It can be concluded that the intensity of this trace not only depends on the size of the separation: it also depends on the quantity of low momentum flow present before the separation either within the suction side boundary layer that is raised above the separation or in the hub boundary layer, which is advected across the passage by the secondary motion and raised within the

separation. The intensity of the trace fades further downstream as energy from the main flow diffuses in, further reducing the total pressure of the main flow.

Summarizing, it is noted that the separation yields first of all a trace of low total pressure in the outlet plane caused by the shear within the separation where reversed flow might occur and the shear with the main flow at its border. Stratford notes in [Stratford 1973] that in a real compressor, the relative movement of the downstream blade row largely converts the loss of total pressure […] into an increase of incidence. The low total pressure concentration is thus detrimental for the stage matching. Furthermore, it was observed here that the separation pushes low total pressure flow of the suction side boundary layer into the blade channel, causing further loss. The separation constitutes a significant aerodynamic blockage that reduces the pressure recovery within the blade channel. The pressure rise by diffusion is delayed past the separation. Furthermore, the separation prevents the main flow from following the suction side of the blade over a large span. This affects the deflection: first, the flow pushed away from the suction side quits the blade channel underturned. Second, immediately behind the trailing edge, the flow from the pressure side is attracted and bent towards the low pressure of the separated region on the suction side losing some of the deflection achieved by the pressure side. The resulting flow is highly three-dimensional and far from the design conditions.

Hub passage vortex

The helicity plot based on the measurements presented in Figure 11-12 shows a region of negative helicity close to the hub. It goes with increased secondary velocity oriented from the pressure side, across the passage, towards the suction side along the hub and subsists past the cascade. This will be further investigated based on the secondary velocity plot in Figure 11-26. It coincides with the region with remarkably low flow angles close to the hub indicating a significant overturning. These observations indicate the secondary flow motion of boundary layer fluid on the hub that crosses the passage from the pressure side towards the suction side and subsists past the cascade. This cross channel motion is called the hub passage vortex as described in section 4.2.1. It is caused by the influence of the circumferential pressure gradient on the hub boundary layer: the circumferential pressure gradient in the blade channel adjusts itself to produce the deflection of the main flow by counteracting its centrifugal force. This pressure gradient subsists in the boundary layer where the slower particles have far less centrifugal force and are hence pushed by the gradient towards the suction side. As noted in section 4.2.1, the intensity of the hub passage vortex is related to the size of the hub boundary layer and the amount of the deflection by the blade passage. In the present case the significant intensity indicates that a thick hub boundary layer was already present at inlet. Beyond this the significant passage vortex intensity reflects that a certain level of streamwise vorticity hence helicity with negative sign was already present at inlet and was conserved through the cascade.

The increased deflection in the hub passage vortex is advantageous for the overall deflection level. However it also indicates that a significant cross passage motion must exist, that feeds the separated region with low momentum fluid. The overturning also indicates a deviation from homogeneous design conditions which can impact the matching with later compressor stages.

Clearance vortex

A spot of high helicity with negative sign can be noted close to the casing in the helicity plot in Figure 11-12. This indicates a clearance vortex induced by the clearance flow. The semi-circular form of the spot as well as the nature of the phenomenon as described in section 4.3 suggests that the main part of the clearance vortex is located outside the measurement region, right above the visible spot. It is not uncommon for this kind of vortex to extend and persist far past the trailing edge. The related mechanisms are analyzed with the support of the numerical hereafter.
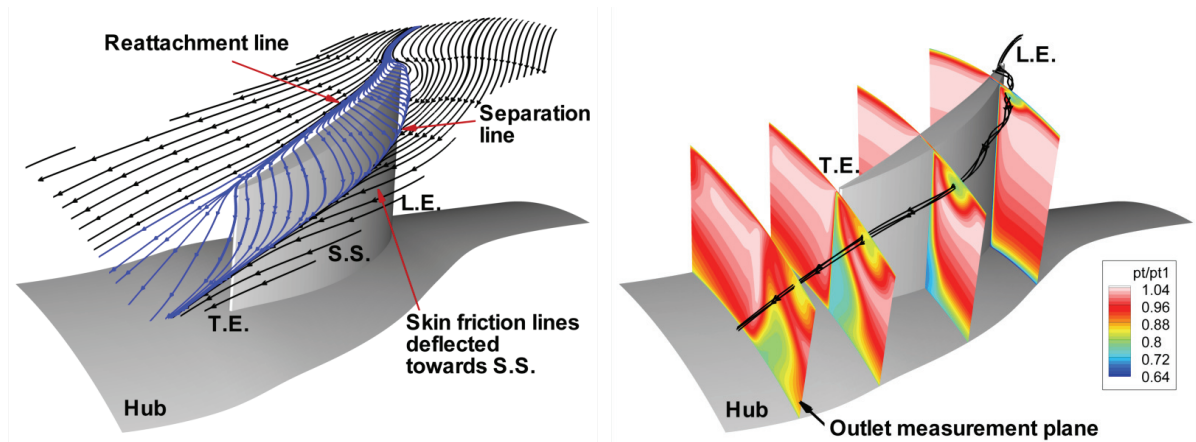
Figure 11-21. On the left: skin friction lines at the casing. On the right: some streamlines involved in the clearance vortex indicate where the clearance vortex crosses the plotted total pressure distributions. Both plots are based on the CFD results.

The plot of skin friction lines on the casing on the left of Figure 11-21 illustrates the macroscopic development of the flow related to the clearance vortex. A reattachment line and a separation line are identified. The lines in between are coloured blue. The clearance flow is pushed through the clearance by the pressure difference from the pressure side towards the suction side. However, the clearance flow is so important that the casing boundary layer next to the clearance is not sufficient to feed it. Hence most of the clearance flow comes from lower spanwise positions on the pressure side. The flow is aspirated from lower spanwise positions, then reaches the casing at the indicated reattachment line and crosses the clearance forming the clearance jets on the opposite side. These are denoted by parallel skin friction lines directed away from the suction side. It can be noted that all the streamlines that apparently share the reattachment line for some distance are actually coming from lower spanwise positions.

The clearance jets cross the clearance gap flowing with a certain velocity away from the suction side. As a consequence they also entrain some low momentum flow from the suction side boundary layer away from the neighbouring suction side. At some distance, the jets slow down their motion away from the suction side due to the adverse circumferential pressure gradient. Different effects then induce that the clearance flow separates along the indicated separation line on the casing and move away from the casing, reorienting towards the suction side. The circumferential pressure gradient prevents that the flow from moving further away from the suction side and pushes the flow back to it instead at lower span. Since the jets closer to the suction side entrain some particles, some of the separated flow is attracted back towards the casing, completing the circular motion of the clearance vortex. The velocity gradients involved in this motion reflect the stretching and transport of the vorticity formed in the boundary layers of the blade tip, the blade suction side and the casing carried in the clearance flow. Hence the involved vorticity is actually formed by the wall friction but reoriented and amplified by the clearance flow separation concentrating it in the clearance vortex. The main flow entrains this flow downstream, producing a spiralling motion with vorticity of sign opposed to that of the passage vortex. Further downstream the vortex is continuously fed by the repeating of these mechanisms by the following clearance jets.

The clearance vortex starts close to the leading edge where some flow first crosses the clearance. However, the equilibrium between the momentum of the clearance jets and the circumferential pressure gradient causes that the clearance vortex does not stick to the suction side but has increasing distance from it further downstream: the plot on the right of Figure 11-21 shows some streamlines within the clearance vortex. It can be noted that the clearance vortex position is located close below the separation line observed earlier but always closer to the suction side than the separation line.

The clearance vortex accumulates low energy flow from the neighbouring boundary layers and the regions of increased shear caused by it. As a consequence the region close to the clearance vortex is denoted by a particularly low level of total pressure as shown by the total pressure distributions in different axial planes also presented in the plot on the right of Figure 11-21.

The influence of the clearance vortex is manifold: the clearance vortex can have a remarkable size. The high vorticity, the relevant velocity and the low static pressure within the clearance vortex render it very stable. Hence it persists far past the trailing edge. As a consequence, the clearance vortex constitutes a significant aerodynamic blockage within and also past the blade channel, which reduces the effective flow area and hence the static pressure rise by diffusion. The low static pressure in the core of the clearance vortex makes the affected region accumulate low total pressure and low momentum fluid from the adjacent boundary layers. Nevertheless, the velocity in the clearance vortex is relatively high hence its mass flow is significant. For this reason, the properties of the clearance vortex can have a significant detrimental impact in the mass flow weighted averages of e.g. the total pressure and the flow angles. This regards the average level of total pressure as well as the flow orientation that is distorted by the clearance vortex: underturning is found in the half close to the casing and overturning in the half further away from the casing.

Casing passage vortex

In analogy to the hub passage vortex, a passage vortex close to the casing must be expected since the casing boundary layer is also deflected. As described in section 4.2.1, also in the casing passage vortex the flow is overturned heading from regions close to the pressure side towards the suction side along the casing. The orientation of the casing passage vortex is hence always reversed to the orientation of the hub passage vortex. This is also coherent with the fact that it is induced by the casing boundary layer at inlet which has a vorticity that is reversed compared to that of the boundary layer at hub. Consequently, the casing passage vortex in the present case manifests as region of helicity with positive sign.

In Figure 11-12, some moderate traces of helicity with positive sign are visible in the measurement region close to the casing. However this also indicates that the casing passage vortex is in large part outside the measurement region. Hence no evident underturning marked by low flow angles is visible in the corresponding region of Figure 11-11. The region of helicity with positive sign is interrupted by what is identified as the clearance vortex with its opposed vorticity orientation. Other measurement cases that capture larger parts of these features will give more insight on their interaction. Especially the LDA measurements for cases with lower inlet Mach number presented later on will confirm the described feature. In the present case where only a small part is detected, the secondary velocity plots appear dominated by other features in the detected region.

Casing passage vortex and casing boundary layer

As illustrated by the streamlines plot in Figure 11-23, the initially parallel lines of the incoming casing boundary layer are increasingly deflected towards the suction side. This reflects the secondary motion constituting the casing passage vortex that makes the casing boundary layer overturn and flow across the passage towards the suction side.
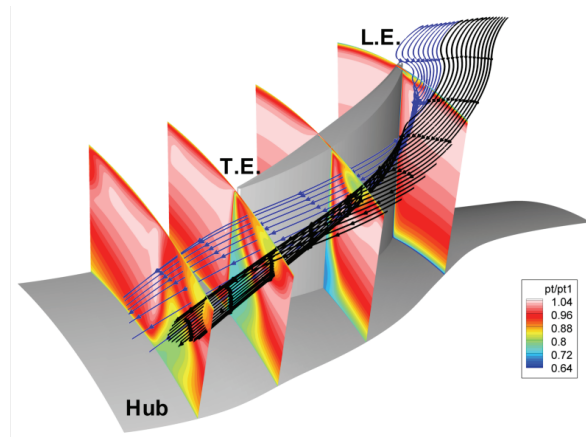
Figure 11-22. Streamlines in the casing boundary layer: streamlines close to the suction side (blue) get across the clearance vortex. More distant streamlines (black) reach the clearance vortex after it is grown such that they cannot cross it within the computational domain. The plot is based on the CFD results.

The motion of the casing boundary layer towards the suction side is perturbed by the clearance flow, such that the casing boundary layer separates too, on the opposite side of the separation line. As a result, flow from both sides converges towards the separation line and separates from the casing along a separation surface. In a similar mechanism as that illustrated by [Crabtree 1963] presented in Figure 4-3, considerable quantities of casing boundary layer are pushed towards lower span. This flow is furthermore affected by the streamwise vorticity of both the casing passage vortex and the clearance vortex. Figure 11-22 shows streamlines of the incoming casing boundary layer that are involved in the separation. After the separation, the streamlines plotted in blue eventually deflect towards the suction side. The streamlines plotted in black are more distant from the suction side in the beginning and reach the separation surface only when the clearance vortex has already grown to a considerable size. Hence they remain constrained to that side of the vortex until past the channel outlet. Together, these streamlines indicate the shape of the separation surface. As indicated by the total pressure distributions which are also plotted in Figure 11-22, the casing boundary layer accumulates in the region around the clearance vortex widening the region with low total pressure. Under the line, the intensification of the low total pressure accumulation close to the clearance vortex can hence be directly related to the advection of casing boundary layer by the casing passage vortex.

Filament of condensed water between clearance jets and casing passage vortex

The high acceleration of the flow within the clearance yields almost a step change in static temperature towards lower values. Such step change makes the humid flow saturate and condensation occurs. Coalescing droplets form water drops that persist even when the flow temperature increases again. In certain test cases performed on days with high levels of atmospheric humidity, a small filament formed by such drops could be observed through the optical access to climb along the casing wall, as shown in Figure 11-23. The filament location is emphasized by green dots. The gravity pointing in upstream direction (marked red) counteracts the drag of the flow that would else rapidly entrain the water downstream. The droplets are carried away from the suction side by the clearance jets (marked cyan) before the clearance flow separates from the casing to form the clearance vortex. The gravity also drags the droplets away from the suction side. In contrast, the secondary flow of the casing vortex (marked orange) drags the filament towards the suction side. Hence the filament must adjust at a circumferential position where the secondary flow equilibrates both gravity and clearance jets drag. It is very probable that this must be somewhere at moderate distance from where the clearance jets separate, thus indicating

the shape of the separation line. The filament position is very stable for a given flow condition. This could be observed by its interference with the LDA measurements that occurred always at the same location.
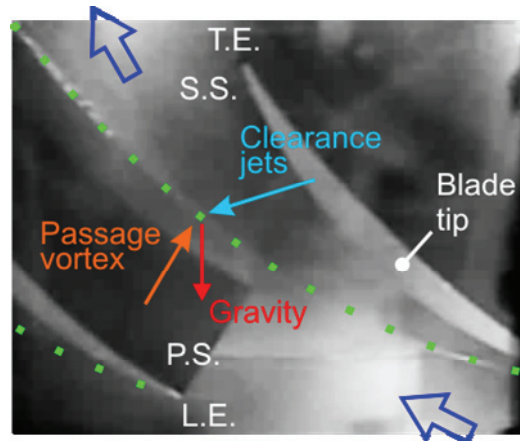
Figure 11-23. Picture of the filament of condensed water (marked green). The direction of the gravity force acting on the filament as well as the drag force from passage vortex and clearance jets are also indicated.

Region of high helicity with positive sign

A large region of high helicity with positive sign can be noted at about mid span in Figure 11-12. Since this feature is not commonly documented, it deserves a more detailed analysis. Interestingly, it is predicted with very good agreement by the numerical results as can be noted in the comparison in Figure 11-15. Comparison of the increasing occurrence of regions of positive helicity in planes approaching the outlet measurement plane as plotted in Figure 11-24 give first indications on its origins. Its origin is explained by the following mechanisms:

1) Suction side boundary layer raised by the separation

The plot to the right of Figure 11-24 shows the vorticity magnitude distribution in different planes. In addition, in-plane vorticity lines are plotted, to indicate the orientation of the vorticity at each point. These lines are parallel to the in-plane vorticity components at each point. Thus, the axial component is not considered since it is not relevant for the present observation.

As can be noted considering the second and third plane, the suction side boundary layer denoted by high magnitude of vorticity is raised away from the suction side to pass above the separated region. As indicated by the vorticity lines on the third plane, this results in a vorticity orientation that is not longer parallel to the suction side. Instead, the vorticity in that region is inclined, pointing towards the corner between hub and pressure side of the opposite blade. As can be seen on the fourth plane, this vorticity orientation is still conserved in the outlet measurement plane and the vorticity magnitude is still higher than in the adjacent regions. Since the main flow past the trailing edge has a significant circumferential component, its orientation is close to the vorticity orientation in the measurement plane that was caused by the raised boundary layer. This is quantified by the plot to the left of Figure 11-25 showing the angle between vorticity direction and flow direction: it approaches zero in the considered region. Streamwise aligned vorticity and high levels of both vorticity and velocity result in the high helicity levels with positive sign in the observed region. The trace hence reflects the quantity of boundary layer raised away from the suction side affecting a significant mass flow.

2) Pressure gradient past the trailing edge

The production of helicity in streamwise direction is given by the transport equation introduced earlier in section 3.2 :

$$\rho\frac{DH}{Dt} = -2\vec{\Omega}\cdot\nabla p + \mu\,\vec{\Omega}\cdot\Delta\vec{V} - \rho\,\vec{\Omega}\cdot\frac{\partial\vec{V}}{\partial t} + \mu\,\Delta H \qquad (11.6)$$

$$(1) \qquad (2) \qquad (3) \qquad (4) \qquad (5)$$

An important term of production of positive or negative helicity is term (2) related to the coincidence of existing vorticity with the gradient of static pressure. Considering the static pressure distribution in the third plane of the static pressure plot in Figure 11-25, a strong gradient can be noted right past the trailing edge as indicated by the arrow. The gradient is due on the one hand to the high pressure occurring on the pressure side close to the casing, which is natural. On the other hand it is due to the particularly low pressure occurring on the suction side close to the hub, which is caused by the separated region. Herewith the static pressure gradient is almost antiparallel to the orientation of the vorticity in the corresponding region of Figure 11-24. This yields an important magnitude of term (2) which means that that region is prone to high helicity production. In other terms: the pressure gradient induces a progressive inwards deflection of the flow. That flow is rich in vorticity from the raised boundary layer. As a consequence the direction of the flow increasingly coincides with the direction of the vorticity yielding increased values of helicity in the outlet measurement plane.

3) Casing passage vortex pushed inwards by clearance vortex

In the helicity plot in Figure 11-24, it can be noted that a certain amount of helicity with positive sign is related to the casing passage vortex. In fact, as noted earlier with respect to Figure 11-22, a certain amount of flow coming from the passage vortex separates from the casing and is pushed to lower spanwise positions by the clearance vortex. Its helicity with positive sign is conserved and adds into the region of raised boundary layer analysed here.

Summarizing, a significant amount of suction side boundary layer is pushed towards the main flow by the separation. The high values of helicity quantify this. This flow is not detected by outstandingly reduced values of momentum or total pressure since shearing diffusion makes it mix out with the main flow. Nevertheless, the mixing increases the overall loss level. The helicity thus constitutes an indicator to indirectly measure this particular mechanism not visible in other plots. It can thus be observed how it is influenced by the aspiration.

Besides the reduced momentum and total pressure, the subsisting helicity denotes a region with inhomogeneous flow orientation caused by the described mechanisms. Beyond affecting the stage matching due to deviation from design conditions, further diffusion by mixing out of the velocity and orientation heterogeneity will cause loss production further on. It is thus of interest to control this effect.
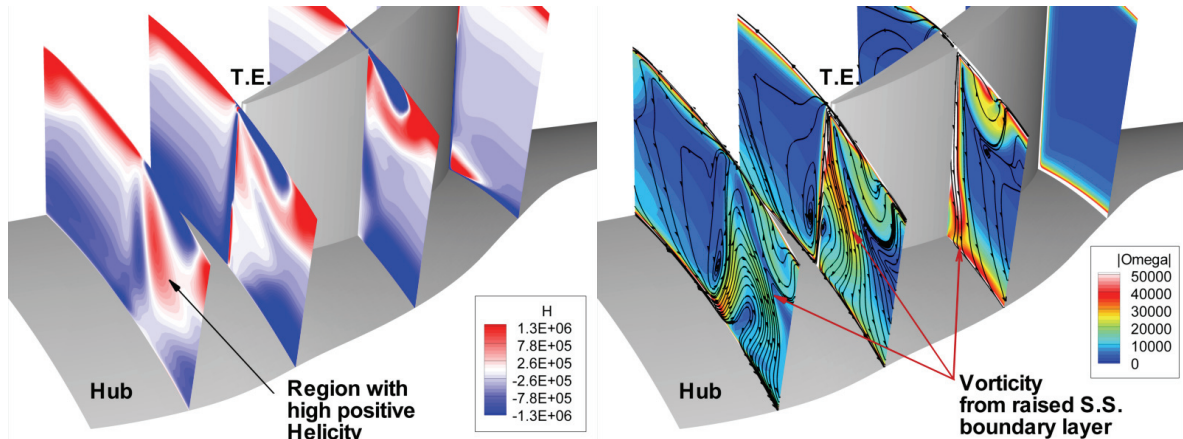
Figure 11-24. On the left: helicity distribution (CFD) in the outlet plane and some preceding planes. On the right: magnitude of vorticity (CFD) and in-plane vorticity lines (axial component neglected) on the same planes.
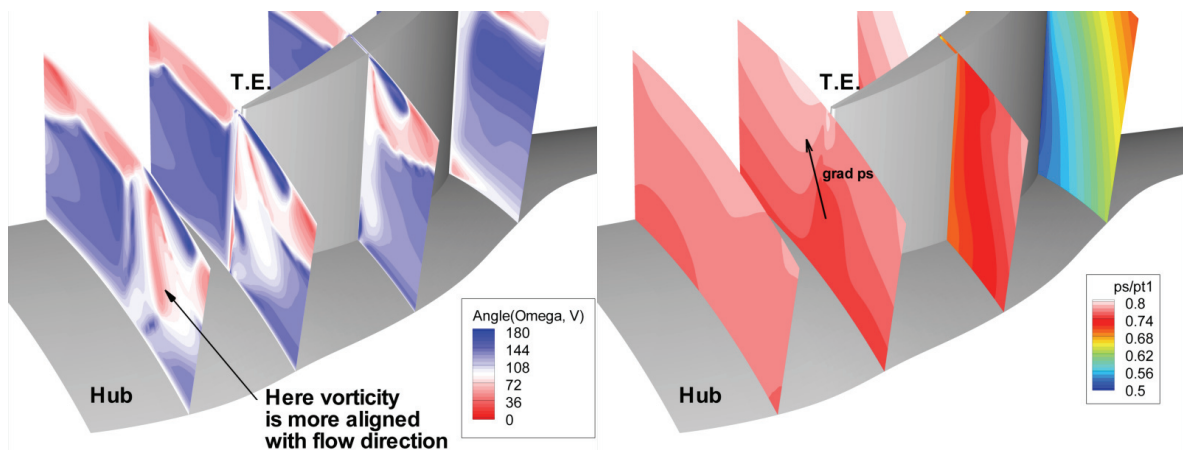
Figure 11-25. On the left: angle between the vorticity and velocity vectors in the outlet plane (CFD) and some preceding planes. On the right: static pressure distribution (CFD) in the same planes.

Secondary motion analysis based on the experimental results

The secondary velocity plot presented in Figure 11-26 gives a cumulative summary of the deviating motions induced by secondary flow. As defined, secondary motion is streamwise vorticity caused by the deflection and amplification of existing vorticity as found e.g. in the boundary layers. The secondary velocities are the resulting velocity components superposed to the main flow causing inhomogeneous flow orientation and flow velocities. Identifying the traces produced by the described features in the secondary velocity plot allows observing and quantifying how the intensity and structure of these features change when applying aspiration to the cascade or when changing the inlet flow conditions.

126
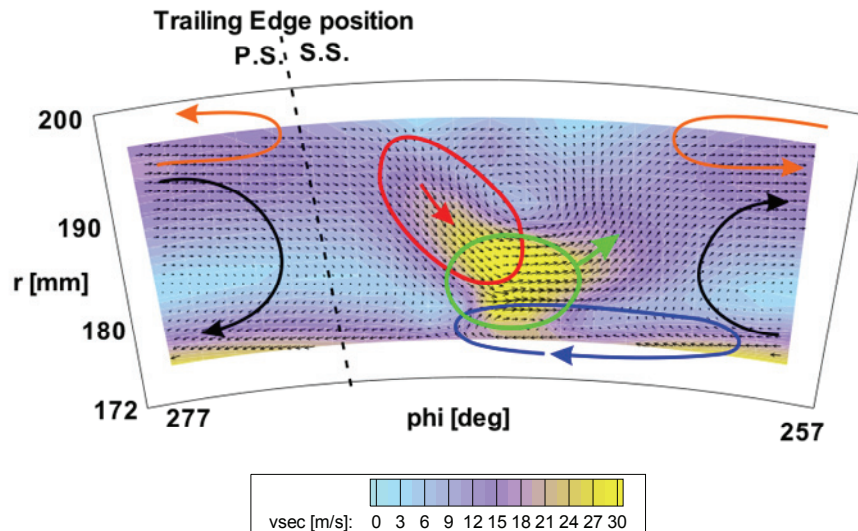
Figure 11-26. Secondary velocity plot based on the outlet plane measurement results of the reference case based on experimental results.

First, indicated by the red circle a significant motion inwards and heading away from the suction side as indicated by the red arrow can be noted. This secondary motion coincides with the region with high helicity with positive sign. As noted earlier, it is hence induced by the suction side boundary layer that was raised away from the suction side by the separation. This flow has a momentum deficit compared to the main flow and thus is pushed towards the hub by the radial pressure gradient.

The blue arrow denotes the secondary motion of the hub passage vortex, advecting flow to the suction side along the hub. Its motion reverses where this flow met the suction side, hence close to the wake in the outlet plane. In the green circle, the secondary motion of the hub passage vortex coincides with the motion away from the separation of the flow marked by the red circle. This yields a region of particularly high secondary velocity oriented away from the separation as indicated by the green arrow. This causes a region of significant underturning, hence high flow angles, in the outlet plane.

Close to the casing, the orange arrows indicate the secondary motion of the casing passage vortex, of which only the bottom half is visible in the measurement region as reflected by the secondary velocity vectors.

The black arrow indicates the more macroscopic motion induced by the streamwise vorticity present already at the inlet of the cascade. It was denoted by a diffuse helicity with negative sign showing a skewed inlet flow. It is conserved through the blade passage and is still superposed with variable intensity to the main flow.

Following can be retained: first, the secondary flow structure reflects the flow mechanisms occurred within the blade passage. Second, it indicates deviations from undisturbed, irrotational and rather ideal flow as is also reflected by the flow angle distributions departing from ideal design conditions. The velocity of this deviation locally reaches up to 33 m/s, thus 17% of the average outlet flow velocity magnitude, which is significant. The involved energy is thus not converted to pressure rise by the cascade but to deviating motion. The secondary motion furthermore indicates regions prone to shear and mixing out and hence production of loss further on. Thus the secondary velocity plot derived from the measurement data by the method described earlier on yields a summary of the flow mechanisms analyzed in this section.

High flow angle region

A region with high flow angles hence significant underturning can be seen in Figure 11-11 at mid span. It is far more pronounced in the measurements than in the numerical simulations. After the preceding evaluations it can be ascribed to the coincidence of at least two mechanisms: first, the flow deflection past the trailing edge towards the low pressure region caused by the separation noted when analyzing the wake trace; second, the streamwise vorticity of the boundary layer raised away from the suction side coinciding with that of the hub passage vortex. It is thus partially caused by the separation. All together this is reflected by high components of secondary velocity pointing away from the suction side presented earlier in Figure 11-26.

The inhomogeneous flow orientation at outlet is detrimental for the matching in later stages. It furthermore indicates underturning and hence reduced diffusion and static pressure rise.

12. Influence of aspiration

The influence of aspiration on cases with different inlet flow incidence and blade pitch (i.e. different number of blades) is evaluated by analyzing experimental results and numerical results.

12.1 Verification of the experimental results for aspirated cases

12.1.1 Comparability of the inlet flow conditions

The average properties listed in Table 12-1 and Table 12-2 quantify the comparability of cases with different aspiration configurations. The achieved agreement is good: the average inlet Mach number is 0.792 ± 0.01 and the average flow angle is $62.7°\pm0.5°$ for the cases with 3° incidence and $65.0°\pm0.4°$ for the cases with 5° incidence. This is sufficient to distinguish the influence of the aspiration configuration from the variation of inlet conditions. The absolute values of the total pressure at inlet vary since they adjust themselves to the daily atmospheric pressure and the static pressure rise achieved by the cascade. In the following, absolute pressure results are thus non-dimensionalized dividing them by the average total pressure at inlet to compensate these effects.

$i = 3°$	Aspi. Hub	Aspi. Blade	Pitch	$\overline{Ma_1}$	$\overline{\alpha}_1$	$\hat{p}_{t1}$ [Pa]
A1	no	no	20°	0.797	62.23°	$1.123\cdot10^5$
B1	2 %	no	20°	0.795	62.58°	$1.109\cdot10^5$
B2	4 %	no	20°	0.791	62.59°	$1.103\cdot10^5$
C1	2 %	0.8 %	20°	0.791	62.75°	$1.093\cdot10^5$
C2	2 %	1.5 %	20°	0.795	62.87°	$1.084\cdot10^5$
D1	2 %	0.8 %	26°	0.784	62.98°	$1.097\cdot10^5$
D2	2 %	1.5 %	26°	0.784	62.86°	$1.091\cdot10^5$

Table 12-1. Average inlet flow properties for the cases with 3° incidence.

$i = 5°$	Aspi. Hub	Aspi. Blade	Pitch	$\overline{Ma_1}$	$\overline{\alpha}_1$	$\hat{p}_{t1}$ [Pa]
A1	no	no	20°	0.792	64.75°	$1.114\cdot10^5$
B1	2 %	no	20°	0.792	64.84°	$1.108\cdot10^5$
B2	4 %	no	20°	0.802	65.01°	$1.100\cdot10^5$
C1	2 %	0.8 %	20°	0.795	65.00°	$1.091\cdot10^5$
C2	2 %	1.5 %	20°	0.796	64.80°	$1.084\cdot10^5$
D1	2 %	0.8 %	26°	0.785	65.40°	$1.104\cdot10^5$
D2	2 %	1.5 %	26°	0.788	65.40°	$1.101\cdot10^5$

Table 12-2. Average inlet flow properties for the cases with 5° incidence.

12.1.2 Comparison of LDA and probe measurement results

As illustrated by the comparison of outlet Mach number, outlet flow angle and outlet plane helicity in Figure 12-1 to Figure 12-3, the agreement between LDA and probe measurements is relatively good. Nevertheless, three particular differences can be noted: first, the hub separation trace in the Mach number distribution in Figure 12-1 has slightly smaller extents in the LDA measurements than in the probe measurements. Second, the increased flow angles in the corresponding region in Figure 12-2 are less pronounced in the LDA results than in the probe measurements. This reflects also in a smaller region of high helicity with positive sign for the LDA measurements in Figure 12-3. Third, a region of underturning close to the casing, denoted by high flow angles is detected by the LDA measurements in Figure 12-2. This causes a region of important helicity of negative sign in Figure 12-3.

The reduced separation trace size and the reduced flow angle intensities can be ascribed either to effects related to the measurement technique differences or to real differences in the flow. The first argument is supported by the fact that the concerned region close to the wake is affected by significant gradients and may be affected by unsteadiness as vortex shedding from the trailing edge. As mentioned in the introduction, strong gradients can slightly reduce the measurement accuracy of the probe. Unsteadiness would affect the two measurements differently because the probe measurement would average a pressure effect thus related to ρV^2 and the LDA would average an effect of the momentum thus related to ρV. The significant level of fluctuations in the same region indicated by Figure 12-4 suggests that this effect could indeed affect the results. The second argument, which ascribes the differences to real differences in the flow, can also not be completely excluded, since as shown in Figure 7-2, the outlet plane measurements with probe and LDA were performed on two different sides of the wind tunnel. As noted in section 8.1, small differences in the axisymmetry of the inlet flow cannot be excluded. Since in the present test case, small changes in the inlet flow conditions can trigger the separation onset position, it would be possible that the cascade was less loaded on the side where the LDA measurement took place. This could yield a smaller separation. This tells that case to case comparisons should be performed comparing results produced with the same measurement technique. In the following, comparisons intended to evaluate the aspiration performance will thus mainly compare the outlet measurements performed with the aerodynamic probe.

Similar considerations can be made on the third noted difference: the region of underturning and high helicity with negative sign noted close to the casing in the LDA measurements compared to the probe measurements. Here, the larger size of the LDA measurement plays a role: part of this effect is actually visible at the border close to casing of the probe measurements and it is ascribed to the clearance flow. However, in the LDA results, this effect reaches down to lower spanwise positions. Thus again, strong gradients as well as some unsteadiness which can be noted in Figure 12-4 can cause a certain divergence of the time-averaged result related to the measurement technique. Or differences that really occur in the flow can be the cause: small variations of the inlet flow angles could cause a higher loading at the casing that would yield a stronger clearance flow in the LDA measurement. Or the small wall shape difference caused by the optical access could influence the separation point of the clearance flow.

Summarizing, the similarity of the measurement results largely validates the reliability of both measurement techniques and the wind tunnel flow. However, certain differences are observed. They are ascribed to either local unsteadiness of the flow or the different sensitivities of the techniques to certain flow features as strong gradients or unsteadiness. Or, in the flow at the two different measurement locations differences can be present. Thus, sensitive case to case comparisons should always be based the same measurement technique. Since LDA measurements with inlet Mach number 0.8 were performed only for case B2, the following comparisons will be based mainly on the probe measurements.

130
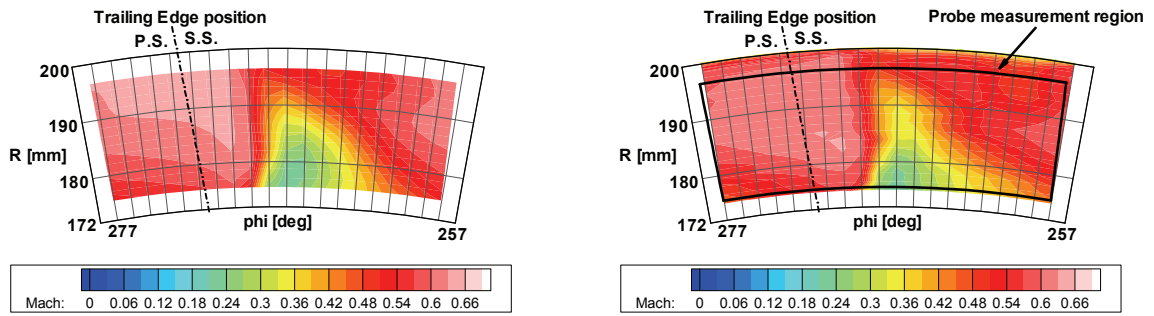
Figure 12-1. Comparison of outlet Mach number distributions (5-hole probe measurements to the left, LDA measurements to the right) for configuration B1 with 3° inlet flow incidence.
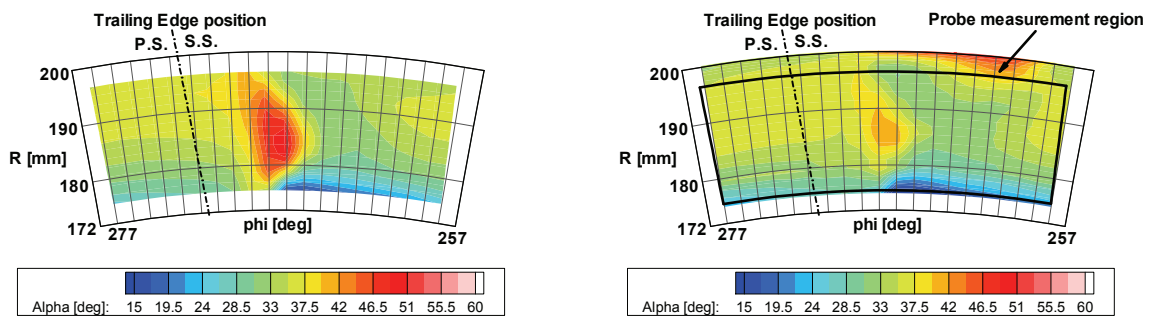
Figure 12-2. Comparison of outlet flow angle distributions (5-hole probe measurements to the left, LDA measurements to the right) for configuration B1 with 3° inlet flow incidence.
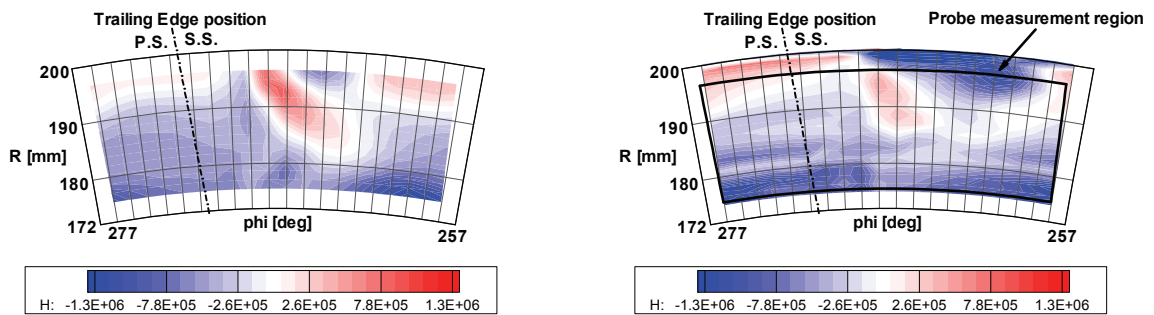
Figure 12-3. Comparison of outlet plane helicity distributions (5-hole probe measurements to the left, LDA measurements to the right) for configuration B1 with 3° inlet flow incidence.
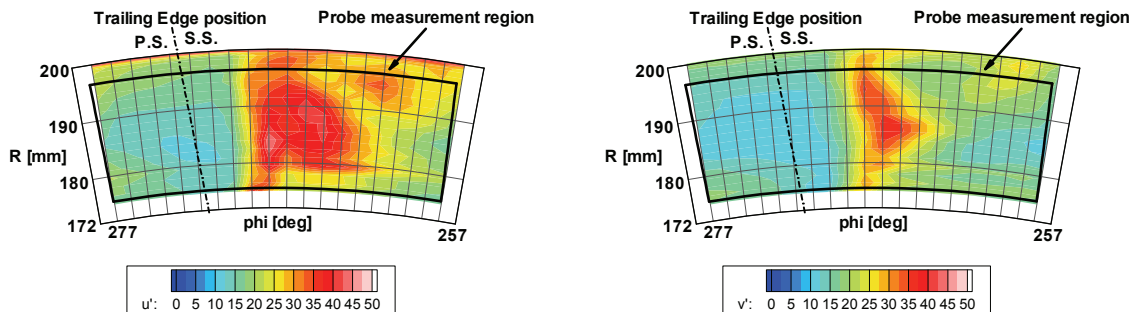
Figure 12-4. LDA measurements of the fluctuations (RMS) in streamwise (left) and normal (right) direction in the outlet plane for configuration B1 with 3° inlet flow incidence.

12.2 Analysis of the experimental results for aspirated cases

First, the needed depression levels applied to the aspiration chambers to achieve the required aspiration pressures are briefly discussed. The following sections then analyse the influence of aspiration by comparing the results of the blade pressure measurements, the outlet plane measurements and averaged performance parameters. The blade static pressure measurements are presented for all the cases in Figure 12-5 to Figure 12-7. The outlet plane measurements are presented as radial distributions for the cases with 3° incidence in Figure 12-9 to Figure 12-11 and as contour plots in Figure 12-12. Analogously the radial distributions for the cases with 5° incidence are presented as radial distributions in Figure 12-13 to Figure 12-15 and as contour plots in Figure 12-16. The average performance parameters are presented in Table 12-4 and Table 12-5. Chapter 12.3.1 will evaluate the representativeness of these averages despite of the limited measurement region. The following discussion guides the reader through the results.

12.2.1 Pressure levels in the aspiration chambers

Table 12-3 indicates the pressures applied to the aspiration chambers behind the hub aspiration ducts and the blade aspiration ducts respectively to achieve the required aspiration massflows.

Case	Incidence	Hub aspiration			Blade aspiration			Pitch
		C_Q	$C_{Q,Slot}$	$\dfrac{p_{s,chamber}}{\hat{p}_{tl}}$	C_Q	$C_{Q,Slot}$	$\dfrac{p_{s,chamber}}{\hat{p}_{tl}}$	
A1	+3° +5°	no	no	-	no	no	-	20°
B1	+3° +5°	2 %	0.11 %	0.63 0.65	no	no	-	20°
B2	+3° +5°	4 %	0.22 %	0.58 0.61	no	no	-	20°
C1	+3° +5°	2 %	0.11 %	0.61 0.64	0.8 %	0.04 %	0.66 0.66	20°
C2	+3° +5°	2 %	0.11 %	0.60 0.63	1.5 %	0.08 %	0.55 0.54	20°
D1	+3° +5°	2 %	0.14 %	0.58 0.60	0.8 %	0.05 %	0.63 0.63	26°
D2	+3° +5°	2 %	0.14 %	0.58 0.60	1.5 %	0.11 %	0.43 0.41	26°

Table 12-3. Pressures in the settling chambers to achieve the indicated aspiration massflows.

The resulting pressure levels presented in Table 12-3 indicate that to achieve the same overall aspiration rate in the 26° blade pitch cases as for the comparable 20° blade pitch cases, the chamber pressure must be further reduced. This reflects the increased effort needed to suck an increased mass flow through each slot in the cases with a reduced number of blades.

Furthermore it can be observed that the hub aspiration usually needs a slightly lower pressure to achieve the same aspiration mass flow for the cases with 3° incidence than for the cases with 5° incidence. For the blade pressures, the opposite occurs: a slightly higher pressure is sufficient to obtain the same aspiration mass flow for the cases with 3° incidence as for the cases with 5° incidence.

12.2.2 General observations

The blade loading is indicated by the difference between the pressures measured on the suction side and on the pressure side of the blades presented in Figure 12-5 to Figure 12-7. The static pressure taps in the presented measurements are located at mid span of the blades. Hence they are only indirectly influenced by the observed separation occurring close to the hub or the casing.

Since the blade passage tends to produce the same outlet flow angle α_2, increasing the inlet flow incidence by increasing the inlet flow angle α_1 increases the deflection $\Delta\alpha = \alpha_1 - \alpha_2$. This results in a higher blade loading in the cases with 5° incidence than in the cases with 3° incidence. This can be noted by the higher spread of the pressure curves close to the inlet for 5° incidence than for 3° incidence, e.g. in Figure 12-5. It is also reflected by generally higher average pressure rise p_2/p_1 for the 5° incidence cases listed in Table 12-5 than for the 3° incidence cases listed in Table 12-4.

In all cases in Figure 12-5 to Figure 12-7, the blade pressure on the pressure side close to the leading edge is already almost settled to the final pressure level at the first measurement location. Thus it does not change significantly between the first and the last measurement location. Only in cases without aspiration (black) the pressure side pressure level slightly decreases towards the outlet. This indicates that the aerodynamic blockage due to the observed separation actually yields an acceleration thus a reduction of static pressure in this case.

In the cases without aspiration (black curves in Figure 12-5 to Figure 12-7) an inflection of the pressure rise on the suction side can be seen. The inflection is annotated in Figure 12-5. In agreement with the preceding observations, this indicates that the pressure rise is limited due to the presence of a separation. In the 5° incidence cases, the inflection occurs earlier, which can be ascribed to the just described increased loading in cases with higher incidence. The higher loading increases the adverse pressure gradient and makes the separation onset start earlier, i.e. further upstream. If the pressure measurement was taken within the separation, the pressure would stop increasing after separation onset close to the inflection location. However, the measured blade pressure level keeps increasing, although less steep than before the inflection. This indicates that the mid-span pressure measurement location is outside of the separated region but is suffering indirectly of the reduced pressure rise due to the deteriorated diffusion. This reflects the three-dimensional nature of the flow with significant variation in radial direction. This agrees with the outlet flow field for the cases A1 without aspiration presented in Figure 12-12 and Figure 12-16: as analyzed earlier on, a large trace with low total pressure and high flow angles indicates the presence of a large separation that extends from the hub up to above mid-span, but with its maximum intensity below mid-span. The related significant non-uniformity of the outlet flow angle distribution reflects the three-dimensionality of the flow.

Incidence = 3°

Incidence = 5°
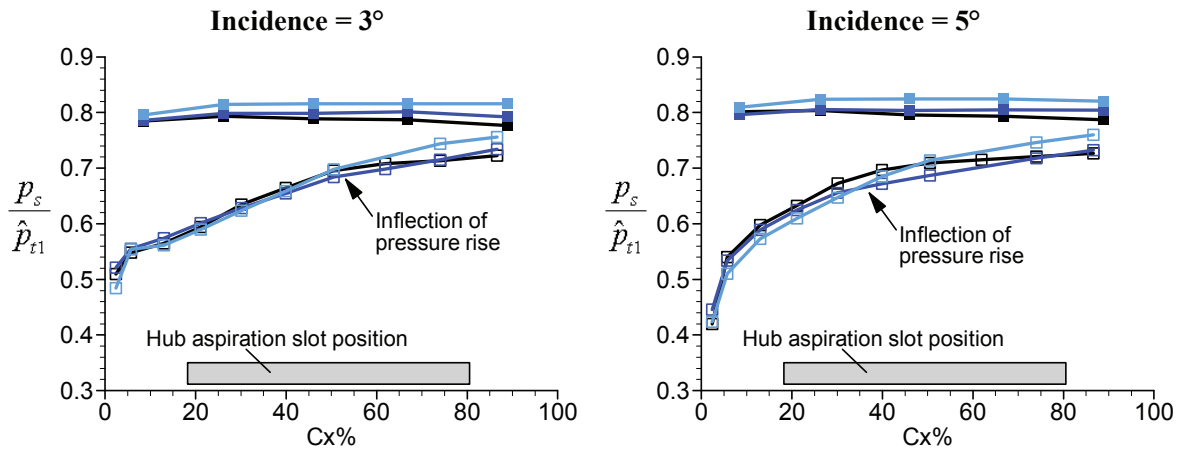
Figure 12-5. Mid-span blade pressures: influence of adding and varying aspiration on the hub.
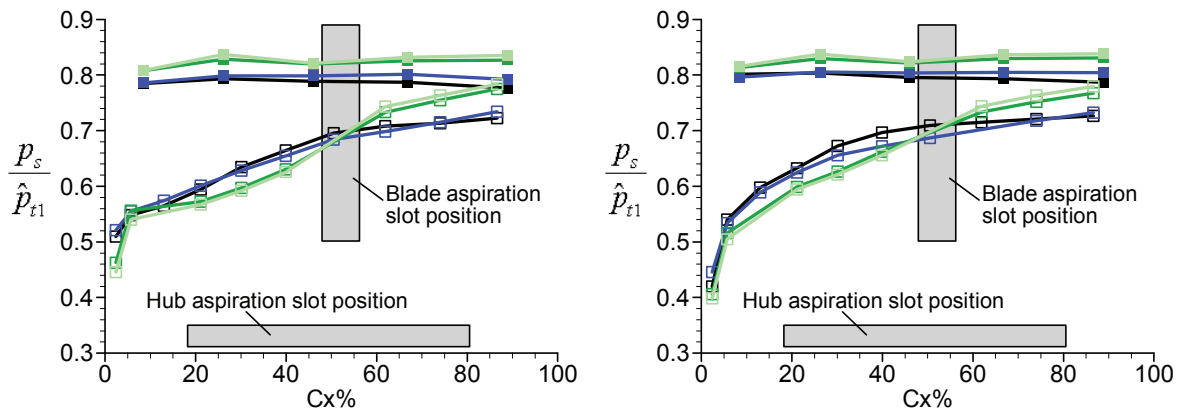
Figure 12-6. Mid-span blade pressures: influence of adding and varying the aspiration on the blades.
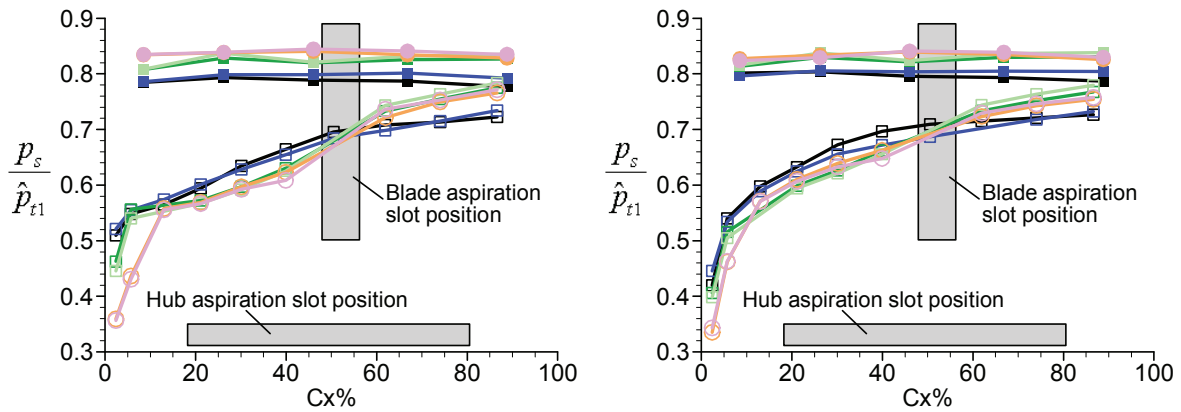
Figure 12-7. Mid-span blade pressures: influence of increasing the blade pitch and adding and varying the aspiration on the blades.

- A1 - 18 blades
- B1 - 18 blades - Hub: 2% asp.
- B2 - 18 blades - Hub: 4% asp.
- C1 - 18 blades - Hub: 2% asp. - Blades: 0.75% asp.
- C2 - 18 blades - Hub: 2% asp. - Blades: 1.5% asp.
- D1 - 14 blades - Hub: 2% asp. - Blades: 0.75% asp.
- D2 - 14 blades - Hub: 2% asp. - Blades: 1.5% asp.

12.2.3 Aspiration on the hub

As indicated by the blade pressures in Figure 12-5, increasing the aspiration on the hub to 2% (B1, blue curve) and then to 4% (B2, light blue curve) progressively smoothens the inflection in pressure rise compared to the reference case. This indicates a reduction of the separation size. This is confirmed for the cases B1 and B2 by the contour plots in Figure 12-12 and Figure 12-16, by the reduced size of the trace of low total pressures and high flow angles. As a result, the blade pressures of the cases with aspiration on the hub in Figure 12-5 reach a higher pressure level at outlet than the reference case. According to the discussions in section 2.3.2, this can be ascribed as well to an improved diffusion and deflection due to reduced separation size, as to the reduction of mass flow by the extraction. Thus the pressure rise p_2/p_1 is increasingly improved in cases B1 and B2 compared to A1 as can be appreciated by the average pressure rise values in Table 12-4 and Table 12-5. The separation is however not completely prevented.

As reflected by the radial distributions of static pressure in Figure 12-9 and Figure 12-13, at the outlet measurement plane the distribution of static pressure is rather uniform. Thus the increased static pressure rise with increased aspiration manifests essentially as an offset of the radial pressure to a higher level over the whole channel height. As shown in the same figures, the change in the radial distributions of outlet total pressure and outlet flow angle is more tortuous: in all cases, increasing the aspiration on hub improves the total pressure levels in the region going from the hub up to at least 63% of the span. The highest improvement in total pressure level occurs at mid-span. The explanation can be seen in the contour plots in Figure 12-12 and Figure 12-16: in the cases B1 and B2, more flow with higher total pressure takes the place that in case A1 is occupied by the separation. However, in all cases, in the radial distributions in Figure 12-9 and Figure 12-13, deterioration of the total pressure level in the region close to the casing can be noticed. Two reasons are identified: first, when the blockage due to the hub separation is reduced, a redistribution of the total pressure level occurs from the casing region towards lower spanwise positions to the disadvantage of the level at the casing. Second, as outlined in Figure 12-8 by an enhanced colour scale, a low total pressure region at the casing increasingly appears in the measurement region influencing the total pressure level at the casing. This region was identified as the clearance vortex earlier on. Its increasing intensity can be ascribed either to the reduced blockage close to the hub, or to the increased blade loading augmenting the intensity of the clearance jets and thus the clearance vortex. As noted for instance in [Horlock et al. 2005] hub corner separation and clearance jets are in fact in an equilibrium, where reduction of the first yields an intensification of the others et vice versa : "This [hub corner] separation is greatly influenced by both secondary flows, which tend to exacerbate it, and tip leakage flows, which tend to prevent separation." With one exception (case B1), in all cases, increasing the aspiration on the hub progressively improves the resulting average total pressure level as can be noted comparing the total pressure loss values for cases A1, B1 and B2 in Table 12-4 and Table 12-5. According to the discussions in section 2.3.2, reduced loss goes with further improved pressure rise. In case B1 for 3° incidence, the addition of aspiration slots on hub with the application of a moderate aspiration level appears to actually increase the average loss level.
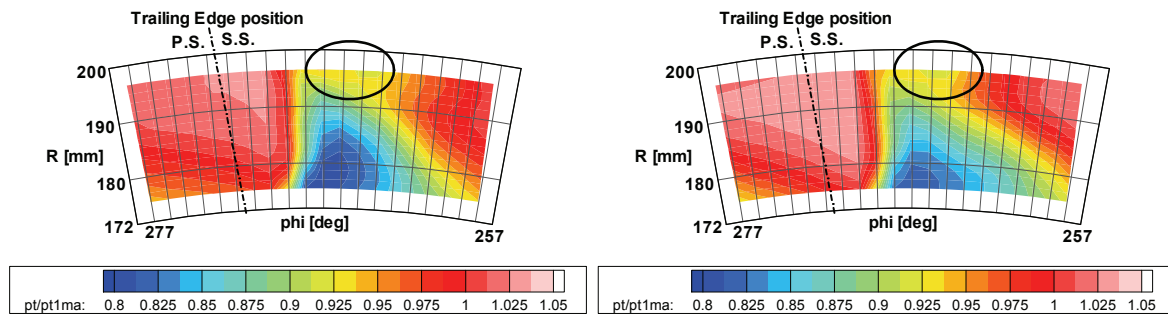
Figure 12-8. Cases B1 and B2 for 3° incidence: accentuation of the low total pressure region of the clearance vortex progressively growing into the measurement region for increased levels of aspiration.

On the radial distributions of outlet flow angles in Figure 12-9 and Figure 12-13, the following can be noted: according to the averaged results, the flow angles for case B1 and B2 are not improved compared to the reference case A1 by the aspiration on hub. Instead, especially close to the casing, the flow angles are increased reflecting a reduced deflection. This is confirmed by the increased average outlet flow angle values listed in Table 12-4 and Table 12-5 for cases B1 and B2. Though when considering the flow angle distributions presented in Figure 12-12 and Figure 12-16, the high flow angle trace occurring at mid-span appears significantly reduced by the addition of aspiration on hub in case B1 and further reduced by an increased aspiration rate in case B2. This reflects the reduction of the blockage induced by the corner separation that was identified as cause for the high flow angles. Two are the reasons for which this improvement is not reflected by the average outlet flow angles: first, the high flow angles in case A1 affected regions with low momentum. Thus the impact of this underturning to the mass flow weighted averages is rather low. Second, the reduction of the improvements induced by the aspiration on hub yield more uniform flow conditions on the outlet flow plane. The flow conditions settle at an uniform but slightly higher level of flow angles, thus yielding higher averages. Comparing the flow angle distributions in Figure 12-12 and Figure 12-16, it should finally be noted that although a reduction of the high flow angle regions can be noted in the 5° incidence case, the improvement is not as good as in the case with 3° incidence.

Summary of the main findings

For all the cases, adding aspiration on the hub reduces the inflection of mid-span blade static pressure related to the close separation onset. The level of total pressure at the outlet is improved mostly at mid-span but also close to the hub. This is related to the reduced size of the low total pressure trace of the separation at hub. At the casing, the total pressure is not improved since compared to the case without aspiration, high total pressure flow is redistributed and attracted to lower spanwise positions, away from the casing region. Furthermore, the influence of the clearance vortex in the casing region becomes more important. Either it is reinforced by the higher loading or it is attracted by the aspiration or both. This also lowers the total pressure at the casing. Excepted for case B1 at 3° incidence, all cases with aspiration on hub achieve better loss levels than the reference case. Even though the average flow angles at outlet are not improved, the flow angle distributions indicates that the underturning region is significantly reduced by the aspiration. For the 5° cases the improvements are less pronounced.

12.2.4 Aspiration on the hub and on the blades at the same blade pitch

The suction side blade pressures in Figure 12-6 show the influence of adding aspiration on the blades at an aspiration rate of 0.8% (C1, green curve) and 1.5% (C2, light green curve) with the aspiration on hub fixed to 2%. For comparison, the results for 2% aspiration on the hub only (B1, blue curve) and for the case without aspiration (A1, black curve) are also plotted within the graphs. First of all, in the cases with aspiration on blade, a notable pressure drop upstream of the location of the blade aspiration slot can be seen. This is coherent with the observations of Prandtl described in section 1.2.2.1 and plotted in Figure 1-3 taken from [Durand et al. 1934] of the flow close to an aspiration slot: the streamlines upstream of the aspiration slot on the blade are deflected and contracted towards the slot. This goes with an acceleration and a drop in static pressure compared to a case without aspiration. Thus the effect of the aspiration slot is visible upstream of the slot location. In a two-dimensional case, the implicit reduction of the adverse pressure gradient upstream of the slot prevents or delays the onset of a separation. Though, in the present case of three-dimensional flow, this is not obligatory: for instance, the aspiration can attract flow from other radial positions. This degree of freedom is not available in the two-dimensional model. However, the two-dimensional model seems to well apply at the midspan measurement location in the present case: there it can be noted with certainty that the upstream flow is accelerated towards the aspiration slot. Furthermore, the inflection of blade pressures upstream of the aspiration slot location that was earlier related to the separation at hub disappears when aspiration on blade is applied. This is visible for both incidences. This indicates that the separation onset is removed or its region of influence is displaced from midspan to other radial positions. After the location of the blade aspiration slot, the blade pressure steps up to a significantly higher level. As noted by Durand, in the two-dimensional case, a stagnation point must occur past the aspiration slot, where the flow reattaches forming a new, thin and resistant boundary layer. In the present case, the measurement resolution is not high enough to identify the peak of high pressure that would go with a stagnation point. However the flow past the slot shows a smooth pressure rise up to the last measurement location, indicating that a successful reattachment occurred past the slot. This takes place although the streamwise pressure gradient past the aspiration slot is higher, i.e. the increase of the blade pressure level is steeper, than in the cases without aspiration. The step change in pressure level past the aspiration slot is comprehensible: the streamtubes of the reattached flow past the slot are dilated in contrast to those upstream of the slot. Thus the flow is decelerated and the static pressure is increased yielding the notable step increase in static pressure. Past the aspiration slot, the mass flow flowing through the blade channel is reduced compared to the case without aspiration and the deflection is improved by the reattachment. Hence, as for the aspiration on hub, according to the discussions in section 2.3.2, the pressure rise is improved by the aspiration on blade. This is reflected by an increased blade pressure level at outlet in Figure 12-6. This is also clearly reflected by higher average pressure rise p_2/p_1 for increased aspiration on blade in the cases C1 and C2 compared to cases A1-B1 listed in Table 12-4 and Table 12-5. The cases C1 and C2 with 3° incidence even outperform case B2 with 4% aspiration on the hub in terms of pressure rise. The cases C1 and C2 with 5° incidence however perform only very similar in terms of pressure rise to case B2. As can be noted in Table 12-5, in these cases the average loss increases and the higher outlet flow angles indicate deteriorated deflection. This suggests disturbing effects in regions other than the mid-span where the blade pressures are measured and will be analyzed hereafter. According to section 2.3.2, increased loss and reduced deflection counteracts the pressure rise. This can thus explain that the pressure rise is much more moderate for the 5° incidence cases than for the 3° incidence cases.

As for the cases with aspiration on hub, at the outlet measurement location, the static pressure distribution is rather uniform. The increased pressure rise with increased rate of aspiration on the blades reflects in an offset of the outlet pressure level for the cases C1 and C2 compared to A1 and B1 in the radial distributions in Figure 12-10 and Figure 12-14.

For the cases with 3° incidence, the radial distributions of total pressure presented in Figure 12-10 indicate that the cases C1 and C2 with aspiration on the blade achieve slightly better total pressure levels than the case B1 with same aspiration rate on the hub but no aspiration on the blades. This is especially the case close to the hub and at mid-span. There B1, C1 and C2 all outperform the reference case without aspiration, A1. However, close to the casing, case C1 and C2 present a lower total pressure level than the reference case A1, performing very similarly to case B1. Comparison of the total pressure distributions in Figure 12-12 for the case C1 and C2 with case B1 indicates that the improvement of the total pressure level can be ascribed to a very successful reduction in size of the low total pressure separation trace and thus the separation. This goes with an equally remarkable reduction of the underturning region denoted by high flow angles in the flow angle plot presented in the same figure. The improvements increase when increasing the rate of aspiration on blade from C1 to C2. As for the case B1 with aspiration on the hub, the deterioration of the total pressure level close to the casing is ascribed to two effects visible in the contour plots in Figure 12-12: the redistribution of flow with high total pressure towards lower spanwise positions and an increase in size of the flow region influenced by the clearance vortex. The average loss values listed in Table 12-4 behave in agreement with these observations: 2% aspiration on the hub and 0.8% aspiration on the blades for the case C1 yields a similar but slightly better loss level than case B1 with aspiration only on the hub, at the same rate. This loss level is thus higher than for the reference case A1. Further increasing the aspiration on blade to 1.5% for the case C2 reduces the loss level below that of case B1, yielding an even better loss level than the reference case A1 without aspiration. From all presented cases, only case B2 with 4% aspiration on the hub performs better than C2 in terms of loss.

More detailed consideration of the flow angles for the cases with 3° incidence is obtained by comparing the radial distributions in Figure 12-10 to the cases without aspiration on blade. This indicates that the cases with aspiration on blade yield slightly higher outlet flow angles. This occurs in spite of the outstanding reduction of the high flow angle region size noted for cases C1 and C2 in Figure 12-12. The explanation is found in that the overall outlet flow angle distribution is more uniform for cases C1 and C2, adjusting itself to an average level. This average level is slightly higher than the average level caused by certain non-uniformities in case B1. Thus the value of the average outlet flow angles for the cases C1 and C2 with aspiration on blade listed in Table 12-4 is slightly higher than for the case with same aspiration on hub but no aspiration on the blades, B1. However, C1 and C2 outperform the case with maximum aspiration on hub B2: case C1 shows an average outlet flow angle that is better than that of case B2 by modest 0.1°, but case C2 outperforms it by 0.3° which begins to be significant for the pressure rise. Case C2 is thus better in terms of loss level and pressure rise than the reference case A1 and with 0.7° higher outlet flow angle, which is not too far from the level of case A1.

For the cases with 5° incidence, the aspiration on blade is less effective with respect to total pressure level and deflection: the radial total pressure distributions for the cases C1 and C2 presented in Figure 12-14 show lower total pressure levels than the case with aspiration on hub B1 and the reference case A1 excepted in the region close to the hub. Increasing the aspiration rate slightly improves the total pressure level but it is still lower than in cases B1 and A1. The causes can be inferred by the total pressure and flow angle contour plots for cases C1 and C2 in Figure 12-16: the aspiration on blade achieves a small improvement of the total pressure level in the trace of the separation: the total pressure level in this region are better for cases C1 and C2 than for case B1 with same hub aspiration but no aspiration on blade. However the size of the region affected by the separation is increased: the low total pressure region extends to higher spanwise positions up to the casing. The outlet flow angle plots also indicate a deteriorating feature manifesting as high flow angles extending now up to the casing in the cases with aspiration on blade. When the level of aspiration on the blades is increased, the total pressure level is slightly improved. Thus, in the 5° incidence cases, the presence of the aspiration slot on the blades severely perturbs the flow close to the casing and this can only partly be repaired by increasing the rate of aspiration on the blade. As mentioned earlier, increased loss and reduced deflection are reflected by the

average parameters in Table 12-5: the loss is significantly increased for case C1 compared to B1 or A1. For case C2 it is slightly reduced compared to C1 but it is still above the values of the cases without aspiration on the blade. Likewise, the average outlet flow angle is higher for cases C1 and C2. Thus, due to the persisting blockage, the high loss level and the reduced deflection, the cases with 5° incidence and added aspiration on blade achieve only a slightly increased static pressure level compared to the cases without aspiration on blade.

Summary of the main findings

The aspiration on the blades causes an acceleration upstream of the streamtubes, reflected by reduced blade pressures in that region. The consequently reduced adverse pressure gradient is beneficial for the flow attachment up to the slot. Past the aspiration slot, the pressure level increases stepwise. This is explained by the dilated streamtubes and the reduced mass flow past the slot compared to cases without aspiration. The blade pressures past the aspiration increase steeper than without aspiration indicating a successful reattachment of the flow at the spanwise location of the measurement and a thin, strong boundary layer. All cases with added aspiration on blade achieve a better pressure rise than the cases without. Case C1 with a total of 2.8% aspiration rate even outperforms case B2 with a total of 4% aspiration rate in terms of static pressure rise. Though, the improvements for the 5° incidence cases are less outstanding than for the 3° incidence cases. With respect to the other parameters, 3° and 5° incidence cases behave differently: at 3° incidence the achieved total pressure levels at hub are better than for the reference case and the cases with aspiration on hub, due to a good reduction of the low total pressure trace of the hub separation. Increasing the aspiration yields better results. At the casing, the redistribution of high total pressure flow to lower spanwise positions and the increased influence of the clearance vortex reduces the total pressure level. Thus, case C1 with moderate aspiration on blade and 2% aspiration on hub achieves better levels than case B1 with 2% aspiration on the hub only but not better than the reference case. Case C2 however with 1.5% aspiration on blade and 2% aspiration on the blades performs better than both B1 and the reference case without aspiration A1 in terms of loss. Amongst all results it is outperformed only by case B2 with 4% aspiration on the hub. The outlet flow angles for the cases with aspiration on the blades are not improved in terms of average value. However the outlet flow angle distribution is significantly more uniform. The average outlet flow angles of case C2 are only 0.7° higher than the reference case, thus case C2 performs very good: better pressure rise, better loss level and similar flow angles compared to the reference case. The cases with 5° incidence perform worse than the comparison cases except for the pressure rise. This indicates a detrimental influence of the blade slot for flow topology occurring at 5° incidence. Increasing the aspiration rate slightly improves this.

12.2.5 Aspiration on the hub and on the blades with increased blade pitch

In cases D1 and D2 analyzed hereafter, the blade pitch is increased from 20° to about 26° by decreasing the number of blades on the cascade from 18 to 14 with otherwise unchanged channel geometry. The same aspiration rates with respect to the inlet flow as for the cases C1 and C2 were applied: thus a hub aspiration rate fixed to 2% as for case B1, C1 and C2 and blade aspiration rates of 0.8% and 1.5% as for cases C1 and C2. Since the number of slot reduces with the reduced number of blades, keeping the same aspiration mass flow increases the aspiration rate per slot. Thus, the cost in terms of aspirated mass flow is the same as for the comparable cases with 18 blades. However the reduction in number of blades by about 22% yields a significant reduction both in mass as well as friction surface with the flow. To achieve similar performance as the cases with more blades, the loading of the single blades must increase, thus this configuration is defined as the highly loaded configuration. The intention of keeping the same aspiration rates is to herewith compensate increased loss that goes with the increased loading.

Figure 12-7 shows the blade pressures measured at midspan for the cases with blade pitch increased to 26° but hub aspiration rate fixed to 2% as in cases B1, C1 and C2. Case D1 (orange curve) has 0.8% aspiration on blade as the case C1 with lower blade pitch. Case D2 (pink curve) has 1.5% aspiration on blade which is comparable to case C2. First of all, it can be noted that cases D1 and D2 have indeed a slightly higher blade loading than the cases with lower blade pitch: this is indicated by an increased spread between the suction side and the pressure side blade pressures. It is notable especially close to the leading edge and on the pressure side. However this effect decays towards the trailing edge. The aspiration on blade shows a similar effect as for the cases with lower pitch C1 and C2. Higher aspiration rate slightly increases the loading. However, the increased loading close to the inlet of cases D1 and D2 compared to C1 and C2 decays towards the trailing edge. If comparing the average pressure p_2/p_1 rise in Table 12-4 and Table 12-5 it can be noted that cases D1 and D2 in fact do not achieve the same static pressure rise as C1 and C2 but are outperformed of 0.02 to 0.03 points for comparable aspiration rates. This is well illustrated by the comparison of the radial profiles of static pressure in Figure 12-11 and Figure 12-15. As can be noted, the cases with 3° incidence reach closer to the comparison cases. Nevertheless, the performance of the cases D1 and D2 with increased pitch is better than for the case with only 2% aspiration on the hub B1 and for the reference case A1. Thus, for 3° incidence, the cases D1 and D2 with higher blade pitch and the present aspiration configuration succeed in achieving a similar pressure rise as the cases with lower blade pitch. This is relevant since this is obtained with fewer blades and thus a more lightweight cascade.

For the cases with 3° incidence, the radial distributions of total pressure presented in Figure 12-11 indicates that the cases D1 and D2 with higher blade pitch reach lower levels of total pressure in the region between hub and about midspan than C1 and C2. The explanation is found when considering the outlet contour plots of total pressure in Figure 12-12: it can be noted that the low total pressure trace from the hub separation in cases D1 and D2 has a spanwise extension similar to cases C1 and C2. However it is more dilated in circumferential direction. It is probable that the larger hub surface crossed by the secondary flow in the cases with increased blade pitch feeds the separation with more low momentum fluid than in the cases with smaller blade pitch. Furthermore, since the loading in cases D1 and D2 is slightly but not drammatically increased compared to that of cases C1 and C2, the cross-passage pressure gradient and thus the deflection of the higher channel mass flow must be reduced. This can also prevent the main flow from counteracting the circumferential growth of the separated region. Anyhow, a larger flow region is affected by low total pressure levels and this causes the noted lower levels in the radial distribution between hub and about midspan. Interestingly, the total pressure level towards the casing in the radial distribution in Figure 12-11 is better for cases D1 and D2 than for case C1 and C2. According to the total pressure contours in Figure 12-12, this is caused by an increased circumferential portion of flow with high total pressure compared to the cases with smaller blade pitch. Thus, the leakage flow is similar to that of cases C1 and C2. A further explanation for the higher amount of high total pressure flow close to the casing is a reduced friction loss due to a reduced number of blades. Table 12-4 indicates the loss level resulting of the observed total pressure distributions: cases D1 and D2 achieve similar but slightly higher total pressure loss levels as case C1 and C2. Case D2 with 1.5% aspiration on the blade and higher blade pitch actually outperforms case C1 with 0.8% aspiration on the blade and lower blade pitch. Thus the loss level of case D2 is also better than case B1 with only aspiration on the hub at a level of 2%.

The radial flow angle distribution for the 3° incidence cases presented in Figure 12-11 indicate similar deflection close to the hub in the cases D1 and D2 with higher blade pitch as the cases with comparable aspiration configuration C1 and C2. This is supported by the overturning caused by the low flow angles of the hub passage vortex visible close the hub in the related distributions in Figure 12-12. However, above about 30% blade span, the outlet flow angles of case D1 and D2 in Figure 12-11 are higher than in cases C1 and C2 indicating a reduced deflection. Comparison of the distributions for case D1 and D2 in Figure 12-12 with those for C1 and C2 indicates the reasons: first, the dilated trace of the separated region

noted earlier yields increased flow angles. Second, the overall level of flow angle is increased. Due to the noted similar circumferential pressure gradient, as indicated by the quite similar blade loading, at higher blade pitch and same inlet flow velocity, the deflection is reduced. Consequently, the average outlet flow angle for cases D1 and D2 listed in Table 12-4 are higher than for cases C1 and C2.

For the cases D1 and D2 with 5° incidence and increased blade pitch, the resulting radial distribution of total pressure shown in Figure 12-15 indicates overall reduced values of total pressure compared to the other cases. This renews the observations made for case C1 and C2: at the higher level of incidence, the blade aspiration does not only appear to have reduced effect on the separation. The presence of the aspiration actually seems to accentuate it. Where even for the higher blade pitch with 3° inlet flow incidence the blade aspiration still yields a relative improvement of total pressure level close to the casing, the present case with 5° incidence shows an overall deterioration. The distributions of total pressure and flow angles for case D1 and D2 in Figure 12-16 illustrate that in fact the trace of the separation significantly increases in size and intensity compared to cases C1 and C2. It not only dilates in circumferential direction as for the cases with 3° incidence, where the radial extension is relatively well controlled by the aspiration. In the 5° incidence case, also the radial extents of the separation trace are significant with low total pressure values and high flow angles. Increasing the blade aspiration rate in case D2 slightly milders the intensity of this feature compared to case D1. However the aspiration device seems more ineffective to control the separation at 5° incidence than for the cases with lower blade pitch. This is reflected by the average parameters for cases D1 and D2 listed in Table 12-5: resulting loss levels are by 50% higher than in the reference case and the outlet flow angle increases by 2°, yielding a significantly reduced deflection. This explains the lower pressure level at outlet. The fact that the blade pressures for cases D1 and D2 at 5° incidence in Figure 12-7 do not suggest the severity of the separation growth in this case indicates that significant loss must be produced close to the hub and might be generated past the trailing edge, e.g. by mixing out of significantly non-uniform flow.

Summary of the main findings

The measurements of the static pressure on the blades shows that increasing the blade pitch by reducing the number of blades from 18 to 14 only slightly increases the loading of the single blades. The reduced deflection and increased loss yield a reduced pressure rise. Nevertheless, in the 3° incidence cases the aspiration influence elevates the cascade performance to a level similar to that of the case with more blades: cases D1 and D2 reach pressure ratios that are only 0.02 to 0.03 units smaller than the comparable cases C1 and C2 with more blades and are even better than case B1 with more blades and aspiration on the hub only. The loss level behaves similarly: it is close but above the level of the cases with more blades and the same aspiration configuration and better than the level of case B1. The additional loss arises from a dilation in circumferential direction of the hub separation trace. This can be caused by reduced guidance and by the higher friction of the hub passage vortex flow due to the increases hub surface between two blades. The deflection is better close to the hub due to an increased intensity of the overturning caused by the hub passage vortex. However, the overall level at outlet is higher yielding reduced deflection in the cases with fewer blades. In the cases with 5° incidence, the separated region and the related underturning are significantly higher. Even though increasing the rate of aspiration on the blades reduces the intensity of the separation traces, the loss level, the deflection and thus the pressure rise are lower than in cases with more blades. The achieved pressure rise is better than for the reference case but this is mainly an effect of the flow extraction. Summarizing, even though for the cases with 5° incidence the aspiration does not perform as well as cases with more blades, the cases with 3° incidences are brought to achieve similar performance: with less blades, similar loading, loss and pressure rise are achieved. Though, the deflection is slightly lower than in the comparison cases.

i = 3°	Aspi. Hub	Aspi. Blade	Pitch	ω [%]	$\bar{\alpha}_2$ [°]	$\tilde{p}_2$ / $\tilde{p}_1$ [-]
A1	no	no	20°	8.9	33.4	1.16
B1	2 %	no	20°	9.6	34.0	1.18
B2	4 %	no	20°	7.8	34.4	1.20
C1	2 %	0.8 %	20°	9.4	34.3	1.22
C2	2 %	1.5 %	20°	8.5	34.1	1.24
D1	2 %	0.8 %	26°	9.8	35.2	1.20
D2	2 %	1.5 %	26°	9.1	35.0	1.21
				◄ better	◄ better	better ►

Table 12-4. Average parameters resulting for the cases with 3° incidence and different configurations.

i = 5°	Aspi. Hub	Aspi. Blade	Pitch	ω [%]	$\bar{\alpha}_2$ [°]	$\tilde{p}_2$ / $\tilde{p}_1$ [-]
A1	no	no	20°	10.9	34.8	1.17
B1	2 %	no	20°	10.2	35.0	1.19
B2	4 %	no	20°	9.4	35.2	1.23
C1	2 %	0.8 %	20°	13.3	35.4	1.23
C2	2 %	1.5 %	20°	12.3	35.2	1.24
D1	2 %	0.8 %	26°	15.4	37.1	1.20
D2	2 %	1.5 %	26°	15.1	37.3	1.21
				◄ better	◄ better	better ►

Table 12-5. Average parameters resulting for the cases with 5° incidence and different configurations.
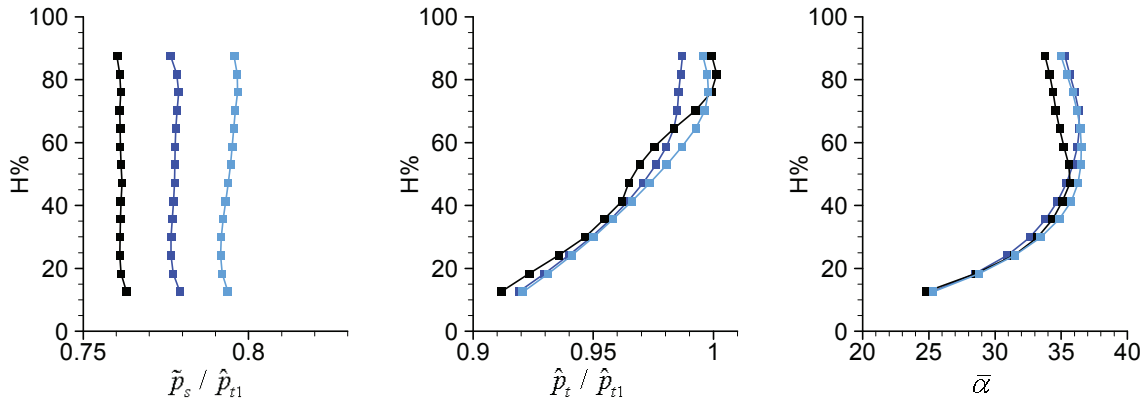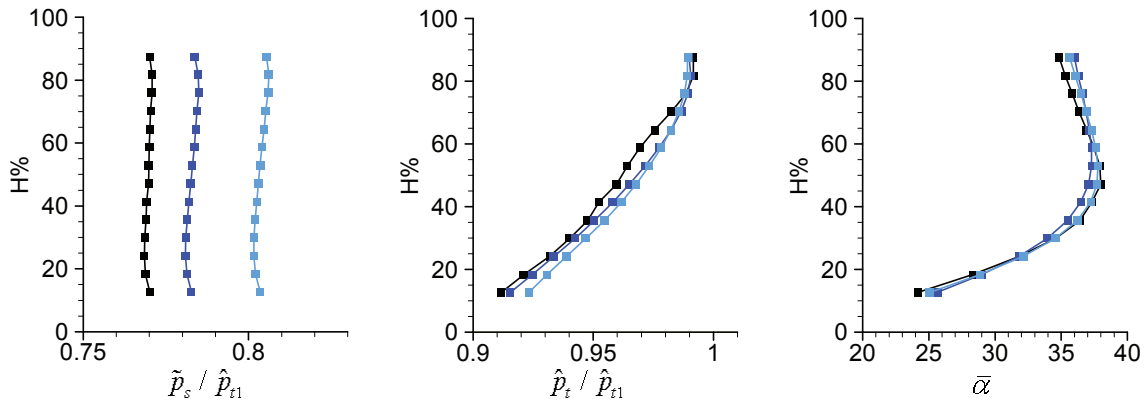
Figure 12-9. Outlet radial profiles for 3° incidence: influence of adding and varying aspiration on the hub
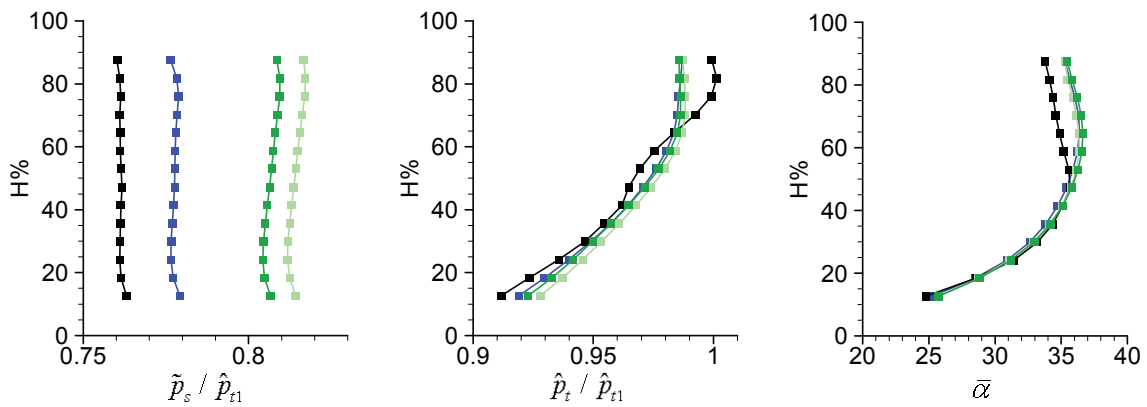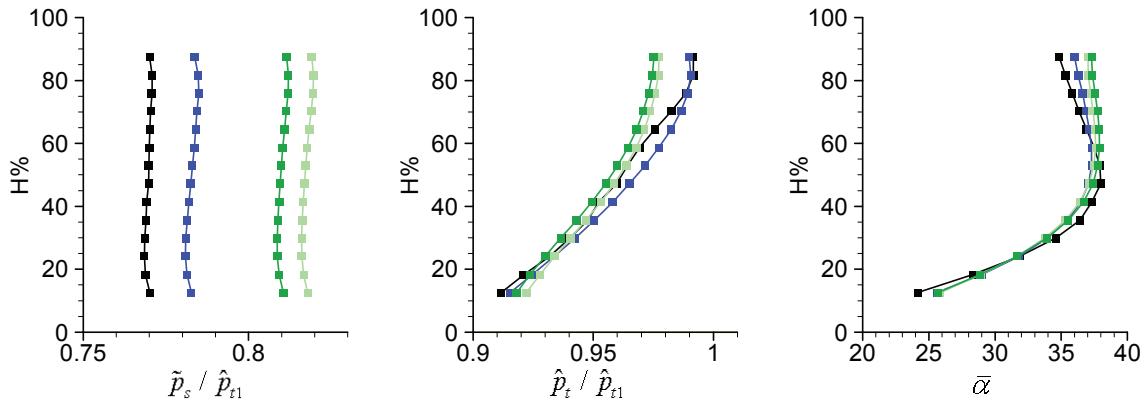

Figure 12-10. Outlet radial profiles for 3° incidence: influence of adding and varying aspiration on the blades.
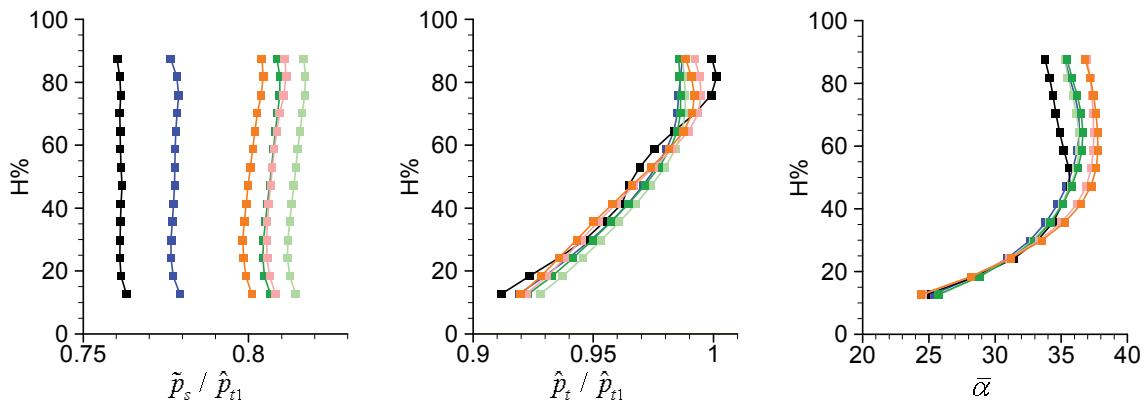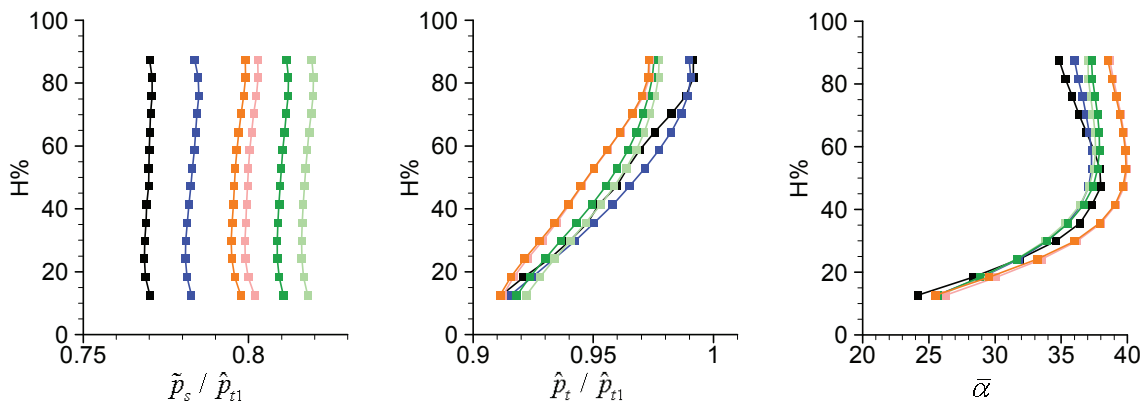

Figure 12-11. Outlet radial profiles for 3° incidence: influence of increasing the blade pitch and varying the aspiration on the blades.

- A1 - 18 blades
- B1 - 18 blades - Hub: 2% asp.
- B2 - 18 blades - Hub: 4% asp.
- C1 - 18 blades - Hub: 2% asp. - Blades: 0.75% asp.
- C2 - 18 blades - Hub: 2% asp. - Blades: 1.5% asp.
- D1 - 14 blades - Hub: 2% asp. - Blades: 0.75% asp.
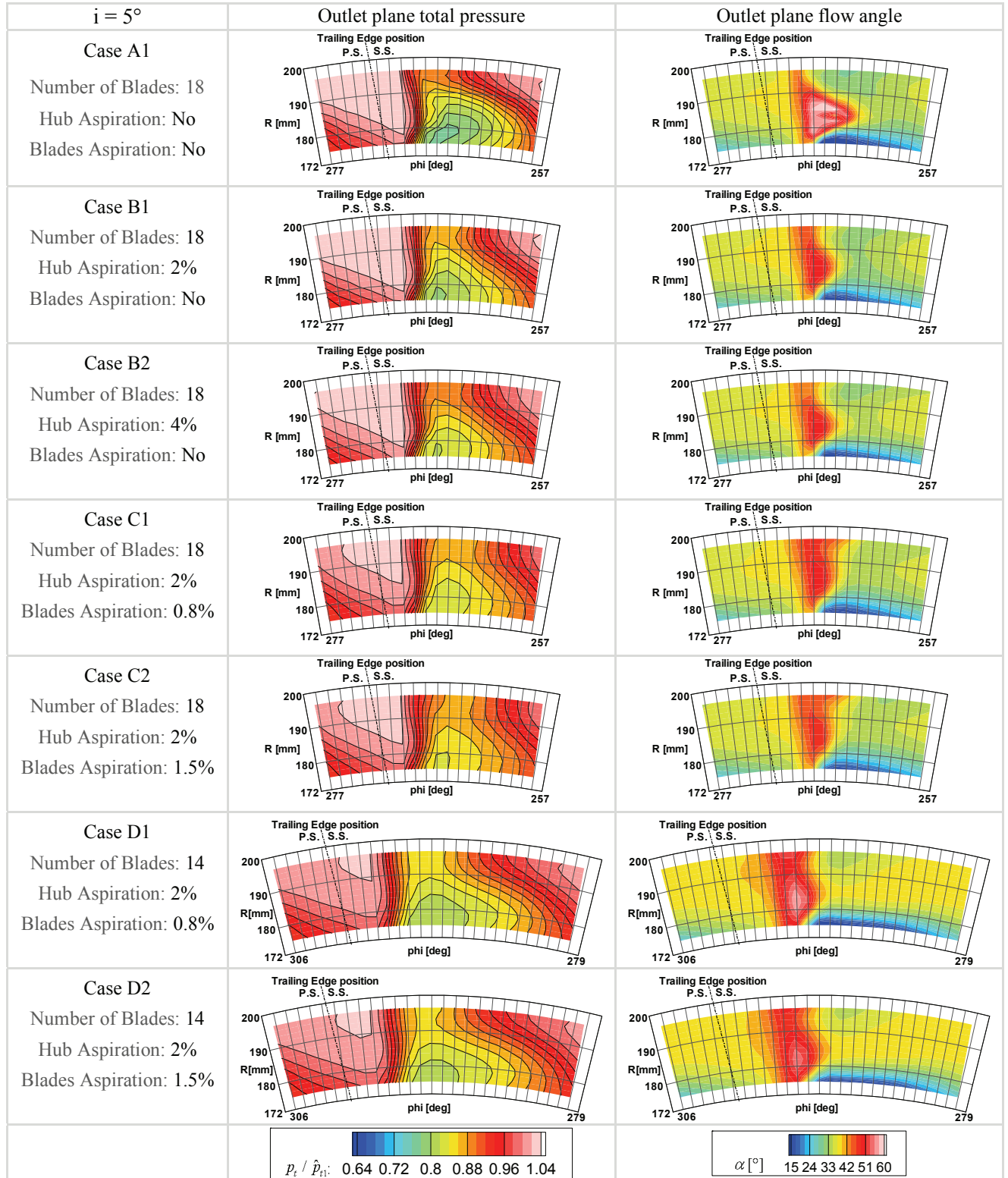- D2 - 14 blades - Hub: 2% asp. - Blades: 1.5% asp.

Figure 12-12. Distributions of non-dimensionalized total pressure and flow angle measured at outlet for the 3° incidence cases and different configurations.

Figure 12-13. Outlet radial profiles for 5° incidence: influence of adding and varying aspiration on the hub.

Figure 12-14. Outlet radial profiles for 5° incidence: influence of adding and varying aspiration on the blades.

Figure 12-15. Outlet radial profiles for 5° incidence: influence of increasing the blade pitch and varying the aspiration on the blades.

- ■ A1 - 18 blades
- ■ B1 - 18 blades - Hub: 2% asp.
- ■ B2 - 18 blades - Hub: 4% asp.
- ■ C1 - 18 blades - Hub: 2% asp. - Blades: 0.75% asp.
- ■ C2 - 18 blades - Hub: 2% asp. - Blades: 1.5% asp.
- ● D1 - 14 blades - Hub: 2% asp. - Blades: 0.75% asp.
- ● D2 - 14 blades - Hub: 2% asp. - Blades: 1.5% asp.

Figure 12-16. Distributions of non-dimensionalized total pressure and flow angle measured at outlet for the 3°incidence cases and different configurations.

12.2.6 Secondary motion

The plots of outlet plane helicity and secondary velocity in Figure 12-17 and Figure 12-18 illustrate the influence of the aspiration on the secondary motion for the cases with 3° incidence.

The most notable feature is the region of high helicity with positive sign and high secondary velocity in the reference case A1 observed earlier with respect to Figure 11-24 and Figure 11-26. It was noted that it mainly consists in suction side boundary layer that is raised away from the suction side by the separation causing a secondary motion that persists up to the outlet measurement plane. A small part of this secondary flow close to the casing is originated by casing passage vortex that is pushed away from the clearance vortex denoted by a region with high helicity of negative sign. It can be noted, that adding and increasing aspiration on hub in the cases B1 and B2 progressively decreases the severity of this feature, both in terms of helicity as well as secondary velocity. Recalling the suction side boundary layer visualisation illustrated by the vorticity magnitude in Figure 11-20 suggests two mechanisms that can cause this: first, as noted comparing the contours in Figure 12-12 the aspiration on hub reduces the size of the separation trace and thus probably of the separation itself. Thus the suction side boundary layer is raised away less from the suction side preventing the formation of a stable concentration of streamwise vorticity carried by the main flow. Second, recall furthermore that the hub aspiration slot begins early before the separation onset predicted by the numerical simulations. It is probable that the hub aspiration attracts a certain amount of suction side boundary layer towards the aspiration slot and away from the blade passage. This removed boundary layer cannot longer contribute to the formation of the region with high positive helicity and thus increased secondary flow.

Adding aspiration on blade as is done in case C1 and C2 completely removes this feature. The same two mechanisms as for added aspiration on hub can be assumed, but furthermore, the aspiration on blade directly removes suction side boundary layer which must further prevent suction side boundary layer to be raised away from the suction side.

In cases D1 and D2, where the blade pitch is increased interestingly a region of positive helicity reappears as can be noted in Figure 12-18 . However, it occurs above the region affected by the separation according to the total pressure distributions in Figure 12-12. Furthermore the secondary motion it generates in the plots in Figure 12-18 is of completely different nature than what seen for cases A1-B2. Both observations rather suggest a relation with the casing passage vortex. This suggests that the helicity trace is rather an appendix of the casing passage vortex that is attracted towards the blade suction side by the aspiration on blade. This can be caused by an increased momentum of the blade aspiration due to a reduced number of blades and slots at constant aspiration rate. Especially, since at the higher blade aspiration ratio, this feature slightly approaches the suction side both in the secondary velocity plot as in the helicity plot. Nevertheless, the intensity of the hub passage vortex trace is slightly reduced by increased aspiration rates.

Summarizing it can be noted that the aspiration on hub and on blade contribute to a more uniform flow distribution by reducing the secondary flow formation. Only in the cases where the blade pitch is increased, the influence of the aspiration slots seems to slightly promote the attraction of the casing passage vortex towards the suction side, which counteracts the uniformity.

Table 12-6 lists the secondary velocity averages and the average ratio that the kinetic energy of the secondary motion represents with respect of the outlet kinetic energy. This is of interest in comparison with past estimations of the relevance of the energy estimated in former investigations. It can be noted that the kinetic energy ratio of the secondary motion is relatively low respected to the overall kinetic energy. It can be assumed that the values will be more significant in cases of turbine cascades, where deflection and acceleration significantly promote the secondary flow formation. Nevertheless it can be

appreciated how the averages quantify the intensity of the flow non-uniformity and thus represent a new figure of merit for the cascade performance: the secondary kinetic energy is reduced when aspiration on the hub is added in case B1 and B2. It increases when adding aspiration on blade in case C1 but when the rate of aspiration on blade is increased, the level is reduced somewhat C2. In cases D1 and D2, the intensity of hub and casing passage vortices are significantly increased yielding an increase of secondary kinetic energy which is slightly reduced by increasing the aspiration rate.

i = 3°	Aspi. Hub	Aspi. Blade	Pitch	$\hat{V}_{sec,2}$ [m/s]	$\hat{e}_{sec,2}/\hat{e}_2$ [%]
A1	no	no	20°	11.8	0.413
B1	2 %	no	20°	10.5	0.373
B2	4 %	no	20°	10.3	0.369
C1	2 %	0.8 %	20°	9.9	0.384
C2	2 %	1.5 %	20°	9.6	0.372
D1	2 %	0.8 %	26°	12.0	0.559
D2	2 %	1.5 %	26°	11.5	0.537

Table 12-6. Average secondary velocity and ratio of secondary kinetic energy to total kinetic energy in the outlet plane based on experimental results at 3° incidence.

The secondary velocity fields obtained from the 5° incidence measurements are presented for reference in Appendix A on page 175.

148

Outlet plane helicity	Outlet plane secondary velocity

Case A1 − 18 blades − No aspiration

Case B1 − 18 blades − Hub: 2% asp.

Case B2 − 18 blades − Hub: 4% asp.

Case C1 − 18 blades − Hub: 2 % asp. − Blades: 0.75% asp.

Case C2 − 18 blades − Hub: 2 % asp. − Blades: 1.5% asp.

H: -1.3E+06 -7.8E+05 -2.6E+05 2.6E+05 7.8E+05 1.3E+06

vsec [m/s]: 0 3 6 9 12 15 18 21 24 27 30
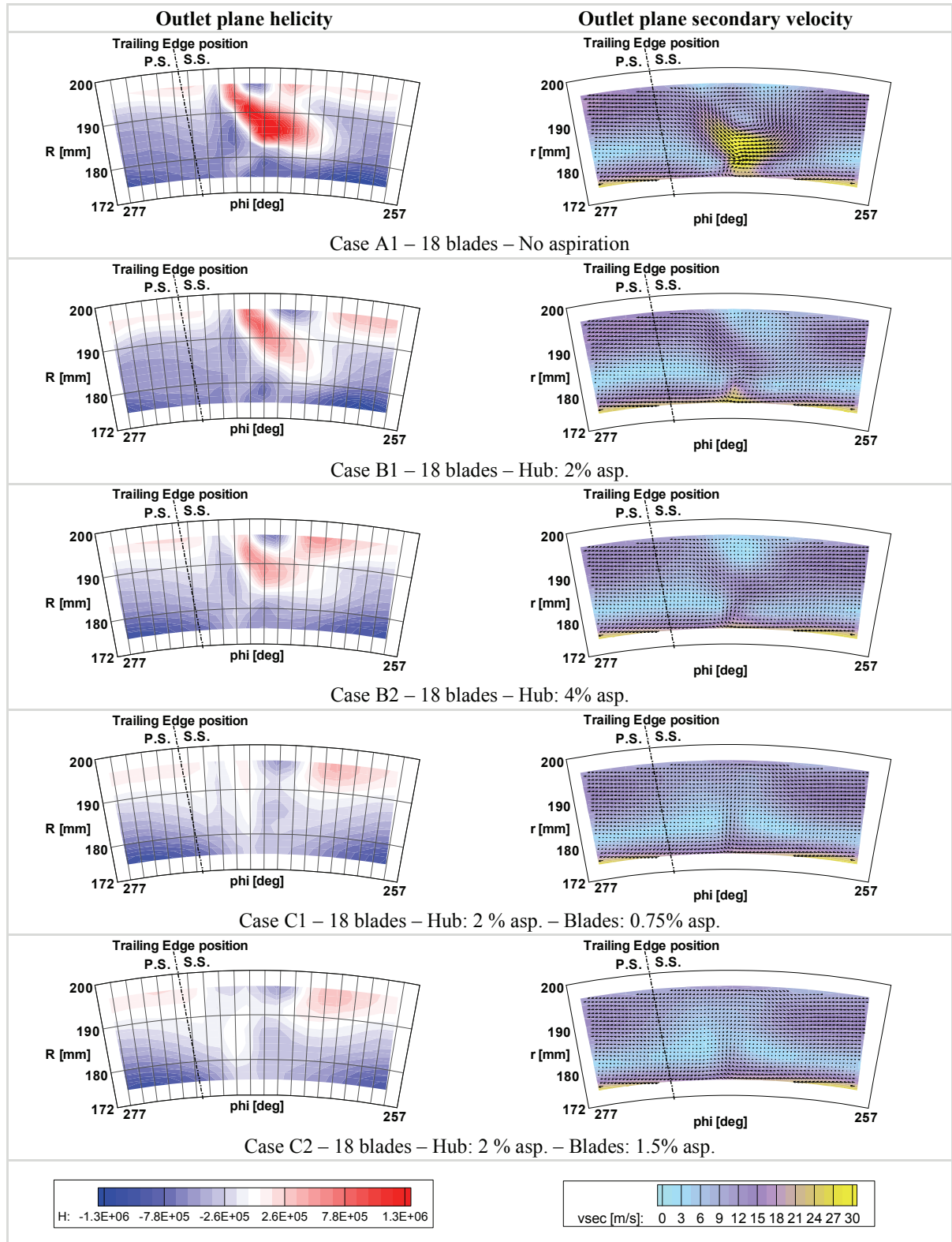
Figure 12-17. Contour plots of helicity and secondary velocities in the outlet planes based on experimental results for 3° incidence.
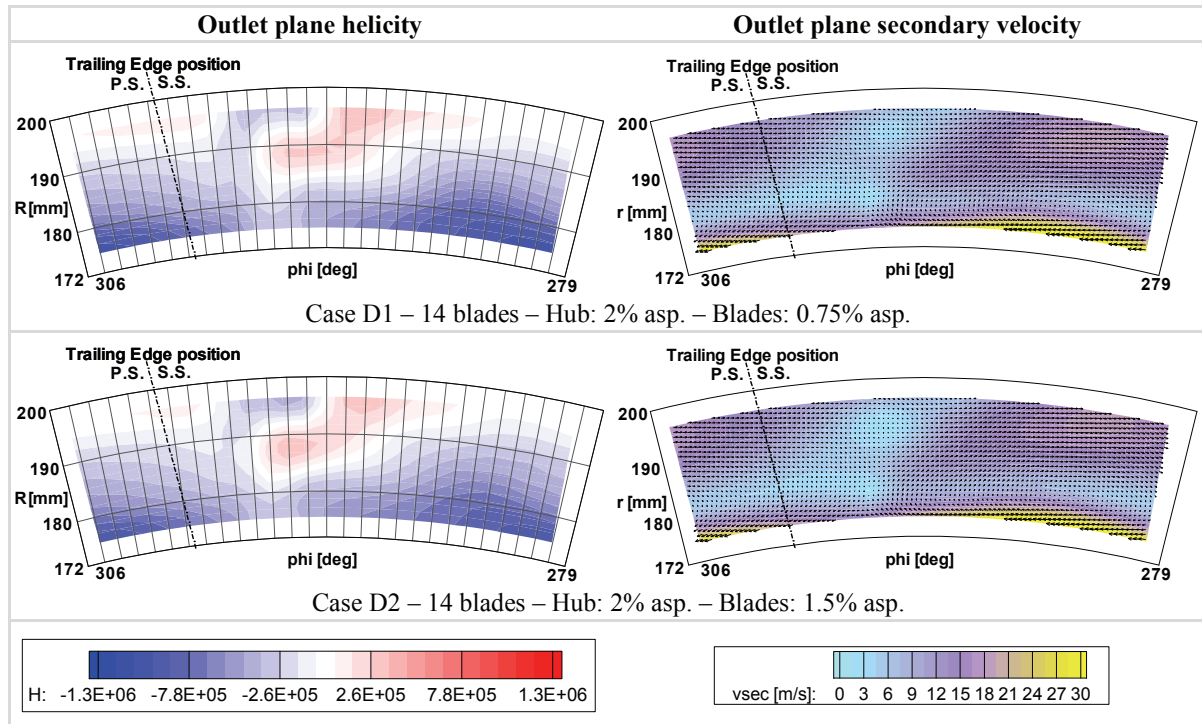
Figure 12-18. Contour plots of helicity and secondary velocities in the outlet planes based on experimental results for 3° incidence (continued from Figure 12-17).

12.3 Validation of the numerical simulations

The following section will introduce the numerical results that are used to support the analysis of the flow mechanisms related to the aspiration technique. They are based on the computation on the numerical models introduced in chapter 9. The discussion will focus on cases with 3° incidence that were computed based on the inlet conditions of the experimental results presented in the preceding section. Results are available for the configurations A1, B1, C1, C2, D1 and D2. Only for case B1, the inlet conditions used for the computations do not correspond exactly to the conditions of the experimental case discussed earlier: the computations for case B1 are based on a measurement case with inlet conditions that are very similar to that of the reference case in terms of inlet Mach number, total pressure and flow angles, but where the inlet boundary layer at hub was thicker. Thus in the region close to the hub, the low momentum and low total pressure region is thicker than in the reference case. Nevertheless, these results give insight to the flow mechanisms related to the aspiration on hub and are thus also presented here.

First of all, a certain agreement of the aspiration impact for the 3° incidence results can be noted by the comparison of the outlet plane measurement results presented in Figure 12-12 and the corresponding outlet plane computational results presented in Figure 12-19. Globally the numerical results indicate a similar influence on the separation trace as observed for the probe measurements in the discussion so far. However, the numerical predictions are more pessimistic on the influence of the aspiration on blade on the hub corner separation in the cases with 18 blades and more optimistic in the cases with 14 blades. The numerics also reproduce the clearance vortex and its increased attraction towards the suction side when the aspiration is increased. This is better visible in the numerical results, since the region close to the wall is modeled, which was only partly visible in the aerodynamic probe measurements. With respect to the outlet flow angles, the numerical results are generally more optimistic on the control of the aspiration. This is particularly the case for the high flow angle trace visible in the center of the flow field related to the flow raised away from the suction side by the blockage constituted by the corner separation. In cases D1 and D2 this trace completely disappears in the simulations. Generally it can be noted that the main flow features and trends are well reproduced by the numerical results, allowing to use them to get more insight into the flow mechanisms related to the influence of the aspiration. Quantitatively, differences are undeniable. Although not crucial for the qualitative investigation of the involved flow mechanisms, the differences and the resulting trends are analyzed by the comparison of the average values hereafter.

12.3.1 Impact of the measurement region limitation on the average results

The computational domain is not limited to the regions accessible by the measurement instrumentation but considers the whole flow area up to the hub and casing wall. To compare averaged results it is hence necessary that the averaging of simulation and measurement results is performed over corresponding regions. Thus first, the impact of averaging over different regions is analyzed based on the numerical results. The results of averaging over the measurement region or the entire outlet plane are listed next to each other in Table 12-7.

i = 3°	Aspi. Hub	Aspi. Blade	Pitch	ω [%]	$\bar{\alpha}_2$ [°]	$\tilde{p}_2 / \tilde{p}_1$ [-]
A1	no	no	20°	9.5	33.5	1.18
				10.5	32.5	1.17
B1	2 %	no	20°	9.3	34.0	1.19
				9.0	32.8	1.18
C1	2 %	0.8 %	20°	7.3	33.8	1.21
				8.5	32.6	1.21
C2	2 %	1.5 %	20°	7.0	33.7	1.21
				8.0	32.6	1.21
D1	2 %	0.8 %	26°	8.1	34.6	1.20
				8.8	33.4	1.20
D2	2 %	1.5 %	26°	7.9	34.5	1.21
				8.4	33.3	1.20

■ CFD (meas. region ave.) ■ CFD (overall ave.) ◄ better   ◄ better   better ►

Table 12-7. Comparison of averages from CFD results considering either only the region corresponding to the measurement region or the overall outlet plane region.

Average loss

In all cases, computing the average over the entire outlet plane region yields a higher loss value than when integrating only over the region of measurement. The reasons are promptly identified when considering the outlet plane total pressure plots in Figure 12-19: the larger integration window includes large regions of low total pressure close to the hub in the hub separation trace, and close to the casing in the trace of the clearance vortex. However, most general trends are reflected consistently by both averaging approaches: the highest loss occurs in the reference case A1, although the loss level appears less drammatic when considering only the region of measurement. Adding aspiration on hub in case B1 reduces the loss to a level that is overscored only by the reference case A1. Adding aspiration on the blades in case C1 and C2 further reduces the loss level. If averaging only over the measurement region, C1 and C2 have respectively the second best and the best performance meaning the lowest loss. However, if the averages over the entire outlet plane are considered, case D2 with less blades but maximum aspiration yields actually even lower loss levels than case C1, the lowest loss levels still being found for case C2. In all comparisons, case D1 with reduced number of blades and moderate level of aspiration on blade performs just better than case B1 with aspiration only on the hub. If considering only the available cases with maximum aspiration rate, the ranking is clear: case C2 yields the highest reduction of loss, case D2 comes next followed by case B1 and finally case A1. The reflection of the overall average loss trends by the averages over the limited region of measurement indicates that the average loss computed based on the measurement results can yeld with a certain confidence the trends of the overall flow improvement or deterioration.

Outlet flow angle

The comparison of the averages of the outlet flow angles indicates that finding a trend based on the average outlet flow angle results is more hazardous. A general trend indicated without doubt by both averaging approaches is that cases D1 and D2 produce the highest outlet flow angles and thus the lowest deflection: the average outlet flow angle is at least 0.9° higher than the other cases when averaging only over the measurement region (comparison of case D1 and C2) and it is at least 0.6° higher when considering the overall average (comparison of case D2 and B1). The average flow angles for the other cases (A1, B1, C1 and C2) are very close to each other with only 0.2° maximum difference for each averaging approach. Thus, at least with respect to the numerical results, it is not possible to recognise clear trends based on the outlet flow angle. Besides, as can be noted comparing the outlet flow angle

distributions in Figure 12-19, the average can easily be shifted by significant features occurring right outside the measurement region: the overturing caused by the passage vortices and the underturning caused by the clearance vortex. Thus, besides the clear trend of cases D1 and D2 with less blades producing a lower deflection than the other cases, the present results indicate that a qualification based on flow angle averages that are averaged only over the mesurement plane should be avoided.

Average pressure rise

The comparison of the averages obtained for the pressure rise reflects the fact that the static pressure level in the outlet flow plane is rather homogeneous. Thus, the results obtained if considering the entire outlet plane or only the measurement region are almost identical with a maximum spread of 0.01. As noted earlier, the difference in static pressure rise for different aspiration configurations based on the numerical results is mostly surprisingly low. Thus, they rather suggest that there is no drammatic improvement in static pressure rise when comparing cases A1, B1, B2, C1 and C2. Nevertheless, the average pressure rise clearly points out that the pressure rise is reduced when lowering the number of blades as is done for cases D1 and D2. But in the experimental results, the difference in static pressure rise is more relevant. The fact that the averaging results is practically independent of the averaging region confirms that comparing the experimentally obtained average static pressure rise allows to reliably compare the performance of different configurations.

Summary

The following conclusions can be retained for the averages computed considering only the measurement region instead of the entire outlet flow plane: the static pressure rise is perfectly representative of the overall average. The average loss is representative if the differences are important enough, which in the numerical results is the case when comparing cases with maximum aspiration rates. The average outlet flow angle is usually similar in all cases and can be easily biased by the features occurring right outside the measurement region. Thus, this parameter should not be compared without care. Only the reduced deflection occurring when the number of blades is reduced is clear enough. The present observations reduce the reliability of average value comparisons. But this confirms the following statement: the most reliable qualification and understanding of the resulting flow condition can be obtained only if most information available and thus the flow conditions of the entire outlet flow plane are considered. Only this approach can show which flow mechanisms are captured and how they are influenced by the aspiration. The average values are a good indicator, especially the static pressure rise and, to some extent, the average loss, but the evaluation should not be limited to the comparison of the averages, especially if they are close to each other.

12.3.2 Average values

Table 12-8 compares the results of the experiments and of the simulations averaged over corresponding regions. The average results are relatively similar for the reference case A1 and the case with aspiration on the hub B1 with a maximum difference of 0.6% for case A1, even though the trends in the loss values are not reflected. However, the simulations are far more optimistic on the beneficial influence of aspiration on blade on the average loss values with maximum differences of 2.1% for case C1. The absolute value of the average outlet flow angle is generally well reflected with a maximum difference of 0.6° for case D1. However, the trends do not agree, except for case D1 and D2 having significantly higher outlet flow angles than the other cases. As noted in the preceding section, the differences in the average flow angles are relatively small, thus it is not surprising that a precise ranking based on these values is not possible. With respect to the pressure rise, as for the average flow angles, the numerical predictions yield values that are very close to the experimentally measured values, excepted for case C2, where the experiment yields a significantly better static pressure rise.

i = 3°	Aspi. Hub	Aspi. Blade	Pitch	ω [%]	$\bar{\alpha}_2$ [°]	$\tilde{p}_2 / \tilde{p}_1$ [-]
A1	no	no	20°	8.9	33.4	1.16
				9.5	33.5	1.18
B1	2 %	no	20°	9.6	34.0	1.18
				9.3	34.0	1.19
B2	4%	no	20°	7.8	34.4	1.20
				-	-	-
C1	2 %	0.8 %	20°	9.4	34.3	1.22
				7.3	33.8	1.21
C2	2 %	1.5 %	20°	8.5	34.1	1.24
				7.0	33.7	1.21
D1	2 %	0.8 %	26°	9.8	35.2	1.20
				8.1	34.6	1.20
D2	2 %	1.5 %	26°	9.1	35.0	1.21
				7.9	34.5	1.21

■ Experiment, ■ CFD (meas. region average)   ◄ better   ◄ better   better ►

Table 12-8. Comparison of average results from experiments and CFD. As indicated, the averaging of the CFD results was performed over a region corresponding to the measurement region.

12.3.3 Conclusions

The comparison of the distributions of total pressure and flow angles indicate that the most relevant features are well reproduced by the numerical simulations. However, especially in the cases with added aspiration on the blades, the intensity of the features indicates that the numerical results present some quantitative differences to the experimental results. However, features that were only partially visible in the experimental results due to the limitations of the measurement region, are clearly visible in the numerical results. This demonstrates already that the qualitative analysis of the numerical results can significantly support the analysis of the influence of the aspiration.

As shown in section 12.3.1, the numerical results allow estimating the reliability of average parameters obtained integrating only results from the region of measurement. It can be noted that the static pressure rise is practically unaffected by the size of the measurement region and thus very reliable. The average loss appears to be reliable if the differences are important enough. The average flow angle presents generally variations that are too small to determine trends caused by the aspiration for the present cases. It is concluded that the main importance given to the experimental results should be given to the identificaiton of the occurring features and the influence of aspiration on it by considering the entire measured distributions and not only average parameters.

The comparison of average resulting parameters obtained by integrating experimental and numerical results over corresponding regions indicate that the absolute values of average flow angles and average pressure rise agree with maximum differences of respectively 0.6° and 0.03, which macroscopically is relatively good. A more significant difference can be noted in the average loss when comparing the cases with aspiration both on hub and blades to the experiments. The predictions differ by up to 2.1% from the experimental results. Nevertheless the macroscopic agreement and the reproduction of flow features caused by complex three-dimensional flow mechanisms allow using the numerical results to obtain indications on how the aspiration influences the flow.
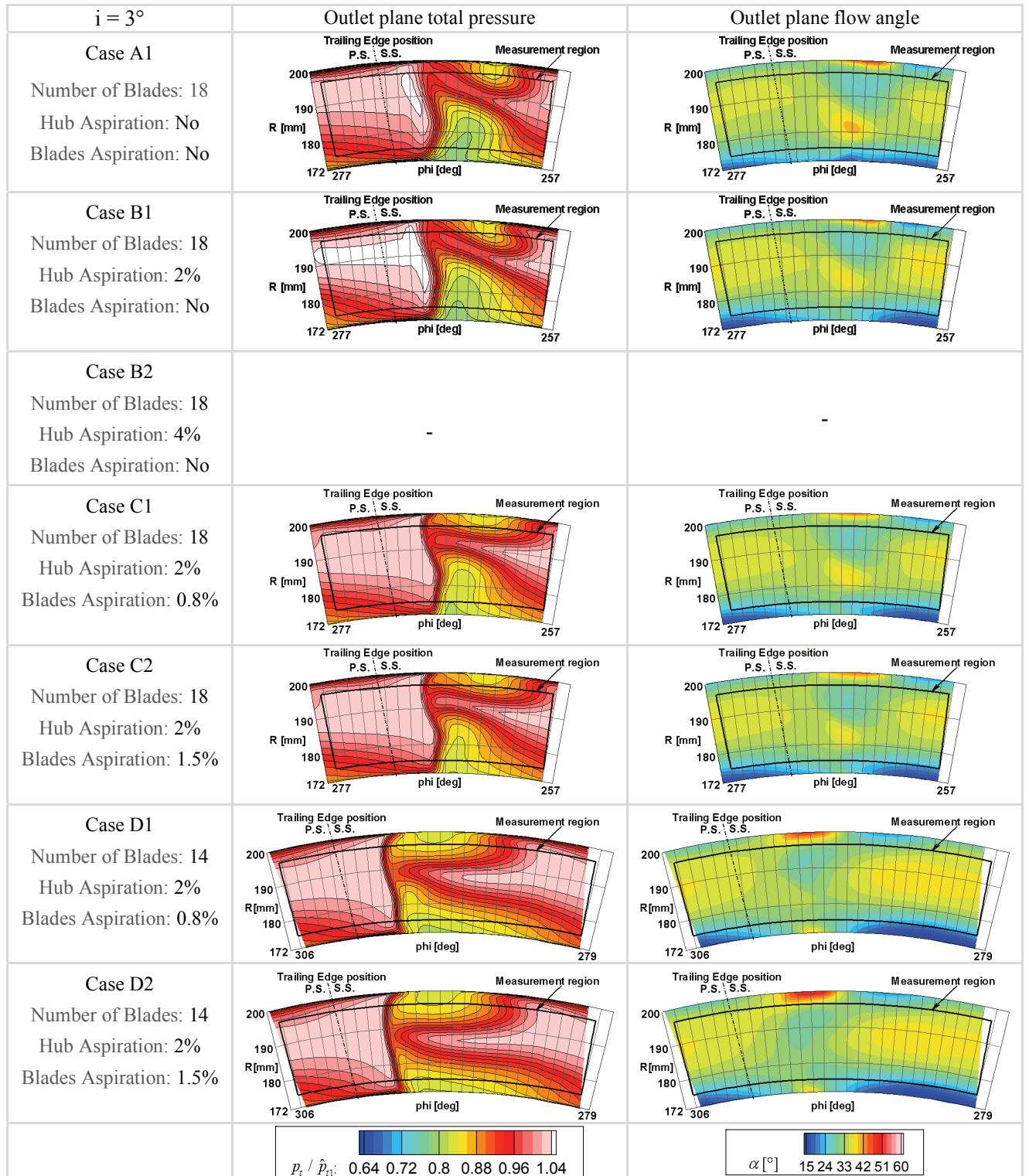
Figure 12-19. *Non-dimensionalized total pressure and flow angle resulting from the simulations in a plane corresponding to the outlet measurement plane for the 3° incidence cases and different configurations.*

12.4 Detailed analysis of the influence mechanisms of the aspiration

12.4.1 Influence of the aspiration on the total pressure distributions

Figure 12-20 shows the total pressure distributions resulting from the numerical simulations. The total pressure is plotted in corresponding axial planes for different configurations with inlet flow incidence 3°. As noted in the preceding section, case B1 is computed with an inlet flow boundary layer at hub that is thicker than the hub boundary layer that occurred in the measurements. This can be seen when comparing the total pressure level at hub in plane A with that in the other cases. These simulation results are nevertheless presented here since they give indications on the mechanisms involved with the aspiration on the hub.

With respect to the aspiration on the hub, in the interblade plane B, case B1 with 2% aspiration presents a thinner low total pressure region on the blade compared to case A1 and thus a thinner boundary layer on the blade, especially close to the hub. This results in higher total pressure levels in the separation trace in plane C. As a result, in the outlet plane D, even though the inlet boundary layer at hub was thicker than for case A1, the separation trace is less pronounced than in the case without aspiration. Thus the aspiration on the hub succeeds in reducing the accumulation of low total pressure fluid in the hub corner region.

In case C1, aspiration on blade with an aspiration rate of 0.8% is added compared to case B1 and the aspiration rate on blade is further increased to 1.5% in case C2. The level of aspiration on hub is kept at the same level as for case B1. In the results for case C1 it can be noted that in plane B, located right behind the blade aspiration slot, the low total pressure region is further reduced compared to the reference case A1 both in terms of spanwise and of circumferential extents. In case C2, this effect is increased. Thus, further on, in plane C, the resulting separation trace appears significantly reduced in size and intensity compared to case A1, especially close to the hub. This suggests that the aspiration on blade relieves the aspiration on the hub such that it can more effectively remove low total pressure flow from the corner region. This results in better total pressure levels in the outlet plane D. It must also be noted, that the trace of the clearance vortex, denoted by a low total pressure level close to the casing, is increasingly attracted towards the suction side in cases C1 and C2 starting in plane B. This can be ascribed both to an increased loading reinforcing the clearance flow as to the bending of the clearance flow streamlines towards the low pressure region caused by the aspiration on blade. As noted earlier, this yields an increased loss in the casing region in the cases with aspiration on blade that counterbalances to some degree the improvements obtained closer to the hub.

Cases D1 and D2 have a reduced number of blades and thus a reduced number of aspiration slots for the same total aspiration rate as cases C1 and C2. The aspiration momentum per slot is consequently higher than in the cases with more blades yielding an increased effect on the flow: the size of the low total pressure region on the blade is significantly reduced right after the blade aspiration slot in plane B. The size of the affected region increases in plane C compared to plane B but it does not reach the levels seen in the preceding cases. As a result, the trace of the separation in the outlet plane D is smaller in terms of spanwise extents. This further improves for the higher aspiration rate in case D2 compared to case D1. However, as noted earlier, the circumferential extents of the separation trace are more significant in the cases with reduced number of blades. Furthermore, also the intensification of the clearance vortex increases. These two effects counterbalance somewhat the improvements achieved by the aspiration close to the blade suction side.

A1: 18 blades – No aspiration

B1: 18 blades – Hub: 2% asp.

C1: 18 blades – Hub: 2 % asp. – Blades: 0.75% asp.

C2: 18 blades – Hub: 2 % asp. – Blades: 1.5% asp.

D1: 14 blades – Hub: 2% asp. – Blades: 0.75% asp.

D2: 14 blades – Hub: 2% asp. – Blades: 1.5% asp.
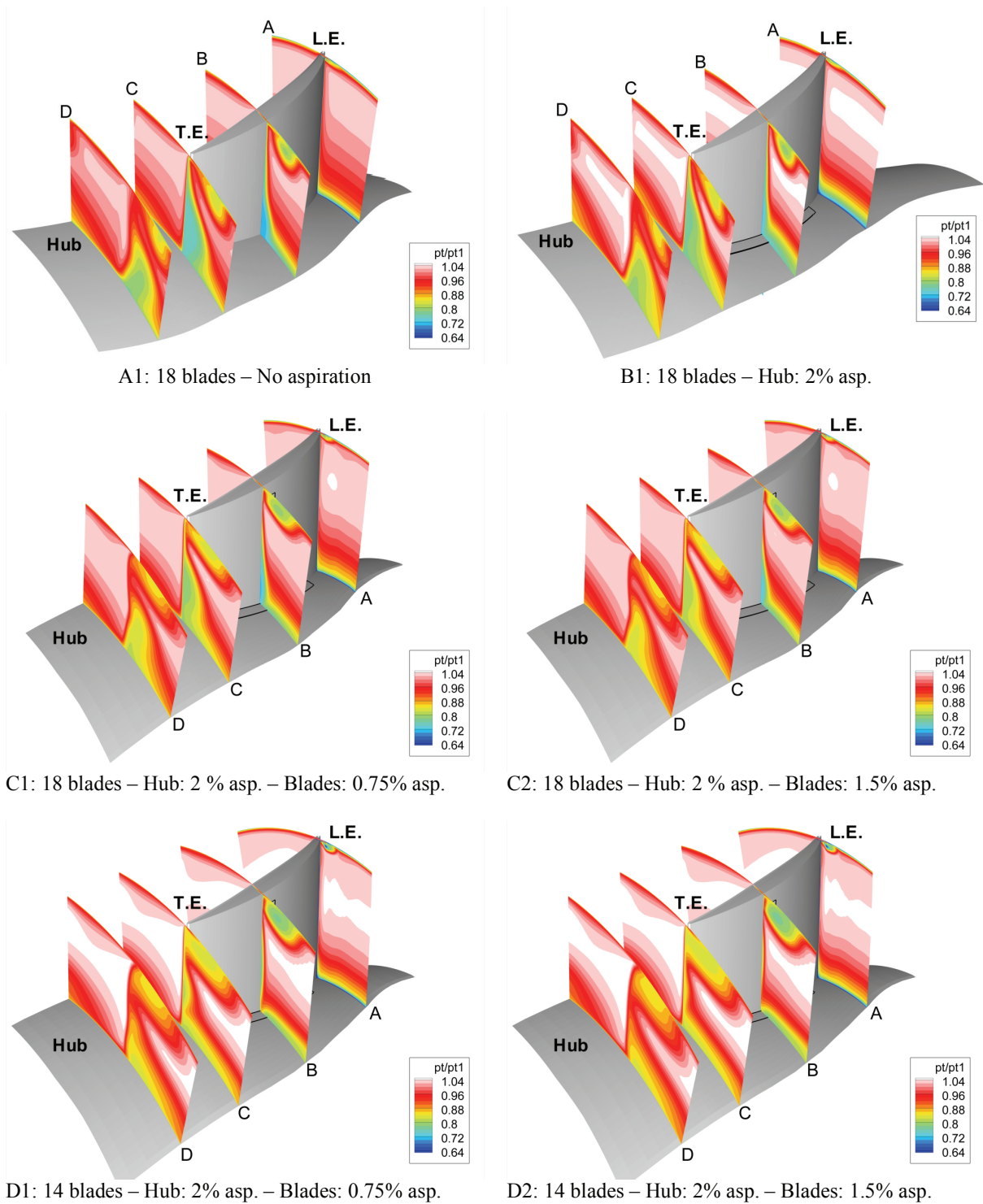
Figure 12-20. Total pressure plots based on numerical results for cases with 3° incidence and different configurations.

12.4.2 Influence of the aspiration on the vorticity magnitude distributions

In analogy to Figure 12-20, Figure 12-21 shows the vorticity magnitude distributions resulting from the numerical simulations. As annotated, these plots point out three significant flow features: the suction side boundary layer, the vorticity related to the clearance vortex and the vorticity related to the wake.

In the reference case A1, it can be clearly noted in plane B that close to the hub, the suction side boundary layer begins to rise above the corner separation. In contrast, for case B1, the boundary layer in plane B seems diminished close to the hub by the added hub aspiration and does not rise away from the suction side. However further on, in plane C, the suction side boundary layer of case B1 appears clearly rised away from the suction side, but the length of the trace is reduced compared to case A1. This yields a slightly diminished intensity of the suction side boundary layer trace in the outlet plane D. Thus, the hub aspiration prevents some low momentum and high vorticity flow of the suction side boundary layer from rising into the main flow, which reduces the caused mixing loss and thus the average loss. However, the vorticity related to the clearance vortex and the vorticity in the wake are intensified. This might be ascribed to the increased loading that promotes the blade boundary layer growth and the clearance flow. The intensification of the clearance vortex can also be related to the increased attraction of the vortex by the aspiration.

Adding aspiration on blade as is done in case C1 remarkably reduces the suction side boundary layer trace in plane B. This effect is augmented when the aspiration on blade is increased in case C2. Still, the subsisting boundary layer is rised above the separated region as can be noted on plane C. However, the intensity of the trace resulting in plane D is significantly reduced compared to the preceding cases, which is beneficial due to the improved flow uniformity and the prevention of mixing loss. However, as for case B1, the intensity of the vorticity related to the clearance vortex is increased. The wake trace in the outlet plane is more distinct. Both effects might be related to the increased loading. As for case B1, the intensification of the clearance vortex can also be related to the increased attraction of the clearance vortex by the aspiration.

In case D1 and D2, the trace of the suction side boundary layer in plane B is further, significantly reduced compared to cases C1 and C2. As a result its trace in the outlet plane can not be distinguished. This can be ascribed to the increased aspiration rate per slot that is caused by the reduction of the number of blades with unchanged overall aspiration rate. The beneficial influence of the aspiration seems thus augmented in cases D1 and D2. As for the preceding cases, the higher aspiration momentum also increases the intensity of the vorticity related to the clearance vortex. The wake trace intensity is comparable to that of cases C1 and C2 which might be related to the fact that the loading is only slightly increased in cases D1 and D2 compared to C1 and C2. Differently than in the preceding cases, the relevance of a further effect increases: the trace of the hub boundary layer in cases D1 and D2 has increased intensity in plane B compared to case C1 and C2. This produces a diffuse trace of increased vorticity in planes C and D which is parallel to the hub but slightly rised away from it. This suggests that some of the low momentum fluid observed in this region in Figure 12-20 actually comes from hub boundary layer that did not reach the suction side and not from the corner separation. An explanation based on two factors is proposed: first, the increased blade pitch increases the hub wall length between the blades. Second, the increased aspiration momentum promotes the cross-passage flow. As a result of these two factors, more flow crosses the passage along the hub over an increased wall length, yielding an increased growth of the boundary layer size and thus a higher intensity of the trace in the outlet plane.

A1: 18 blades – No aspiration

B1: 18 blades – Hub: 2% asp.

C1: 18 blades – Hub: 2 % asp. – Blades: 0.75% asp.

C2: 18 blades – Hub: 2 % asp. – Blades: 1.5% asp.

D1: 14 blades – Hub: 2% asp. – Blades: 0.75% asp.

D2: 14 blades – Hub: 2% asp. – Blades: 1.5% asp.
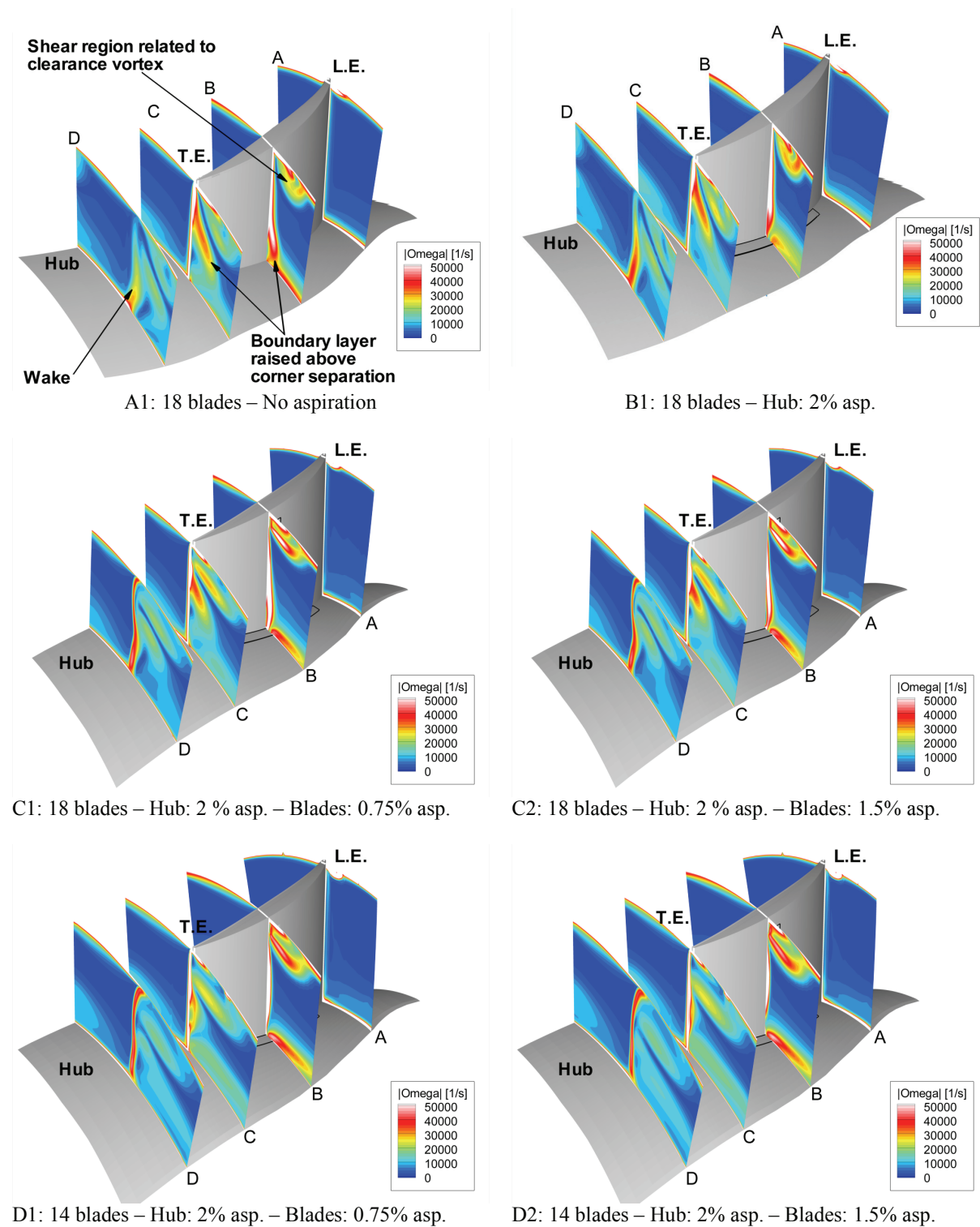
Figure 12-21. Vorticity magnitude plots based on numerical results for cases with 3° incidence and aspiration for configurations A1, B1, C1, C2, D1 and D2.

12.4.3 Detailed analysis of a case with aspiration on the hub

To understand the flow mechanisms related to the aspiration, a more detailed analysis must be performed: Figure 12-22 shows the flow visualization results for inlet conditions close to 3° incidence and aspiration configuration B1 with 2% aspiration on the hub. As can be noted on the picture to the left, the skin friction lines along the hub are directed towards the aspiration slot. This is normally induced by the secondary motion of the hub passage vortex but it is natural to assume that it is augmented by the sink effect of the aspiration. Most skin friction lines in this region of the hub are directed towards the aspiration slot. Only the skin friction lines that reach the suction side past the aspiration slot are oriented towards the trailing edge and not towards the aspiration slot on the hub.

On the blade suction side, the trace of a separated region is denoted by an area without paint. On the separation line that delimits the trace, paint is continuously advected and removed forming white foam. The separation trace starts close to the beginning of the hub aspiration slot, growing in spanwise direction when approaching the trailing edge. The skin friction lines on the suction side above the separated region are compressed together. This reflects the aerodynamic blockage constituted by the separated region.

The interpretation is supported by considering the skin friction line distribution resulting from the simulations for the case B1. They are presented on the left column in Figure 12-23: the plot indicates a comparable separated region on the suction side as noted in the visualization. In the plot, a further important feature can be noted in the front region of the hub aspiration slot: the numerical results predict a reversed flow orientation. This is indicated by the positive sign of the velocity component oriented normal to the aspiration surface V_{norm}, as well as by the skin friction line orientation. Thus, according to the simulation, the flow is not aspirated in to the aspiration slot in the front region but it spills out from the slot instead. The experimental flow visualization picture to the right of Figure 12-22 showing a close-up view of the front part of the hub aspiration slot confirms this flow behaviour in the experiment: the skin friction lines on the hub approaching the slot side opposed to the suction side are not attracted directly to the slot but rather bent away from the slot for a certain distance before turning towards it. This can be explained by the fact that the slot is blowing in this region instead of sucking. This is not contradicted by the stream traces to the right in Figure 12-22 that approach the aspiration slot closer to the suction side: they appear to head directly to the front edge of the slot. As plausibly suggested by the numerical results, this is the trace of streamlines that indeed head towards the front part of the slot, but eventually separate from the hub and rise above the flow spilling out from the slot.

As can be noted in the close-up view of the numerical results for case B1 shown in the right column of Figure 12-23, the flow spilling out from the front region of the hub aspiration slot makes the flow in case B1 actually separate earlier than in the reference case A1 of which a close-up view is presented right above in the same figure. However further downstream of the region of case B1 with flow spilling out from the slot, the skin friction lines on the suction side and on the hub bend back towards the aspiration slot. This indicates that starting there, the aspiration successfully removes flow from the hub boundary layer and from within the separation. This causes a reduced spanwise size of the separation in this region compared to the results for the case A1. Only towards the trailing edge, the separated region in case B1 grows to a spanwise size that is similar to that of the reference case. Nevertheless, as observed in the total pressure plots in Figure 12-20, the removal of low total pressure flow by the aspiration slot on the hub yields reduced circumferential extents and reduced intensity of the low total pressure trace of the hub corner separation. The complex conditions that induce the flow to spill out from the front part of the hub aspiration slot will be investigated more in detail in the section 12.4.6.
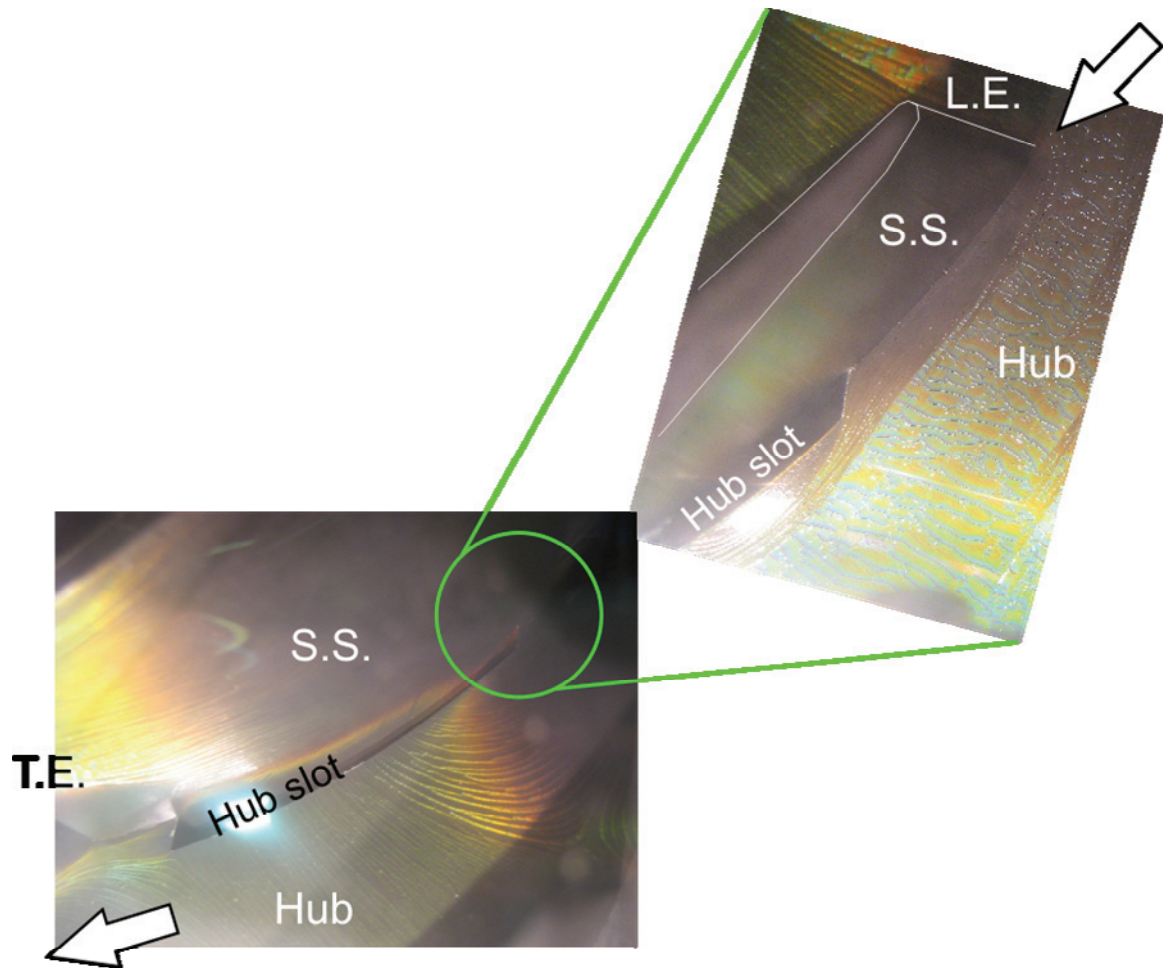
Figure 12-22. Flow visualization for flow conditions close to 3° incidence with aspiration on the hub (B1). The picture to the right was taken earlier than the picture to the left, thus most skin friction traces on the hub did not form yet.

The fact that in the numerical results the skin friction lines in the separated region on the suction side are all originated from the front part of the aspiration slot suggests why there is no trace of paint in the separated region of the flow visualization inFigure 12-22: the separated region is mainly fed by flow spilling out from the front section of the slot. Within the duct of the aspiration slot, no paint was applied before the experiment. Thus, the aspirated flow most probably disperses the paint that it might carry within the aspiration duct during the recirculation that makes it reverse its flow direction. Thus the flow spills out from the slot rather clean causing a clean blade surface within the separation.

A1: 18 blades – No aspiration:

B1: 18 blades – Hub: 2% aspiration ($C_{Q,Slot} = 0.11\%$)
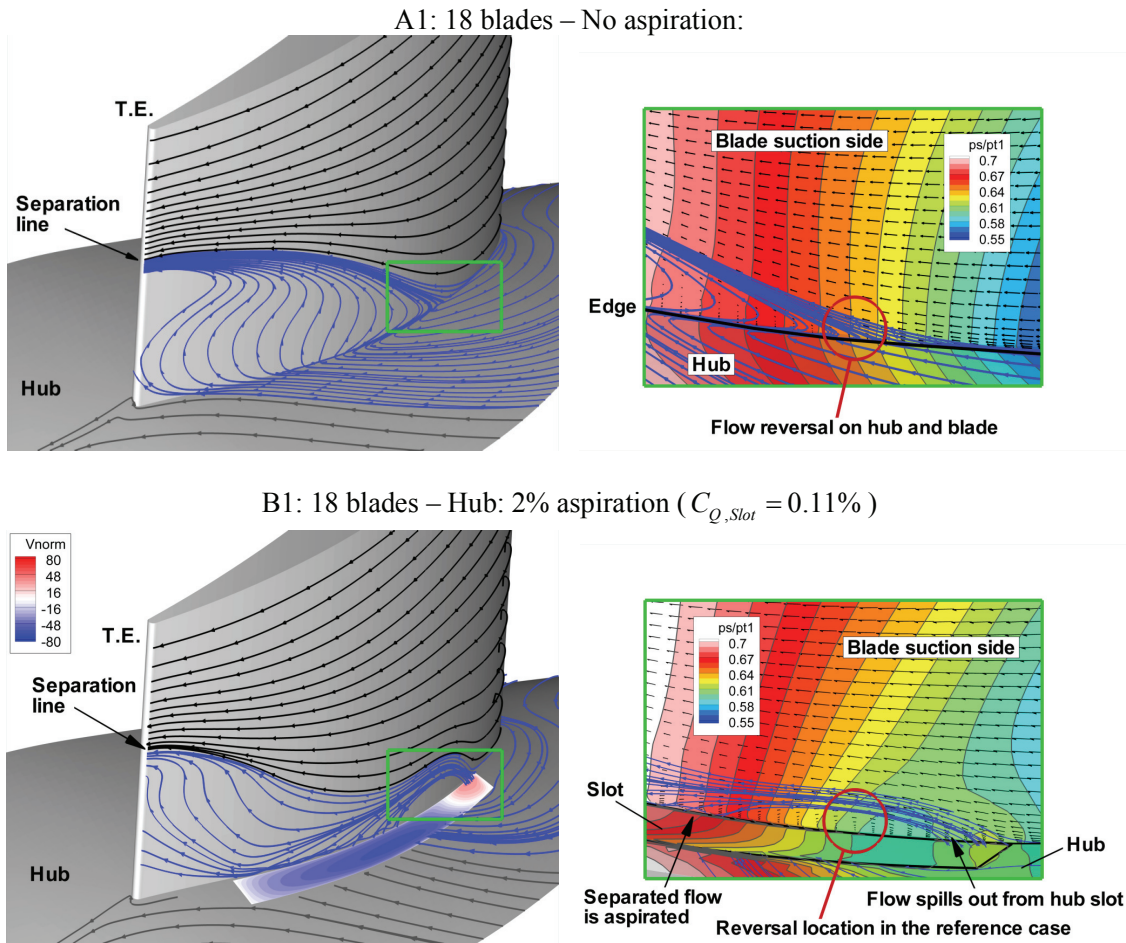
Figure 12-23. Comparison of the skin friction line and the static pressure plots based on the numerical results for cases with 3° incidence and different aspiration configurations (A1 and B1).

Summarizing, the aspiration slot on the hub is noted to induce an earlier separation start compared to the reference case. This is ascribed to flow spilling out from the front part of the aspiration slot. However, due to the successful removal of low momentum flow from the hub boundary layer and the separated region further on, the low momentum and the low total pressure trace in the outlet plane is reduced. The successful extraction on most of the aspiration slot length causes the noted improvements as reduced separation trace, reduced blockage, improved deflection and pressure rise.

12.4.4 Detailed analysis of a case with aspiration on the hub and on the blade

For the cases with aspiration both on the blades and on the hub, no flow visualization is available since the paint would have compromised the accuracy of the measurement instrumentation used to measure the mass flow aspirated from the blades. However, since the numerical results yield similar distributions in the outlet flow planes as the experiments, the underlying macroscopic mechanisms are assumed to be correctly reproduced by the numerical model. Thus the simulation results are analysed hereafter to yield insight to the flow mechanisms caused by the added aspiration. It must be however noted that the numerical results for cases with aspiration on blade were noted to be more optimistic on the impact of the aspiration than the experiments. Thus especially the significant improvement predicted by the simulations for configuration D2 reflect trends that are also noted but that are less pronounced in the the experimental results.

C2: 18 blades – Hub: 2 % asp. ($C_{Q,Slot} = 0.11\%$) – Blades: 1.5% aspiration ($C_{Q,Slot} = 0.08\%$):
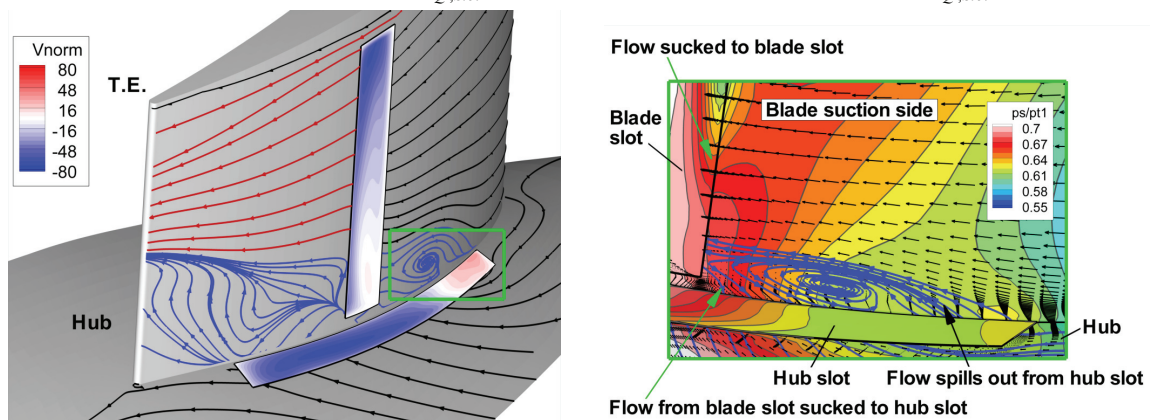
Figure 12-24. Skin friction line plot and the static pressure distributions based on the numerical results for cases with 3° incidence and configuration C2.

In Figure 12-24, the skin friction line plot for case C2 with same number of blades and hub aspiration rate as case B1 but added 1.5% aspiration rate on the blade is presented. It can thus be compared to the analogous plots for case B1 and A1 presented in the preceding section. The flow situation in case C2 is rather complex. Thus the skin friction lines are coloured to allow distinguishing them in the discussion: the black skin friction lines come directly from the inlet of the cascade. Most of the black lines on the hub end up at the hub aspiration slot indicating that the flow right above, consisting mainly of hub boundary layer, is successfully aspirated. Similarly, the black lines on the blade suction side ending up in the blade aspiration slot indicate that the flow right above, thus the blade boundary layer, is aspirated into the slot. This is reflected by the reduced vorticity magnitude of the suction side boundary layer noted in plane C in Figure 12-21 for cases C1 and C2 compared to the suction side boundary layer traces for cases A1 and B1. Back in the skin friction line plot for case C2 in Figure 12-23, the red skin friction lines start right behind the blade aspiration slot. They indicate that the flow right above reattaches to the blade suction side, replacing the flow that was removed by the aspiration. The skin friction lines involved in separated regions close to the hub are coloured in blue.

It can be noted that similarly to the cases with aspiration only on the hub, the simulations indicate that the flow spills out from the front region of the hub aspiration slot. This is indicated by the positive sign of the flow velocity component normal to the aspiration surface V_{norm} plotted in the slot region. However, the region affected by flow reversal is larger than in the cases with aspiration on the hub only. Furthermore, a nodal point of type separation focus appears on the skin friction line pattern on the suction side. It is located above the hub slot in coincidence with the region where the normal velocity changes sign. This

nodal point denotes a separation above a point (compare to Figure 4-2 in section 4.1.2), thus the flow converges to this point before separating from the surface spinning around a separation line and forms a vortex. To illustrate the flow behaviour above this point, streamlines coloured in green are added to the skin friction line plot in Figure 12-25. They indicate that the vortex arised from the focus is aspirated back into the aspiration duct. The focus represents the center of the recirculation formed by the flow spilling outwards at the front of the hub slot and back inwards further downstream. It was present also in case B1 but it was hidden within the hub aspiration slot duct. In case C2, the aspiration on the blade apparently pulls the center of the recirculation into the blade channel such that it can be seen in the skin friction line pattern on the suction side. It causes thus a larger disturbance to the main flow in the close region. A more detailed analysis investigating the reasons for this vortical structure to occur is given in section 12.4.6.
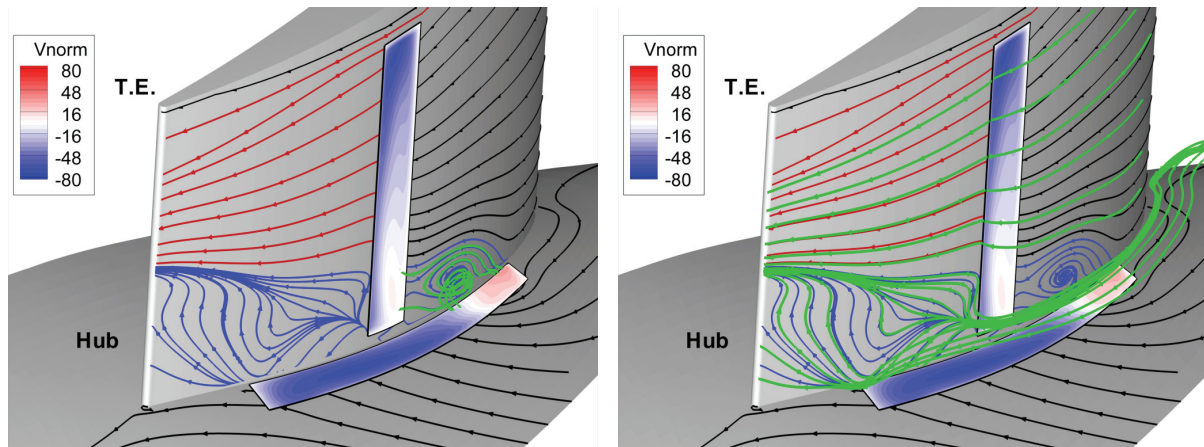
Figure 12-25. Streamline plots (green) superposed to the skin friction line plots for case C2 with 3° incidence. Left: streamlines highlighting the vortex aspirated into the hub slot. Right: streamlines reattaching after the blade aspiration slot.

As can be noted in the close-up view for case C2 on the right column of Figure 12-24 the separated region begins at a very similar location to that in case B1. Furthermore, up to the node location, the flow is involved in the separation for a similar spanwise height as in case B1. However, further downstream, up to the blade aspiration location, the spanwise height of the separation does not decrease as as much as in in case B1 but is higher than in case B1. As a consequence, the size of the separated region at this location is slightly higher in spanwise direction in case C2 than in case B1. This is related to a further mechanism that must be noted: close to the hub, the flow through the plotted inlet plane of the aspiration slot on the blade has almost zero normal velocity. The flow direction is even reversed at the front edge of the slot. The blade aspiration slot effectively aspirates flow only on its upper part, towards the casing. Thus, close to the hub, some flow spills out from the blade aspiration slot and is also attracted towards the separation focus before being aspirated into the hub aspiration slot in the observed vortex.

Behind the blade aspiration slot, the skin friction line pattern shown in the plot on the left column of Figure 12-24 for case C2 indicates that the flow separation close to the hub persists. To clarify the separation structure, the region occupied by the separation is illustrated by the isosurface rejoining points with Mach number 0.10 presented in Figure 12-26. The separation trace is surprisingly undisturbed by the aspiration on the blade in the region close to the hub. This can be related to the indicated low aspiration velocity close to the hub. Nevertheless, the separation has a slightly reduced spanwise height in the region behind the blade aspiration slot compared to case B1. When considering the overall flow, it can be noted that apart of the problematic regions described above, certain amounts of low momentum flow are successfully removed by the aspirations, yielding the improved total pressure levels that can be noted in Figure 12-20 compared to cases B1 and A1: especially close to the hub, for case C2, the extents in

circumferential direction (and not in spanwise direction) of the separation trace in plane C is reduced compared to cases B1 and A1, reflecting the extraction of low momentum fluid. At small distance from the hub, the circumferential size of the separation trace increases, but it is still smaller than for cases B1 and A1. The green streamlines added to the skin friction line plot for case C2 presented to the right of Figure 12-25 indicate the origin of the flow in the separation behind the blade aspiration slot: the separation is fed by flow reattaching to the blade surface right after the aspiration slot at the spanwise height where the flow velocity into the blade aspiration slot is low or reversed. The flow is then partially attracted back towards the aspiration slot on the blade and partially down towards the aspiration slot on the hub. Closer to the trailing edge, the separation is fed by flow coming from above the hub boundary layer that first reattaches to the hub close behind the hub aspiration slot and is then raised into the separated region.
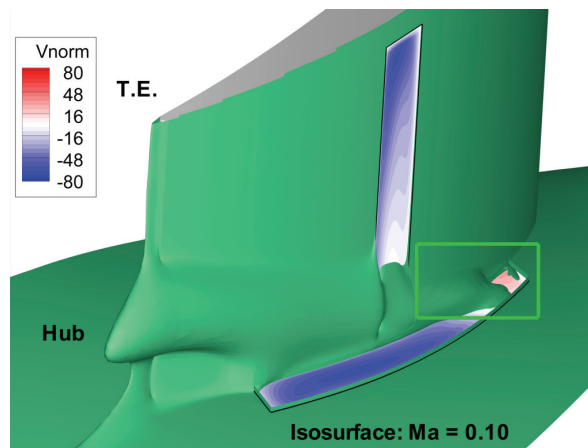
Figure 12-26. Isosurface plot for configuration C2 with 3° incidence connecting points with Mach number 0.10 to highlight the regions affected by the corner separation.

Summarizing, the aspiration slot on the blade removes some fluid from the suction side in the region between the casing and down to some distance of the hub. In this region it yields the reduced blade boundary layer thickness observed in Figure 12-21. This influence of the blade aspiration must relieve the hub aspiration slot, since the hub aspiration slot more effectively removes low momentum fluid very close to the hub, yielding the reduced circumferential extents of the separation close to the hub noted in the total pressure plots in Figure 12-20. However, still, a separation region forms on the suction side. Differently than in case A1 where the separation onset is spontaneous, in the analyzed case C2, as in case B1, it seems initiated where the flow spills out from the front of the hub aspiration slot. It can be assumed that if this effect could be avoided, the improvement due to the aspiration would be higher. In case C2, the separated region is slightly higher in spanwise direction close before the blade aspiration slot. This is caused by the recirculation vortex occurring in the hub aspiration duct involved in the flow spilling out from the hub aspiration slot that is most probably attracted by the aspiration on blade into the blade passage. In its bottom part, the blade aspiration slot is ineffective: the flow crossing its inlet plane is slow or even reversed and attracted towards the hub aspiration slot. Thus the separation sets forth past the blade aspiration slot. There, its spanwise size is only slightly reduced compared to case B1 and A1 and the aspiration on blade causes some flow reversal within the separation. However, in contrast to the spanwise extents at the described locations, the circumferential extents of the separation are reduced compared to case A1 and B1 by the increased removal of low momentum flow from the hub boundary layer and from within the corner separation. This yields the improved total pressure level at outlet. The consequently reduced blockage improves the diffusion and deflection of the flow, herewith improving the compressor performance in this region.

12.4.5 Detailed analysis of a case with aspiration on the hub and on the blade and reduced number of blades

Figure 12-27 shows the skin friction line plot and static pressure distributions for case D2. Case D2 has the same overall aspiration rates on the hub and on the blades as case C2 discussed above but a reduced number of blades. Thus the aspiration rate per slot on the hub is 0.14% in case D2 instead of the 0.11% in case C2 and the aspiration rate per slot on the blade is 0.11% in case D2 instead of the 0.08% in case C2. The skin friction line plot of the numerical results for case D2 indicates that the spilling out from the flow from the hub aspiration slot does not occur in case D2: the increased aspiration rate per slot supported by the lower pressure in the aspiration chamber behind the duct (see Table 12-3) draws the recirculation back into the aspiration duct on the hub. Hence, the onset of the separation on the suction side is successfully prevented. This is indicated by the black skin friction lines on the suction side that are mostly directed either to the hub or to the aspiration slot on the blade. The red skin friction lines indicate that behind the aspiration slot on the blade, the flow successfully reattaches to the suction side and stays attached up to the trailing edge. It is also noteworth that the aspiration velocity over the blade aspiration slot is more uniform than in the other cases. This is ascribed both to the increased aspiration rate as to the absence of the corner separation that in the other cases was triggered by the flow spilling out from the aspiration slot on the hub. This will be considered more in detail in section 12.4.7.

D2: 14 blades – Hub: 2 % asp. ($C_{Q,Slot} = 0.14\%$) – Blades: 1.5% aspiration ($C_{Q,Slot} = 0.11\%$):
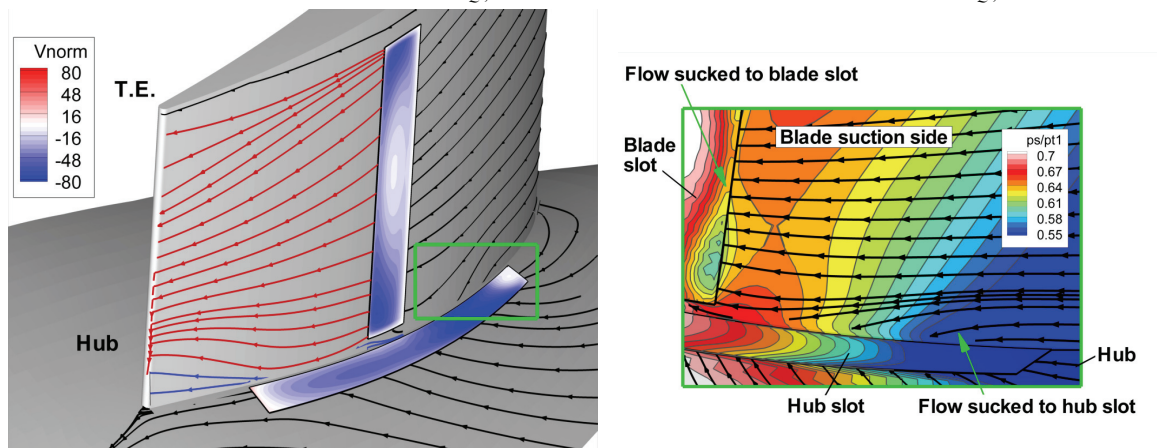
Figure 12-27. Skin friction line plot and static pressure distributions based on the numerical results for cases with 3° incidence and configuration D2 with reduced number of blades.

The close-up view for case D2 to the right of Figure 12-27 confirms how the skin friction lines are directed towards the aspiration slots. Furthermore it indicates how the regions of successful aspiration towards the slots correspond to regions of low static pressure that can be ascribed mainly to the increased aspiration rate per slot and thus to the lower static pressure in the aspiration duct (see Table 12-3).

The improved influence of the aspiration on the hub and on the blades in case D2 yield a significant reduction of the low total pressure traces noted in Figure 12-20. The low total pressure trace caused by the corner separation in the other cases is almost completely replaced by higher total pressure levels in case D2. However, as noted earlier, the increased aspiration rate per slot as well as the increased blade pitch cause an increased low total pressure trace of the clearance vortex that counter-balances the improvements related to the supression of the corner separation. Furthermore, as was observed in the plots of vorticity magnitude in Figure 12-21, the size of the boundary layer close to the hub is increased due to the increased blade pitch and the cross passage motion along the hub towards the suction side supported by the aspiration on the hub. Summarizing, the performance of case D2 is improved by the

increased aspiration rate per slot, but this improvement is reduced by the increased intensity of the clearance vortex and by the thicker hub boundary layer. Thus, applying aspiration in case D2 with the same overall aspiration rate as in case C2, can counter-balance to some extent the detrimental effects of reducing the number of blades. This is achieved by the improved control of the corner separation that is improved mainly by the prevented flow spilling out from the front region of the hub aspiration slot.

12.4.6 Flow in the hub aspiration duct

Since the recirculation causing the flow to spill out from the hub aspiration slot is identified as being relevant in the initiation of the corner separation in the cases with aspiration, its causes are investigated here more in detail. The analysis will first focus on case C2, where the recirculation is observed directly in the blade passage. After this, case D2 will be considered, where no trace of the recirculation is visible in the blade passage, but where it retreats into the hub aspiration duct.

First, it must be considered that even though a low pressure is applicated at the bottom of the hub aspiration duct, the pressure field within the duct will adjust itself according to the pressures caused by the main flow within the blade channel above it. Of course these are in turn influenced by the aspiration slot. However, macroscopic features as the low pressure caused by the main flow deflected and accelerated by the blade suction side geometry are not necessarily overmatched by the influence of the aspiration slot. As can be noted by the close-up views on the right of Figure 12-23 and Figure 12-27, the pressures levels occurring on the suction side extend into the aspiration slot. As a result, the adverse pressure gradient occurring on the suction side will also occur within the aspiration duct, at least close to the slot edge. As a consequence, low momentum flow within the slot will be deflected towards the lower pressure in the front section of the slot.

A second indication for the causes of the recirculation is given by the following analysis of the flow based on the numerical results for a case with 3° incidence and aspiration configuration C2. The plot in Figure 12-28 shows selected streamlines entering the hub aspiration slot and their behaviour in the aspiration duct. The plot of the velocity component normal to the aspiration slot surface in the same figure indicates that a region of reversed flow occurs on the duct wall that is opposed to the suction side. This indicates that the incoming hub boundary layer flow separates right after passing the sharp edge of the aspiration slot. As indicated by the plotted streamlines, some of the incoming low momentum fluid recirculates in a separation bubble close to the wall instead of being aspirated further into the duct. As denoted by the streamlines, the flow within this recirculation region is attracted towards the front part of the slot. This can be explained by the adverse pressure gradient imposed by the main flow described in the preceding paragraph. The flow reaching the front part of the slot has low momentum and increased levels of vorticity caused by the wall friction and the redirection. Thus this flow is prone to induce vortical structures as will be analyzed further on. This low momentum flow accumulation in the front part of the slot is exposed to the low pressure occurring on the suction side, which can explain why it is attracted out of the aspiration slot causing the disturbances to the main flow observed earlier.
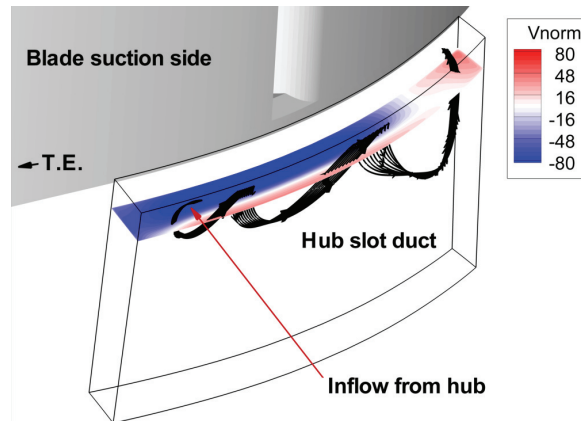
Figure 12-28. Plot of streamlines entering the hub aspiration duct, separating and being attracted towards the front region for configuration C2 with 3° incidence. Vnorm is oriented normal to the slot surface.

As noted, the flow separating in the aspiration duct short after crossing the aspiration slot edge can induce complex vortical structures. The skin friction line plots in Figure 12-29 for case C2 give an idea of the nature of those structures and how they can induce the focal point observed on the blade suction side. The plot to the left of Figure 12-29 shows the skin friction lines on the duct wall opposed to the blade suction side. There it can be noted that the skin friction lines within the separated region are oriented towards the front of the aspiration slot. The annotated reattachment line indicates the region where further aspirated flow reattaches to the duct wall and is successfully aspirated towards the duct outlet.

C2: 18 blades – Hub: 2 % asp. ($C_{Q,Slot} = 0.11\%$) – Blades: 1.5% aspiration ($C_{Q,Slot} = 0.08\%$):
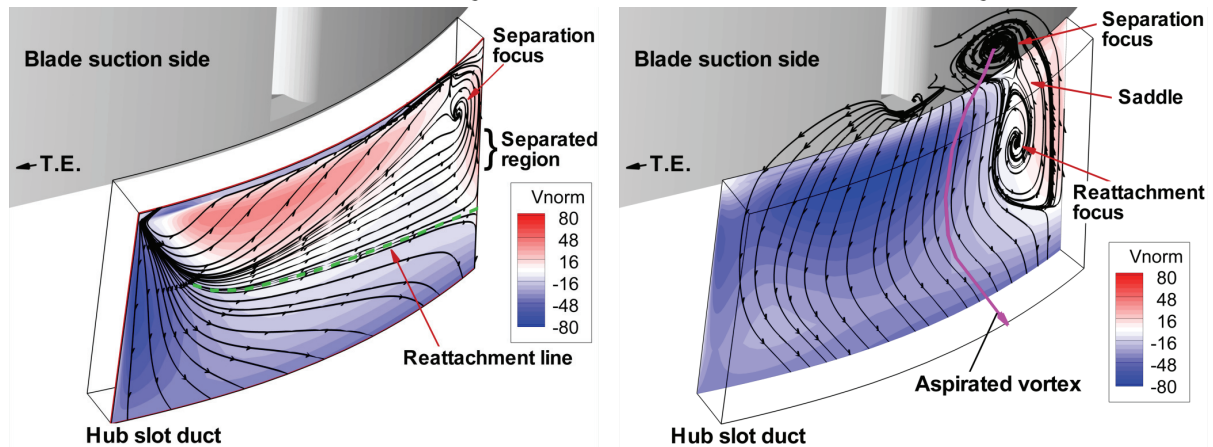
Figure 12-29. Plots of the skin friction lines on the hub aspiration duct walls for configuration C2 with 3° incidence. Vnorm is oriented normal to the slot surface. It is plotted for a plane at some distance from the wall.

The flow from the separation bubble induces a separation focus on the duct wall from which a vortex starts that is directed towards the opposed wall below the blade suction side. The vortex ends on the reattachment focus on the opposite wall that is shown to the right of Figure 12-29. The reattaching flow is then attracted to the blade channel and the flow spills out from the hub aspiration slot. However it is soon reattracted towards the hub aspiration slot forming the separation focus observed on the suction side wall. This flow is certainly also influenced by the close aspiration slot on the blade. As can be noted, the separation focus is closely related with the reattachment focus: a saddle can be noted between the two

focal points, suggesting that a separation surface exists that crosses the saddle and is rolled up by both foci. Finally, the flow arising from the separation focus on the suction side forms a vortex attached to the suction side wall that is aspirated back into the aspiration slot as indicated by the arrow coloured magenta in Figure 12-29.

As observed in section 12.4.5, the flow spilling out from the hub aspiration slot in to the blade channel does not occur in case D2. This is explained by the plots of the skin friction lines on the hub aspiration duct walls for case D2 presented in Figure 12-30. As can be noted by the location of the reattachment line in the plot to the left, the separated region in case D2 is significantly smaller than in case C2. Furthermore,, as indicated by the plot to the right, the region of recirculation occurs deeper within the aspiration duct and thus does not cause flow to spill out from the aspiration slot. Since the static pressure distribution for this case presented in Figure 12-27 does not indicate a reduced static pressure gradient in case D2, this must be excluded as cause for the improvement. Thus the cause is identified in the increased aspiration rate going with lower static pressure levels at the outlet of the hub aspiration duct.

D2: 14 blades – Hub: 2 % asp. ($C_{Q,Slot} = 0.14\%$) – Blades: 1.5% aspiration ($C_{Q,Slot} = 0.11\%$):
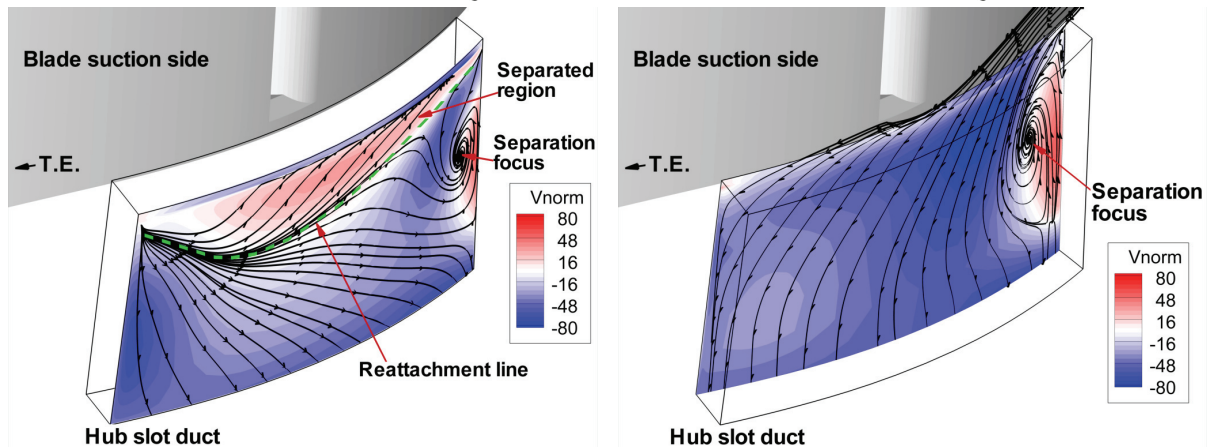
Figure 12-30. Plots of the skin friction lines on the hub aspiration duct walls for configuration D2 with 3° incidence. Vnorm is oriented normal to the slot surface. It is plotted for a plane at some distance from the wall.

Summarizing, the observed complex recirculation zones in the hub aspiration duct can be related to the separation on the aspiration duct wall submitted to the pressure gradients induced by the blade passage pressures above the slot. Since in case C2 the recirculation extends into the flow path, it makes flow spill out of the hub aspiration duct causing the problematic separation onset. Thus a solution to avoid this phenomenon would be an optimisation of the aspiration slot with the target of avoiding either the separation on the duct wall or the flow redirection caused by the adverse pressure gradient. The separation could be prevented by geometrical modifications as avoiding the sharp edge of the slot. The influence of the adverse pressure gradient can be mildered by adding a segmentation of the slot to limit the reversed motion in the duct. Observing the results for case D2, another solution can be an increased aspiration massflow in the slot. In case D2 this occurs at no additional cost in terms of overall aspiration rate since the number of blades is reduced. However if the number of blades would be kept constant, a further increase of aspiration rate would increase the cost in terms of aspirated mass flow.

12.4.7 Flow in the blade aspiration duct

In the preceding sections it was observed that in case C2, only the region of the aspiration slot on the blade located closer to the casing effectively removes flow. The part closer to the hub was noted not to remove flow and even a small region of reversed flow can be seen in Figure 12-24 indicating that flow from the blade aspiration slot is attracted towards the aspiration on the hub. Instead, in case D2 with

reduced number of blades and thus increased aspiration rate per slot, the aspiration slot on the blade removes flow much more effectively as can be seen in Figure 12-27. To investigate this effect, the Mach number distribution in a median plane through the aspiration duct within the blade are plotted based on the numerical results of cases C1, C2 and D2 in Figure 12-31. In addition, the skin friction line distribution on the back wall of the duct (the wall oriented towards the pressure side of the blade) are plotted, as well as the Mach numbers resulting at the aspiration slot inlet.

The plots in Figure 12-31 indicate that the highest Mach numbers occur in the part of the slot oriented towards the trailing edge of the blade whereas in the other parts of the duct the Mach number is significantly lower. This can be explained by the fact that the aspirated flow has a certain forward momentum pressing it againts the trailing edge side of the duct. Comparing the results for case C1, C2 and D2 it can be noted that most flow enters into the slot outside of the separated region identified in the hub corner of the blade passage earlier on. In case D2, where no separation occurs, the flow enters effectively also close to the hub. This suggests that the aspiration slot is most effective, where the forward momentum of the flow supports the movement into the slot. This can certainly be related to the geometry of the slot which is bent towards the trailing edge as illustrated in Figure 6-6. Thus, in cases C1 and C2, most flow will enter close to the casing, while close to the hub, internal recirculations occur in the duct that don't support the aspiration. Comparison of the plot for case C1 to the plot of case C2 where only the rate of aspiration on the blade is increased indicates that higher aspiration rates progressively counteract aspiration from being favoured only in the casing region. A larger spanwise height of the blade slot effectively removes flow. The lower pressure in the aspiration duct promotes that the incoming flow is even deflected backwards, increasing the flow velocity in the duct part oriented towards the leading edge. Hence the increased rate of aspiration on the blade reduces the size of the separated region on the blade. In case D2, the onset of the corner separation is successfully prevented. This is ascribed mostly to the fact that the recirculation making flow spill out from the hub aspiration duct in other cases is completely drawn back into the hub aspiration duct in case D2 as noted in the preceding section. Due to the absence of the corner separation, all the flow passing the aspiration on the blade is oriented forward. The forward momentum promotes the aspiration into the blade slot and the aspiration is further promoted by the higher aspiration rate due to the reduced number of blades. This results in a more effective aspiration in the duct as indicated by the higher Mach numbers and reduced recirculations in the blade aspiration duct for case D2 in Figure 12-31. According to the mechanisms indicated in Figure 1-3, the aspiration on the blade reduces the pressure gradient that the boundary layer on the blade must override on the suction side up to the blade slot location, preventing separation. The aspiration removes some low momentum fluid of the blade boundary layer thus reducing the low momentum trace for case D2 as noted in Figure 12-20. These effects improve the diffusion, the deflection and thus the static pressure rise.
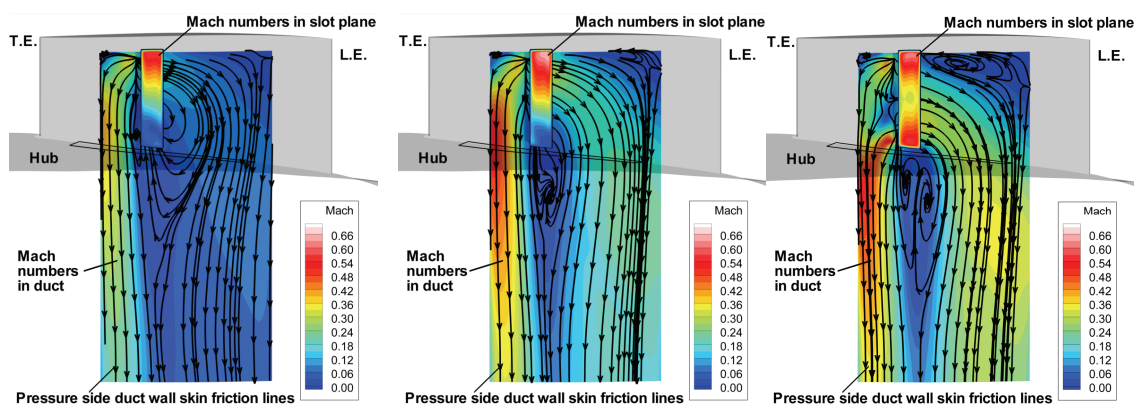
Figure 12-31. Flow within the blade aspiration duct for configurations C1, C2 and D2.

Summarizing, the blade aspiration slot is observed to most effectively remove flow that is oriented forward and thus oriented in direction of the slot geometry. In the cases where a separation in the hub corner occurs, this favours the aspiration close to the casing to the detriment of the aspiration in the separated region close to the hub. Increasing the rate of aspiration on the blade progressively counteracts this effect. However the best results are found in the case where the separation in the hub corner favoured by the recirculation in the hub aspiration slot is prevented. This is the case for configuration D2, where additionally the aspiration rate into the blade slot is further increased by the reduced number of blades. In this case the aspiration on the blade slot is very effective over most of its spanwise extents. It should be considered if the inclination of the slot should be modified to avoid favouring the aspiration of relatively sane, forward oriented flow. As for the hub aspiration slot it could be considered if by combination of segmentation of the slot and different slot diameters, the aspiration in specific regions could be augmented. In this case it should be augmented close to the hub. It should also be investigated if the gains due to suction side boundary layer removal close to the casing justify the slot to protrude up to the casing. Otherwise, the spanwise height of the slot could be reduced focusing the flow region close to the hub. This way, the slot would more effectively control the corner separation. As for the aspiration slot on the hub, also an increased aspiration rate is seen to improve the effectiveness of the flow removal. However, if the increase of aspiration rate is not related to a reduction of the number of extraction slots, this would cause increased costs in terms of extracted mass flow and is thus not recommended.

13. Conclusions

A simple model is introduced at the begining of this work for estimating the static pressure rise obtained by a stator cascade thanks to the application of the aspiration technique. It is based on the conservation of mass and total enthalpy. The model shows that static pressure rise in cases with aspiration compared to cases without aspiration can be increased by the reduction of the total pressure loss, by the increase of the deflection but also implicitly by the flow extraction per se. This is due to the fact that in the case with aspiration a reduced flow quantity crosses the same flow surface and thus diffuses more. The improvements targeted by the aspiration techniques investigated in this work go beyond the implicit effect: by aspiration at well determined locations, mechanisms causing loss, blockage and reduced deflection as the corner separation shall be prevented or at least be reduced. Furthermore, the extraction removes certain amounts of the low momentum fluid from the boundary layers. These effects yield gains in total pressure level and flow uniformity, increasing thus the deflection, the diffusion and the static pressure rise. In this work, it is furthermore investigated how this technique allows compensating the performance loss occurring when the number of blades of a cascade is reduced for otherwise unchanged conditions. If aspiration is applied to high pressure compressor stages, this aspiration can be driven by the pressure difference between the aspirated stage and the consumer of the aspirated flow without the need of additional pumps. The overall efficiency of the engine can be increased, if the gains obtained by the improvements in the compressor stages compensate the extraction of a certain amount of flow from the compressor. This is especially the case if the aspirated flow is used to feed other engine subsystems, as the turbine cooling or the leakage prevention. Of course this implies a minimazion of the pressure drop in the aspiration ducts by further optimization of the geometry of aspiration slots and ducts investigated here.

To verify and better understand the influence of aspiration, annular cascades with different aspiration configurations were tested experimentally in the EPFL Non-Rotating Annular Cascade Test Facility. The experimental results discussed in this work are based on measurements performed with same inlet Mach number of 0.8 and two inlet flow incidence angles: 3° and 5° with respect to a design inlet flow angle of 60° measured against the axis. Configurations without aspiration (reference cases), with aspiration only on the hub and with aspiration both on the hub and on the blades were tested with varied aspiration rates. Further tests were performed on a cascade with reduced number of blades to evaluate if the aspiration can compensate the increased loss caused by the reduced number of blades. Most measurements are based on aerodynamic five-hole probe measurements performed at the inlet and the outlet of the tested cascades. They are completed by static pressure measurements with pressure taps located on the mid-span section of selected blades, on the hub wall and on the casing wall. The probe measurements are complemented by detailed LDA measurements for selected cases that validate the probe measurements, allow estimating the uncertainty of the measurements and quantify the fluctuations. The measurements are complemented by numerical simulations for selected cases with 3° incidence. The computations were performed by the project partners and re-processed and analyzed in detail in this work. The results reproduce the main flow features encountered in the experimental investigations as well as the main trends. Thus the simulation results can be used and are thus used to analyze the flow mechanisms related to the features identified in the measurements and in particular to investigate the flow mechanisms related to the aspiration.

To analyze the trace of the complex three-dimensional flow features occurring within the cascades, a new method to extract the secondary velocities from the aerodynamic probe measurements is implemented. New results are compared to the results of a classical approach for secondary velocity extraction showing significantly improved detail and plausibility. Several flow features related to the secondary flow are identified with the support of the secondary velocity fields complemented by the analysis of the vorticity

and helicity fields. The explanation of certain features is supported by consideration of the transport equations for the vorticity and the helicity.

With respect to the aspiration technology, the experimental results indicate that if a sufficient aspiration rate is applied, the aspiration on the hub reduces the total pressure loss by removal of the low momentum fluid that is carried along the hub towards the suction side by the secondary flow. In the reference case without aspiration, this low momentum fluid accumulates in the hub corner separation. The separation disturbs the static pressure rise due to the aerodynamic blockage that it constitutes: first, the flow separated from the suction side yields a reduced deflection. Second, the helicity plots based on the probe measurements in the outlet planes indicate traces of the boundary layer raised away from the suction side by the separation, as confirmed by the numerical analysis. The suction side boundary layer raised into the main flow causes flow non-uniformities detected in the outlet plane measurement results and further total pressure loss due to the mixing with the main flow. The results show that by removing fluid from within the separated region and herewith reducing the separation size, the aspiration on the hub thus reduces the loss in terms of low total pressures at outlet, improves the static pressure rise and increases the blade loading. However the measurement results also show that the size of the clearance vortex trace in the outlet plane is increased by increased levels of aspiration. This effect partially counter-balances the observed improvements due to the low momentum fluid caried within this vortex. This was noted especially in the 3° incidence cases for the case with the lower tested aspiration rate on the hub, where the deterioration of the total pressure level at the casing exceptionally exceeds the improvements in the hub region. However, the best improvement was measured for the 3° incidence case with the higher aspiration rate on the hub of 4%, where the average total pressure loss was reduced from 8.9% in the reference case to 7.8% and the static pressure rise was increased from 1.16 to 1.20. The measured flow angle distributions show that the extents of large regions of underturning occurring in the reference case are reduced by the aspiration, even though not reflected by the mass flow weighted averages of the flow angles. This yields more uniform outlet flow conditions that are closer to the design conditions and are thus advantageous for the matching with later compressor stages in a real machine. Also in the cases with 5° incidence, the aspiration on the hub improved the performance in terms of total pressure loss and static pressure rise for both tested rates of aspiration on the hub.

Further cases were investigated with aspiration both on the hub and on the blades. If applied with sufficient aspiration rate on the cases with 3° incidence, the aspiration on the blades complements the aspiration on the hub in the reduction of the corner separation. This is reflected by a reduced size and intensity of the separation trace in the measurement results. In all cases the pressure rise and the blade loading is increased compared to the cases without aspiration or with aspiration on the hub only. With 3.5% total aspiration rate (2% on the hub, 1.5% on the blades) a static pressure rise of 1.24 is obtained and the deflection is improved compared to the case with the highest tested aspiration applied on the hub only of 4%. The measured total pressure loss level with 8.5% is not as good as for the case with 4% aspiration on the hub only but it is improved compared to the reference case. The complementary analysis of the numerical results indicates that the improvements can be ascribed both to the increased removal of separated flow as to the removal of a certain amount of suction side boundary layer. In the cases with 5° incidence, adding the aspiration on blade increases the level of total pressure loss. The measurement results indicate that addition of the aspiration slot on the blade for the 5° incidence cases increases the separation trace in the casing region indicating an unfortunate interaction in these cases. An increased aspiration rate reduces the level of loss but it still exceeds that of the reference case. Thus adding aspiration on the blades is significantly less effective for the cases with 5° incidence than for the cases with 3° incidence.

If the number of blades is reduced while keeping the aspiration rate constant, the aspiration rate per aspiration slot increases. It was investigated if this effect can compensate the reduction in performance occurring when the number of blades is reduced from 18 to 14 thus by 22%. A positive result would be

advantageous for the overall engine mass, since less blades would be needed to achieve the same performance. The measurements show that the increase of blade loading in the cases with reduced number of blades is almost negligible compared to the corresponding cases with a higher number of blades and the same rates of aspiration. Nevertheless, in the cases with reduced number of blades, 3° incidence and maximum aspiration rate of 3.5% (2% on the hub, 1.5% on the blades), the measurements show that a total pressure loss level close to that of the reference case with more blades is obtained. The obtained static pressure rise is significantly higher than that of the reference case. However, the deflection level of the reference case is not achieved. This is ascribed mainly to the reduced overall flow guidance by the reduced number of blades. Compared to the cases with more blades and same aspiration rate applied, the performance is less good, since those cases achieve lower levels of loss and even higher static pressure rise. Thus for the higher aspiration level tested, the cases with less blades perform similarly in terms of loss and better in terms of static pressure rise than the reference case with more blades, but they do not achieve the performance of the case with more blades and same aspiration rate applied. The investigated aspiration system was however ineffective to compensate the deteriorations due to the reduced number of blades in the cases with 5° incidence.

The complementary analysis of the experimental and the numerical results yields explanations on the complex flow mechanisms by which the aspiration influences the cascade flow. With respect to the aspiration on the hub, as expected, the aspiration attracts mostly hub boundary layer flow over a large part of the slot length but also low momentum flow from within the corner separation. However, a recirculation zone can be observed in the upstream part of the hub aspiration slot, making flow spill out from the slot. This occurred in all cases excepted in those with reduced number of blades and thus higher aspiration rate per slot. The flow spilling out from the aspiration slot on the hub significantly reduces the effectiveness of the aspiration. This is visible in the experimental flow visualization and is reproduced by the simulations. The analysis allows identifying two factors that if considered together, induce the recirculation: first, the aspirated hub boundary layer separates in the hub aspiration duct short after crossing the sharp edge of the aspiration slot; second, the pressure gradient occurring on the suction side above the slot influences the flow in the slot. The latter is due to the fact that the aspiration slot on the hub extends over a significant length of the suction side. Thus the slot is exposed to the strong static pressure gradients caused by the acceleration of the main flow on the suction side. As a result, the low momentum flow of the separation in the aspiration duct is attracted towards the lower pressure occuring further upstream, forming the recirculation and making the flow spill out from the slot. This flow spilling out from the slot promotes the corner separation on the suction side, thus the slot makes the separation start further upstream instead of preventing it. In the cases with less blades and thus increased aspiration rate per slot, this effect is prevented since the recirculation is completely attracted back into the aspiration duct by the increased aspiration rate per slot and thus the lower pressure in the aspiration chamber behind it. The understanding of this mechanism gives indications on how the aspiration can be improved: a possible solution is to replace the sharp edge by a fillet on the slot to avoid separation. A further solution is to avoid that the slot connects regions that are exposed to very different pressure levels. The large slot could be replaced by a number of smaller slots connected to the internal settling chamber via independent ducts of variable sizes. The different sizes would induce different pressure drop within the ducts and compensate the different pressures occurring at the inlet of the slots. Alternatively, the slot segments could be equipped with simple and robust check valves preventing flow reversal in certain segments.

The analysis indicates that also the aspiration on the blade can be further optimized. In all cases where the corner separation is not prevented by the hub aspiration but supported by the flow spilling out at the front of the hub slot, the main flow on the suction side is raised above the separation towards the casing. The higher forward momentum of the flow close to the casing supports the aspiration into the blade slot in this region. Thus more flow is aspirated into the blade aspiration slot close to the casing than close to the hub. The high momentum and the vorticity of the aspirated flow that is deflected within the aspiration duct in the blade causes significant recirculations to occur within the duct. These separated, recirculating regions

cause a blockage that prevents further aspiration of flow into the blade slot in the region close to the hub. As a result, the aspiration on the blades is very effective close to the casing but rather ineffective close to the hub, where almost no flow is aspirated. In the cases with lower aspiration rates, the simulations indicate that some flow is even attracted out of this part of the aspiration slot on the blade towards the aspiration slot on the hub. Thus the corner separation can extend itself almost undisturbed over this part of the aspiration slot on the blade. However, in the cases with reduced number of blades, and thus increased aspiration rate per slot, the situation is significantly improved. Since the flow spilling out from the hub slot inducing the separation onset is prevented by the increased aspiration rate, the flow has a significant forward momentum over the whole blade span. This favours the aspiration over the entire height of the aspiration slot on the blade. This is further supported by the fact that in the cases with reduced number of blades, also the aspiration rate per slot of the aspiration on the blades is increased. The numerical simulations are more optimistic on the aspiration effectiveness in these configurations than the experiments. However the experiments confirm that in these cases especially the corner separation is significantly better controlled. As for the cases with added aspiration on the hub however, the size of the clearance vortex is increased by increased levels of aspiration. In the cases with reduced number of blades, also the hub boundary layer accumulating close to the suction side is thickened, probably also due to the increased blade pitch causing an increased wall friction of the cross passage flow. These observations yield a number of indications on how the aspiration concept can be improved: first, as noted in the preceding paragraph, it is essential to prevent that flow spills out from the aspiration on the hub since this deteriorates the function of the aspiration on the blade. Second, the aspiration on blade should be redesigned to ensure a more homogeneous aspiration. This can be achieved by segmentation, but also by re-orientation to avoid favouring aspiration of flow with higher forward momentum. Slots oriented normal to the blade surface should be considered. Third, close to the casing, the aspiration indeed removes the suction side boundary layer promoting the formation of a new, more resistant boundary layer; however, it should be considered if more importance should be given to flow removal close to the hub, where the separation is most relevant, renouncing to some aspiration in the rather healthy flow region close to the casing. Fourth, the growth of the clearance vortex for increased aspiration rates should be prevented, e.g. by casing treatment using part of the aspirated flow, or by a reduced clearance size, or by particular blade tip geometries as labyrinth sealings.

The results and observations of the present investigation give indications on aspects that future investigations should focus on: the measurements in the region close to the aspiration ducts and within the aspiration ducts should be multiplied to verify the numerical results in these regions. The proposed improvements to the aspiration slots should be tested. This implies testing several aspiration geometries and could be reached by concieving modular inserts allowing to test different slot geometries without rebuilding the entire cascades. The performance improvements could thereby be further increased and the needed aspiration rate could be reduced. A further step would then be the optimisation of the aspiration ducts to minimize the pressure drop within the ducts and make more pressure available to the consumers. Finally, a target engine to demonstrate this technique should be selected and a cycle analysis based on the present findings in terms of loss reduction and extraction rates should be applied to it. This will allow quantifying the overall influence on the engine performance of the aspiration technique.

Appendix A Secondary velocity results for 5° incidence
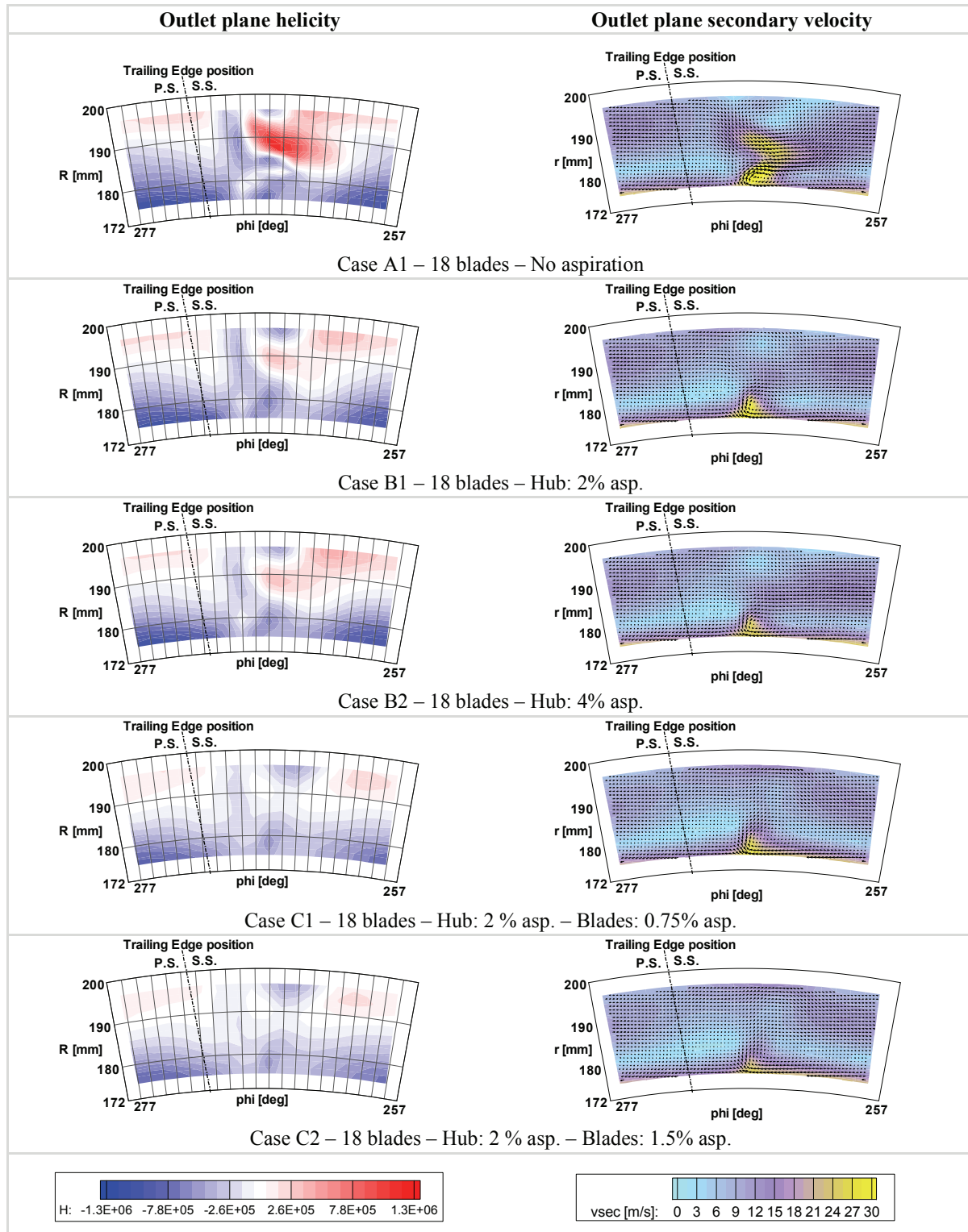
Figure 13-1. Contour plots of helicity and secondary velocities in the outlet planes based on experimental results for 5° incidence.
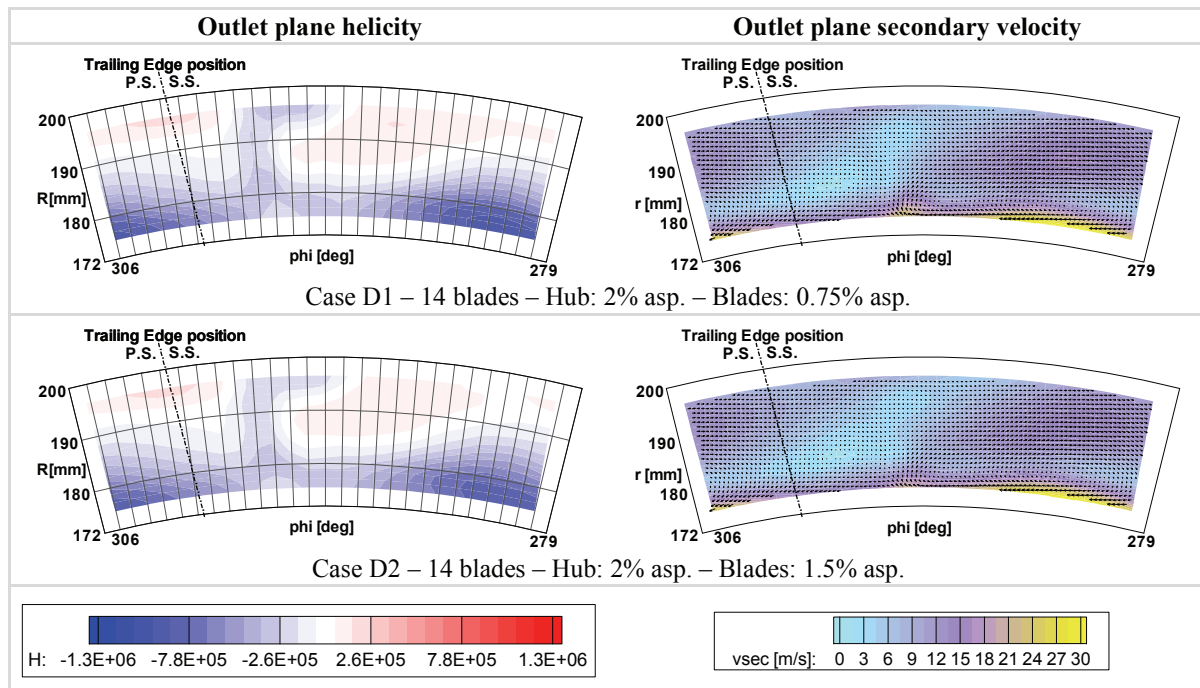
Figure 13-2. Contour plots of helicity and secondary velocities in the outlet planes based on experimental results for 5° incidence.

178

Appendix B   Casing pressure measurements

	18 blades	14 blades
Hub: No slots Blade: No slots	A1	
Hub: 2% Blade: No slots	B1	
Hub: 4% Blade: No slots	B2	
Hub: 2% Blades: 0.75%	C1	D1
Hub: 2% Blades: 1.5%	C2	D2

ps/pt1_ave: 0.40 0.45 0.49 0.54 0.58 0.63 0.67 0.71 0.76 0.81 0.85 0.90
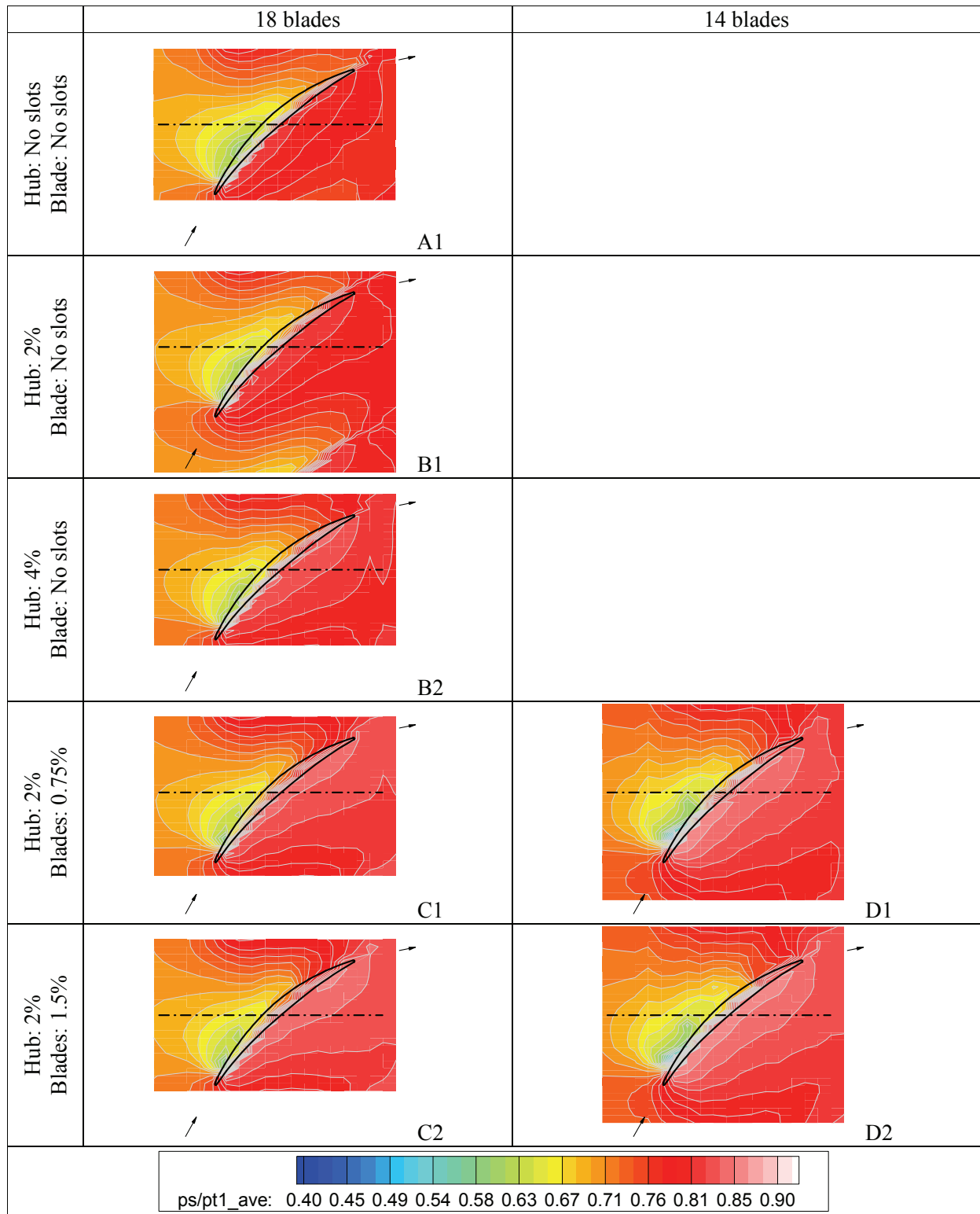
Figure 13-3. Dimensionless pressures at the casing, Ma1 ≈ 0.8, α1 ≈ 63°, 18 and 14 blades, different blade aspiration cases compared to the case without aspiration.

	18 blades	14 blades
Hub: No slots Blade: No slots	A1	
Hub: 2% Blade: No slots	B1	
Hub: 4% Blades: No slots	B2	
Hub: 2% Blades: 0.75%	C1	D1
Hub: 2% Blades: 1.5%	C2	D2

ps/pt1_ave: 0.40 0.45 0.49 0.54 0.58 0.63 0.67 0.71 0.76 0.81 0.85 0.90
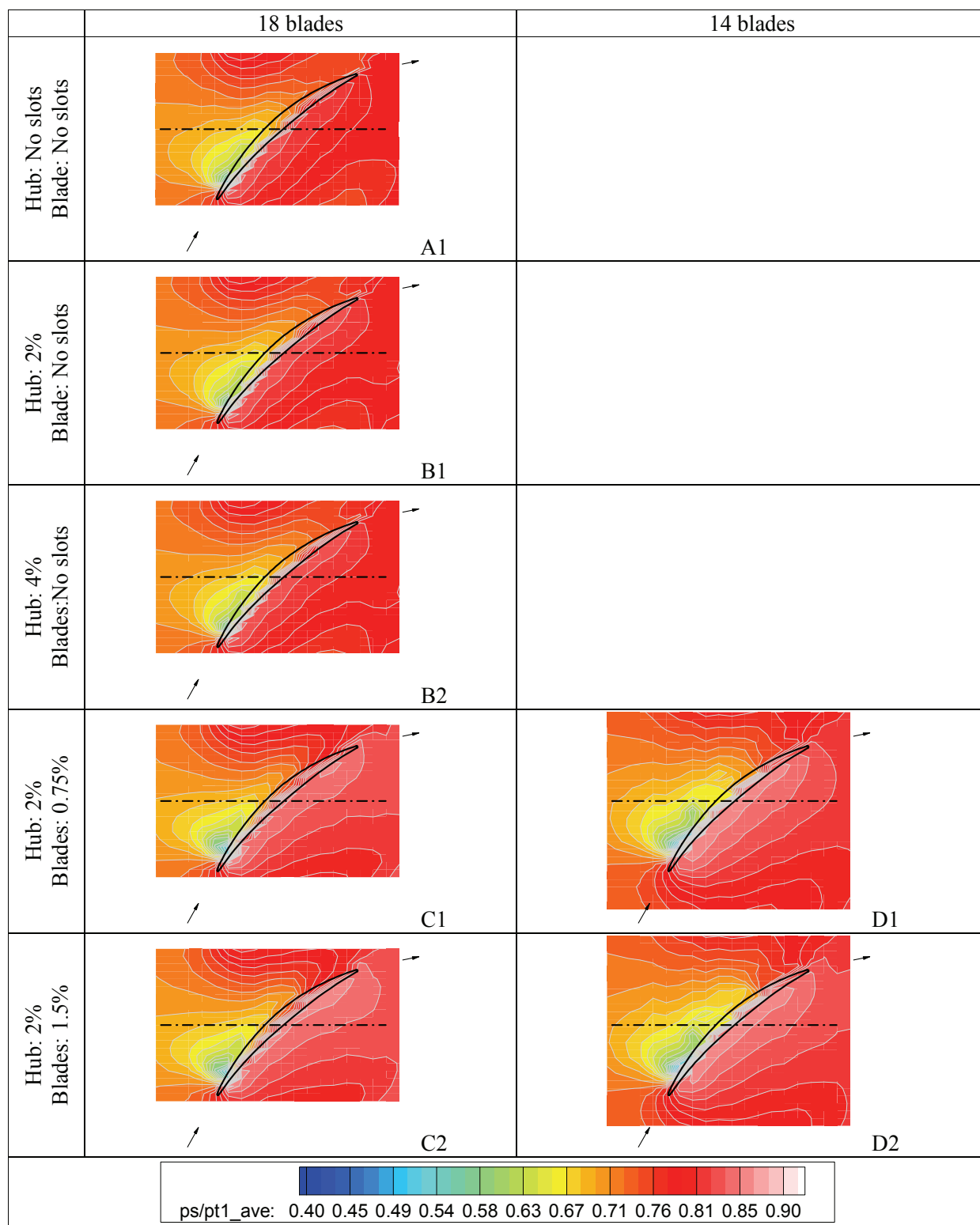
Figure 13-4. Dimensionless pressures at the casing, Ma1 ≈ 0.8, α1 ≈ 65°, 18 and 14 blades, different blade aspiration cases compared to the case without aspiration.

Appendix C   Overview of the averaged parameters

Parameter: Serie			Hub: No slots	Hub: 0	Hub: M		Hub: H
Ma_1	Alpha1	Blade aspi	18 blades	18 blades	18 blades	14 blades	18 blades
0.8	61°	No slots	s0052	s0105	s0046		s0103
	63°	No slots	s0056	s0042	s0040 s0040L		s0094
		0			s0155	s0223	
		M			s0162	s0227	
		H			s0157	s0225	
	65°	No slots	s0061	s0118	s0096		s0116
		0			s0168	s0229	
		M			s0166	s0233	
		H			s0164	s0231	
	67°	No slots		s0114	s0099		s0101
0.68	61°	0			s0177	s0253	
		M			s0181	s0251	
		H			s0179	s0249	
	63.6°	0			s0171	s0236	
		M			s0175 s0175L	s0240 s0240L	
		H			s0173 s0173L	s0238 s0238L	
	65.7°	0			s0183	s0243	
		M			s0187	s0247	
		H			s0185	s0245	

Table 13-1. Overview of the principal investigation cases. The suffix "L" indicates LDA measurements. The aspiration levels "0", "M" and "H" are defined in Table 13-9 and Table 13-10.

Applies to Ma1	Aspiration level	Aspiration rate (Table 13-6)	Aspirated Mass flow [g / s]	Aspiration per blade channel [g / s]	
				18 blades	14 blades
all	Medium	≈ 2%	105	5.8	7.5
	High	≈ 4 %	210	11.1	14.3

Table 13-2. Definition of the HUB ASPIRATION levels "Medium" and "High" for the measurements with inlet Mach number Ma1=0.8 and Ma1=0.68.

Applies to Ma1	Aspiration level	Aspiration rate (Table 13-7)	Aspirated Mass flow [g / s]	Aspiration per blade channel [g / s]	
				18 blades	14 blades
0.8	Medium	≈ 0.75%	37.5	2.1	2.7
	High	≈ 1.5 %	75	4.2	5.4
0.68	Medium	≈ 1%	50	2.8	3.6
	High	≈ 2%	100	5.6	7.1

Table 13-3. Definition of the BLADE ASPIRATION levels "Medium" and "High" for the measurements with inlet Mach number Ma1=0.8 and Ma1=0.68.

(pt1-pt2)/(pt1-ps)			Hub: No slots	Hub: 0 g/s	Hub: 100 g/s		Hub: 200 g/s
Ma1	Alpha1	Blade aspi	18 blades	18 blades	18 blades	14 blades	18 blades
0.8	61°	No slots	0.082	0.118	0.092		0.070
	63°	No slots	0.089	0.126	0.096 0.000		0.078
		0			0.100	0.104	
		M			0.094	0.098	
		H			0.085	0.091	
	65°	No slots	0.109	0.131	0.102		0.094
		0			0.141	0.158	
		M			0.133	0.154	
		H			0.123	0.152	
	67°	No slots		0.191	0.173		0.151
0.68	61°	0			0.126	0.116	
		M			0.120	0.115	
		H			0.120	0.118	
	63.6°	0			0.115	0.108	
		M			0.087 0.000	0.101 0.000	
		H			0.085 0.000	0.085 0.000	
	65.7°	0			0.140	0.166	
		M			0.132	0.162	
		H			0.126	0.163	

Legend: 0.070, 0.077, 0.085, 0.092, 0.100, 0.107, 0.115, 0.122, 0.130, 0.138, 0.145, 0.153, 0.160, 0.168, 0.175, 0.183, 0.191, LDA

Table 13-4. Averaged CD=(pt1-pt2)/(pt1-ps1) based on the aerodynamic probe measurements.

(pt1-pt2)/pt1			Hub: No slots	Hub: 0 g/s	Hub: 100 g/s		Hub: 200 g/s
Ma1	Alpha1	Blade aspi	18 blades	18 blades	18 blades	14 blades	18 blades
0.8	61°	No slots	0.027	0.040	0.031		0.023
	63°	No slots	0.031	0.043	0.033 0.000		0.027
		0			0.034	0.035	
		M			0.032	0.033	
		H			0.029	0.030	
	65°	No slots	0.037	0.045	0.034		0.033
		0			0.049	0.053	
		M			0.045	0.051	
		H			0.042	0.051	
	67°	No slots		0.066	0.060		0.052
0.68	61°	0			0.034	0.031	
		M			0.032	0.031	
		H			0.033	0.032	
	63.6°	0			0.031	0.028	
		M			0.023 0.000	0.026 0.000	
		H			0.023 0.000	0.025 0.000	
	65.7°	0			0.038	0.045	
		M			0.036	0.043	
		H			0.034	0.044	

Legend: 0.023, 0.026, 0.028, 0.031, 0.034, 0.036, 0.039, 0.042, 0.045, 0.047, 0.050, 0.053, 0.056, 0.058, 0.061, 0.064, 0.066, LDA

Table 13-5. Averaged stagnation pressure loss (pt1-pt2/pt1) based on the aerodynamic probe measurements.

mdot_aspi_hub/mdot1			Hub: No slots	Hub: 0 g/s	Hub: 100 g/s				Hub: 200 g/s	Legend
Ma1	Alpha1	Blade aspi	18 blades	18 blades	18 blades	LDA	14 blades	LDA	18 blades	
0.8	61°	No slots	0.0%	0.0%	1.9%				3.8%	0.0%
	63°	No slots	0.0%	0.0%	2.0%	0.000			4.1%	0.3%
		0			2.1%		2.0%			0.6%
		M			2.1%		2.1%			0.9%
		H			2.1%		2.1%			1.2%
	65°	No slots	0.0%	0.0%	2.2%				4.6%	1.5%
		0			2.2%		2.3%			1.8%
		M			2.3%		2.3%			2.2%
		H			2.3%		2.3%			2.5%
	67°	No slots		0.0%	2.4%				4.9%	2.8%
0.68	61°	0			2.1%		2.2%			3.1%
		M			2.2%		2.2%			3.4%
		H			2.1%		2.2%			3.7%
	63.6°	0			2.4%		2.4%			4.0%
		M			2.4%	0.000	2.4%	0.000		4.3%
		H			2.4%	0.000	2.4%	0.000		4.6%
	65.7°	0			2.5%		2.6%			4.9%
		M			2.5%		2.6%			
		H			2.6%		2.6%			LDA

Table 13-6. Mass flow ratio of aspiration on the hub (considering the decrease of inlet mass flow for higher inlet flow angles with inlet Mach number kept constant).

mdot_aspi_blades/mdot1			Hub: No slots	Hub: 0 g/s	Hub: 100 g/s				Hub: 200 g/s	Legend
Ma1	Alpha1	Blade aspi	18 blades	18 blades	18 blades	LDA	14 blades	LDA	18 blades	
0.8	61°	No slots	0.0%	0.0%	0.0%				0.0%	0.0%
	63°	No slots	0.0%	0.0%	0.0%	0.000			0.0%	0.1%
		0			0.0%		0.0%			0.3%
		M			0.7%		0.7%			0.4%
		H			1.5%		1.5%			0.6%
	65°	No slots	0.0%	0.0%	0.0%				0.0%	0.7%
		0			0.0%		0.0%			0.9%
		M			0.8%		0.8%			1.0%
		H			1.6%		1.6%			1.2%
	67°	No slots		0.0%	0.0%				0.0%	1.3%
0.68	61°	0			0.0%		0.0%			1.4%
		M			1.0%		1.0%			1.6%
		H			2.0%		1.9%			1.7%
	63.6°	0			0.0%		0.0%			1.9%
		M			1.1%	0.000	1.2%	0.000		2.0%
		H			2.3%	0.000	2.1%	0.000		2.2%
	65.7°	0			0.0%		0.0%			2.3%
		M			1.2%		1.3%			
		H			2.3%		2.1%			LDA

Table 13-7. Mass flow ratio of aspiration on the blades (considering the decrease of inlet mass flow for higher inlet flow angles with inlet Mach number kept constant).

alpha1-alpha2 [°]			Hub: No slots	Hub: 0 g/s	Hub: 100 g/s		Hub: 200 g/s	Legend
Ma1	Alpha1	Blade aspi	18 blades	18 blades	18 blades	14 blades	18 blades	
0.8	61°	No slots	27.398	26.948	27.415		27.446	26.948
	63°	No slots	28.816	28.121	28.601 28.531		28.237	27.262
		0			28.138	27.595		27.577
		M			28.450	27.818		27.891
		H			28.757	27.852		28.205
	65°	No slots	29.935	29.589	29.831		29.857	28.519
		0			29.231	28.679		28.833
		M			29.583	28.300		29.147
		H			29.606	28.052		29.461
	67°	No slots		31.692	31.571		31.214	29.775
0.68	61°	0			28.691	27.658		30.090
		M			29.627	28.604		30.404
		H			29.786	28.701		30.718
	63.6°	0			29.477	28.873		31.032
		M			30.738 31.513	29.691 31.461		31.346
		H			31.203 31.974	29.899 31.648		31.660
	65.7°	0			30.832	29.557		31.974
		M			30.993	28.895		
		H			31.690	28.729		LDA

Table 13-8. Averaged deflection (α1-α2) based on the aerodynamic probe measurements.

ps2/ps1 from probe			Hub: No slots	Hub: 0 g/s	Hub: 100 g/s		Hub: 200 g/s	Legend
Ma1	Alpha1	Blade aspi	18 blades	18 blades	18 blades	14 blades	18 blades	
0.8	61°	No slots	1.140	1.107	1.162		1.190	1.107
	63°	No slots	1.159	1.132	1.181 0.000		1.202	1.116
		0			1.205	1.187		1.124
		M			1.221	1.203		1.133
		H			1.237	1.213		1.141
	65°	No slots	1.167	1.151	1.186		1.229	1.150
		0			1.216	1.186		1.158
		M			1.230	1.198		1.167
		H			1.243	1.207		1.175
	67°	No slots		1.155	1.184		1.216	1.184
0.68	61°	0			1.135	1.129		1.192
		M			1.150	1.144		1.201
		H			1.156	1.148		1.209
	63.6°	0			1.158	1.141		1.218
		M			1.178 0.000	1.161 0.000		1.226
		H			1.187 0.000	1.168 0.000		1.235
	65.7°	0			1.163	1.139		1.243
		M			1.178	1.152		
		H			1.186	1.157		LDA

Table 13-9. Averaged static pressure rise (ps2/ps1) based on the aerodynamic probe measurements.

Ma1	Alpha1	Blade aspi	Hub: No slots 18 blades	Hub: 0 g/s 18 blades	Hub: 100 g/s 18 blades	Hub: 100 g/s 14 blades	Hub: 200 g/s 18 blades
0.8	61°	No slots	1.314	1.267	1.372		1.421
	63°	No slots	1.358	1.333	1.425 / 1.462		1.472
		0			1.512	1.445	
		M			1.556	1.493	
		H			1.593	1.518	
	65°	No slots	1.417	1.389	1.463		1.575
		0			1.619	1.517	
		M			1.671	1.559	
		H			1.701	1.585	
	67°	No slots		1.481	1.558		1.646
0.68	61°	0			1.468	1.419	
		M			1.522	1.480	
		H			1.537	1.502	
	63.6°	0			1.561	1.473	
		M			1.622 / 1.659	1.560 / 1.583	
		H			1.659 / 1.686	1.586 / 1.603	
	65.7°	0			1.631	1.530	
		M			1.699	1.593	
		H			1.760	1.624	

Legend: 1.267, 1.298, 1.329, 1.359, 1.390, 1.421, 1.452, 1.483, 1.513, 1.544, 1.575, 1.606, 1.637, 1.667, 1.698, 1.729, 1.760; LDA

Table 13-10. Averaged deceleration (Ma1/Ma2) based on the aerodynamic probe measurements.

Appendix D   References

Anxionnaz, R. (1955). *Perfectionnements aux machines axiales de compression de fluide*. S. d. l. P. Industrielle. France.

Arts, T., Boerrigter, H. L., Buchlin, J.-M., Carbonaro, M., Degrez, G., Dénos, R., Fletcher, D., Olivari, D., Riethmuller, M. L. and Braembussche, R. A. V. d. (2002). *Measurement Techniques in Fluid Dynamics*. Von Karman Institute for Fluid Dynamics.

Bario, F., Halter, G., Azouzi, A. and Jeandot, M. (2008). *Mesures LDA sur NEWAC*. Internal presentation of project NEWAC 21/01/2008.

Bölcs, A. (1983). *A Test Facility for Investigation of Steady and Unsteady Transonic Flows in Annular Cascades*. 83-GT-34, ASME Turbo Expo 1983, Phoenix, Arizona, March 27-31, 1983.

Cambier, L. and Veuillot, J. P. (2008). *Status of the elsA CFD Software for Flow Simulation and Multidisciplinary Applications*. 46th AIAA Aerospace Science Meeting and Exhibit, Reno, Nevada, Jannuary 7-10, 2008.

Carmody, R. H., Horn, R. A., Jr. and Seren, G. (1969). *Single-stage experimental evaluation of boundary layer bleed techniques for high lift stator blades. Part 4 - Data and performance of triple-slotted 0.75 hub diffusion factor stator* NASA, 19690030287.

Cartieri, A. (2008). *NEWAC – WP5.3.1 Aspiration aube EPB9 – Point des activités ONERA*. ONERA.

Castillon, L. and Gaveriaux, R. (2009). *NEWAC - WP5.3 - Configuration aspirée: Calculs sur la séconde campagne d'essais*. presentation during WP5.3 technical meeting.

Castillon, L. and Gavériaux, R. (2006). *NEWAC - WP5.3 - Configuration aspirée - Aspiration sur paroi interne*. ONERA.

Colombo, E. (2008). *NEWAC Deliverable D5.3.1B : Test report of the first configuration without aspiration*. D5.3.1B.

Colombo, E. (2009). *NEWAC Deliverable D5.3.1D : Test report of the first configuration with blade aspiration.*, D5.3.1D.

Colombo, E. (2009). *Reference frame transformations for measurements with L-shaped 5-hole-probes in an annular cascade*. LTT-09-01.

Colombo, E. (2010). *Investigations on axial compressor cascades with aspiration on blades and hub*. European Workshop on New Aero Engine Concepts, Munich, June 30th to July 1st.

Colombo, E., Bario, F., Ott, P. (2009). *Experimental Investigations on Active Flow Control by Aspiration slots on the Hub of an Axial Compressor Rotor Geometry in a Non Rotating Annular Cascade*. 8th European Turbomachinery Conference, Graz

Colombo, E., Castillon, L. and Ott, P. (2011). *Influence of Blade Aspiration on the Flow Quality of an Annular Axial Compressor Cascade*. European Turbomachinery Conference, Istanbul, Turkey, March 21-25, 2011.

Colombo, E., Deslot, C. and Ott, P. (2010). *NEWAC WP5.3.1 presentation: Investigations on the inlet flow conditions*. Lausanne.

Colombo, E., Deslot, C., Ott, P., Bario, F. and Castillon, L. (2010). *NEWAC Deliverable D5.3.1E - Test report of the second configuration (highly loaded blade)*.

Conrad, O. (1969). *Leitschaufeln von Axialverdichtern*. D. Patentamt. Germany.

Crabtree, L. F., Küchemann, D. and Sowerby, L. (1963). *Three-Dimensional Boundary Layers*. Laminar Boundary Layer Theory, Sect. VIII 26, ed. L. Rosenhead, Oxford University Press.

Cumpsty, N. A. (2004). *Compressor aerodynamics*. Malabar, Florida, Krieger Publishing.

Cumpsty, N. A. and Horlock, J. H. (2006). *Averaging Nonuniform Flow for a Purpose*. Journal of Turbomachinery 128(1): 120-129.

Délery, J. and Meauzé, G. (2003). *A detailed experimental analysis of the flow in a highly loaded fixed compressor cascade: the iso-cascade co-operative programme on code validation*. Aerospace Science and Technology 7(1): 1-9.

Délery, J. M. (2001). *Livret du cours: Décollement en écoulement tridimensionnel stationnaire - Points singuliers, lignes séparatrices et tourbillons*. ONERA.

Délery, J. M. (2001). *Robert Legendre and Henri Werlé: Toward the Elucidation of Three-Dimensional Separation*. Annual Review of Fluid Mechanics 33(1): 129.

Denton, J. D. (1993). *The 1993 IGTI Scholar Lecture: Loss Mechanisms in Turbomachines*. Journal of Turbomachinery 115(4): 621-656.

Deslot, C. and Colombo, E. (2010). *NEWAC WP5.3.1 presentation: Numerical investigations on the flow mechanisms related to the turbulence and helicity levels identified at the test section inlet of the LTT Non Rotating Annular Cascade*. Lausanne.

Deslot, C., Colombo, E., Leboeuf, F., Charbonnier, D. and Ott, P. (2011). *Characterization of the Flow Generated in an Annular Test Facility*. European Turbomachinery Conference, Istanbul, Turkey, March 21-25, 2011.

Durand, W. F. and Daniel Guggenheim Fund for the Promotion of Aeronautics. (1934). *Aerodynamic theory; a general review of progress, under a grant of the Guggenheim fund for the promotion of aeronautics*. Berlin,, J. Springer.

Ellis, D. L. (1937). *Improvements in or connected with Airscrews*. UK.

Erwin, J. R. (1955). *Continuous Boundary Layer Control in Compressors*. U. S. P. Office. US.

Gbadebo, S. A., Cumpsty, N. A. and Hynes, T. P. (2005). *Three-Dimensional Separations in Axial Compressors*. Journal of Turbomachinery 127(2): 331-339.

Godard, A., Fourmaux, A., Burguburu, S. and Leboeuf, F. (2008). *Design Method of a subsonic aspirated cascade*. ASME Turbo Expo 2008, Berlin

Goldstein, S. (1965). *Modern Developments in Fluid Dynamics Volume II*.

Greitzer, E. M., Epstein, A. H., Kerrebrock, J. L. and Tan, C. S. (1996). *Unsteady and Three-Dimensional Flow in Turbomachines*. Massachusettes Inst. of Tech. Cambridge. Dept. of Aeronautics and Astronautics.

Greitzer, E. M., Tan, C. S. and Graf, M. B. (2004). *Internal flow concepts and applications*. Cambridge, Cambridge University Press.

Grieb, H. (2009). *Verdichter für Turbo-Flugtriebwerke*. Springer.

Hathaway, M. D., Chriss, R. M., Wood, J. R. and Strazisar, A. J. (1993). *Experimental and Computational Investigation of the NASA Low-Speed Centrifugal Compressor Flow Field*. Journal of Turbomachinery 115(3): 527-541.

Hebert, G. J. and Tiederman, W. G. (1990). *Comparison of Steady and Unsteady Secondary Flows in a Turbine Stator Cascade*. Journal of Turbomachinery 112(4): 625-632.

Horlock, J. H. and Denton, J. D. (2005). *A Review of Some Early Design Practice Using Computational Fluid Dynamics and a Current Perspective*. Journal of Turbomachinery 127(1): 5-13.

Horlock, J. H. and Lakshminarayana, B. (1973). *Secondary Flows: Theory, Experiment, and Application in Turbomachinery Aerodynamics*. Annual Review of Fluid Mechanics 5(1): 247-280.

Horlock, J. H., Louis, J. F., Percival, P. M. and Lakshmin.B (1966). *Wall Stall in Compressor Cascades*. Journal of Basic Engineering 88(3): 637-&.

Hubrich, K. (2005). *Highly loaded compressor with boundary layer suction*. LTT. Lausanne, EPFL. PhD.

Japikse, D. and Baines, N. C. (1994). *Introduction to turbomachinery*. Norwich, Vt. Oxford, Concepts ETI ; Oxford University Press.

Joseph, D. D. (2010). *The Role of Potential Flow in the Theory of the Navier-Stokes Equations*. Advances in Mathematical Fluid Mechanics: 311-317.

Joslyn, H. D. and Dring, R. P. (1985). *Axial Compressor Stator Aerodynamics*. Journal of Engineering for Gas Turbines and Power 107: 485-493.

Kang, S. and Hirsch, C. (1996). *Tip Clearance Flow and Loss in Axial Compressor Cascades*. Loss Mechanisms and Unsteady Flows in Turbomachines R. E. Henderson and D. K. Hennecke. AGARD CP-571.

Kenwright, D. N., Henze, C. and Levit, C. (1999). *Feature Extraction of Separation and Attachment Lines*. IEEE Transactions on Visualization and Computer Graphics 5(2).

Kerrebrock, J. L., Drela, M., Merchant, A. A. and Schuler, B. J. (1998). *A Family of Designs for Aspirated Compressors*. 98-GT-196, International Gas Turbine & Aeroengine Congress & Exhibition, Stockholm, Sweden

Kerrebrock, J. L., Reijnen, D. P., Ziminsky, W. S. and Smilg, L. M. (1997). *Aspirated Compressors*. 97-GT-525, Gas Turbine & Aeroengine Congress & Exhibition, Orlando, Florida, June 2-June 5, 1997.

Lakshminarayana, B. (1996). *Fluid dynamics and heat transfer of turbomachinery*. New York [etc.], Wiley.

Langston, L. S. (2001). *Secondary Flows in Axial Turbines—A Review*. Annals of the New York Academy of Sciences 934.

Leboeuf, F. (2007). *Sur le calcul de l'énergie cinétique secondaire*.

Leboeuf, F. (2008). *Ecoulements 3D dans les turbomachines*. Cours d'Option Aéronautique, Filière Propulsion de l'Ecole Centrale de Lyon. Lyon.

Lei, V. M., Spakovszky, Z. S. and Greitzer, E. M. (2006). *A criterion for axial compressor hub-corner stall*. Proceedings of the ASME Turbo Expo 2006, Vol 6, Pts A and B: 475-486.

Lei, V. M., Spakovszky, Z. S. and Greitzer, E. M. (2008). *A criterion for axial compressor hub-corner stall*. Journal of Turbomachinery-Transactions of the Asme 130(3).

Levy, Y., Degani, D. and Seginer, A. (1990). *Graphical Visualization of Vortical Flows by means of Helicity*. Aiaa Journal 28(8): 1347-1352.

Lighthill, M. J. (1963). *Attachment and separation in three-dimensional flows*. Laminar Boundary Layers, Sect. II 2.6, ed. L. Rosenhead, Oxford University Press.

Lighthill, M. J. (1963). *Introduction to Boundary Layer Theory*. Laminar Boundary Layers, Sect. II, ed. L. Rosenhead, Oxford University Press.

Lord, W. K., MacMartin, D. G. and Tillman, T. G. (2000). *Flow Control Opportunities in Gas Turbine Engines*. AIAA 2000-2234, Fluids 2000, Denver, CO, 19-22 June 2000.

Loughery, R. J., Horn, R. A., Jr. and Tramm, P. C. (1971). *Single stage experimental evaluation of boundary layer blowing and bleed techniques for high lift stator blades*. NASA, 19710009274.

Marchal, P. and Sieverding, C. H. (1977). *Secondary flows within turbomachinery bladings*. Secondary Flows in Turbomachines. AGARD, AGARD CP No. 214 Paper No. 11.

Merchant, A. (2003). *Aerodynamic Design and Performance of Aspirated Airfoils*. Journal of Turbomachinery 125(1): 141-148.

Merchant, A. A. (2002). *Aerodynamic Design and Performance of Aspirated Airfoils*. GT2002-30369, ASME Turbo Expo

Merchant, A. A., Drela, M. and Kerrebrock, J. L. (2000). *Aerodynamic Design and Analysis of a High Pressure Ration Aspirated Compressor Stage*. 2000-GT-2619, ASME Turbo Expo, Munich, Germany

Merchant, A. A., Kerrebrock, J. L., Adamczyk, J. J. and Braunscheidel, E. P. (2004). *Experimental Investigation of a High Pressure Ratio Aspirated Fan Stage*. GT2004-53679, ASME Turbo Expo

Miller, M. L. and Chapman, D. C. (1968). *Single stage experimental evaluation of boundary layer blowing and bleed techniques for high lift stator blades - I. Compressor Design*. NASA, 19680019149.

Mirzaei, E. and Colombo, E. (2008). *Setup, Calibration and Testing of the Aspiration Mass Flow Monitoring System for the Non Rotating Annular Cascade Test Facility*. Master Thesis. S.-I.-L. EPFL.

Moffatt, H. K. (1969). *Degree of Knottedness of Tangled Vortex Lines*. Journal of Fluid Mechanics 35: 117-&.

Moffatt, H. K. and Tsinober, A. (1992). *Helicity in Laminar and Turbulent-Flow*. Annual Review of Fluid Mechanics 24: 281-312.

Moore, J., Shaffer, D. M. and Moore, J. G. (1987). *Reynolds Stresses and Dissipation Mechanisms downstream of a Turbine Cascade*. Journal of Turbomachinery-Transactions of the Asme 109(2): 258-267.

Morino, L. (1990). *Helmholtz and Poincaré Potential - Vorticity Decompositions for the Analysis of Unsteady Compressible Viscous Flows*.

Peacock, R. E. (1971). *Boundary-Layer Suction to Eliminate Corner Separation in Cascade Aerofoils*. Aeronautical Research Council Reports and Memoranda. C. University Engineering Department. Cambridge, Ministry of Defence.

Peng, W. W. (2008). *Fundamentals of turbomachinery*. Hoboken, N.J., J. Wiley.

Pianko, M. and Wazelt, F. (1982). *Propulsion and energetics panel working group 14 on suitable averaging techniques in nonuniform internal flows*. AGARD, AGARD-AR-182.

Powers, J. M. (2011). *Lecture Notes on Intermediate Fluid Mechanics*. Department of Aerospace and Mechanical Engineering, University of Notre Dame, Indiana.

Prandtl, L. (1904). *Über Flüssigkeitsbewegung bei sehr kleiner Reibung*. Verh. III. Intern. Math. Kongr., Heidelberg, 1904, S. 484-491, Teubner, Leipzig, 1905, III. Internationaler Mathematiker Kongress, Heidelberg

Prandtl, L. and Tietjens, O. (1929). *Hydro- und Aeromechanik nach Vorlesungen von L. Prandtl*. Berlin.

Quentin, F. and Szodruch, J. (2008). *ACARE 2008 Addendum to the Strategic Research Agenda*. A. C. f. A. R. i. E. (ACARE).

Reijnen, D. P. (1997). *Experimental study of boundary layer suction in a transonic compressor*. Dept. of Aeronautics and Astronautics, Massachusetts Institute of Technology. PhD.

Remy, S. (2010). *Aircraft Requirements for Future Aero Engine (presentation by the Head of Airbus CoC Powerplant)*. European Workshop on New Aero Engine Core Concepts, München

Sachdeva, A. (2007). *Sensitivity Analysis for EPB9 - Hub separation*. Snecma.

Sachdeva, A. (2010). *Application of boundary layer aspiration on blades and endwalls to improve the performance of gas turbine compressors*. Ecole Centrale de Lyon. PhD.

Sachdeva, A., Touyeras, A., Obrecht, T., Leboeuf, F. (2008). *Control of Hub Corner Separation on a Stator Blade with Boundary Layer Aspiration*. 3AF, Poitiers, France

Schlichting, H. (1965). *Grenzschicht-Theorie*. Karlsruhe, Braun.

Schuler, B. J., Kerrebrock, J. L. and Merchant, A. A. (2002). *Experimental Investigation of an Aspirated Fan Stage*. GT-2002-30370, ASME Turbo Expo

Schulz, H. D. and Gallus, H. D. (1988). *Experimental Investigation of the Three-Dimensional Flow in an Annular Compressor Cascade*. Journal of Turbomachinery 110(4): 467-478.

Schulz, H. D., Gallus, H. E. and Lakshminarayana, B. (1990). *Three-Dimensional Separated Flow Field in the Endwall Region of an Annular Compressor Cascade in the Presence of Rotor-Stator Interaction: Part 1---Quasi-Steady Flow Field and Comparison With Steady-State Data*. Journal of Turbomachinery 112(4): 669-678.

Sieverding, C. H. (1985). *Recent Progress in the Understanding of Basic Aspects of Secondary Flows in Turbine Blade Passages*. Journal of Engineering for Gas Turbines and Power-Transactions of the Asme 107(2): 248-257.

Stalker, E. A. (1946). *Axial Blower*. U. S. P. Office. US.

Stalker, E. A. (1952). *Compressors*. U. S. P. Office. US.

Stratford, B. S. (1973). *The prevention of separation and flow reversal in the corners of compressor blade cascades*. Aeronautical Journal 77: 249-256.

Surana, A., Grunberg, O. and Haller, G. (2006). *Exact theory of three-dimensional flow separation. Part 1. Steady separation*. Journal of Fluid Mechanics 564(-1): 57-103.

Tobak, M. and Peake, D. J. (1982). *Topology of Three-Dimensional Separated Flows*. Annual Review of Fluid Mechanics 14: 61-85.

Traupel, W. (1977). *Thermische Turbomaschinen*. Berlin [etc.], Springer.

Ubaldi, M., Zunino, P., Cattanei, A. (1993). *Relative Flow and Turbulence Measurements Downstreqam of a Backward Swept Centrifugal Impeller*. Journal of Turbomachinery 115: 543-551.

Vogel, G. (1998). *5 Hole probe: Calibration, aquisition and data reduction under Labview*. LTT.

Wojciak, J., Colombo, E. and Chenaux, V. (2007). *Calibration, Testing and Measuring within the Scope of Non Rotating Annular Cascade Experiments*. LTT, EPFL. Master Project.

Zhang, H., Wang, S. and Wang, Z. (2007). *Variation of Vortex Structure in a Compressor Cascade at Different Incidences*. Journal of Propulsion and Power 23(1).

Diplom-Ingenieur
Elia Colombo

elia.colombo@gmail.com

Born 06.05.1981
German and Italian nationality
Fluent in German, French and Italian, good in English

Work experience

2006 – 2011 **Swiss Federal Institute of Technology, Lausanne (EPFL)**
Laboratory of applied Thermodynamics and Turbomachinery (LTT)
Scientific assistant: Project work, organisation, tutoring, responsible for the machine park, design of installation modifications, procurements, experimentation and analysis

2003 – 2005 **German Aerospace Center Stuttgart, Germany (DLR)**
Student assistant at the Institute of Combustion Technology and Laser Diagnostics
Laser-diagnostic combustion measurements, development of analysis software for result post-processing and image treatment (OH-LIF, 1D-RAMAN)

2001 – 2002 **Orbitale Hochtechnologie Bremen System AG, Germany (OHB System)**
Internship at the department of thermal analysis for space applications
Development of analysis tools, performing of thermal component validation experiments

1999 – 2000 Different internships in Germany and Italy: domains of mechanical engineering, manufacturing and casting

Part-time: Translation; private lessons in engineering design, mathematics, chemistry, languages

Education

2006 – 2011 **Swiss Federal Institute of Technology in Lausanne, Switzerland (EPFL)**
Laboratory of applied Thermodynamics and Turbomachinery (LTT)
PhD research within the European project NEWAC with industrial and academic partners
Post-grade courses: Project management, measurement techniques, numerical methods

1999 – 2006 **Stuttgart University, Germany**
Dipl.-Ing. in Aerospace Engineering, specialities: turbomachinery and thermodynamics
Diploma project, EPFL: Numerical analysis on a showerhead-cooled blade model
Student project, DLR: Laserdiagnostic 1D-RAMAN system, software dev. and experiments

1987 – 1999 **Scuola Europea di Varese, Italy**
European A-Levels, specialities: mathematics, physics, chemistry, biology, languages

Personal interests

Sport: Cross country ski, climbing, hiking, mountain-bike
Misc.: Languages, music, IT